Aus der Klinik für Strahlentherapie und Radioonkologie

Direktorin: Prof. Dr. med. Rita Engenhart-Cabillic

des Fachbereichs Medizin der Philipps-Universität Marburg

Monte-Carlo-Simulationen zur Referenzdosimetrie hochenergetischer Photonen und Elektronenstrahlung in der Radioonkologie

Inaugural-Dissertation

zur
Erlangung des Doktorgrades der Medizinwissenschaften
(Dr. rer. med.)
dem Fachbereich Medizin der Philipps-Universität Marburg

vorgelegt von

Philip William von Voigts-Rhetz
aus Starnberg

Marburg, 2019

Angenommen vom Fachbereich Medizin der Philipps-Universität Marburg am: 16.05.2019

Gedruckt mit Genehmigung des Fachbereichs.

Dekan:	Prof. Dr. Helmut Schäfer
Referent:	Prof. Dr. med. Dipl.-Phys. Hilke Vorwerk
	Prof. Dr. rer. nat. Klemens Zink
1. Korreferent:	Prof. Dr. rer. nat. Christoph Bert

Die vorliegende kumulative Dissertation stellt eine Zusammenfassung der Forschungsergebnisse dar, die in den folgen Publikationen in internationalen Zeitschriften veröffent-licht wurden sind:

[1] **von Voigts-Rhetz, P.**; Czarnecki, Damian; Zink, Klemens: Effective point of measurement for parallel plate and cylindrical ion chambers in megavoltage electron beams. In: Z Med Phys 24 (2014) 216-223 DOI: 10.1016/j.zemedi.2013.12.001

[2] Zink, K.; Czarnecki, D.; Looe, H. K.; **von Voigts-Rhetz, P.**; Harder, D.: Monte Carlo study of the depth-dependent fluence perturbation in parallel-plate ionization chambers in electron beams. In: Med. Phys. 41 (2014) 111707 DOI: 10.1118/1.4897389

[3] **von Voigts-Rhetz, P.**; Vorwerk, H.; Zink, K.: On the perturbation correction factor pcav of the Markus parallel-plate ion chamber in clinical electron beams. In: Int. J. Med. Phys. Clin.Eng. Rad. Oncol.6 (2017) 150-161 DOI: 10.4236/ijmpcero.2017.62014

[4] Anton, M.; Kapsch, R-P; Krauss, A.; **von Voigts-Rhetz, P.**; Zink, K.; McEwen, M.: Difference in the relative response of the alanine dosimeter to megavoltage x-ray and electron beams. In: Phys. Med. Biol. 58 (2013) 3259-3282 DOI: 10.1088/0031-9155/58/10/3259

[5] Anton, M.; Hackel, T.; Zink, K.; **von Voigts-Rhetz, P.**; Selbach, H-J: Response of the alanine/ESR dosimeter to radiation from an Ir-192 HDR brachytherapy source. In: Phys. Med. Biol. 60 (2015) 175-193 DOI: 10.1088/0031-9155/60/1/175

[6] **von Voigts-Rhetz, P.**; Anton, M.; Vorwerk, H.; Zink, K.: Perturbation correction for alanine dosimeters in different phantom materials in high-energy photon beams. In: Phys. Med. Biol. 61 (2016) N70-N79 DOI: 10.1088/0031-9155/61/3/N70

[7] Wagner D.M.; Hüttenrauch P; Anton, M.; **von Voigts-Rhetz, P.**; Zink, K.; Wolff H.A: Feasibility study of entrance and exit dose measurements at the contra lateral breast with alanine/electron spin resonance dosimetry in volumetric modulated radiotherapy of breast cancer. In: Phys. Med. Biol. 62 (2017) 5462-5472 DOI: 10.1088/1361-6560/aa6ee2

Alle Publikationen der vorliegenden Dissertation sind online verfügbar und jeweils mit einer Abdruckgenehmigung ([1] Elsevier, [2] American Association of Physicists in Medicine (AAPM) und [4,5,6,7] bei Institute of Physics (IOP) Publishing) versehen.

Zusammenfassung

In den letzten Jahren haben sich neue Bestrahlungstechniken (Intensitätsmodulierte Strahlentherapie, Rapid Arc, Stereotaxie oder Bestrahlung am Linearbeschleuniger ohne Ausgleichsfilter) in der Radioonkologie etabliert, welche eine stetige Anpassung und Erweiterung an die Qualitätssicherungs-Anforderungen mit sich bringt. Eine für die Strahlentherapie wesentliche Norm ist die DIN 6800-2, in der die grundlegenden Anforderungen und Korrektionsfaktoren für die Dosimetrie hochenergetischer Röntgen- und Elektronenstrahlung festgelegt sind.

In der klinischen Referenz-Dosimetrie nach DIN 6800-2 werden größtenteils luftgefüllte Ionisationskammern oder Festköperdetektoren verwendet. Diese werden in einem Kalibrierlabor zuvor unter Referenzbedingungen kalibriert und im klinischen Einsatz an die veränderten Bezugsbedingungen angepasst.

Als gängiges Verfahren zur Verbesserung der Qualitätssicherung wird in der medizinischen Physik die Monte-Carlo-Simulation eingesetzt. Mit diesem numerischen Ansatz lässt sich der komplexe Strahlentransport in Materie nachvollziehen. Darüber hinaus lassen sich mit der Monte-Carlo-Simulation experimentelle Untersuchungen verifizieren und für die Referenzdosimetrie benötigte Korrektions- und Störungsfaktoren für verschiedene Detektortypen berechnen.

In der vorliegenden kumulativen Dissertation werden neue Ergebnisse aus dem Bereich der Referenzdosimetrie mittels Monte-Carlo-Simulation für hochenergetischer Photonen und Elektronenstrahlung vorgestellt. Die peer-review Publikationen aus dem Gebiet der Elektronendosimetrie mit Ionisationskammern stellen neue Erkenntnisse, welche die Annahmen der Normung bezüglich der Fluenzstörung revidieren, vor. Des Weiteren wurde das Konzept der Positionierung im effektiven Messort von Flachkammern in hochenergetischer Photonenstrahlung und Elektronenstrahlung erweitert und überarbeitet. Im zweiten Teil dieser Arbeit wurden Alanin Festkörper-Dosimeter untersucht und Korrektionsfaktoren für die Anwendung in hochenergetischen Photonen- und in ^{192}Ir-Strahlung vorgestellt. Aufbauend auf diesen Ergebnissen wurde das Ansprechvermögen von Alanin-Dosimetern in Abhängigkeit des Messumgebungsmaterials untersucht und in einer klinischen Studie angewendet.

Die Ergebnisse dieser Arbeiten stellen einen weiteren Schritt im Rahmen der stetigen Verbesserung der Qualitätssicherung in der Strahlentherapie da. Neben der Optimierung bereits etablierter Dosimetrie-Verfahren wurde an der Entwicklung eines neuen Sekundärstandards mitgearbeitet.

Summary

In recent years, new irradiation techniques (intensity modulated radiation therapy, rapid arc, stereotaxy or irradiation on a flattening filter free linear accelerator) established successful in radiooncology, which entail a constant adaptation and expansion to quality assurance requirements. An essential code of practice for radiation therapy is DIN 6800-2, which defines the basic requirements and correction factors for the dosimetry of high-energy X-ray and electron radiation.

In clinical reference dosimetry according to DIN 6800-2, mostly air-filled ionization chambers or solid-state detectors are used. These are previously calibrated in a calibration laboratory in accordance with reference conditions and later adapted to the measurement conditions.

Monte Carlo simulations are a common procedure in medical physics for improving quality assurance. With this numerical approach, the complex beam transport in matter can be understood. Furthermore, experimental investigations can be verified or correction and perturbation factors can be calculated for different detector types.

This cumulative dissertation presents new results from the field of reference dosimetry using Monte Carlo simulation for high-energy photons and electron radiation. The peer-review publications from the field of electron dosimetry with ionization chambers present new results which revise the assumptions of the code of practice in relation to fluence disturbance. Furthermore, the concept of positioning in the effective point of measuring for parallel plate chambers in high-energy photon radiation and electron radiation was extended and revised. In the second part of this thesis, solid-state alanine dosimeters were investigated and correction factors for their application in high-energy photons and ^{192}Ir radiation were presented. Based on these results, the response of alanine dosimeters was investigated as a function of the measurement environment material and applied in a clinical study.

The results of this work represent a further step in the continuous improvement of quality assurance in radiation therapy. In addition to the optimization of already established procedures, a contribution to the development of a new dosimetric secondary standard has been made.

Inhaltsverzeichnis

1 Einleitung

Tumorerkrankungen stellen die zweithäufigste Todesursache in den industrialisierten Ländern dar. Die Behandlung onkologischer Patienten erfolgt mittels Chirurgie, systemischer Therapie und/oder Radiotherapie, wobei etwa 50% aller Tumorpatienten im Laufe ihrer Krebserkrankung eine strahlentherapeutische Behandlung erhalten. Bei etwa 95% der Patienten erfolgt die Behandlung mit hochenergetischer Photonen- und Elektronenstrahlung an klinischen Linearbeschleunigern [25, 82]. Ziel jeder strahlentherapeutischen Behandlung ist die Vernichtung aller Tumorzellen bei weitestgehender Schonung des umliegenden gesunden Gewebes. Da sowohl das Tumorgewebe als auch das gesunde Gewebe im betroffenen Dosisbereich einen steilen Gradienten der Dosis-Wirkungs-Beziehungen aufweisen, ist die präzise Kenntnis der im Patienten verabreichten Dosis die Grundlage jeder erfolgreichen strahlentherapeutischen Behandlung.

Das Dosimetrieprotokoll DIN 6800-2 [27], welches in der Strahlentherapie mit hochenergetischen Photonen und Elektronen angewendet wird, wurde seit der Erstveröffentlich-ung im Jahre 1980 fünfmal überarbeitet. Die Normung einhält unter anderem die Regelung für die Bestimmung der Wasser-Energiedosis in der perkutanen Strahlentherapie unter Referenzbedingungen, Nicht-Referenz-Bedingungen und der Bestimmung der relativen Dosis in Wasser [27]. Die aktuelle Fassung ist aus dem Jahre 2008 und befindet sich aufgrund der technischen Weiterentwicklung und verbesserten Messtechnik in Revision.

Die Grundlage für die in der DIN 6800-2 verwendeten Ionisationskammern stellt das Dosis-Messverfahren nach der Sondenmethode dar, diese wird in der DIN 6800-1 [26] vorgestellt. Das genannte Messerverfahren basiert auf in ^{60}Co-Gammastrahlung kalibrierten luftgefüllten Ionisationskammern. Die Kalibrierung von Ionisationskammern für die Bestimmung der Wasser-Energiedosis D_w findet unter definierten Bezugsbedingungen statt [70]. Für die klinische Dosimetrie von Referenzstrahlungsfeldern mit Ionisationskammern werden die Abweichungen zu den Kalibrierbedingungen korrigiert. Damit die Wasser-Energiedosis mit möglichst geringen Unsicherheiten bestimmt werden kann, müssen neben den Korrekturen der externen Einflussgrößen (Temperatur, Luftdruck, etc.) auch Korrekturen hinsichtlich des Ansprechvermögens der Detektoren in den unterschiedlichen Strahlenarten (Photonen und Elektronen) sowie die Strahlenqualitäten berücksichtigt werden. Diese Faktoren sind auf Grundlage einer Vielzahl von Publikationen in internationalen und nationalen (TG-51, TRS-398 und DIN 6800-2) Dosimetrieprotokollen [3, 5, 27] festgelegt. Unterschiedliche Arbeitsgruppen arbeiten mit Experimenten und Monte-Carlo-Simulationen an einer stetigen Verbesserung der Korrektions- und Störfaktoren [22, 51, 56, 23, 24, 72, 44, 41, 14, 71]. Das angestrebte Ziel ist, die Unsicherheit bei der Bestimmung der Wasser-Energiedosis D_w in klinischen Photonenfeldern von derzeit etwa 2.1%(1σ) auf

$< 1\%(1\sigma)$ zu senken [48].

Unter Nicht-Referenz-Bedingungen, wie z.B kleine Bestrahlungsfelder welche in der stereotaktischen Radiochirurgie auftreten, können Ionisationskammern aufgrund ihres großen Messvolumens nur begrenzt eingesetzt werden. Für diesen Anwendungsbereich werden alternative Messmethoden benötigt. Die Physikalisch Technischen Bundesanstalt (PTB) hat hierzu ein Verfahren mit Alanin Festkörper-Dosimetern etabliert [17, 11, 12, 9, 10, 7], wobei das Dosimeter aus der Aminosäure Alanin besteht. Neben dem geringen Messvolumen hat es gegenüber den Ionisationskammern den Vorteil, dass Sie während der Bestrahlung am beliebigen Ort der Messung positioniert werden können und im Anschluss ausgelesen werden. Analog zu Ionisationskammern benötigen Alanin-Dosimeter auch präzise Korrektionsfaktoren für die Bestimmung der Wasser-Energiedosis. Da Alanin-Dosimeter auch in-vivo eingesetzt werden, besteht ein Bedarf an weiteren Studien über das Ansprechvermögen von Alanin-Dosimetern. Im Hinblick auf die Fragestellung der Bestimmung des Ansprechvermögens von verschiedenen Umgebungsmaterialien (von Luftgewebe bis Knochenmaterial) ist die Monte-Carlo-Simulation ein besonders gut geeignetes Hilfsmittel.

In dieser Inaugural-Dissertation werden aufeinander aufbauende peer-review Publikationen zum Thema Monte-Carlo-Simulationen in der Referenzdosimetrie hochenergetischer Elektronen [74, 86, 75] (siehe Kapitel 2) und Alanin-Dosimeter in der Photonen-Strahlentherapie vorgestellt [78, 73, 6, 8] (siehe Kapitel 3).

1.1 Grundlagen der Hohlraumtheorie

In der von Bragg 1912 formulierten Hohlraumtheorie [21] wird von einem idealen, wandlosen Detektoren ausgegangen. Es wird ein Proportionalitätsfaktor $f(Q)$ in Abhängigkeit der Strahlenqualität Q bestimmt, welcher sich aus dem Verhältnis der deponierten Dosis im Umgebungsmaterial D_{med} zu der über das im Detektorvolumen gemittelten Dosis $\bar{D}_{det}$ ergibt.

$$f(Q) = (\frac{D_{med}}{\bar{D}_{det}})_Q \tag{1}$$

Die ersten Hohlraumsonden wurden von Bragg experimentell [21] sowie von Fricke [29] empirisch untersucht. Für die Gültigkeit der Hohlraumtheorie stellten Bragg und Gray Bedingungen auf, welche fordern dass die Abmessungen des eingebrachten Hohlraumes die Energiefluenz der geladenen Teilchen nicht beeinflusst. Des Weiteren muss sichergestellt werden, dass die deponierte Energie der Photonen im Verhältnis zu der deponierten Gesamtenergie verschwindend gering ist und die spektrale Flußdichtenverteilung aller Elektronen, welche in der Kavität des Detektors deponiert werden, ortsunabhängig sind [59].

Das daraus folgende Konzept der Energiedeposition von geladenen Teilchen ist allgemein als Bragg-Gray (BG) Hohlraumtheorie bekannt [32, 33].

Aus den Grundlagen der Hohlraumtheorie leitete Attix [68] das Stoßbremsvermögen $s_{w,a}^{BG}$ als das Verhältnis der deponierten Energiedosis im Umgebungsmaterial D_w zur Energiedosis im Hohlraum D_a ab.

$$s_{w,a}^{BG} = \frac{D_w}{D_a} \tag{2}$$

In der ICRU 14 [37] wird das Bremsvermögen unter Bragg-Gray Bedingungen $s_{w,a}^{BG}$ als das Verhältnis der gemittelten spektralen Fluenz von Elektronen der ersten Generation $\Phi_{E,w}^{1.}$ für das Umgebungsmaterial w zu dem Detektormaterial a beschrieben. Das unbeschränkte Massenstoßbremsvermögen wird als $\frac{S^{col}}{\rho}$ angegeben. Durch die ICRU 35 [38] wird das Konzept als Bragg-Gray Näherung (BG) bezeichnet.

$$s_{w,a}^{BG} = \frac{D_w}{D_a} = \frac{\int_0^{E_{max}} \Phi_{E,w}^{1.}(\frac{S^{col}}{\rho})_w \; dE}{\int_0^{E_{max}} \Phi_{E,w}^{1.}(\frac{S^{col}}{\rho})_a \; dE} \tag{3}$$

Spencer und Attix [67] ergänzten die Hohlraumtheorie, durch die Berücksichtigung der δ-Elektronen, um die Größe des beschränkten Massenstoßbremsvermögens $(\frac{L}{\rho})_\Delta$. Die dafür eingeführte Energieschwelle Δ soll der mittleren Weglänge eines Elektrons, welches den Hohlraum durchquert, entsprechen.

$$s_{w,a}^{SA} = \frac{D_w}{D_a} = \frac{\int_\Delta^{E_{max}} \Phi_{E,w}(\frac{L}{\rho})_{\Delta,w} \; dE}{\int_\Delta^{E_{max}} \Phi_{E,w}(\frac{L}{\rho})_{\Delta,a} \; dE} \tag{4}$$

In der Spencer Attix Näherung (SA) wird das Bremsvermögenverhältnis $s_{w,a}^{SA}$ der geladenen Teilchen aller Generationen des Energiespektrums $\Phi_{E,w}$ in zwei Energiebereiche eingeteilt: $E < \Delta$ und $E > \Delta$. Fällt die Energie der geladenen Teilchen unterhalb die Energieschwelle Δ, werden diese als lokal deponiert angesehen.
Ein Untersuchung der geladenen Teilchen unterhalb der Energieschwelle Δ führte Nahum [54, 13] durch. Er erweiterte die Spencer Attix Näherung um die sogenannten „track ends“ $(\Phi_E(\Delta)_w \cdot (\frac{S_{col}}{\rho})_\Delta \cdot \Delta)$.

$$s_{w,a}^{\Delta} = \frac{D_w}{D_a} = \frac{\int_\Delta^{E_{max}} \Phi_{E,w}(\frac{L}{\rho})_{\Delta,w} \; dE + \Phi_E(\Delta)_w \cdot (\frac{S_{col}}{\rho})_{\Delta,w} \cdot \Delta}{\int_\Delta^{E_{max}} \Phi_{E,w}(\frac{L}{\rho})_{\Delta,a} \; dE + \Phi_E(\Delta)_w \cdot (\frac{S_{col}}{\rho})_{\Delta,a} \cdot \Delta} \tag{5}$$

Ma und Nahum untersuchten und bestätigten die Anwendbarkeit der Hohlraumtheorie auf Zylindrische- und Flachionisationskammern für verschiedenen Photonenenergien [50, 49].

1.1.1 Störfaktoren

Wandlose Detektoren, die den Anforderungen der Bragg-Gray Bedingungen entsprechen, sind nicht realisierbar, weshalb auftretende Fluenzstörungen in realen Detektoren durch Störfaktoren p berücksichtigt werden müssen. Für luftgefüllte Ionisationskammern verhält sich das beschränkte Massenstoßbremsvermögen multipliziert mit dem Gesamtstörfaktor p wie das Verhältnis der deponierten Dosis im Umgebungsmaterial Wasser D_w zum Detektor D_{det}.

$$\frac{D_w}{D_{det}} = s^{\Delta}_{w,a} \cdot p \tag{6}$$

Der Gesamtstörfaktor ergibt sich aus dem Produkt der Einzelstörfaktoren:

$$p = p_{wall} \cdot p_{cell} \cdot p_{stem} \cdot p_{cav} \cdot p_{dis} \tag{7}$$

Die Störfaktoren lassen sich experimentell oder mit Hilfe der Monte-Carlo-Simulation bestimmen. Ein in der Literatur häufig diskutierter Störfaktor untersucht den Einfluss der Kammerwand p_{wall} [4, 30, 19]. Den Einfluss der Mittelelektrode wird durch p_{cell} korrigiert [51]. Der Störfaktor des Kammerstiels wird als p_{stem} beschrieben [36]. Den Einfluss des unterschiedlichen Streuverhaltens zwischen Umgebungs- und Detektormaterial wird als p_{cav} [71] bezeichnet. Der Störfaktor p_{dis} korrigiert den Einfluss des Verdrängungseffektes durch das Einbringen einer Ionisationskammer in das Phantom [40]. Dieser Störfaktor kann auch durch das verschieben der Messkammer in den sogenannten effektiven Messort berücksichtigt werden [27].

1.2 Konzept der Bestimmung der Wasser-Energiedosis

Die in der Radioonkologie verwendete Messgröße ist die Wasser-Energiedosis $D_w = (\frac{dE}{dm})_w$ [46]. Basierend auf den internationalen und nationalen (TG-51, TRS-398 und DIN 6800-2) Dosimetrieprotokollen [27, 3, 5] gilt für die Wasser-Energiedosis D_w mit luftgefüllten Ionisationskammern:

$$D_w = (M - M_0) \cdot N \cdot \prod k_i \tag{8}$$

Der für Ionisationskammern spezifische Kalibrierfaktor wird als N dargestellt. Dieser wird über ein Primär- oder Sekundärstandardlabor eines Metrologieinstituts, in Deutschland der z.B. Physikalische Technische Bundesanstalt, bestimmt. M ist die Anzeige des Elek-

trometers, welches um die Nullanzeige M_0 korrigiert wird. Das Produkt der Ionisationskammer spezifischen und Umwelt abhängigen Korrektionsfaktor wird als $\prod k_i$ bezeichnet [55].

1.2.1 Korrektionsfaktoren

Für die exakte Bestimmung der Wasser-Energiedosis wird in der DIN 6800-2 eine Korrektur der Abweichung zu den Bezugsbedingungen gefordert. Diese berücksichtigen Abweichungen des Kalibrierfaktors N durch äußere Einflüsse (Temperatur, Luftdichte und Luftfeuchte), innere Einflüsse (Nullpunktwanderung, Alterung der Bauteile und Anlaufzeit des Gerätes) und bestrahlungsabhängige Einflüsse (Strahlenqualität und Dosisleistung) [35, 27].

1.3 Monte-Carlo-Simulation

Die Monte-Carlo-Simulation ist ein stochastisches Verfahren zur Lösung komplexer Integralgleichungen (hier: Boltzmann Transportgleichung [53, 20]). Das Verfahren basiert auf der Idee von de Buffon der im Jahre 1777 gezeigt hat, dass mit Hilfe von Zufallszahlen über eine Integralgleichung sich die Zahl π bestimmen lässt [20]. Die Weiterentwicklung wurde federführend durch das Los Alamos National Laboratory vorangetriebenen [52, 58, 80]. Basierend auf diesen Grundlagen wurden General Purpose Monte-Carlo Codes für unterschiedliche Anwendungen aus dem Bereich der Hochenergie- und Medizinischen Physik entwickelt. Für die Simulation des Transportes von geladenen schweren Teilchen ist unter anderem MCNP [81], TOPAS [57], GIANT4 [1, 2] und FLUKA [28] zu erwähnen. In dem Bereich der konventionelle Radioonkologie haben sich Penelope [15, 66, 64] und EGSnrc [42, 43, 45] durchgesetzt.

1.3.1 EGSnrc Monte-Carlo

Das in dieser Arbeit genutzte Simulationsprogramm EGS (Elekctron-Gamma-Shower) wurde Anfang den 1970er am Stanford Linear Accelerator Center einwickelt [61]. Die Weitereinwicklung zu EGS4, mit den ersten Anwendungen für die Medizinische Physik, wurde in den 1980er vorangetrieben [60]. Die aktuelle Version EGSnrc wurde am National Research Council of Canada entwickelt [42, 43] und ist ein Programmpaket für die Simulation des Strahlungstransportes von Photonen und Elektronen. Die implementierten User-Codes finden Anwendung in unterschiedlichen Bereichen, wie zum Beispiel die Simulation von Ionisationskammern mit egs_chamber [83] oder die Modellierung von Linearbeschleunigern und Röntgenröhren in BEAMnrc [62].

1.3.2 Photonen und Elektronentransport

Die in EGSnrc implementierte Physik unterteilt sich in die Bereiche des Photon- und Elektronen-Transportes. Der komplexe Strahlentransportes wird durch die Boltzmann Transportgleichung beschrieben und in viele einzelne Wechselwirkungen unterteilt [20]. Der Elektronentransport ist der zeitaufwendigste Bestandteil einer Simulation. Die physikalischen Grundlagen des Transportes wurden mit der Vielfachstreuung zu Beginn des 20. Jahrhunderts beschrieben [63, 18, 31, 34]. Die exakte Beschreibung des Elektronentransportes ist im „Singel-Step-Modus“ möglich, jedoch aufgrund der benötigten Simulationszeit ($<$ 30000 CPU-Stunden für eine Simulation mit der statistischen Genauigkeit geringer als 0,1%) in der Anwendung unpraktikabel. Um diese Problematik zu umgehen stellte Berger 1963 das Condensed Histroy (CH) Verfahren vor [16]. Das CH Verfahren ist ein Monte-Carlo Elektronentransportalgorithmus bei dem mehrere Elektronenwechselwirkungen zu einem Schritt zusammengefasst werden [47].

2 Zusammenfassung der peer-review Publikationen aus dem Bereich der Referenzdosimetrie mit Elektronen

2.1 Effective point of measurement for parallel plate and cylindrical ion chambers in megavoltage electron beams

Das Vorhandensein einer luftgefüllten Ionisationskammer in einem Umgebungsmaterial führt zu verschieden Fluenzstörungen der hochenergetischen Photonen und Elektronenstrahlung. Der Verdrängungseffekt ist einer dieser Störungen und kann auf zwei Arten korrigiert werden: mit einem Störungsfaktor p_{dis} [3] oder durch eine Verschiebung der Kammer in den effektiven Messort (EPOM) [27].

Im Rahmen dieser Studie wurde der EPOM für vier verschiedene Flachkammern und zwei zylindrische Ionisationskammern in hochenergetischer Elektronenstrahlung mittels Monte-Carlo-Simulationen bestimmt. Die Positionierung der Kammern mit dem EPOM in der Messtiefe hat zur Folge, dass der verbleibende Störungsfaktor weitestgehend unabhängig von der Messtiefe ist. Der Störungsfaktor p wurde erstmalig in dieser Studie für alle Kammern für den gesamten Bereich klinischer Elektronenenergien bestimmt. Während für die Advanced Markus Kammer die Position des EPOM mit dem Referenzpunkt der Kammern übereinstimmt, müssen die anderen Flachkammern (ROOS, NACP und Markus) mehrere Zehntel Millimeter in Strahlrichtung verschoben werden (siehe Publikation 1 Figure 2). Für die zylindrischen Kammern ist eine zunehmende Verschiebung des EPOM mit ansteigender Elektronenenergie zu beobachten (siehe Publikation 1 Figure 4). Diese Verschiebung ist entgegen der Strahlenrichtung, d.h. von dem Bezugspunkt der Kammern in Richtung des Fokus. Für die höchste Elektronenenergie im Rahmen der Untersuchung ist die ermittelte Verschiebung des EPOM in guter Übereinstimmung mit der Empfehlung gültiger Dosimetrieprotokolle. Für die kleinste Energie zeigt sich eine Abweichung von circa 30% zu diesen Empfehlungen [76, 74]. Die erhobenen Daten sind in die Revision der DIN 6800-2 eingeflossen.[1]

[1] Abstrakt aus: Z Med Phys 24 (2014) 216-223 10.1016/j.zemedi.2013.12.001

von Voigts-Rhetz, P.; Czarnecki, D.; Zink, K.: Effective point of measurement for parallel plate and cylindrical ion chambers in megavoltage electron beams. In: Z Med Phys 24 (2014) 216-223 DOI: 10.1016/j.zemedi.2013.12.001

Impact Factor: 1.531
Eigener Anteil: 80%
Festlegung der Zielsetzung, Monte-Carlo-Simulationen, Auswertung der Daten, Interpretation und Diskussion der Ergebnisse, Verfassen des Manuskripts

2.2 Monte Carlo study of the depth dependent flucence perturbation in parallel plate ionization chambers in electron beams

Die Elektronenfluenz im inneren einer Flachkammer, welche in einem Wasserphantom positioniert ist und mit einem klinischen Elektronenstrahl bestrahlt wird, weicht von der ungestörten Fluenz in Wasser ohne Messerkammer ab. Ein Grund für diese Fluenzstörung in Flachkammern ist der bekannte „inscattering effect“, deren physikalische Ursache das fehlen von Elektronenstreuung in der gasgefüllten Kavität ist [38]. Korrekturfaktoren die bestimmt wurden um diesen Effekt zu korrigieren, werden in der Normung DIN 6800-2 [27] gegeben. Jedoch haben aktuelle Monte-Carlo Berechnungen zu Zweifeln an der Gültigkeit dieser Korrekturen geführt [77]. Das Ziel der vorliegenden Studie ist aus diesem Grund die Entwicklung der Fluenzstörung neu zu analysieren. Zur Analyse wurden ortsaufgelöste Monte-Carlo-Simulationen der Dosisprofile innerhalb der gasgefüllten Kavitäten in klinischen Elektronenfeldern durchgeführt, mit dem Ziel die Veränderungen des Fluenzstörfaktors in Abhängigkeit der Tiefe zu untersuchen.

Die Monte-Carlo-Simulationen zeigen eindeutig einen großen „in- and outscattering effect“ der Elektronen über die laterale Kavitätsgrenze. Daraus ergibt sich, durch das umgebende Medium, ein stärkerer Einfluss auf die tiefenabhängige Entwicklung des Elektronenfeldes der deponierten Dosis in der Kammer. Im Aufbaubereich der Tiefen-Dosis-Kurve ist das In-Out-Verhältnis der Elektronenfluenz positiv und zeigt die bekannte Dosisoszillation in der Nähe der Hohlraum/Wasser-Grenze. Mit zunehmender Messtiefe, nach dem Dosismaximum, befindet sich das „in-out-Verhältnis“ im Gleichgewicht und im fallenden Teil der Tiefendosiskurve ist das Verhältnis negativ (siehe Publikation 2 Figure 2).

Zink, K.; Czarnecki, D.; Looe, H. K.;von Voigts-Rhetz, P.; Harder, D.: Monte Carlo study of the depth-dependent fluence perturbation in parallel-plate io-

nization chambers in electron beams. In: Med. Phys. 41 (2014) 111707 DOI: 10.1118/1.4897389

Impact Factor: 2.617
Eigener Anteil: 20%
Monte-Carlo-Simulationen, Interpretation und Diskussion der Ergebnisse

2.3 On the perturbation correction factor p_{cav} of the Markus parallel-plate ion chamber in clinical electron beams

Alle aktuellen Dosimetrieprotokolle empfehlen für die Elektronendosimetrie die Verwendung von Flachkammern mit Guardring. Für die Markus Kammer, welche keinen Guardring besitzt, wird anstatt dessen ein energieabhängiger Fluenzstörfaktor p_{cav} in der DIN 6800-2 [27] angegeben. Dieser Störfaktor basiert auf einer experimentellen Arbeit von van der Plaetsen [71] in der die Markus Kammer mit der als störungsfrei angenommenen NACP Kammer verglichen wurde. Ziel dieser Arbeit ist eine erneute Untersuchung des Fluenzstörfaktors p_{cav} mit Monte-Carlo-Simulationen. Für diese Untersuchung wurden vier Flachkammern (Roos, Markus, NACP und Advanced Markus) detailgetreu in der Monte-Carlo-Simulationssoftware EGSnrc [42, 43, 45] modelliert und in einem Wasserphantom positioniert. Das sensitive Volumen aller Kammern wurde mit „Low-Density-Water“ [79] gefüllt und für dreizehn verschiedene Elektronenspektren ($E_0 = 6 - 21MeV$) und drei Energien eines Elekta Linearbeschleuniger Modells untersucht. Für alle Simulationen wurde der Referenzpunkt der Ionisationskammer in der Messtiefe positioniert. Dazu wurde die Wasser-Energiedosis D_w in der dazugehörigen Tiefe (Referenztiefe z_{ref} und Maximaltiefe z_{max}) in einem Wasservoxel bestimmt. Das berechnete Verhältnis D_{NACP}/D_{Markus} hat eine geringere Abweichung von Eins ($p = 1$) als die Ergebnisse von van der Plaetsen zeigen. Hingegen wird von der Markus zur NACP Kammer eine identische Energieabhängigkeit aufgezeigt. Wird die deponierte Dosis in der Kammern mit der Wasser-Energiedosis verglichen, zeigt die Markus Kammer die geringste Energieabhängigkeit für die beiden untersuchten Tiefen auf (siehe Publikation 3 Figure 2 und 3). Allgemein werden die Messungen von van der Plaetsen mit dieser Arbeit bestätigt, jedoch sollte die dort gegebene Schlussfolgerung überdacht werden: die Markus Kammer, ohne Guardring, hat im Gegenteil zu den Kammern mit Guardring (ROOS, NACP und Advanced Markus) den geringsten nahezu energieunabhängigen Gesamtstörfaktor.

von Voigts-Rhetz, P.; Vorwerk, H.; Zink, K.: On the perturbation correcti-

on factor pcav of the Markus parallel-plate ion chamber in clinical electron beams. In: Int. J. Med. Phys. Clin.Eng. Rad. Oncol.6 (2017) 150-161 DOI: 10.4236/ijmpcero.2017.62014

Impact Factor: 0.61
Eigener Anteil: 80%
Festlegung der Zielsetzung, Monte-Carlo-Simulationen, Auswertung der Daten, Interpretation und Diskussion der Ergebnisse, Verfassen des Manuskripts

3 Zusammenfassung der peer-review Publikationen aus dem Bereich der Referenzdosimetrie mit Photonen

3.1 Difference in the relative response of the alanine dosimeter to megavoltage x-ray and electron beams

Bisher ist der Nutzen von Alanin als Detektor in der Strahlentherapie im Bereich der hochenergetischen Photonen eingeschränkt, da das Ansprechvermögen im Bezug auf die Messgröße Wasser-Energiedosis D_w nicht detailliert bekannt ist. Diese Studie verfolgt das Ziel, das relative Ansprechvermögen von Alanin-Dosimetern im Detail zu untersuchen und zu beschreiben. Dieses Ansprechvermögen wurde experimentell relativ zu ^{60}Co für 4, 6, 8, 10, 15 und 25 MV Photonenstrahlung von klinischen Linearbeschleunigern bestimmt. Für die Kalibrierung wurden k_Q Faktoren von Ionisationskammern mit einer Unsicherheit von 0,31% aus kalorimetrischen Messungen verwendet. Die Ergebnisse zeigen einen langsamen Abfall von etwa 0,996 bei niedrigen Energien (4-6 MV-X) auf 0,989 bei der höchsten Energie (25 MV-X). Die Unsicherheit für das relative Ansprechvermögen schwankt zwischen 0,35% und 0,41%. Die Ergebnisse wurden durch überarbeitete experimentelle Daten aus dem NRC (National Research Council of Canada) sowie mit Monte-Carlo-Simulationen, welche mit einer Dichtekorrektur für kristallines Alanin angepasst wurden, verglichen (siehe Publikation 4 Figure 4 und 5).

Anton, M.; Kapsch, R-P; Krauss, A.; von Voigts-Rhetz, P.; Zink, K.; McEwen, M.: Difference in the relative response of the alanine dosimeter to megavoltage x-ray and electron beams. In: Phys. Med. Biol. 58 (2013) 3259-3282 DOI: 10.1088/0031-9155/58/10/3259

Impact Factor: 2.742
Eigener Anteil: 35%
Monte-Carlo-Simulationen, Auswertung der Daten, Interpretation und Diskussion der Ergebnisse, Unterstützung beim Verfassen des Manuskripts

3.2 Response of the alanine/ESR dosimeter to radiation from an Ir-192 HDR brachytherapy source

Das Verhalten von Alanin-Dosimetern, bezogen auf die Bezugs-Strahlenqualität ^{60}Co, wurde durch Experimente und Monte-Carlo-Simulationen für ^{192}Ir Strahlung bestimmt. Die experimentellen und Monte-Carlo Ergebnisse des Ansprechvermögens stimmen innerhalb der Grenzen der Unsicherheit gut überein. Das relative Ansprechvermögen nimmt mit zunehmender Entfernung zwischen Messvolumen und der Quelle von ca. 0.98 bei 1 cm Entfernung auf 0.96 bei 5 cm ab (siehe Publikation 5 Figure 4 und 5). Die vorliegenden Daten sind umfangreicher und in guter Übereinstimmung mit den veröffentlichen Daten von Schaeken et al. [65]. Die Abnahme des relativen Ansprechvermögens mit zunehmenden Entfernung, die bereits zuvor beobachtet wurde, ist bestätigt.

Anton, M.; Hackel, T.; Zink, K.; von Voigts-Rhetz, P.; Selbach, H-J: Response of the alanine/ESR dosimeter to radiation from an Ir-192 HDR brachytherapy source. In: Phys. Med. Biol. 60 (2015) 175-193 DOI: 10.1088/ 0031-9155/60/1/175

Impact Factor: 2.742
Eigener Anteil: 30%
Monte-Carlo-Simulationen, Auswertung der Daten, Interpretation und Diskussion der Ergebnisse, Unterstützung beim Verfassen des Manuskripts

3.3 Perturbation correction for alanine dosimeters in different phantom materials in high-energy photon beams

In der modernen Strahlentherapie wird die Verifikation der Dosisverteilung eines Bestrahlungsplans oftmals in inhomogenen und anthropomorphen Phantomen durchgeführt. Zu diesem Zweck werden besonders kleinvolumige Dosimeter benötigt. Für diese Messungen sind Alanin Festkörper-Dosimeter besonders geeignet, da das Ansprechvermögen von Alanin über alle gängigen klinischen Photonen-Energien für Wasser gut untersucht sind [8]. Für alle anderen Umgebungsmaterialien liegen keine Informationen über das Ansprechvermögen von Alanin-Dosimetern vor. Ziel dieser Studie ist, das Ansprechvermögen von Alanin-Dosimetern für zwanzig verschiedene Umgebungsmaterialien in klinischen Photonenfeldern mittels Monte-Carlo-Simulation zu untersuchen. Die relativen Elektronendichten $n_e/n_{e,w}$ der verschiedenen Materialien liegt in Bezug zu Wasser zwischen 0.20 und 1.69, dies umfasst nahezu alle im Menschen auftretenden Materialien. Die Untersuchungen wurden für drei verschiedene Photonenenergien zwischen 6 und 25 MV-X sowie ^{60}Co durchgeführt. Ein Korrektionsfaktor für den Einfluss des Umgebungsmaterials k_{env} wurde in der Arbeit vorgestellt. Die Monte-Carlo-Simulationen zeigen, dass nur eine kleine Abhängigkeit des Phantommaterials auf k_{env} vorhanden ist (siehe Publikation 6 Figure 3).

von Voigts-Rhetz, P.; Anton, M.; Vorwerk, H.; Zink, K.: Perturbation correction for alanine dosimeters in different phantom materials in high-energy photon beams. In: Phys. Med. Biol. 61 (2016) N70-N79 DOI: 10.1088/0031-9155/61/3/N70

Impact Factor: 2.742
Eigener Anteil: 80%
Festlegung der Zielsetzung, Monte-Carlo-Simulationen, Auswertung der Daten, Interpretation und Diskussion der Ergebnisse, Verfassen des Manuskripts

3.4 Feasibility study of entrance and exit dose measurements at the contra lateral breast with alanine/electron spin resonance dosimetry in volumetric modulated radiotherapy of breast cancer

Die Physikalisch-Technische Bundesanstalt hat für die Bestimmung der Wasser-Energiedosis einen Sekundärstandard, basierend auf Alanin-Dosimetern [9, 10, 8], etabliert. Ziel dieser Studie ist es, das vorgestellte System an Mammakarzinom Patienten, mit Mes-

sungen außerhalb des Strahlenfeldes, zu testen. Insgesamt fünf Dosimeter-Pellets aus Alanin wurden auf die Haut des Patienten geklebt. Die Dosimeter wurden seitlich auf der gegenüberliegenden gesunden Brust von Sternum bis zum distalen Ende angebracht. Während der nächsten 28 Fraktionen, jede mit 2,2 Gy, wurde die aufaddierte Dosis für vier Patienten gemessen. Für die Positionsbestimmung wurde vor jeder Behandlung eine ConeBeam Computertomographie (CBCT) durchgeführt. Das als Referenz aufgenommene CT wurde rigide registriert und auf alle CBCTs der 28 Fraktionen angepasst, um die unterschiedlichen Alanin Pellet Positionen zu berücksichtigen. Im Anschluss wurde die Dosis auf den angepassten CBCTs, mit Hilfe des Acuros XB Algorithmus berechnet. Die mit den Alanin-Dosimeter gemessen Ergebnisse wurden mit den aus dem Bestrahlungsplanungssystem verglichen. Die maximale gemessene Dosis beträgt 19,9 Gy ± 0,4 Gy am Sternum, abnehmend auf 6,8 Gy ± 0,2 Gy in der nähe der Brustwarze und 4,5 Gy ± 0,1 Gy an der distalen Oberfläche der kontralateralen Brust. Die absoluten Unterschiede zwischen den berechneten und gemessenen Dosen reichten von -1,9 Gy bis 0,9 Gy (siehe Publikation 7 Figure 1 und 2).

Wagner D.M.; Hüttenrauch P; Anton, M.;von Voigts-Rhetz, P.; Zink, K.; Wolff H.A: Feasibility study of entrance and exit dose measurements at the contra lateral breast with alanine/electron spin resonance dosimetry in volumetric modulated radiotherapy of breast cancer. In: Phys. Med. Biol. 62 (2017) 5462-5472 DOI: 10.1088/1361-6560/aa6ee2

Impact Factor: 2.742
Eigener Anteil: 10%
Monte-Carlo-Simulationen, Auswertung der Daten, Unterstützung beim Verfassen des Manuskripts

4 Diskussion

Die erarbeiteten Daten im Rahmen dieser kumulativen Dissertation stellen einen Ausgangspunkt für die Überarbeitung der Normung im Bereich der Referenzdosimetrie dar. Das Ziel der Revision ist eine stetige Verbesserung der Qualitätssicherung in der Strahlentherapie.

Im Bereich der klinischen Elektronenfelder, mit kalibrierten Ionisationskammern, wurde ein Schwerpunkt auf die Untersuchung des Fluenzstörfaktors p_{cav} von Flachkammern

gelegt. In der Publikationen „Monte Carlo study of the depth-dependent fluence perturbation in parallel-plate ionization chambers in electron beams“ [86] werden die Grundlagen und Auswirkungen des Fluenzstörfaktors beschrieben. Die Arbeit befasst sich mit dem in der ICRU37 [39] beschrieben „inscattering-effect“ von luftgefüllten Kavitäten und der Auswirkung auf die klinische Eletronendosimetrie. Die darauf aufbauende Publikation „On the perturbation correction factor p_{cav} of the Markus parallel-plate ion chamber in clinical electron beams“ [75] untersucht den in der DIN 6800-2 angebenden Fluenzstörfaktor und dessen Interpretation. Die vorgestellte Arbeit revidiert die Ergebnisse von van der Plaetsen [71].

Das Konzept des effektiven Messortes zur Korrektion des Verdrängungseffektes p_{cav} ist mir der Originalarbeit für Photon tiefgehend diskutiert [44, 69]. In der Arbeit „Effective point of measurement for parallel plate and cylindrical ion chambers in megavoltage electron beams“ [74] wurden die Untersuchungen für die Empfehlung der Positionierung von Zylindrischen- und Flachionisationskammern fortgeführt und bis zu diesem Zeitpunkt nicht berücksichtige Kammern, neu erstellt. Erstmalig wurde eine umfangreiche Studie für alle gängigen Flachkammer in Elektronenstrahlung vorgestellt. Die vorgestellten Änderungen werden Bestandteil der überarbeiteten Version der DIN 6800-2 werden und neben einer Korrektur für Zylindrischeionisationskammer in Photonen auch für Kompaktionisationskammern in Elektronen angegeben.

Ein weiterer Schwerpunkt dieser Arbeit wurde im Bereich der Festkörper-Dosimetrie mit Alanin-Dosimetern gelegt und die Ergebnisse wurden in vier Publikationen vorgestellt. Untersuchungen über das Ansprechvermögen im Energiebereich von 4-25 MV wurden experimentell und mit Hilfe der Monte-Carlo-Simulation im Rahmen der Arbeit „Difference in the relative response of the alanine dosimeter to megavoltage x-ray and electron beams“ [8] durchgeführt. Die erhaltenen Ergebnisse stimmen mit denen von Zeng et al. überein [84, 85], haben jedoch eine geringere Messunsicherheit. Basierend auf den Erkenntnissen wurde das relative Ansprechvermögen von Alanin-Dosimetern für die Brachytherpie erweitert. In der Arbeit „Response of the alanine/ESR dosimeter to radiation from an Ir-192 HDR brachytherapy source“ [6] wurde der Fokus auf die Veränderung des radialen tiefenabhängigen Ansprechvermögens in Phantommaterial Wasser gelegt.

Für eine Anwendung von klinischen Fragestellungen wurde neben dem Ansprechvermögen von Alanin-Dosimetern in Wasser weitere Umgebungsmaterialien benötigt. Diese werden in der Arbeit „Perturbation correction for alanine dosimeters in different phantom materials in high-energy photon beams“ [73] beschrieben. In diesen Studie wurde das Ansprechvermögen von Alanin-Dosimetern für verschiedene Strahlenqualitäten in unterschiedlichen Umgebungsmaterialien untersucht.

In einer Machbarkeitsstudie „Feasibility study of entrance and exit dose measurements at the contra lateral breast with alanine/electron spin resonance dosimetry in volumetric modulated radiotherapy of breast cancer“ [78] wurden die Messungen von Alanin-Dosimetern mit einem Bestrahlungsplanungssystem verglichen.

Die aufgeführten peer-review Publikationen bieten mit ihren Ergebnissen eine solide Basis für die Verwendung von Alanin-Dosimetern als Sekundärstandard, sowie für die Anwendung in der klinischen Qualitätssicherung.

5 Quellenverzeichnis

[1] S. Agostinelli and et al. Geant4—a simulation toolkit. *Nuclear Instruments and Methods in Physics Research Section A: Accelerators, Spectrometers, Detectors and Associated Equipment*, 506(3):250–303, 2003.

[2] J. Allison and et al. Geant4 developments and applications. *IEEE Transactions on Nuclear Science*, 53(1):270–278, 2006.

[3] P. R. Almond, P. J. Biggs, B. M. Coursey, W. F. Hanson, M. S. Huq, R. Nath, and D. W. Rogers. Aapm's tg-51 protocol for clinical reference dosimetry of high-energy photon and electron beams. *Medical Physics*, 26(9):1847–1870, 1999.

[4] P. R. Almond and H. Svensson. Ionization chamber dosimetry for photon and electron beams. theoretical considerations. *Acta radiologica: therapy, physics, biology*, 16(2):177–186, 1977.

[5] P. Andreo, D. T. Burns, K. Hohlfeld, M. S. Huq, T. Kanai, F. Laitano, V. Smyth, and S. Vynckier. Absorbed dose determination in external beam radiotherapy. an international code of practice for dosimetry based on standards of absorbed dose to water. *Technical Reports Series TRS-398 (Vienna: International Atomic Energy Agency)*, 2000.

[6] M. Anton, T. Hackel, K. Zink, P. von Voigts-Rhetz, and H-J Selbach. Response of the alanine/esr dosimeter to radiation from an ir-192 hdr brachytherapy source. *Physics in Medicine and Biology*, 60(1):175–193, 2015.

[7] M. Anton, R.-P. Kapsch, and T. Hackel. Is there an influence of the surrounding material on the response of the alanine dosimetry system? *Physics in Medicine and Biology*, 54(7):2029–2035, 2009.

[8] M. Anton, R-P Kapsch, A. Krauss, P. von Voigts-Rhetz, K. Zink, and M. McEwen. Difference in the relative response of the alanine dosimeter to megavoltage x-ray and electron beams. *Physics in Medicine and Biology*, 58(10):3259–3282, 2013.

[9] M. Anton, R.-P. Kapsch, M. Krystek, and F. Renner. Response of the alanine/esr dosimetry system to mv x-rays relative to 60 co radiation. *Physics in Medicine and Biology*, 53(10):2753–2770, 2008.

[10] M. Anton, D. Wagner, H.-J. Selbach, T. Hackel, R. M. Hermann, C. F. Hess, and H. Vorwerk. In vivo dosimetry in the urethra using alanine/esr during 192 ir hdr brachytherapy of prostate cancer - a phantom study. *Physics in Medicine and Biology*, 54(9):2915–2931, 2009.

[11] Mathias Anton. Development of a secondary standard for the absorbed dose to water based on the alanine epr dosimetry system. *Applied radiation and isotopes : including data, instrumentation and methods for use in agriculture, industry and medicine*, 62(5):779–795, 2005.

[12] Mathias Anton. Uncertainties in alanine/esr dosimetry at the physikalisch-technische bundesanstalt. *Physics in Medicine & Biology*, 51(21):5419, 2006.

[13] F. H. Attix. Radiation dosimetry: Physical and biological aspects edited by c. g. orton. *Medical Physics*, 13(5):769–770, 1986.

[14] B. Nilsson, A. Montelius, and P. Andreo. Wall effects in plane-parallel ionization chambers. *Phys Med Biol*, 41(4):609–623, 1996.

[15] J. Baró, J. Sempau, J. M. Fernández-Varea, and F. Salvat. Penelope: An algorithm for monte carlo simulation of the penetration and energy loss of electrons and positrons in matter. *Nuclear Instruments and Methods in Physics Research Section B: Beam Interactions with Materials and Atoms*, 100(1):31–46, 1995.

[16] M. J. Berger. Monte carlo calculation of the penetration and diffusion of fast charged particles. In B. Alder, S. Fernbach, and M. Rotenberg, editors, *Methods in Comput. Phys*, pages 135–215. Academic, New York, 1963.

[17] E. S. Bergstrand, K. R. Shortt, Carl K. Ross, and E. O. Hole. An investigation of the photon energy dependence of the epr alanine dosimetry system. *Physics in Medicine and Biology*, 48(12):1753–1771, 2003.

[18] H. A. Bethe, M. E. Rose, and L. P. Smith. The multiple scattering of electrons. *Proceedings of the American Philosophical Society*, 78(4):573–585, 1938.

[19] A. F. Bielajew. Ionisation cavity theory: a formal derivation of perturbation factors for thick-walled ion chambers in photon beams. *Physics in Medicine and Biology*, 31(2):161–170, 1986.

[20] A. F. Bielajew. Fundamentals of the monte carlo method for neutral and charged particle transport. 2001.

[21] W. H. Bragg. *Studies in radioactivity*. Macmillan, 1912.

[22] G. Bruggmoser, R. Saum, A. Schmachtenberg, F. Schmid, and E. Schule. Determination of the recombination correction factor ks for some specific plane-parallel and cylindrical ionization chambers in pulsed photon and electron beams. *Physics in Medicine and Biology*, 52(2):N35–50, 2007.

[23] L. A. Buckley and D. W. O. Rogers. Wall correction factors, p_wall, for parallel-plate ionization chambers. *Med Phys*, 33(6):1788–1796, 2006.

[24] L. A. Buckley and D. W. O. Rogers. Wall correction factors, p_wall, for thimble ionization chambers. *Med Phys*, 33(2):455–464, 2006.

[25] G. Delaney, S. Jacob, C. Featherstone, and M. Barton. The role of radiotherapy in cancer treatment: Estimating optimal utilization from a review of evidence-based clinical guidelines. *Cancer*, 104(6):1129–1137, 2005.

[26] DIN6800-1. Procedures of dosimetry with probe-type detectors for photon and electron radiation - part 1: General.

[27] DIN6800-2. Procedures of dosimetry with probe-type detectors for photon and electron radiation - part 2: Ionization chamber dosimetry of high energy photon and electron radiation.

[28] A. Ferrari, P. R. Sala, A. Fasso, and J. Ranft. Fluka: a multi-particle transport code. *CERN-2005-010*, 20015.

[29] H. Fricke and O. Glasser. Eine theoretische und experimentelle untersuchung der kleinen ionisationskammern. *Fortschr. Röntgenstr. 33*, pages 239–250, 1925.

[30] M. T. Gillin, R. W. Kline, A. Niroomand-Rad, and D. F. Grimm. The effect of thickness of the waterproofing sheath on the calibration of photon and electron beams. *Medical Physics*, 12(2):234–236, 1985.

[31] S. Goudsmit and J. L. Saunderson. Multiple scattering of electrons. *Physical Review*, 57(1):24–29, 1940.

[32] L. H. Gray. The absorption of penetrating radiation. *Proc. R. Soc*, 122:647–668, 1929.

[33] L. H. Gray. An ionisation method for the absolute measurement of gamma-ray energy. *Proc. R. Soc*, 156:578–596, 1936.

[34] Dietrich Harder. Einfluß der vielfachstreuung von elektronen auf die ionisation in gasgefüllten hohlräumen. *Biophysik*, 5(2):157–164, 1968.

[35] G. Hartmann and W. Schlegel. Physikalische grundlagen. In M. Wannenmacher, J. Debus, and F. Wenz, editors, *Strahlentherapie*, pages 49–80. Springer-Verlag, s.l., 2006.

[36] G. S. Ibbott, J. E. Barnes, G. R. Hall, and W. R. Hendee. Stem corrections for ionization chambers. *Medical Physics*, 2(6):328–330, 1975.

[37] ICRU-14. Icru report 14: Radiation dosimetry: X rays and gamma rays with maximum photon energies between 0.6 and 50 mev. 1981.

[38] ICRU-35. Icru report 35: Radiation dosimetry: Electron beams with energies between 1 and 50 mev. 12, 1985.

[39] ICRU-37. Icru report 37: Stopping powers for electrons and positrons. 1984.

[40] K. A. Johansson, L. O. Mattsson, L. Lindborg, and H. Svensson. Absorbed-dose determination with ionization chambers in electron and photon beams having energies between 1 and 50 mev, 1978.

[41] K. Zink and J. Wulff. On the wall perturbation correction for a parallel-plate nacp-02 chamber in clinical electron beams. *Med Phys*, 38(2):1045–1054, 2011.

[42] I. Kawrakow. Accurate condensed history monte carlo simulation of electron transport. i. egsnrc, the new egs4 version. *Med Phys*, 27(3):485–498, 2000.

[43] I. Kawrakow. Accurate condensed history monte carlo simulation of electron transport. ii. application to ion chamber response simulations. *Med Phys*, 27(3):499–513, 2000.

[44] I. Kawrakow. On the effective point of measurement in megavoltage photon beams. *Med Phys*, 33(6):1829–1839, 2006.

[45] I. Kawrakow, E. Mainegra-Hing, D. W. O. Rogers, F. Tessier, and B. R. B. Walters. The egsnrc code system: Monte carlo simulation of electron and photon transport. *National Research Council of Canada, Report PIRS-701*, 2017.

[46] N. D. Kessaris. Absorbed dose and cavity ionization for high-energy electron beams. *Radiation Research*, 43(2):288–301, 1970.

[47] A. Kling, F. J. C. Baräo, M. Nakagawa, L. Távora, P. Vaz, E. W. Larsen, and D. R. Tolar. A “transport” condensed history method: Advanced monte carlo for radiation physics, particle transport simulation and applications. 2001.

[48] H. Krieger. Strahlungsmessung und dosimetrie. 2013.

[49] C. M. Ma, R. T. Knight, A. E. Nahum, and W. P. Mayles. An investigation of the response of a simple design of plane-parallel chamber. *Physics in Medicine and Biology*, 39(10):1593–1608, 1994.

[50] C. M. Ma and A. E. Nahum. Bragg-gray theory and ion chamber dosimetry for photon beams. *Physics in Medicine and Biology*, 36(4):413–428, 1991.

[51] C. M. Ma and A. E. Nahum. Effect of size and composition of the central electrode on the response of cylindrical ionization chambers in high-energy photon and electron beams. *Physics in Medicine & Biology*, 38(2):267, 1993.

[52] N. Metropolis and S. Ulam. The monte carlo method. *Journal of the American Statistical Association*, 44(247):335, 1949.

[53] H. J. W. Müller-Kirsten. Basics of statistical physics.

[54] A. E. Nahum. Water/air mass stopping power ratios for megavoltage photon and electron beams. *Phys Med Biol*, 23(1):24–38, 1978.

[55] A. E. Nahum. Cavity theory, stopping power ratios, correction factors. *Clinical dosimetry measurements in radiotherapy*, pages 91–136, 2009.

[56] Å. Palm and O. Mattsson. Experimental study on the influence of the central electrode in farmer-type ionization chambers. *Physics in Medicine & Biology*, 44(5):1299–1308, 1999.

[57] J. Perl, J. Shin, J. Schümann, B. Faddegon, and H. Paganetti. Topas: An innovative proton monte carlo platform for research and clinical applications. *Medical Physics*, 39(11):6818–6837, 2012.

[58] R. Eckhardt. Stan ulam, john von neumann, and the monte carlo method. *Los Alamos Science - Special Issue*, pages 131–137, 1987.

[59] H. Reich and U. Burmester. Dosimetrie ionisierender strahlung: Grundlagen und anwendungen ; 50 tabellen. 1990.

[60] D. W. O. Rogers. How accurately can egs4/presta calculate ion-chamber response? *Medical Physics*, 20(2 Pt 1):319–323, 1993.

[61] D. W. O. Rogers. Fifty years of monte carlo simulations for medical physics. *Physics in Medicine and Biology*, 51(13):R287–301, 2006.

[62] D. W. O. Rogers, B. Walters, and I. Kawrakow. Beamnrc users manual. *National Research Council of Canada Report PIRS-509(a)revL*, 2013.

[63] E. Rutherford. Lxxix. the scattering of alpha and beta particles by matter and the structure of the atom. *The London, Edinburgh, and Dublin Philosophical Magazine and Journal of Science*, 21(125):669–688, 1911.

[64] F. Salvat. A generic algorithm for monte carlo simulation of proton transport. *Nuclear Instruments and Methods in Physics Research Section B: Beam Interactions with Materials and Atoms*, 316:144–159, 2013.

[65] B. Schaeken, R. Cuypers, J. Goossens, D. van den Weyngaert, and D. Verellen. Experimental determination of the energy response of alanine pellets in the high dose rate 192ir spectrum. *Physics in Medicine and Biology*, 56(20):6625–6634, 2011.

[66] J. Sempau and P. Andreo. Configuration of the electron transport algorithm of penelope to simulate ion chambers. *Phys Med Biol*, 51(14):3533–3548, 2006.

[67] L. V. Spencer and F. H. Attix. A cavity ionization theory including the effects of energetic secondary electrons. *Radiology*, 64(1):113, 1955.

[68] L. V. Spencer and F. H. Attix. A theory of cavity ionization. *Radiat Res*, 3(3):239–254, 1955.

[69] F. Tessier and I. Kawrakow. Effective point of measurement of thimble ion chambers in megavoltage photon beams. *Medical Physics*, 37(1):96, 2010.

[70] TRS 469. Calibration of reference dosimeters for external beam radiotherapy. no. 469, 2009.

[71] A. van der Plaetsen, J. Seuntjens, H. Thierens, and S. Vynckier. Verification of absorbed doses determined with thimble and parallel-plate ionization chambers in clinical electron beams using ferrous sulphate dosimetry. *Med Phys*, 21(1):37–44, 1994.

[72] F. Verhaegen, R. Zakikhani, A. Dusautoy, H. Palmans, G. Bostock, D. Shipley, and Seuntjens J. Perturbation correction factors for the nacp-02 plane-parallel ionization chamber in water in high-energy electron beams. *Phys Med Biol*, 51(5):1221–1235, 2006.

[73] P. von Voigts-Rhetz, M. Anton, H. Vorwerk, and K. Zink. Perturbation correction for alanine dosimeters in different phantom materials in high-energy photon beams. *Physics in Medicine and Biology*, 61(3):N70–9, 2016.

[74] P. von Voigts-Rhetz, D. Czarnecki, and K. Zink. Effective point of measurement for parallel plate and cylindrical ion chambers in megavoltage electron beams. *Zeitschrift fur medizinische Physik*, 2014.

[75] P. von Voigts-Rhetz, H. Vorwerk, and K. Zink. On the perturbation correction factor pcav of the markus parallel-plate ion chamber in clinical electron beams. *International Journal of Medical Physics, Clinical Engineering and Radiation Oncology*, 06(02):150–161, 2017.

[76] P. von Voigts-Rhetz and K. Zink. Ep-1130: Determination of the effective point of

measurement for parallel plate and cylindrical ionization chambers. *Radiotherapy and Oncology*, 106:S426, 2013.

[77] P. von Voigts-Rhetz and K. Zink. Su-e-t-448: On the perturbation factor p_cav of the markus parallel plate ion chambers in clinical electron beams, monte carlo based reintegration of an historical experiment. *Medical Physics*, 41(6):329, 2014.

[78] D. M. Wagner, P. Hüttenrauch, M. Anton, P. von Voigts-Rhetz, K. Zink, and H. A. Wolff. Feasibility study of entrance and exit dose measurements at the contra lateral breast with alanine/electron spin resonance dosimetry in volumetric modulated radiotherapy of breast cancer. *Physics in Medicine and Biology*, 62(13):5462–5472, 2017.

[79] L. L. W. Wang and D. W. O. Rogers. Calculation of the replacement correction factors for ion chambers im megavoltage beams by monte carlo simulation. *Med. Phys*, 35(5):1747–1755, 2008.

[80] T. Warnock. Random-number generators. *Los Alamos Science*, 15:137–141, 1987.

[81] C. J. Werner and et al. Mcnp version 6.2 release notes. *Los Alamos National Lab. (LANL), Los Alamos, NM (United States)*, 2018.

[82] World Health Organization. Cancer, 23.11.2017.

[83] J. Wulff, K. Zink, and I. Kawrakow. Efficiency improvements for ion chamber calculations in high energy photon beams. *Med Phys*, 35(4):1328–1336, 2008.

[84] G. G. Zeng, M. R. McEwen, D. W. O. Rogers, and N. V. Klassen. An experimental and monte carlo investigation of the energy dependence of alanine/epr dosimetry: I. clinical x-ray beams. *Physics in Medicine and Biology*, 49(2):257–270, 2004.

[85] G. G. Zeng, M. R. McEwen, D. W. O. Rogers, and N. V. Klassen. An experimental and monte carlo investigation of the energy dependence of alanine/epr dosimetry: Ii. clinical electron beams. *Physics in Medicine and Biology*, 50(6):1119–1129, 2005.

[86] K. Zink, D. Czarnecki, H. K. Looe, P. von Voigts-Rhetz, and D. Harder. Monte carlo study of the depth-dependent fluence perturbation in parallel-plate ionization chambers in electron beams. *Medical Physics*, 41(11):111707, 2014.

Effective point of measurement for parallel plate and cylindrical ion chambers in megavoltage electron beams

Philip von Voigts-Rhetz[1,*], **Damian Czarnecki**[1], **Klemens Zink**[1,2]

[1] Institut für Medizinische Physik und Strahlenschutz – IMPS, Technische Hochschule Mittelhessen, University of Applied Sciences, Gießen, Germany
[2] University Hospital Marburg, Department of Radiotherapy and Radiation Oncology, Philipps-University, Marburg, Germany

Received 31 July 2013; accepted 2 December 2013

Abstract

The presence of an air filled ionization chamber in a surrounding medium introduces several fluence perturbations in high energy photon and electron beams which have to be accounted for. One of these perturbations, the displacement effect, may be corrected in two different ways: by a correction factor p_{dis} or by the application of the concept of the effective point of measurement (EPOM). The latter means, that the volume averaged ionization within the chamber is not reported to the chambers reference point but to a point within the air filled cavity. Within this study the EPOM was determined for four different parallel plate and two cylindrical chambers in megavoltage electron beams using Monte Carlo simulations. The positioning of the chambers with this EPOM at the depth of measurement results in a largely depth independent residual perturbation correction, which is determined within this study for the first time. For the parallel plate chambers the EPOM is independent of the energy of the primary electrons. Whereas for the Advanced Markus chamber the position of the EPOM coincides with the chambers reference point, it is shifted for the other parallel plate chambers several tenths of millimeters downstream the beam direction into the air filled cavity. For the cylindrical chambers there is an increasing shift of the EPOM with increasing electron energy. This shift is in upstream direction, i.e. away from the chambers reference point toward the focus. For the highest electron energy the position of the calculated EPOM is in fairly good

Der effektive Messpunkt von Flachkammern und Kompaktkammern in hochenergetischer Elektronenstrahlung

Zusammenfassung

Das Vorhandensein einer luftgefüllten Ionisationskammer in einem Umgebungsmaterial führt zu verschiedenen Fluenzstörungen der hochenergetischen Photonen und Elektronenstrahlung. Eine dieser Störungen, der Verdrängungseffekt, kann auf zwei Arten korrigiert werden: mit einem Störungsfaktor p_{dis} oder einer Verschiebung der Kammer in den effektiven Messort (EPOM). Dies bedeutet, dass die über das sensitive Volumen der Kammer gemittelten Ionisationen nicht dem Referenzpunkt sondern dem so genannten effektiven Messort zugeordnet werden. Im Rahmen dieser Studie wurde der EPOM für vier verschiedene Flachkammern und zwei zylindrische Ionisationskammern in hochenergetischer Elektronenstrahlung mittels Monte-Carlo-Simulationen bestimmt. Die Positionierung der Kammern mit dem EPOM in der Messtiefe hat zur Folge, dass der verbleibende Störungsfaktor weitestgehend unabhängig von der Messtiefe ist. Der Störungsfaktor p wurde erstmalig in dieser Studie für alle Kammern für den gesamten Bereich klinischer Elektronenenergien bestimmt. Während für die Advanced Markus Kammer die Position des EPOM mit dem Referenzpunkt der Kammern übereinstimmt, liegt er für die übrigen Flachkammern

* Corresponding author: Philip von Voigts-Rhetz, Institut für Medizinische Physik und Strahlenschutz, Technische Hochschule Mittelhessen, Wiesenstraße 14, 35390 Gießen, Germany.
E-mail: philip.von.voigts-rhetz@kmub.thm.de (P. von Voigts-Rhetz).

agreement with the recommendation given in common dosimetry protocols, for the smallest energy, the calculated EPOM positions deviate about 30% from this recommendation.

Keywords: Monte Carlo simulations, electron dosimetry, effective point of measurement, ionization chambers

mehrere Zehntel Millimeter in Strahlrichtung verschoben im luftgefüllten Volumen der Kammer. Für die zylindrischen Kammern ist eine zunehmende Verschiebung des EPOM mit ansteigender Elektronenenergie zu beobachten. Diese Verschiebung ist entgegen der Strahlenrichtung, d.h. von dem Bezugspunkt der Kammern in Richtung des Fokus. Für die höchste Elektronenenergie im Rahmen der Untersuchung ist die ermittelte Verschiebung des EPOM in guter Übereinstimmung mit der Empfehlung gültiger Dosimetrieprotokolle. Für die kleinste Energie zeigt sich eine Abweichung von etwa 30% zu diesen Empfehlungen.

Schlüsselwörter: Monte-Carlo-Simulation, Elektronendosimetrie, effektiver Messort, Ionisationskammer

1 Introduction

Clinical dosimetry in megavoltage electron and photon beams requires the use of air filled ionization chambers. The determination of the quantity absorbed dose to water from the detector signal is based on cavity theory [1,2], according to which several chamber and energy dependent perturbation corrections p are necessary to calculate the absorbed dose to water at a point $\vec{r}$ in the absence of the detector. The reason for these perturbation corrections are fluence perturbations induced by the finite volume of the detector, the non-water equivalent materials of the chamber etc., resulting in deviations of the detector signal in comparison to an ideal Bragg-Gray detector. One of these perturbations, the so called displacement correction, which comes from the displacement of the surrounding material water by the detector, may be accounted for in two different ways: by a factor commonly denoted as p_{dis} [3] or p_{gr} [4] or by a small chamber shift, to position not the chambers reference point, but the so called effective point of measurement (EPOM) at the point of interest $\vec{r}$ within the water phantom [5]. By definition, the reference point for cylindrical chambers is placed on the chambers symmetry axis, for parallel plate chambers it is the center of the entrance surface of the air filled cavity.

The EPOM concept was first introduced by Skaggs [6] for the measurement of depth dose curves in high energy electron beams and was further developed and also applied to high energy photon beams especially by Dutreix [7] and Johansson et al. [8]. Former dosimetry protocols [9] did apply this concept for reference dosimetry as well as for the measurement of depth ionization curves in high energy photon and electron beams. Today the EPOM concept is still applied for absorbed dose determination with ionization chambers [4] and for electron dosimetry [3,10]. For reference dosimetry in clinical photon beams most dosimetry protocols recommend the application of a perturbation correction p_{dis}; only the German protocol DIN 6800-2 [11] applies the EPOM concept for all types of measurements.

Several newer publications again launched the discussion about the effective point of measurement, not only for thimble chambers in high energy photon beams [12–19], but also in case of electron dosimetry. Monte Carlo calculations performed by Wang and Rogers [20] showed that the EPOM of parallel plate chambers in high energy electron beams may not coincide with the chambers reference point and that for cylindrical chambers the upstream distance Δz from the reference point to the EPOM given in the common dosimetry protocols may be to small. Looe et al. obtained similar results in their experimental investigations including several parallel-plate and cylindrical chambers.

In all these studies the EPOM was determined from relative depth dose curves, i.e. no information about the resulting perturbation correction p is given. According to the next revision of the German dosimetry protocol DIN 6800-2, which will be published within the next two years, a chamber dependent EPOM will be specified. To apply this EPOM not only for relative dose measurements but also for reference dosimetry, the resulting perturbation corrections p has to be known. Therefore the purpose of this paper is to provide a detailed Monte Carlo study to determine not only the EPOM but furthermore the perturbation correction for frequently used ion chambers for the whole range of clinical electron energies. The EPOM in the approach of this study is characterized by the fact, that the resulting overall perturbation correction is as depth independent as possible.

2 Fundamentals

According to cavity theory the absorbed dose to water D_w at the depth z in a water phantom in the absence of the detector

is related to the mean absorbed dose $\overline{D}_{det}$ imparted to the air filled volume of the detector [1,3]:

$$D_w(z) = p \cdot s^{\Delta}_{w,a}(z) \cdot \overline{D}_{det} \quad (1)$$

where $s^{\Delta}_{w,a}$ denotes the ratio of restricted mass collision stopping powers of the materials water and air and p the perturbation correction factor accounting for the different electron fluence perturbations due to the presence of the detector. It is generally assumed, that the perturbation factor p may be factorized [3]:

p_{wall}: change of electron fluence due to the non-water equivalence of the chamber wall and any waterproofing material;
p_{cel}: change of electron fluence due to the central electrode;
p_{cav}: change of electron fluence related to the air cavity, predominantly the in-scattering of electrons (p_{fl} according to AAPM TG-51 [4]);
p_{dis}: accounts for the effect of replacing a volume of water with the detector cavity when the reference point of the chamber is positioned at the depth of measurement (p_{gr} according to AAPM TG-51). If the EPOM concept is applied, $p_{dis} = 1$

The ICRU [21] concept of reporting absorbed dose at a point in a phantom as described in Eq. (1) is a very clear and useful concept from a physical or mathematical point of view. But, as every energy deposition, hence every absorbed dose measurement implies a finite volume, it is a priori not known to which point within the detector the absorbed dose has to be reported. Due to the finite volume of every detector a fluence and also a dose gradient within the detector is present, even if the detector is positioned at the absorbed dose maximum of a depth dose curve [22]. For reference dosimetry in high energy photon beams most present codes of practice [3,4] report the measured absorbed dose value to the chambers reference point, which is by definition for cylindrical chambers a point on the symmetry axis and for parallel plate chambers the center of the entrance surface of the air filled cavity. In that case the displacement effect is corrected by the factor p_{dis}. For relative dose measurements generally the EPOM concept is applied, i.e. the measured absorbed dose is reported to a different point within the chamber, the so called effective point of measurement (EPOM) and no displacement correction is necessary. According to the IAEA and the AAPM protocol, the EPOM for cylindrical chambers for photon beams is at a distance $\Delta z = -0.6 \cdot r$ away from the reference point in upstream direction and $\Delta z = -0.5 \cdot r$ for electron beams. Within these Eqs. r is the radius of the air filled cavity. The German protocol uses a value $\Delta z = -0.5 \cdot r$ for both radiation types. For parallel plate chambers in high energy electron beams $\Delta z = 0$ is assumed in all dosimetry protocols, but some protocols [3,10,11] account for the non-water equivalence of the entrance window of parallel plate chambers, i.e. the chambers reference point has to be positioned at the water equivalent depth z, not at the geometrical depth z.

In a very systematic and comprehensive Monte Carlo study Kawrakow [12] has shown, that the EPOM shift Δz for cylindrical chambers in photon beams is not only a function of the cavity radius, but also depends in a complex way on all other construction details as the cavity length, the central electrode, the chamber walls and also on the energy of the photon beam. That means, the EPOM has to be determined for each individual chamber type as a function of energy. For a large number of cylindrical chambers in megavoltage photon beams this was performed by Tessier and Kawrakow in a recent publication [16].

Regarding clinical electron dosimetry, several authors [24–26] have demonstrated, that there is a strong depth dependence of the overall perturbation correction p. Moreover, Zink and Wulff [27,28] have shown, that the different perturbation corrections mentioned above obey different depth dependencies and the overall perturbation p strongly depends on the positioning of the chamber, i.e. on the choice of the effective point of measurement within the chamber. For practical clinical purposes it would be of great advantage to find an effective point of measurement within the chamber, resulting in a depth independent overall perturbation correction p, which could be applied for all depths of the depth ionization curve to calculate absorbed dose to water (see Eq. (1)).

3 Methods and Material

3.1 EPOM determination in clinical electron beams

Following Wang and Rogers [20] the effective point of measurement was determined as follows: (i): a depth dose curve $D_w(z)$ with sufficient depth resolution and small statistical uncertainty was calculated in a water phantom. To get a continuous function of depth z a spline interpolation of the depth dose curve was performed; (ii) the depth ionization curve of the ionization chamber was calculated within the water phantom, positioned with its reference point at the depth of measurement z; (iii) the depth dose curve $D_w(z)$ was shifted an amount Δz until the root mean square deviation:

$$(rms(\Delta z))^2 = \frac{1}{n} \cdot \sum_i \left(D^i_w(z + \Delta z) - s^{\Delta}_{w,a}(z) \cdot \overline{D}_{deti}(z) \right)^2 \quad (2)$$

reaches a minimum. Within Eq. (2), n is the number of data points of the depth ionization and depth dose curve. The resulting shift Δz corresponds to the (negative) distance from the chambers reference point to the effective point of measurement (EPOM). Positioning the EPOM at the depth of measurement will result in a perturbation correction p, which is as depth independent as possible.

Table 1
Volume V and radius r of the active volume of used ionization chambers. For the parallel plate chambers additionally the thickness of the entrance window d is given, i.e. the distance from the chambers surface to the reference point. The central electrode of all cylindrical ion chambers consists of aluminum. For more details see [23].

chamber	type	V in cm^3	r in cm	d in cm	guard width in cm
Roos PTW-34001	parallel	0.350	0.780	0.112	0.420
Markus PTW-23343	parallel	0.055	0.265	0.130	0.035
Adv. Markus PTW-34045	parallel	0.020	0.250	0.130	0.200
NACP-02	parallel	0.160	0.825	0.060	0.033
					central electrode r in cm
Semiflex PTW - 31010	cylindrical	0.125	0.275		0.055
PinPoint PTW-31014	cylindrical	0.015	0.100		0.015

3.2 Monte Carlo simulations

All Monte Carlo simulations were performed with the EGSnrc code system [29] applying the user code egs_chamber [30] for absorbed dose calculations and SPRRZnrc [31] for the calculation of stopping power ratios necessary to determine the overall perturbation correction p in Eq. (1). In all simulations the particle production thresholds and transport cut-off energies are AE = ECUT = 521 keV and AP = PCUT = 10 keV for electrons and photons, respectively. In preliminary calculations it was ensured, that a further decrease of these energy thresholds will give same results within statistical uncertainties of typical 0.1%. To increase the calculation efficiency variance reduction methods like photon splitting and russian roulette were applied [32].

The EPOM was calculated for four different parallel-plate chambers and two cylindrical chambers (see Tab. 1). They were modeled in detail according to the information provided by the manufacturer using the EGSnrc C++ class library [33]. In case of the Markus and Advanced Markus chamber, the waterproof protection cap is always included in the simulations. More details about the geometry and material composition, especially for the parallel plate chambers, may be found in a previous work [23]. The chambers were positioned in a water phantom dimensioned 30 x 30 x 30 cm^3, the source to surface distance was set to 100 cm in all simulations and the field size at the water phantom surface was 10 x 10 cm^2. The energy deposition was calculated within the active volume of the chambers. The absorbed dose to water was calculated within a small water voxel with a radius of 0.5 cm and a height of 0.02 cm. This voxel size was also used for the calculation of the mass stopping power ratio water to air.

As electron source several fluence spectra of a Varian Clinac 2100C accelerator [34] covering the whole range of clinical applications were applied. The nominal electron energies and depth dose characteristics of these spectra are summarized in Tab. 2.

Table 2
Characteristics of used electron fluence spectra and resulting depth dose curves [34]

nom. energy in MeV	R_{50}	z_{ref} in g / cm^2	R_p
6	2.63	1.48	3.11
9	4.00	2.30	4.85
12	5.18	3.01	6.35
18	7.72	4.53	9.58

4 Results and discussion

4.1 EPOM of parallel plate chambers

In preliminary calculations the dependence of the minimization result (Eq. (2)) on the range of the depth dose data included in the minimization process to determine the EPOM was investigated. As shown in Fig. 1, there is a clear dependence of the effective point of measurement on the considered depth dose range. Based on these results it was decided, to include the depth dose data from the surface (z = 0.1 cm) down to the practical range R_p for each electron energy.

Tab. 3 summarizes the results for the plane parallel chambers examined in this study. The table gives the position of the EPOM in relation to the reference point of each chamber. As can be seen is the position of the EPOM within the chamber for the largest part independent from electron energy. The data of the Roos chamber are in good agreement with the experimental data from Looe et al.; for this chamber the authors published a value of Δz =0.04±0.01 cm. They do also agree within ±0.01 cm with the Monte Carlo data published by Wang and Rogers [20] for the NACP and Markus chamber.

Concerning the Markus chamber, the determined EPOM from the experimental study of Looe et al. [18] deviates from the data given here (0.04 cm vs. 0.026 cm). The reason for this is based on the different method in the determination of

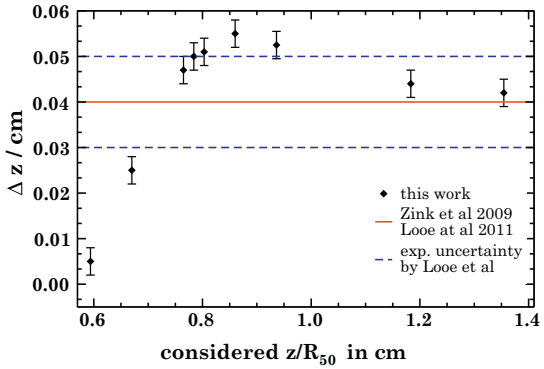

Figure 1. Dependence of the EPOM on the considered part of the depth dose curve. Results are given for a Roos chamber in a 6 MeV electron beam. The solid line displays the results from Looe et al. [18] and Zink et al. [27]. The dashed lines are the experimental uncertainties given by Looe. The error bars indicate the statistical uncertainties of the Monte Carlo simulations (1σ).

the EPOM for the Markus chamber in both studies. According to the German dosimetry protocol [11] the depth dependent perturbation correction p_{cav} has to be applied for the guardless Markus chamber to correct the in-scattering of electrons into the Markus chamber (see ICRU- 35 [35]). In contrast to our simulations and the simulations from Wang and Rogers, this depth dependent correction was applied by Looe et al. before determining the EPOM. This explains the different EPOM's in both studies.

According to present dosimetry protocols [11,4,3] the chambers reference point should be positioned at the water equivalent depth z, i.e. the non-water equivalence of the chambers entrance window should be accounted for. This should be performed by scaling the thickness of the entrance window by the mass density [3], or the electron density [11] of the entrance window material. For the Roos chamber, this would result in a shift of $\Delta z = 0.0017$ cm. For the Markus and Advanced Markus chamber a negative shift of $\Delta z = -0.0026$ cm would be the outcome [23], i.e. the EPOM would be outside the chambers active volume. Regarding our results and the newest literature data summarized in Tab. (3), the positioning recommendation given in DIN 6800-2 is questionable. Therefore in the new edition of the German dosimetry protocol this will be reviewed and it can be assumed that values similar to those given in Tab. (3) will be recommended.

Applying the EPOM shift of Tab. (3) the resulting depth dependence of the overall correction factor $p(z)$ calculated according to Eq. (1) is displayed in Fig. 2. The diagrams clearly show, that the depth dependence of p mostly vanishes if the chamber is positioned with the EPOM given in Tab. 3 at the depth of measurement z. Up to the half value depth R_{50} the variation of p is within 1% for all chambers and energies. Beyond this depth the deviations increase and may reach 3% or more at the practical range R_p. A compilation of the numerical data of the perturbation corrections p is given in Tab. (5).

A closer look to the data given in Fig. (2) shows that the residual variation of the perturbation correction p with

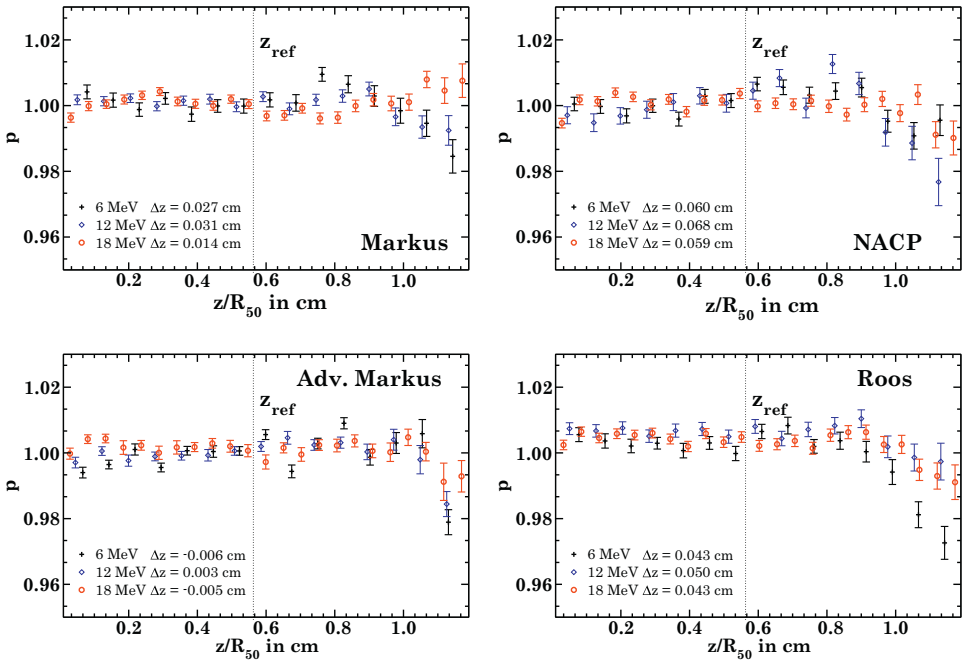

Figure 2. Overall correction factor $p = D_w(z) / \left(\overline{D}_{detEPOM}(z) \cdot s^{\Delta}_{w,a}(z)\right)$ as a function of depth in a water phantom for four parallel plate chambers. The chambers are positioned with their EPOM at the depth of measurement z. The error bars indicate the statistical uncertainty of the Monte Carlo results (1σ).

Table 3
Calculated EPOM for different parallel plate chambers as a function of the electron energy. A positive shift Δz indicates, that the effective point of measurement is downstream the chambers reference point, i.e. away from the focus. The numbers in brackets represent the standard deviation statistical uncertainty in the last digit. Literature data for the Roos, Markus and NACP-02 chamber are taken from 1: [27], 2: [18], 3: [20] and 4:[20].

chamber	EPOM shift Δz relative to the reference point in cm					
	6 MeV	9 MeV	12 MeV	18 MeV	$\overline{\Delta z}$	literature
Roos	0.040(4)	0.048(4)	0.050(4)	0.043(4)	0.045(4)	0.04±0.01[1,2]
Markus	0.027(4)	0.031(4)	0.031(4)	0.014(4)	0.026(4)	0.02±0.01[3], 0.04±0.01[2]
Adv. Markus	0.007(4)	-0.004(4)	0.003(4)	-0.005(4)	0.000(4)	-
NACP-02	0.060(4)	0.065(4)	0.068(4)	0.059(4)	0.065(4)	0.06±0.01[4]

depth is systematical. This was already shown in a previous paper (Zink and Wulff [27]) for the Roos chamber. To get a better understanding of the residual variation of p more detailed Monte Carlo simulations were performed, but the results would go beyond the scope of the present paper and will be published in the near future.

4.2 EPOM of cylindrical chambers

As may be expected from literature data [20], the EPOM shift for cylindrical chambers varies with the energy. In agreement with the mentioned publication, our simulations give a progressive movement of the EPOM toward the focus with increasing electron energy (see Tab. 4 and Fig. 3). For the highest electron energy within this study, the calculated EPOM shift for both chambers is close to the recommended value $\Delta z/r = -0.5$ (see sec. (2)), whereas for the lowest energy the EPOM shift $\Delta z/r$ deviates by more than 30% from this value. But it has to be remarked at this point, that all present dosimetry protocols do not allow the use of cylindrical ion chambers for electron energies below 10 MeV (R_{50} <4 cm). For electron energies above 10 MeV (R_{50} >4 cm) the recommended shift $\Delta z/r = -0.5$ is a fairly good mean value for the chambers investigated in this study.

Fig. 4 displays the resulting overall perturbation corrections p for the investigated cylindrical chambers. As can be seen, the application of the calculated EPOM shift results in a mostly

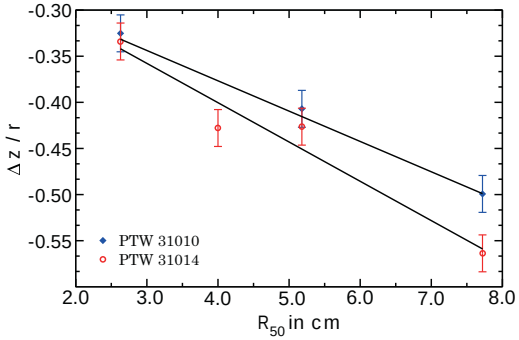

Figure 3. Energy dependence of the EPOM for the cylindrical chambers used in this study. The EPOM shift Δz is given in units of the chamber's cavity radius r. The error bars indicate the statistical uncertainties of the Monte Carlo simulations (1σ).

depth independent perturbation correction p for the Pinpoint chamber with variations ± 1% down to a depth of $z/R_{50} \approx 1.1$. In contrast, the depth dependence of the larger chamber, PTW 31010, is much more pronounced even if the optimal EPOM is chosen. Beyond a depth $z/R_{50} \approx 0.8$ there is an increase of p for all energies. For the smallest energy (6 MeV), the variation Δp is already in the range of 3% concerning the depth range from the surface to the half value depth R_{50}. For the higher energies this variation is within 2%. The numerical data for the perturbation corrections are summarized in

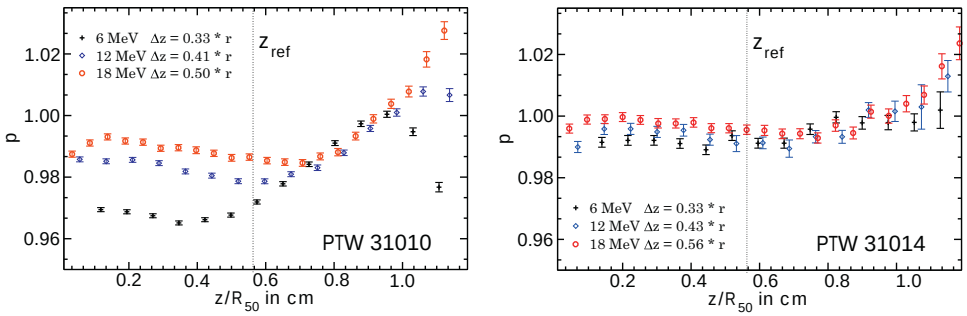

Figure 4. Overall correction factor $p = D_w(z) / \left(\overline{D}_{detEPOM}(z) \cdot s^{\Delta}_{w,a}(z)\right)$ as a function of depth in a water phantom for two cylindrical chambers. The chambers are positioned with their EPOM at the depth of measurement z. Error bars indicate the statistical uncertainties of the Monte Carlo simulations.

Table 4
Calculated EPOM for two cylindrical chambers as a function of the electron energy. A negative shift Δz indicates, that the effective point of measurement is upstream the chambers reference point, i.e. toward the focus. The numbers in brackets represent the standard deviation statistical uncertainty in the last digit.

chamber	EPOM shift Δz normalized to the cavity radius r				
	6 MeV	9 MeV	12 MeV	18 MeV	fit
PTW 31010	-0.335(4)	-0.391(4)	-0.407(4)	-0.499(4)	$-\Delta z/r$ = 0.032 * R50 +0.25
PTW 31014	-0.334(4)	-0.428(4)	-0.426(4)	-0.564(4)	$-\Delta z/r$ = 0.043 * R50 +0.23

Table 5
Calculated overall perturbation correction p for the chambers investigated in this study; p is calculated for the reference depth z_{ref} and is also given as a mean value $\overline{p}$ over depth z with its standard deviation $\Delta\overline{p}$. The depth range calculating the mean value was z/R_{50} = 0 to 1 for parallel plate and z/R_{50} = 0 to 0.8 for cylindrical ion chambers.

chamber	energy in MeV	$\overline{\Delta z}$ in cm	$p(z_{ref})$	$\lvert\Delta p(z_{ref})\rvert$	$\overline{p}$	$\Delta\overline{p}$
Roos	6, 12, 18	0.045	1.005	0.003	1.005	0.003
Markus	6, 12, 18	0.026	1.000	0.003	1.004	0.004
Adv. Markus	6, 12, 18	0.000	1.005	0.002	1.006	0.003
NACP-02	6, 12, 18	0.067	1.005	0.003	1.007	0.005

chamber	energy in MeV	$\overline{\Delta z}/r$	$p(z_{ref})$	$\lvert\Delta p(z_{ref})\rvert$	$\overline{p}$	$\Delta\overline{p}$
	6	-0.335	0.975	0.004	0.971	0.009
PTW 31010	12	-0.391	0.980	0.004	0.982	0.005
	18	-0.499	0.990	0.004	0.988	0.005
	6	-0.334	0.990	0.004	0.991	0.003
PTW 31014	12	-0.428	0.990	0.004	0.992	0.004
	18	-0.564	0.995	0.004	0.998	0.008

Tab. 5. The behavior of the relatively large cylindrical chamber PTW 3010 is a consequence of the well-known inscattering effect [8] and the reason for the recommendation given in all dosimetry protocols, not to use cylindrical chambers for electron energies below 10 MeV (R_{50} <4 cm).

5 Summary and Conclusion

In the present study the effective point of measurement for four parallel plate chambers and two cylindrical chambers in clinical electron beams was investigated by Monte Carlo simulations using a comparable approach as Kawrakow [12] and Wang and Rogers [20]. With the exception of the Markus chamber our results confirm the experimental data from Looe et al. and were extended to the whole range of clinical relevant electron energies and include not only parallel plate chambers but also cylindrical chambers. Moreover, the Monte Carlo calculations did allow the calculation of the perturbation correction p necessary to determine the absorbed dose to water from measured depth ionization curves.

Our results have shown that for all parallel plate chambers there is an effective point of measurement within the air filled cavity and that the resulting depth dependence of the overall perturbation correction is largely depth independent. The variation of p with depth is no more than 1% down to depths of $z/R_{50} \approx 1$. Moreover, the EPOM for these chambers is mostly independent of the energy of the primary electrons. Except for the Advanced Markus chamber the EPOM differs markedly from the chambers reference point. Regarding cylindrical chambers the EPOM shift is energy dependent. For large electron energies its value $\Delta z/r$ is close to the recommended value $|\Delta z/r| = 0.5$ and decreases by more than 30% for the lowest energy considered in this study (6 MeV). Applying the EPOM shift, the small Pinpoint chamber exhibits a depth independent overall perturbation correction p over a comparable range of the depth dose curve as the parallel plate chambers. For the larger Semiflex chamber PTW 31010 this range is reduced to $z/R_{50} \approx 0.8$, i.e. if cylindrical chambers are utilized for electron dosimetry small volumed chambers like the Pinpoint chamber should be preferred.

Applying the proposed EPOM shift from this study would increase the accuracy of depth dose measurements in high energy electron beams, as for the conversion from depth ionization data to depth dose data only the stopping power ratios have to be applied, which may simply be calculated from the fit given by Burns et al. [36]. This is especially of great importance if modern dose calculation algorithms like Monte Carlo based algorithms are compared with measurements.

Reference dosimetry can be performed with the same chamber positioning, if the proposed perturbation correction p at the reference depth z_{ref} is applied, i.e. clinical electron dosimetry will be simplified.

Acknowledgements

The authors thank Dr. E. Schüle of PTW-Freiburg for providing blueprints of the chambers used in this study. Valuable discussions with the members of German working group DIN 6800-2 are also acknowledged.

References

[1] Spencer LV, Attix FH. A theory of cavity ionization. Radiat Res 1955;3(3):239–54.
[2] Spencer LV, Attix FH. A cavity ionization theory including the effects of energetic secondary electrons. Radiology 1955;64(1):113.
[3] Andreo P, Burns DT, Hohlfeld K, Huq MS, Kanai T, Laitano F, Smyth V, Vynckier S. Absorbed dose determination in external beam radiotherapy. An international code of practice for dosimetry based on standards of absorbed dose to water, Technical Reports Series TRS-398,Vienna. International Atomic Energy Agency 2000.
[4] Almond PR, Biggs PJ, Coursey BM, Hanson WF, Huq MS, Nath R, Rogers DW. AAPM's TG-51 protocol for clinical reference dosimetry of high-energy photon and electron beams. Med Phys 1999;26(9):1847–70.
[5] Andreo P, Nahum A. Supplementary details on codes of practice for absolute dose determination: Handbook of radiotherapy physics. Taylor & Francis; 2007.
[6] Skaggs LS. Depth dose of electrons from the betatron. Radiology 1949;53(6):868–74.
[7] Dutreix J, Dutreix A. Comparative study of a series of ionization chambers within 20 and 10 MeV electron fluxes. Biophysik 1966;3(3):249–58.
[8] Johansson KA, Mattsson LO, Lindborg L, Svensson H. Absorbed-dose determination with ionization chambers in electron and photon beams having energies between 1 and 50 MeV, National and International Standardization of Radiation Dosimetry, IAEA Proceedings Series. Vienna 1978;2:243–70.
[9] IAEA, Absorbed Dose Determination in Photon and Electron Beams. IAEA Technical Report Series 277 (2nd edn in 1997) (1987).
[10] Thwaites DI, DuSautoy AR, Jordan T, McEwen MR, Nisbet A, Nahum AE, Pitchford WG, Working Party IPEM. The IPEM code of practice for electron dosimetry for radiotherapy beams of initial energy from 4 to 25 MeV based on an absorbed dose to water calibration. Phys Med Biol 2003;48(18):2929–70.
[11] DIN6800-2, Procedures of dosimetry with probe-type detectors for photon and electron radiation - Part 2: Ionization chamber dosimetry of high energy photon and electron radiation (2008).
[12] Kawrakow I. On the effective point of measurement in megavoltage photon beams. Med Phys 2006;33(6):1829–39.
[13] McEwen MR, Kawrakow I, Ross CK. The effective point of measurement of ionization chambers and the build-up anomaly in MV x-ray beams. Med Phys 2008;35(3):950–8.
[14] Wang LLW, Rogers DWO. The replacement correction factors for cylindrical chambers in high-energy photon beams. Phys Med Biol 2009;54(6):1609–20.
[15] Andreo P. On the p(dis) correction factor for cylindrical chambers. Phys Med Biol 2010;55(5). L9-16; author reply L17-9.
[16] Tessier F, Kawrakow I. Effective point of measurement of thimble ion chambers in megavoltage photon beams. Medical Physics 2010;37(1):96.
[17] Tessier F, Hooten BD, McEwen MR. Zero-shift thimble ionization chamber. Medical Physics 2010;37(3):1161.
[18] Looe HK, Harder D, Poppe B. Experimental determination of the effective point of measurement for various detectors used in photon and electron beam dosimetry. Phys Med Biol 2011;56(14):4267–90.
[19] Legrand C, Hartmann GH, Karger CP. Experimental determination of the effective point of measurement for cylindrical ionization chambers in 60-Co gamma radiation. Phys Med Biol 2012;57(11):3463–75.
[20] Wang LLW, Rogers DWO. Study of the effective point of measurement for ion chambers in electron beams by Monte Carlo simulation. Medical Physics 2009;36(6):2034.
[21] ICRU-33, ICRU Report 33: Radiation Quantities and Units, ICRU, Bethesda / USA, 1980.
[22] Bjärngard BE, Kase KR. Replacement correction factors for photon and electron dose measurements. Med Phys 1985;12(6):785–7.
[23] Zink K, Wulff J. Beam quality corrections for parallel-plate ion chambers in electron reference dosimetry. Phys Med Biol 2012;57(7):1831–54.
[24] Buckley LA, Rogers DWO. Wall correction factors, P_wall, for parallel-plate ionization chambers. Med Phys 2006;33(6):1788–96.
[25] Verhaegen F, Zakikhani R, Dusautoy A, Palmans H, Bostock G, Shipley D, Seuntjens J. Perturbation correction factors for the NACP-02 plane-parallel ionization chamber in water in high-energy electron beams. Phys Med Biol 2006;51(5):1221–35.
[26] Araki F. Monte Carlo calculations of correction factors for plane-parallel ionization chambers in clinical electron dosimetry. Med Phys 2008;35:4033–40.
[27] Zink K, Wulff J. Positioning of a plane-parallel ionization chamber in clinical electron beams and the impact on perturbation factors. Phys Med Biol 2009;54(8):2421–35.
[28] Zink K, Wulff J. On the wall perturbation correction for a parallel-plate NACP-02 chamber in clinical electron beams. Med Phys 2011;38(2):1045–54.
[29] I. Kawrakow, D. W. O. Rogers, The EGSnrc Code System: Monte Carlo Simulation of Electron and Photon Transport; NRCC Report PIRS-701, National Research Council of Canada.
[30] Wulff J, Zink K, Kawrakow I. Efficiency improvements for ion chamber calculations in high energy photon beams. Med Phys 2008;35(4):1328–36.
[31] D. W. O. Rogers, J. P. S. I. Kawrakow, B. R. B. Walters, E. Mainegra-Hing, NRC user codes for EGSnrc, National Research Council of Canada Report PIRS-702.
[32] Kawrakow I, Fippel M. Investigation of variance reduction techniques for Monte Carlo photon dose calculation using XVMC. Phys Med Biol 2000;45(8):2163–83.
[33] I. Kawrakow, E. Mainegra-Hing, F. Tessier, B.R.B. Walter, The EGSnrc C++class library, NRC Report PIRS-898 (rev A), Ottawa, Canada.
[34] Ding GX, Rogers DWO, Mackie TR. Calculation of stopping-power ratios using realistic clinical electron beams. Med Phys 1995;22(5):489–501.
[35] ICRU-35, ICRU Report 35: Radiation Dosimetry: Electron Beams with Energies Between 1 and 50 MeV, Vol. 12, ICRU, Bethesda / USA, 1985.
[36] Burns DT, Ding GX, Rogers DWO. R50 as a beam quality specifier for selecting stopping-power ratios and reference depths for electron dosimetry. Med Phys 1996;23(3):383–8.

Monte Carlo study of the depth-dependent fluence perturbation in parallel-plate ionization chambers in electron beams

K. Zink[a)]
Institute of Medical Physics and Radiation Protection (IMPS), University of Applied Sciences Giessen, Giessen D-35390, Germany and Department of Radiotherapy and Radiooncology, University Medical Center Giessen-Marburg, Marburg D-35043, Germany

D. Czarnecki
Institute of Medical Physics and Radiation Protection (IMPS), University of Applied Sciences Giessen, Giessen D-35390, Germany

H. K. Looe
Clinic for Radiation Therapy, Pius-Hospital, Oldenburg D-26129, Germany and WG Medical Radiation Physics, Carl von Ossietzky University, Oldenburg D-26129, Germany

P. von Voigts-Rhetz
Institute of Medical Physics and Radiation Protection (IMPS), University of Applied Sciences Giessen, Giessen D-35390, Germany

D. Harder
Prof. em., Medical Physics and Biophysics, Georg August University, Göttingen D-37073, Germany

(Received 15 December 2013; revised 19 September 2014; accepted for publication 19 September 2014; published 14 October 2014)

Purpose: The electron fluence inside a parallel-plate ionization chamber positioned in a water phantom and exposed to a clinical electron beam deviates from the unperturbed fluence in water in absence of the chamber. One reason for the fluence perturbation is the well-known "inscattering effect," whose physical cause is the lack of electron scattering in the gas-filled cavity. Correction factors determined to correct for this effect have long been recommended. However, more recent Monte Carlo calculations have led to some doubt about the range of validity of these corrections. Therefore, the aim of the present study is to reanalyze the development of the fluence perturbation with depth and to review the function of the guard rings.
Methods: Spatially resolved Monte Carlo simulations of the dose profiles within gas-filled cavities with various radii in clinical electron beams have been performed in order to determine the radial variation of the fluence perturbation in a coin-shaped cavity, to study the influences of the radius of the collecting electrode and of the width of the guard ring upon the indicated value of the ionization chamber formed by the cavity, and to investigate the development of the perturbation as a function of the depth in an electron-irradiated phantom. The simulations were performed for a primary electron energy of 6 MeV.
Results: The Monte Carlo simulations clearly demonstrated a surprisingly large in- and outward electron transport across the lateral cavity boundary. This results in a strong influence of the depth-dependent development of the electron field in the surrounding medium upon the chamber reading. In the buildup region of the depth-dose curve, the in–out balance of the electron fluence is positive and shows the well-known dose oscillation near the cavity/water boundary. At the depth of the dose maximum the in–out balance is equilibrated, and in the falling part of the depth-dose curve it is negative, as shown here the first time. The influences of both the collecting electrode radius and the width of the guard ring are reflecting the deep radial penetration of the electron transport processes into the gas-filled cavities and the need for appropriate corrections of the chamber reading. New values for these corrections have been established in two forms, one converting the indicated value into the absorbed dose to water in the front plane of the chamber, the other converting it into the absorbed dose to water at the depth of the effective point of measurement of the chamber. In the Appendix, the in–out imbalance of electron transport across the lateral cavity boundary is demonstrated in the approximation of classical small-angle multiple scattering theory.
Conclusions: The in–out electron transport imbalance at the lateral boundaries of parallel-plate chambers in electron beams has been studied with Monte Carlo simulation over a range of depth in water, and new correction factors, covering all depths and implementing the effective point of measurement concept, have been developed.
[http://dx.doi.org/10.1118/1.4897389]

Key words: Monte Carlo simulations, electron dosimetry, parallel-plate chambers, perturbation corrections

1. INTRODUCTION

When a parallel-plate ionization chamber is placed in a water phantom exposed to an electron beam, the fluence of primary and secondary electrons at points within the gas-filled volume of the chamber deviates from that at the corresponding points of the replaced volume of the phantom material. This perturbation, compared to ideal Bragg–Gray conditions, is due to *the strong reduction of the energy losses and multiple scattering of the electrons in the gas-filled cavity* compared with the energy losses and multiple scattering in the same cavity if it were filled with the surrounding phantom material. The result is a disturbance of the transport of electrons into and out of the cavity in comparison with a cavity filled with the phantom material.

These physical effects have already been discussed in ICRU Report 35.[1] This report strongly influenced the common understanding of plane-parallel chambers' behavior in electron beams, and all present dosimetry protocols[2–5] can be traced back to the principles summarized in this report. Moreover, the construction of modern parallel-plate ion chambers with respect to the dimensions of the cavity and guard rings is based on the recommendations given there.

Fig. 1, based on an experiment performed by Svensson,[6] illustrates the physical characteristics of parallel-plate chambers according to ICRU Report 35. At the lateral boundary surface between air cavity and water, the figure shows an oscillation of the dose profile measured in the bottom plane of the cavity, and across the collecting electrode C an approximately homogeneous dose profile is seen at all depths. This oscillation, as theoretically explained by Harder,[7] is due to the fact that multiple scattering of electrons is negligible in the air-filled cavity while unreduced multiple scattering occurs within the adjacent water. Thereby more electrons are scattered into than out of the cavity, and the short hand term "inscattering effect" has been coined to describe this positive balance of the inbound and outbound electron transport.

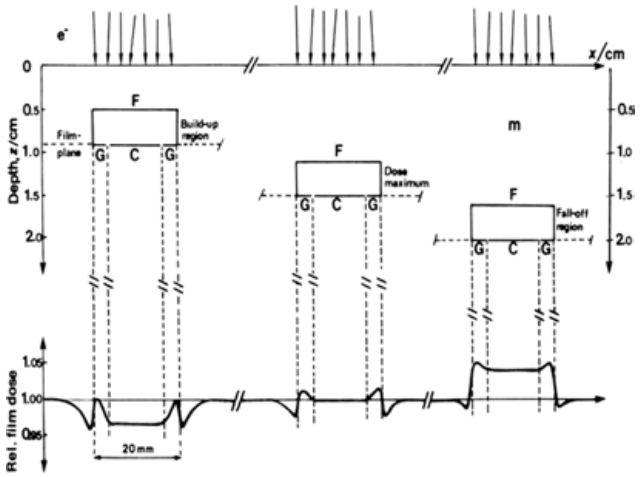

FIG. 1. Relative absorbed dose distribution in the GCG plane behind a 4 mm thick coin-shaped air cavity with surface F at 0.5, 1.1, and 1.6 cm depth in a polystyrene phantom when irradiated by a 6.3 MeV electron beam. The vertical dashed lines indicate the separation between the charge collecting electrode (C) and the adjacent guard ring (G) as well as the outer edge of the guard ring. Note that the 20 mm diameter and the 4 mm thickness of the chamber are here depicted on different scales. The film location for the relative dose determination in the GCG plane, the bottom plane of the cavity, is indicated by the horizontal dashed lines; the relative film dose profile at each depth is indicated at the bottom of the figure (reprint of Fig. 4.2 from ICRU Report 35 (Ref. 1) with permission).

To make the chamber signal insensitive to the in–out electron transport imbalance, modern parallel-plate chambers are equipped with a wide guard ring, thereby attempting to keep the region of fluence perturbation at a safe distance from the collecting volume. According to the recommendations of the IAEA TRS-398 dosimetry protocol,[2] the guard ring width should not be smaller than 1.5 times the cavity height, and a chamber design satisfying this requirement is considered "well-guarded." Based on these considerations, all present dosimetry protocols recommend to use for electron dosimetry well-guarded parallel-plate ion chambers, and for these chambers the perturbation correction for the inscattering effect, p_{cav} [IAEA TRS-398 (Ref. 2)] and p_{fl} [AAPM TG-51 (Ref. 3)], is assumed to be unity. For chambers only equipped with narrow guard rings like the PTW-Markus chamber, a notable perturbation of the signal by the inscattering effect exists, and the necessary correction factor has been studied experimentally[9,13] and by Monte Carlo simulation.[10,11] In the experimental study performed by Van der Plaetsen *et al.*[9] the correct value of the chamber signal was assumed to be supplied by a chamber with an "ideal" guard ring, and accordingly, the TRS-398 protocol as well as the German standard DIN 6800-2 (2008) (Ref. 5) give a fluence perturbation correction p_{cav} for the Markus chamber for the *reference depth* z_{ref} as function of the beam quality specifier R_{50}

$$(p_{cav})_{R_{50}} = 1 - 0.037 \cdot e^{-0.27 \cdot R_{50}}. \quad (1)$$

The relevant experiments summarized in IAEA TRS-381 (Ref. 12) *were all performed at the depth of the dose maximum*, and the mean electron energies at these depths varied from 3.0 to 20 MeV.

However, it has been discussed that the rule according to which the guard ring width should not be smaller than 1.5 times the cavity height might be insufficient to completely avoid the inscattering effect, since for a fraction of the electrons, increasing with depth, the directions of flight form rather large angles with the original beam direction.[10] Moreover with increasing depth, energy loss and multiple scattering of the electrons are *accompanied by a third effect*, the reduction of the electron fluence due to *range straggling* of the electrons, which has an additional influence on the in–out balance of the electron fluence at the lateral boundary surface of the cavity. Actually, we have to consider three typical depth regions, namely, (a) shallow depths where the fluence of electrons in the region lateral from the cavity *increases* with increasing depth due to multiple electron scattering [Fig. 2(a)], (b) the region of the depth-dose maximum where the fluence in the lateral region *shows little change* with depth [Fig. 2(b)], and (c) the region of large depths where the fluence in the lateral region *falls* with increasing depth due to range straggling [Fig. 2(c)]. Evidently, these effects will affect the in–out balance of the electron fluence at the lateral cavity boundary. Thus, we arrive at the insight that

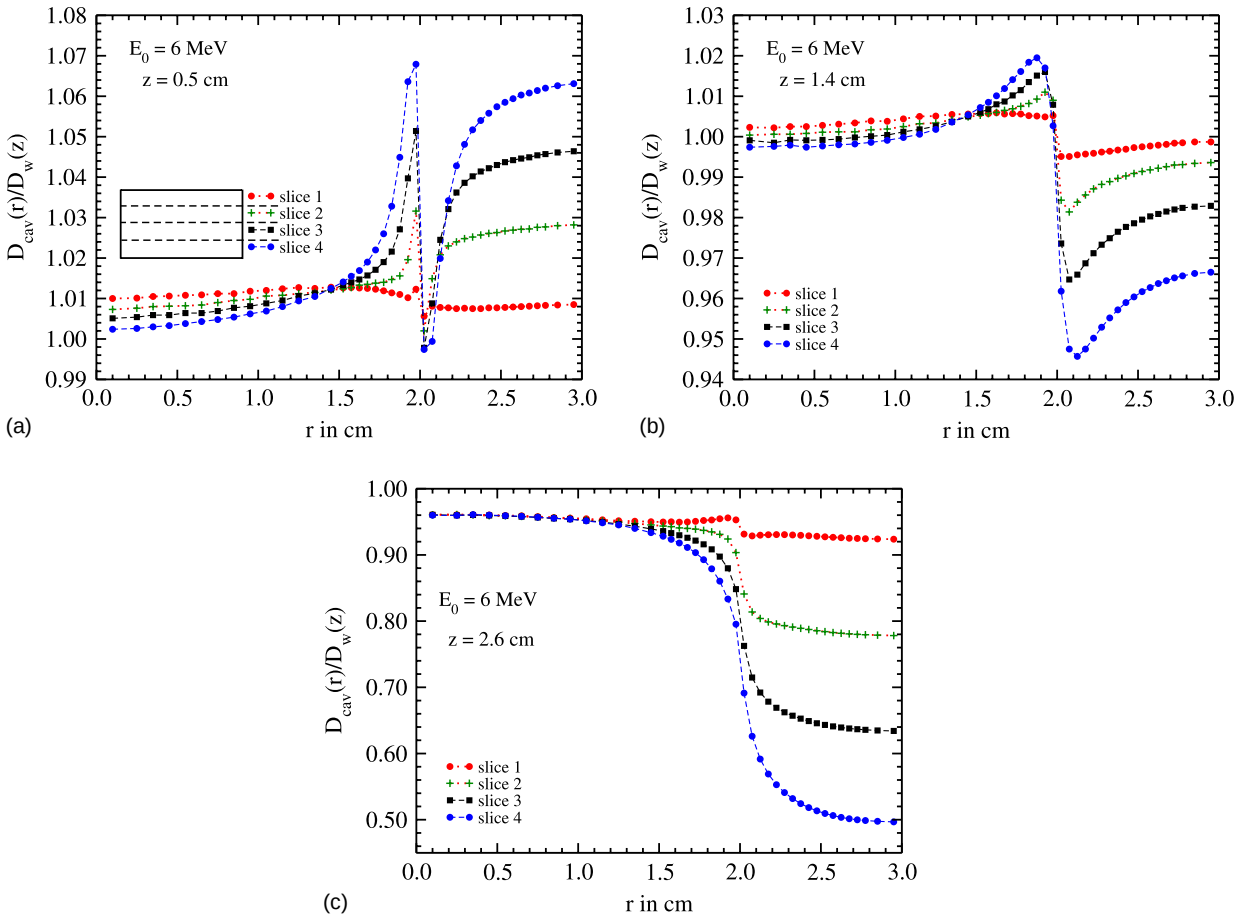

FIG. 2. Monte Carlo simulation of the penetration of a divergent electron beam with energy E_0 = 6 MeV into a water phantom containing an embedded cavity (filled with water of density 1.293 mg/cm^3) of 0.4 cm thickness and 2 cm radius with its front face at 5, 14, and 26 mm depth. For the Monte Carlo simulations, the cavity was divided into slices of 1 mm height. The curves show the transverse profiles of the absorbed dose to water within the four cavity slices (a) at a shallow depth, (b) near the depth-dose maximum and, (c) near the half-value depth R_{50}. The oscillations of the profiles near the lateral cavity boundary, most expressed at the bottom of the cavity, are largest at shallow depth but mostly disappear at large depth, where they are replaced by S-shaped curve wings. The statistical uncertainty of the Monte Carlo results is smaller than the symbol width.

the experiments by Van der Plaetsen *et al.*,[9] performed under the conditions typical for the dose maximum, *do not exactly represent the conditions of shallow and large depths* where the depth-dependent fluence or dose gradient in the phantom material is positive or negative. Moreover, this raises the issue that the cavity correction factor stated in recent protocols to hold at d_{ref} was regarded as equal to the correction experimentally determined at d_{max}; this may become a significant effect for 18 MeV electrons and higher energies where d_{ref} is in the falling portion of the depth-dose curve.

The consequence of these considerations is to acknowledge the need for a *depth-dependent* correction of the indicated value of the chamber which also accounts for the impact of these fluence gradients upon the in–out imbalance of the electron fluence at the lateral cavity boundary. In order to develop this correction, we will use spatially resolved Monte Carlo simulations inside the air gap of parallel-plate ionization chambers to analyze the magnitude of the fluence perturbations. On this basis, we will develop a new depth-dependent cavity correction factor for the signals of parallel-plate chambers in clinical electron beams. An alternative way to account for these fluence perturbations is a shift of the effective point of measurement (EPOM) as already proposed and experimentally verified by Roos *et al.*[13] The influence of an EPOM shift is also investigated here by spatially resolved Monte Carlo simulations of the dose distribution in gas-filled cavities.

The main purpose of this study has not particularly been to provide an updated cavity correction for the Markus chamber, today a still respectable, but already historical design of a parallel-plate chamber for electron dosimetry. Rather, the central aim has been to investigate the surprisingly large but not well known influence of the wide angular distribution and of range straggling of the electron beam at depths beyond the dose maximum upon the fluence imbalance at the boundary surface of a flat, gas-filled cavity in general. Insofar, the present study is a continuation of our previous work about the perturbation corrections of parallel-plate chambers.[14,15] The results will be applicable not only to the Markus chamber but also to the more recent designs of flat ionization chambers for electron beam dosimetry such as the Roos, Exradin A10, and the Advanced Markus chamber. Similarly to the experimental study performed by Johansson,[8] we only consider wall-less cavities, i.e., the impact of the chamber wall always present in real ionization chambers will not be investigated.

2. METHODS

The Monte Carlo simulations were performed with the code system EGSnrc[16,17] (release V4 2.4.0) applying the user code egs-chamber[18] (release 1.21). All geometries were modeled with the egs++ geometry package.[19] To investigate the inscattering effect of gas-filled cavities, Monte Carlo calculations were performed for coin-shaped cavities with radius a placed in a water phantom with their entrance plane at depth z. The cavity height $\xi = 0.2$ cm was chosen comparable to the heights of commercially available parallel-plate chambers used for clinical electron dosimetry. In order to provide spatial dose resolution within the gas-filled cavity and the surrounding water, the cavity itself and also the surrounding water layer were subdivided in cylindrical scoring zones with variable radius r [see Fig. 3(f)]. The dose was scored within these zones, and for a zone extending from r to $r + \Delta r$, the resulting dose $D(r)$ was understood as the mean value over cavity height ξ and zone width Δr. Depending on r, the value Δr varied between 0.01 and 0.1 cm, resulting in 13 cylindrical zones for the smallest cavity with $a = 0.3$ cm and 28 for a cavity with $a = 1.3$ cm.

In order to avoid the calculation of stopping power ratios $s^{\Delta}_{w,\mathrm{gas}}$, all spatially resolved doses for radii r inside the cavity were understood as absorbed doses $D_{\mathrm{cav}}(r)$ to "low-density water" (LDW), i.e., water with the density of air but with a density correction corresponding to normal density water, and all doses for radii r outside the cavity were absorbed doses to water, $D_w(r)$. Wang and Rogers[20] have shown that for electron energies below 30 keV there is only a small fluence perturbation due to material differences between air and low-density water. From the surface to the depth R_{50}, this perturbation results in a small depth dependence of the ratio $D_{\mathrm{LDW}}/\left(D_a s^{\Delta}_{w,a}\right)$ of less than 0.2%. For spatially resolved calculations, we have as well proved in a preliminary study that within statistical uncertainty limits of 0.2%, the spatially resolved dose distributions were the same for air or LDW filling when the former were multiplied by the mass stopping power ratios. The small depth dependencies due to the material differences mentioned above are neglected here. Total perturbation correction factors p for gas-filled cavities at depth z were calculated as the ratio

$$p_{\mathrm{cav}} = \frac{D_w(z)}{\overline{D}_{\mathrm{cav}}}, \tag{2}$$

where $D_w(z)$ is the dose to water and $\overline{D}_{\mathrm{cav}}$ is the average of $D_{\mathrm{cav}}(r)$ over the whole cavity (within the radial region of the collecting electrode) with the cavity's entrance plane positioned at depth z. The impact of a guard ring on the cavity dose $\overline{D}_{\mathrm{cav}}$ and therefore on p_{cav} can be calculated from the spatially resolved dose calculations by integrating the dose not over the whole cavity radius $0 \le r \le a$ but over the interval $0 \le r \le r_C$, where r_C is the radius of that part of the electric field which causes ion charge collection upon the central electrode. For brevity, r_C will be denoted as the "collection electrode radius," and $a - r_C$ as the "guard ring width."

For all dose calculations, a divergent electron beam was incident on a cubic water phantom ($30 \times 30 \times 30$ cm^3), the field size was 10×10 cm^2 at the source-to-surface distance 100 cm. Since scattering effects are largest for low electron energies, all calculations were performed with a spectrum of a clinical linear accelerator of nominal energy 6 MeV [Varian Clinac (Ref. 21)] whose 50% range was $R_{50} = 2.63$ cm and whose reference depth was $z_{\mathrm{ref}} = 1.48$ cm. To calculate the perturbation corrections p_{cav} according to Eq. (2), the highly resolved depth-dose curve in water was calculated within cylindrical water voxels with radius $r = 0.5$ cm and height $h = 0.002$ cm.

In preliminary simulations, the influence of different cutoff/threshold energies upon the photon and electron transport was investigated. The impact of decreasing the cutoff energy from 10 keV for photons and 521 keV for electrons to 1 and 512 keV was <0.1% for the spatially resolved simulations, but the simulation times were increased by a factor of 4. Therefore, it was decided to perform all simulations with cutoff/threshold energies of 10 keV for photons and 521 keV for electrons. Except the bremsstrahlung cross section data [NIST instead of Bethe–Heitler bremsstrahlung cross sections (Ref. 17)] all transport options within the EGSnrc system were set to their defaults.

In order to determine the in–out imbalance of electron transport between the cavity and the surrounding water due to differences in scattering and range straggling, the different geometries shown in Fig. 3 were realized. Geometry (a) is the simplest one, where the cavity is placed in the water phantom at depth z, irradiated with a clinical electron spectrum of primary energy E_0. The radius a of the cavity was varied in the range from 0.3 cm, complying with the radius of the Markus chamber, to 1.3 cm, close to the radius of the Roos chamber. The height of all cavities was 0.2 cm. In geometry (b), a very thin slab of water ($\Delta z = 0.0001$ cm) in front of the cavity was introduced with the cutoff energy for electron transport, ECUT, set larger than the primary electron energy E_0, so that all electrons bound to enter the cavity directly through the front surface were stopped in front of the cavity.

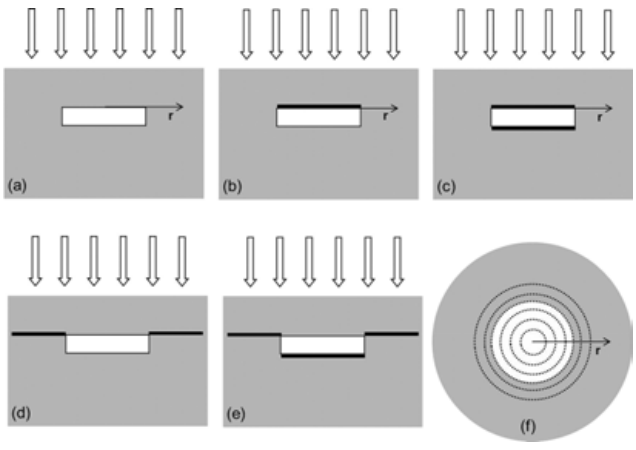

FIG. 3. (a)–(e) Simulation geometries: the cavity filled with low-density water (white) is surrounded by water (gray). The thick black lines symbolize thin slabs of water ($\Delta z = 0.0001$ cm) with cutoff energy $ECUT > E_0$ (E_0: energy of primary electrons). (f) Top view of the simulation geometry. To get spatial information about the dose deposition, the cavity and the surrounding slab of water is divided into cylindrical scoring zones of width Δr varying from 0.01 to 0.1 cm.

In this geometry, the electrons could only enter the cavity via the side or rear surface. In geometry (c), an additional ECUT > E_0 region was placed behind the cavity. In that case no electron can enter the cavity through the rear surface, and also all electrons coming in through the lateral surface and being backscattered at the rear surface are missing. In geometry (d), an ECUT > E_0 region was introduced at depth z for all radii outside the cavity so that no electron from the outside region can reach the cavity through the lateral or rear surfaces. Geometry (e) is the same as in (d) but with an ECUT region placed at the rear surface to prevent any backscattering from the material behind the cavity.

3. RESULTS

3.A. Depth dependence of the electron fluence perturbation at the gas–water boundary

The electron transport phenomena occurring at the gas–water boundary of a parallel-plate ionization chamber, obtained by Monte Carlo simulation of the geometries defined in Fig. 3, are illustrated in Fig. 4. The simulations were performed for a cavity of radius $a = 0.3$ cm and height 0.2 cm filled with LDW and placed at depth 0.5 cm within the water phantom, i.e., in the dose buildup region of an electron beam with $E_0 = 6$ MeV.

The dose profile (a) corresponds to the real geometry, with no ECUT > E_0 regions present. The oscillation of the transverse profile, already mentioned in the Introduction, is visible at the gas–water boundary surface, and its origin will be explained below. When a thin slab of water with ECUT > E_0 is introduced in front of the entrance surface, the resulting profile (b) represents the dose within the cavity due to electrons entering it through the lateral or the rear boundary surfaces ("inscattered" electrons). With an additional ECUT region behind the cavity, the dose profile (c) is obtained whose values are slightly smaller than those in geometry (b) because electrons now cannot enter the cavity from the rear, and electrons coming from the side and backscattered at the rear boundary surface are missing. In geometries (d) and (e), the region with ECUT > E_0 covers the whole field except the front surface of the cavity. The dose profile outside the cavity is now due to electrons that have entered the cavity through the front surface, leaving it mainly through the lateral boundary surface ("outscattered" electrons). In profile (d), the doses within the cavity are somewhat larger compared to profile (e) because (d) contains electrons backscattered at the rear surface.

At first sight, one would expect that the addition of dose profiles (b) and (d) should result in profile (a). However, as shown in Fig. 4, the sum of these two profiles within the cavity is about 1.5% smaller than profile (a) in the real geometry. This difference can be explained by the lack of backscattering of the inscattered electrons from the front surface of the cavity in geometry (b). Thus, the two essential components of the total dose profile are on the one hand the profile (d), exclusively due to electrons that have entered the gas from the cavity's front side and may also be backscattered at its rear surface, and on the other hand the contribution (a)–(d) by all other electrons.

Figure 5 shows the result of this component analysis for several depths z. The predominant feature of (A) and (B) is the surprisingly large effect of *electron transport across the lateral gas–water interface and its deep penetration toward the center of the cavity*. Without the influence of this transport, i.e., for an infinitely large radius of the cavity, the ratio $D_{cav}(r)/D_w(z)$ in Fig. 5(A) would have the value 1.00 since in the almost complete absence of scattering and energy losses in the low-density water gas, the dose $D_{cav}(r)$ would equal $D_w(z)$, the dose to water in the entrance plane of the cavity. However for a real cavity radius, the "outscattering," or *outbound electron transport*, results in a considerable dose reduction even at the center of a cavity with 0.3 cm radius. At depth $z = 0.5$ cm, the extrapolated dose at the center of the cavity is reduced to $D_{cav}/D_w = 0.88$, at depth $z = 2.6$ cm even to the value $D_{cav}/D_w = 0.65$. Figure 5(B) shows the effect of "inscattering," or *inbound electron transport*, which produces considerable dose values at the center of the cavity, namely, $D_{cav}/D_w = 0.14$ at depth $z = 0.5$ cm and $D_{cav}/D_w = 0.30$ at depth $z = 2.6$ cm. This obvious imbalance between inbound and outbound electron transport is caused by the difference between *the almost complete absence of electron interaction events within the gas layer*, in contrast to the

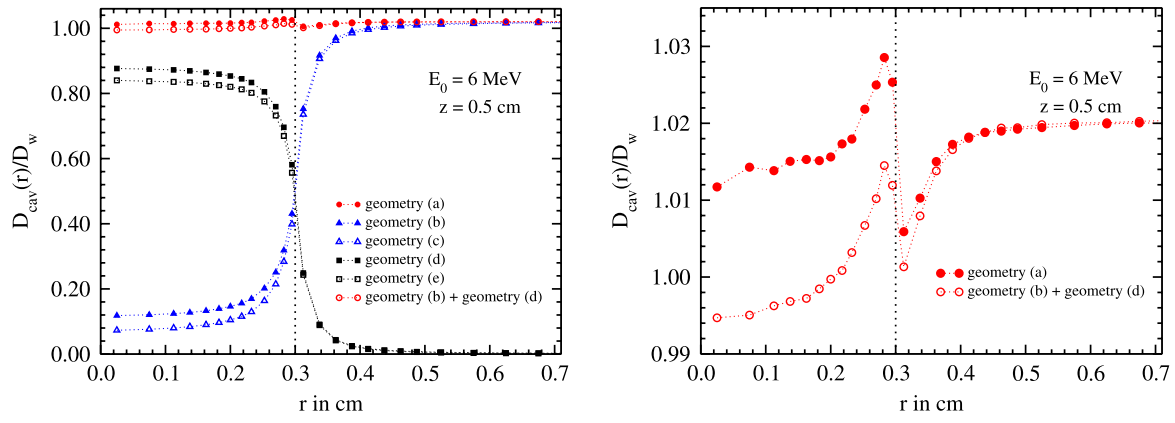

FIG. 4. Monte Carlo results for the simulation geometries defined in Fig. 3. The radius a of the cavity filled with low density water is 0.3 cm. The cavity and the surrounding slab of water is divided into cylindrical sections of width Δr. Each data point corresponds to the dose within one section. The statistical uncertainty of the Monte Carlo results corresponds to the symbol width. The dose $D_w(z)$ was calculated at the depth z of the cavity's reference point, i.e., the depth of the entrance window. In the right panel, the y-axis is expanded to make the dose oscillations at the gas–water boundary visible.

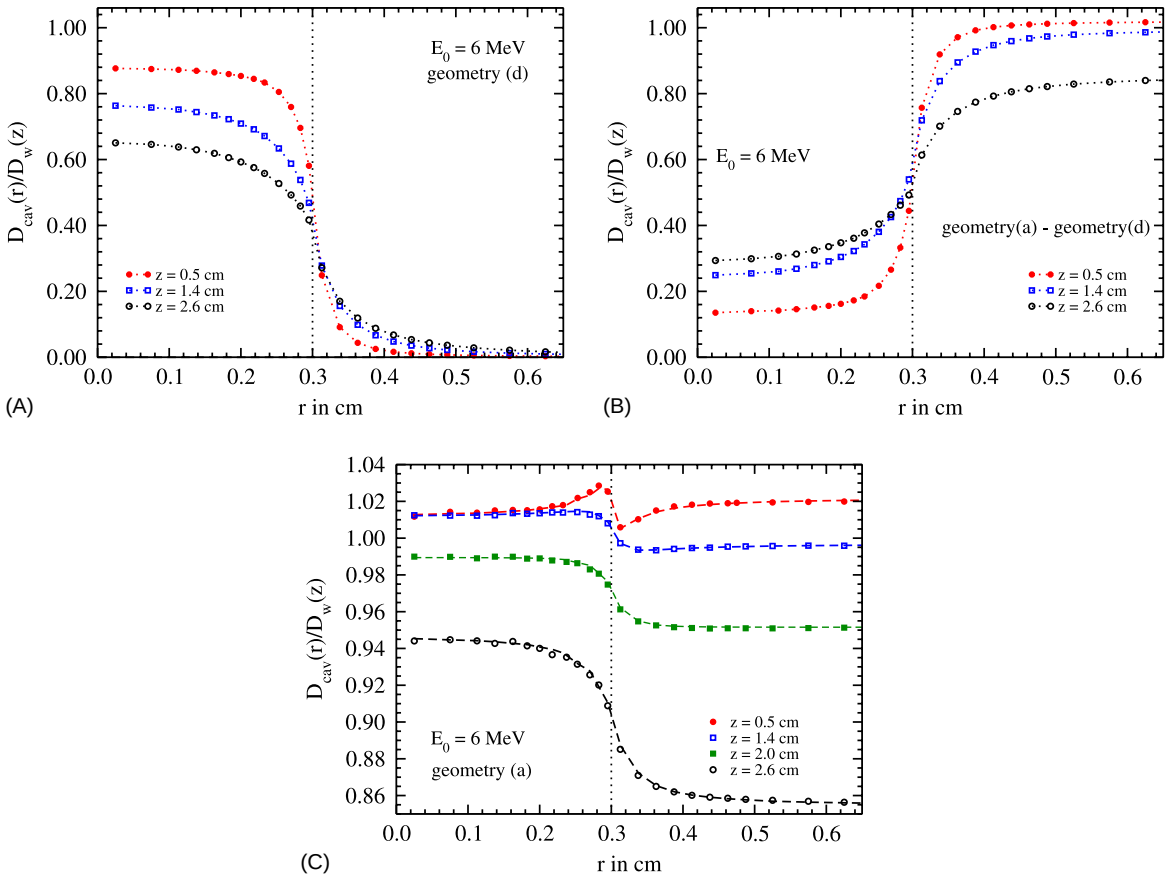

FIG. 5. Spatially resolved Monte Carlo simulations of the dose profiles within the LDW-filled cavity and the adjacent water at different depths z in water. The geometries are labeled according to Fig. 3. The radius $a = 0.3$ cm of the cavity is marked by the dotted line. The statistical uncertainty of the Monte Carlo results corresponds to symbol width. The dose $D_w(z)$ was calculated at the depth of the entrance window.

ongoing electron interactions in the bulk of water laterally from the cavity. The term "interactions" here refers to elastic scattering including backscattering, as well as energy losses, the production of secondary electrons, and even the appearance of track ends of the electrons, an important feature of the electron field in the falling region of the depth-dose curve.

This identification of the underlying physical effect as the inbound–outbound imbalance of electron transport across the lateral cavity boundary is the key to understand the values of the ratio $D_{cav}(r)/D_w(z)$ resulting in the real geometry and thereby the perturbation of the dose in the cavity compared to $D_w(z)$. Figure 5(C) shows the values of $D_{cav}(r)/D_w(z)$ resulting in geometry (a), with values >1.00 associated with an overshoot, and values <1.00 typical for an undershoot of the inbound electron transport. The deviations of these sum values from the ideal value 1.00 are the systematic differences between the dose in a cylindrical cavity and that in water and have to be compensated by appropriate corrections. In particular, the top profile in Fig. 5(C) shows that in the case of an overshoot of inscattering, the superposition of the dose profiles of types (d) and (a)–(d) is leading to the oscillation of the resulting sum dose profile near the boundary, since the penumbra wings of the component profiles (d) and (a)–(d) are not precisely symmetrically shaped. (See also the Appendix where this asymmetry is illustrated by means of small-angle multiple scattering theory.)

3.B. The influence of the cavity radius and the concept of a guard ring

As a consequence of the physical situation illustrated in Figs. 4 and 5, the inbound–outbound imbalance of electron transport between the cavity of a parallel-plate ionization chamber and its surrounding water medium especially influences the $D_{cav}(r)/D_w(z)$ ratio *near the lateral gas–water boundary*. The $D_{cav}(r)/D_w(z)$ ratio was therefore studied for various cavity radii from $a = 0.3$ to 1.3 cm. The left panel of Fig. 6 shows that the dose oscillation typical for the shallow depth $z = 0.5$ cm, so far obtained for cavity radius $a = 0.3$ cm (Fig. 5), regularly appears close to the cavity boundary whatever the cavity radius is. Its shape is always similar; there is merely a slight difference in the dose level reached in the region internal from the boundary, indicating a larger average inscattered dose in case of the smaller cavity radius. In analogy, the right panel of Fig. 6 shows that the "shoulder," typical for the dose profile at the large depth $z = 2.6$ cm and already known from Fig. 5 for the cavity radius $a = 0.3$ cm, regularly appears with its steepest point at the cavity boundary whatever the cavity radius is. Again here, the levels of the dose reached in the region internal from the boundary are slightly different, indicating a larger average outscattered dose in the case of the smaller cavity radius.

This obvious occurrence of the most inhomogeneous sections of the dose profiles near the gas–cavity boundary, clearly

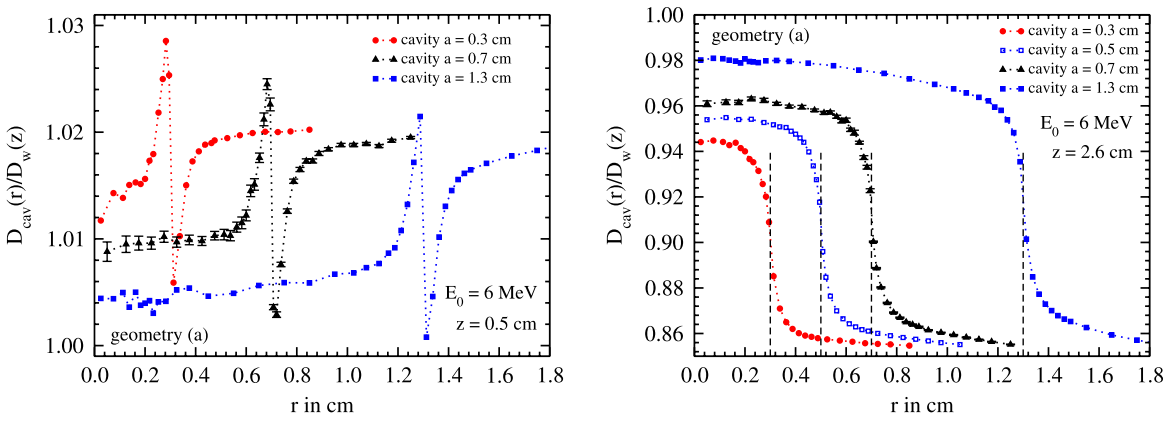

FIG. 6. Spatially resolved Monte Carlo simulations of the dose profiles within the LDW-filled cavity and the adjacent water at different depths z for different cavity radii. The geometries are labeled according to Fig. 3. The error bars represent the statistical uncertainty for the Monte Carlo results of all cavity radii. The vertical lines mark the cavity radius a. The dose $D_w(z)$ was calculated at the depth z of the cavity's reference point, i.e., the depth of the entrance window.

visible in experiments as well (Fig. 1), has lead to the idea of reducing the relative influence of these sections upon the measured value of the parallel-plate chamber by increasing the radius a of the chamber. In order to examine this idea, Fig. 7 shows the dose contributions by inscattered and outscattered electrons expressed as fractions of $D_w(z)$, calculated for the (d) and (a)–(d) profiles of Fig. 5 by integration over the interval $0 \le r \le a$ for chambers with $a = 0.3$ and 1.3 cm at five different depths in the electron beam. As expected, the relative contributions of the inscattered and outscattered fractions and also the differences between them strongly decrease with increasing radius of the cavity.

Furthermore, Fig. 8 describes the variation of the extrapolated dose in the center of the cavity as a function of the cavity's radius a for different depths z. The center dose $D_{cav}(r = 0)$ was approximately obtained as the mean dose of the cavity within $r \le 0.1$ cm.With increasing radius and therefore with decreasing influence of the inbound–outbound electron transport imbalance, the relative doses in the cavity center are tending toward value 1.00, but even a radius of 2 cm is not sufficient for the doses in the center to perfectly reach this limit value. This tendency, owed to the *deep radial penetration* of the in- and outbound transport of electrons into the gas-filled cavity, has been the reason for the choice of a comparatively large collecting electrode radius, namely, $r_C = 0.78$ cm, for the Roos chamber.

The other idea to reduce the relative influence of the near-boundary sections of the disturbed dose profile upon the measured value of a parallel-plate chamber is to use the *guard ring*, originally devised in order to shape the electric field in the chamber, as a means of excluding from the measured value any $D_{cav}(r)$ contributions from $r \ge r_C$, where $a - r_C$ is the guard ring width. The influence of a guard ring has been analyzed in Fig. 9, where the ratio $p = D_w/\overline{D}_{cav}$ has been plotted versus depth in water for $E_0 = 6$ MeV for a set of different guard ring widths. The most prominent feature of Fig. 9 is the difference between the ordinate scales of the two panels which are valid for $a = 0.3$ and 1.3 cm,

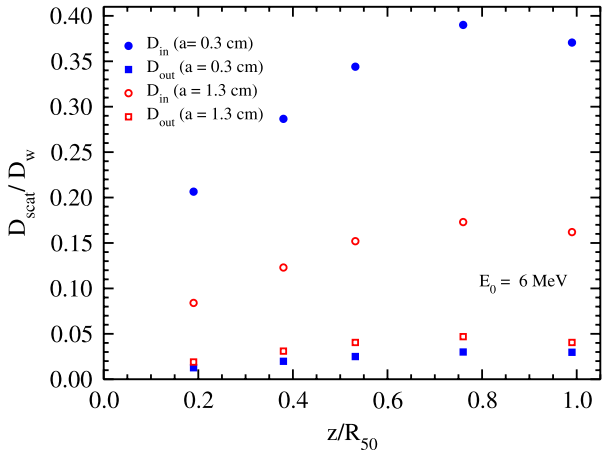

FIG. 7. Ratios of the dose due to in- and outscattered electrons and the dose $D_w(z)$ for two different cavity radii a as a function of scaled depth z/R_{50}. These dose fractions were calculated from spatially resolved Monte Carlo simulations of geometry (d) and the dose profiles resulting from geometry (a)–(d).

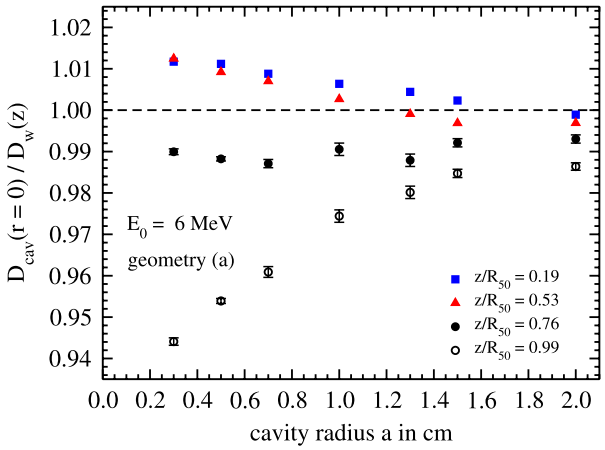

FIG. 8. Dose ratio $D_{cav}(r = 0)/D_w(z)$ for different cavity radii a at different depths z. The extrapolated dose value $D_{cav}(r = 0)$ was approximately obtained as the mean dose of the cavities within $r \le 0.1$ cm and is taken from the spatially resolved simulations of geometry (a). The dose to water $D_w(z)$ was calculated at the depth of the cavity's entrance window. The statistical uncertainties of the Monte Carlo based results are given by the error bars (1σ).

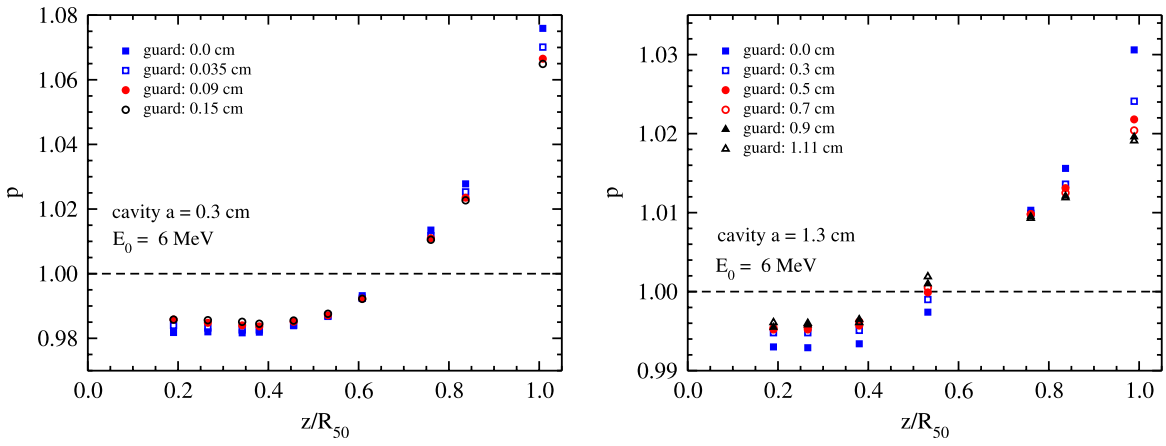

FIG. 9. Total correction factor $p = D_w/\overline{D}_{cav}$ as a function of scaled depth z/R_{50} for two cavities with different guard ring widths and different cavity radii a. The cavity dose $\overline{D}_{cav}$ was determined from the spatially resolved Monte Carlo simulations by volume averaging over the collecting electrode radius r_C. The guard ring width ("guard") was $a - r_C$. The dose D_w is calculated at the depth z of the front face of the cavity.

again indicating the already mentioned reduction of the fluence disturbance with increasing radius of the cavity as a consequence of the concentration of the effect close to the gas–water boundary.

The modification of $D_w(z)/\overline{D}_{cav}(r)$ associated with a variation of the guard ring width is shown by the calculated points in Fig. 9. Narrow guard rings, in the left panel examined in combination with the small cavity radius $r = 0.3$ cm, have little effect on the deviation of $\overline{D}_{cav}(r)$ from $D_w(z)$, whereas a guard ring width of 1.11 cm (right panel) can significantly reduce this deviation. At the depth of the dose maximum, i.e., at $z = 1.4$ cm or $z/R_{50} = 0.53$, a guard ring of 0.5 cm width just happens to yield $p = 1$. With regard to this non-negligible, but not dominating effect, the introduction of a guard ring, e.g., of width 0.4 cm as for the Roos chamber, is not the instrument by which the influence of the inbound–outbound imbalance of electron transport upon the measured value of a parallel-plate chamber can be completely eliminated. Rather, as shown in Fig. 8, the cavity radius a is a more effective instrument to reduce the deviation of the average dose to the gas from $D_w(z)$. This is the consequence of the deep radial penetration of the in- and outbound transport of electrons into the gas-filled cavity mentioned above.

3.C. The effective point of measurement

In consideration of the strong influence of the in- and outbound transport of electrons into the gas-filled cavity, and therefore of the gradient of the electron fluence field in the region laterally from the gas-filled cavity, upon the measured reading of a parallel-plate ionization chamber in an electron beam (Figs. 4, 5, 6, 8, and 9), one may question the underlying idea of regarding $\overline{D}_{cav}(r)$ as the measurable quantity representative of $D_w(z)$, the dose in the *entrance plane* of the cavity. Rather, it is a plausible conjecture that $\overline{D}_{cav}(r)$ might be more closely linked with the dose $D_w(z+\Delta z)$ at a *slightly larger depth* $z+\Delta z$ because that dose would be subjected to the influence of the gradient of the electron fluence field in the lateral region as well. The depth $z+\Delta z$ would then play the role of the "measuring depth" in the water phantom, and a point of the chamber at downstream distance Δz from the entrance plane would appear as the "effective point of measurement" of the chamber, to be placed at the measuring depth. The effective point of measurement has been experimentally determined for the Markus chamber already by Roos *et al.*[13] and for the Markus chamber and the Roos chamber by Looe *et al.*[23]

This idea has been the origin of plotting in Fig. 10 the radial profiles of ratio $D_{cav}(r)/D_w(z+\Delta z)$ for two values of Δz for a cavity with $a = 1.3$ cm and thickness 0.2 cm at various water depths in a 6 MeV electron beam. It is shown that the ratio $D_{cav}(r)/D_w(z+\Delta z)$ is noticeably modified dependent on the choice of Δz, and there may even exist an optimum value of Δz, where the mean value $\overline{D}_{cav}(r)/D_w(z+\Delta z)$ achieves such small depth dependence that this dependence could be neglected in clinical practice.

The search for this optimum value of Δz has been performed by comparing the ranges of the depth-dependent variation of p associated with various Δz values. The result of this search is plotted in Fig. 11 for cavities with $a = 0.3$ cm and $a = 1.3$ cm and different guard ring widths. Accordingly, the ratio $p = D_w(z+\Delta z)/\overline{D}_{cav}(r)$ does not vary more than $\pm 0.5\%$ over all depths up to $z = R_{50} = 2.63$ cm, i.e., $z/R_{50} = 1$. Figure 11 shows that there exists an EPOM which results in a very similar depth dependence of the resulting perturbation correction p for every supposed guard ring width. Thus, for the Markus chamber with its narrow guard ring of 0.035 cm width, the effective point of measurement would lie at $\Delta z = 0.045$ cm, which is in perfect agreement with the Monte Carlo based value given by Wang and Rogers.[22] Experimental investigations on the EPOM of the Markus chamber were performed by Roos *et al.*[13] and Looe *et al.*[23] Regarding the uncertainties of these data, the results given by Roos, $\Delta z = 0.05$ cm, and Looe, $\Delta z = (0.04 \pm 0.01)$ cm, are also in good agreement with the EPOM shift suggested here. For $a = 0.3$ cm, the only remaining correction would be to multiply the measured values of $\overline{D}_{cav}$ by 0.99 in order to obtain $D_w(z+\Delta z)$. On the other hand, for a chamber with $a = 1.3$ cm and guard ring width 0.3 cm, the optimum would

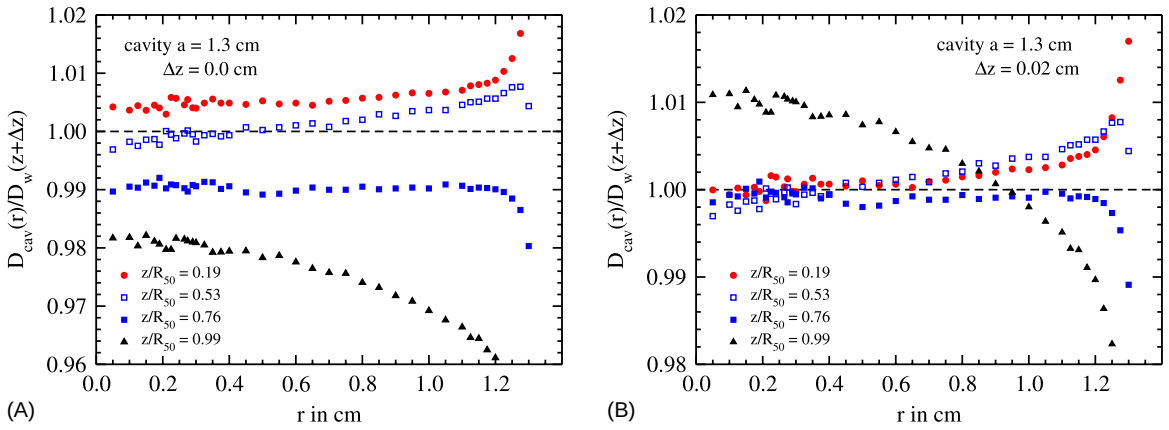

FIG. 10. Impact of a shifted point of measurement on the dose ratio $D_{cav}(r)/D_w(z+\Delta z)$ within a gas-filled cavity. The cavity radius is $a = 1.3$ cm and the cavity is filled with LDW. For the guardless cavity, the value $\Delta z = 0.02$ cm is the optimal shift minimizing the depth dependence of $D_{cav}(r)/D_w(z+\Delta z)$. Be aware of the different ordinate scaling in the left and right panels.

lie at $\Delta z = 0.0155$ cm as shown in Fig. 11(B). For the Roos chamber with $a = 1.2$ cm and guard ring width of 0.4 cm Wang and Rogers[22] published a value $\Delta z = 0.018$ cm. In our previous publication considering the Roos chamber,[14] a value Δz in the same range was determined.

While this optimization of Δz would provide a depth-dependent variation of p that might be negligible in clinical practice, this approach does not prevent determinations of the cavity correction factor p with the highest possible accuracy, e.g., for $z = z_{ref}$ (in this example 1.48 cm). In Fig. 11(A) and for guard ring width 0.035 cm, this would mean $p(z_{ref}) = 0.987 \pm 0.001$. In Fig. 11(B) and for guard ring width 0.3 cm the result would be $p(z_{ref}) = 0.999 \pm 0.001$.

4. DISCUSSION

4.A. Comparison with earlier results

The well-known picture from ICRU Report 35,[1] Svensson's film-dosimetric demonstration of the oscillations of the dose profile of a 6 MeV electron beam near the gas–medium boundary shown here as Fig. 1, has raised concerns because in our calculation such oscillations were obtained at 0.5 cm depth but not at 1.4 cm depth (compare Figs. 4, 5, and 6). However, the conditions were somewhat different as we have here treated a cavity of 2 mm height, whereas Svensson's dose values were obtained at the bottom of a 4 mm height cavity. Thus, his conditions are more closely simulated in Fig. 2 of our paper, where the oscillations have been reproduced at the bottom of a 4 mm high cavity even at 1.4 cm depth .

Depth-dependent measurements of the deviation of the $\overline{D}_{cav}$ values from $D_w(z)$ have been performed by Laub *et al.*[24] for a Markus chamber in a 10 MeV electron beam by comparison with a diamond detector. Although their experimental deviation varied only from −2% to +3%, the calculated variation of the deviation from −2% to +7% for 6 MeV in Fig. 9 is consistent with the experimental result considering the difference in electron beam energy and of the additional uncertainty introduced by using the diamond detector as the reference.

Depth-dependent Monte Carlo calculations of the perturbation correction p at electron energies up to 6 MeV have

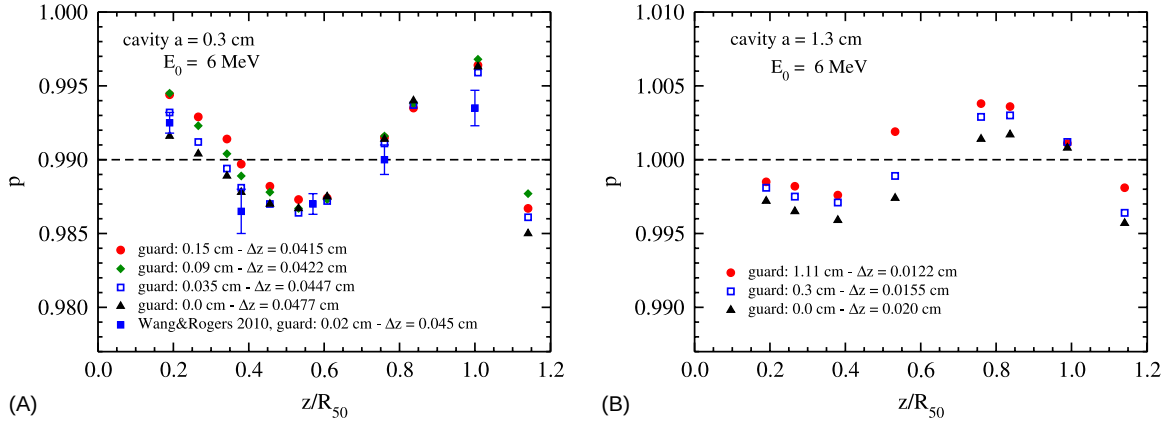

FIG. 11. Total correction factor $p = D_w/\overline{D}_{cav}$ as a function of scaled depth z/R_{50} for two cavities for different guard ring widths. The cavity dose $\overline{D}_{cav}$ was determined from the spatial resolved Monte Carlo simulations by volume averaging over the collecting radius r_C (see Fig. 10). In contrast to Fig. 9, the cavity dose is not scaled to the dose D_w at the cavity's front but to the dose D_w in the EPOM. Δz describes the position of the EPOM relative to the cavity's reference point. $\Delta z > 0$ denotes a shift in downstream direction.

been performed by Lauterbach[25] who found that the magnitude of the necessary correction is most effectively reduced by restricting the height of the cavity. The development of the Advanced Markus chamber was based on this investigation.

The message for the construction of guard rings to be derived from Fig. 9 is that for a cavity of 0.2 cm height and radius $a = 1.3$ cm, a guard ring width of at least 0.8 cm is required in order to completely eliminate the effect of the in–out electron transport imbalance on the measured value of $\overline{D}_{\mathrm{cav}}$ *at the reference depth* z_{ref}. The same result has been obtained experimentally at 6 MeV by Roos *et al.*, as reported in IAEA TRS-381.[12] Thus, the guard ring width of 0.4 cm chosen in the commercially available Roos chamber (PTW) is a practical solution in which a small deviation from the ideal by about 0.2% is accepted. These numbers are all valid for the reference depth.

The impact of an EPOM shift on the resulting perturbation correction p for a Markus-like cavity (cavity radius $a = 0.3$ cm, guard width 0.035 cm) was already investigated by Wang and Rogers.[10] Their Monte Carlo results, showing that the depth dependence of p could be minimized by an EPOM shift of 0.045 cm, are in excellent agreement with our results. The data from Wang and Rogers have been included in Fig. 11(A). It should be noted that Wang and Rogers scored the dose within the whole active volume of the cavity whereas our data for the perturbation correction p are calculated from the spatially resolved simulations by integrating the dose value $D(r)$ over the radius r of the active volume, i.e., $0 \le r \le r_G$. The good agreement of both data sets can be taken as a validation of our spatially resolved dose calculations.

In summary, all available comparisons with other results have shown consistence of our Monte Carlo values with the previous experimental and computational insight into the causes affecting the measured values of quantity $\overline{D}_{\mathrm{cav}}(r)$ for parallel-plate ionization chambers in electron beams. Particularly, the oscillations of the dose profile at shallow depths, the incomplete effect of too narrow guard rings and the turn of the sign of the ratio from about −2% at shallow depths into several percent with positive sign at the larger depths, the consequence of the turn from an overshooting to an undershooting in–out imbalance of the electron transport at the lateral cavity boundary (see Fig. 5), are consistent results.

4.B. Recommended corrections

The cavity correction to be applied to the measured values of $\overline{D}_{\mathrm{cav}}(r)$ for Markus chambers at 6 MeV can therefore be directly obtained from the present Monte Carlo results and will be denoted by p^{MC}. One possibility is $p^{\mathrm{MC}} = D_w(z)/\overline{D}_{\mathrm{cav}}$, i.e., to convert the measured value of the chamber into the dose at the depth of the entrance plane of the cavity. These values taken from Fig. 9 are replotted in Fig. 12. Their disadvantage is their considerable depth dependence. The other possibility is $p^{\mathrm{MC}}_{\Delta z=0.045\ \mathrm{cm}} = D_w(z+\Delta z)/\overline{D}_{\mathrm{cav}}$ for $\Delta z = 0.045$ cm, i.e. to convert the measured value of the chamber into the dose at the effective point of measurement of the chamber, whose values, taken from Fig. 11, have been replotted in Fig. 12. Evidently,

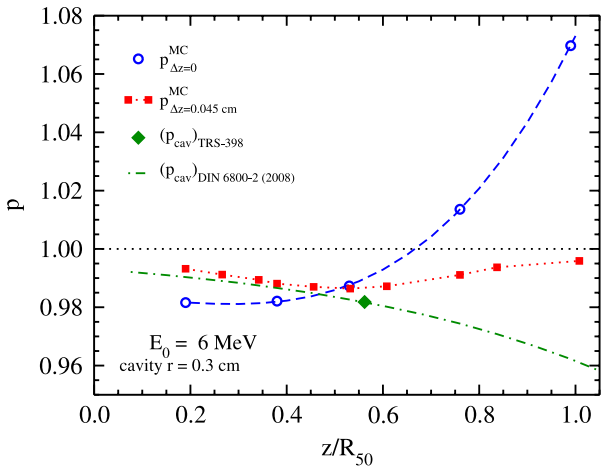

FIG. 12. Perturbation correction $p_{\mathrm{cav}} = D_w/\overline{D}_{\mathrm{cav}}$ for a Markus-like cavity with radius $a = 0.3$ cm in a 6 MeV electron beam as a function of the scaled depth z/R_{50}. The open circles are the results from the Monte Carlo simulations with $\Delta z = 0$ cm, the filled squares those for a shift $\Delta z = 0.045$ cm. The data point at $z/R_{50} \approx 0.55$ and the dashed-dotted line are the p_{cav}-values according to IAEA TRS-398 (Ref. 2) and DIN 6800-2 (Ref. 5).

the correction factor $p^{\mathrm{MC}}_{\Delta z=0.045\ \mathrm{cm}}$ can in practice be regarded as a constant value of 0.990 ± 0.005, which would mean a considerable advantage for practical applications.

These new possibilities for the depth-dependent correction of the indicated values $\overline{D}_{\mathrm{cav}}$ of plane-parallel ionization chambers applied in electron beam dosimetry have to be compared with the previous recommendations. Perturbation correction factors experimentally determined by various groups for a set of flat ionization chambers, all obtained at the depth of the dose maximum and for mean electron energies at this depth from 3 to 20 MeV, have been collected in IAEA TRS-381.[12] Somewhat later, in IAEA TRS-398,[2] the same data for the Markus chamber, now recast to be valid for the reference depth z_{ref}, were represented by the fitting formula for the perturbation correction factor,

$$(p_{\mathrm{Markus}})_{R_{50}} = 1 - 0.037 \cdot e^{-0.27 \cdot R_{50}} \quad (R_{50} \ge 2\ \mathrm{g/cm^2}), \qquad (3)$$

where R_{50} characterizes the incident electron beam. For our 6 MeV electron beam with $R_{50} = 2.63$ cm in water, this formula gives the diamond point in Fig. 12, whose consistence with the present Monte Carlo calculations is within 0.2%. However, IAEA TRS-398 does not recommend perturbation corrections for other depths.

The German standard DIN 6800-2 (Ref. 5) still uses the form of the perturbation correction

$$(p_{\mathrm{Markus}})_{R_{50}} = 1 - 0.039 \cdot e^{-0.2816 \cdot \overline{E}_z}, \qquad (4)$$

originally recommended in IAEA TRS-381, which for the reference depth again yields the value indicated by the diamond symbol in Fig. 12. However, DIN 6800-2 also makes a first attempt to recommend a perturbation correction for other depths by again recasting this formula, always assuming that the in–out electron transport imbalance is the same as in the reference depth. This has led to a lengthy formula not reproduced here but plotted as the dashed-dotted line in Fig. 12. It is evident that this approach now needs to be corrected

in consideration of the increased knowledge about the depth dependence of the in–out electron transport imbalance, as we have shown above.

For the more recent chamber designs such as the Roos, Exradin A10, and Advanced Markus chambers the very small depth dependence of p associated with the optimum choice of Δz as shown in Fig. 11(B) warrants to neglect this depth dependence in clinical practice.

5. CONCLUSION

When an ionization chamber is placed in a water phantom and exposed to an electron beam, the fluence of primary and secondary electrons at points within the gas-filled volume of the chamber deviates from that at the corresponding points of the replaced volume of the phantom material. For a plane-parallel ionization chamber, this fluence perturbation is due to the imbalance of the in- and outbound electron transport across the gas–water boundary surface. In the present investigation, these transport phenomena have been studied by means of a spatially resolved Monte Carlo simulation, which particularly illustrated the deep radially directed penetration of the fluence perturbance into the gas volume and demonstrated the depth dependence of this perturbance. The study of the effects of constructional countermeasures such as increased widths of central collecting electrodes and guard rings showed that some corrections of the indicated values for parallel-plate chambers introduced into clinical practice are still needed. These corrections have been numerically derived for Markus- and Roos-type cavities when applied in a 6 MeV electron beam (Fig. 11). Besides, the traditional correction which converts the indicated value of the chamber into the absorbed dose to water in the entrance plane of the chamber, a correction involving a strong depth dependence, an alternative correction with almost negligible depth dependence is now proposed, based on the idea to convert the indicated value into the absorbed dose to water at the depth of the effective point of measurement of the chamber. Compared with the presently standardized perturbation corrections for plane-parallel ionization chambers, no changes at the reference depths are required, but the depth-dependent correction factor originally proposed in the German standard DIN 6800-2 (Ref. 5) needs to be revised.

APPENDIX: MATHEMATICAL MODEL OF THE ELECTRON TRANSPORT IMBALANCE AT THE LATERAL BOUNDARY OF A FLAT, GAS-FILLED CAVITY IN WATER IN TERMS OF MULTIPLE SCATTERING THEORY

A mathematical model describing the transport of electrons into and out of a flat, gas-filled cavity and the adjacent water medium, based on the Fermi–Eyges multiple scattering theory[26] as summarized in ICRU Report 35,[1] will be briefly described here. Although the small-angle multiple scattering theory is a mathematical instrument correctly applicable only at shallow depths in an electron beam, it is illustrative for a qualitative discussion of the origin of the fluence disturbance at the lateral boundary of a flat, gas-filled cavity.

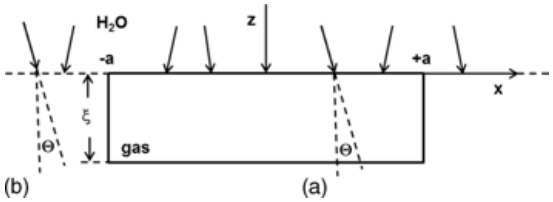

FIG. 13. Geometrical outline of the physical model of electron scattering within and at the lateral boundary surface of a gas-filled cavity in water. (a) Pencil beam originating from the front plane of the gas-filled volume and (b) pencil beam originating from the same plane, but outside the gas-filled volume. See text for more details.

The geometrical layout is described in Fig. 13. A water phantom is exposed to a wide parallel beam of high energy electrons. A cavity filled with gas (low-density water) of thickness ξ and width $2a$, thought to be infinitely long in the direction perpendicular to the drawing plane in order to provide a 1D problem, is positioned in the phantom with its front surface at depth z. The scoring plane at which the lateral profile of the electron fluence will be considered is the bottom plane of the cavity at depth $z+\xi$.

At depth z, the electron beam is thought to have a uniform fluence profile along the x-axis. The directional distribution of the fluence of the electrons at the depth of the cavity's front plane is characterized by $\overline{\Theta^2}(z)$, the mean square of the polar angle Θ at depth z. For low Z materials, it is sufficient to consider that $\overline{\Theta^2}(z)$ increases with z in an almost linear fashion up to a depth of about 50% of the practical range.[1]

To calculate the profile of the electron fluence along the x-axis, including the lateral boundaries at $x=\pm a$, the electron beam is subdivided into pencil beams starting at the front plane of the cavity. Their initial widths shall be zero, but their initial directional distribution shall be Gaussian, with mean square angle $\overline{\Theta^2}(z)$. In the description of the further passage of the electrons toward the bottom plane at depth $z+\xi$, the well-known approximations valid for multiple scattering of electrons in thin layers of matter as described in ICRU Report 35 (Ref. 1) can be applied. Thus, for pencil beams originating from the front surface of the gas-filled volume and passing merely through the gas filling, i.e., with negligible multiple scattering, the mean square lateral displacement at the bottom plane $z+\xi$ will be[1]

$$\sigma_g^2 = \overline{\Theta^2}(z)\xi^2. \tag{A1}$$

By contrast, for a pencil beam originating from the same plane, but outside the gas-filled volume, the mean square lateral displacement will be[1]

$$\sigma_w^2 = \overline{\Theta^2}(z)\xi^2 + \int_0^\xi T(u)(\xi-u)^2 du = \overline{\Theta^2}(z)\xi^2 + \frac{1}{3}T(z)\xi^3, \tag{A2}$$

where $T(u)$ is the linear scattering power of water valid for the energy spectrum of the electrons at depth u; it is here

assumed to maintain the constant value T over the depth interval of the cavity. Note that σ_g^2 and σ_w^2 are mean square lateral displacements in the x, y direction.

The fluence profiles resulting in plane $z+\xi$ due to the transmission of all pencil beams through the gas-filled volume, respectively, through the adjacent layer of water can be described by convolutions of the pencil beams with rectangular functions corresponding to the partial beams hitting the cavity and the adjacent water, respectively. The convolution of a rectangular function with a Gaussian kernel yields the error function, so that the resulting 1D lateral fluence profile and, neglecting changes of the stopping power ratio, absorbed dose to water profile in the x direction valid for plane $z+\xi$ can be written as[1]

$$\frac{D(x,z+\xi)}{D(z)} = \frac{1}{2}\left[erf\left(\frac{x+a}{\sqrt{\sigma_g^2}}\right) - erf\left(\frac{x-a}{\sqrt{\sigma_g^2}}\right)\right] + 1 - \frac{1}{2}\left[erf\left(\frac{x+a}{\sqrt{\sigma_w^2}}\right) - erf\left(\frac{x-a}{\sqrt{\sigma_w^2}}\right)\right]. \quad \text{(A3)}$$

The first term in Eq. (A3) describes the dose contribution by the electrons having passed the gas layer, and the other two terms describe the contribution by the electrons having passed the water layer lateral from the gas layer, i.e., having missed a water layer of width $2a$. Equation (A3) can be generalized by considering that the depth gradient of the dose in the water layer lateral from the gas layer due to multiple scattering and range straggling might be non-negligible, so that it will then take the more general form

$$\frac{D(x,z+\xi)}{D(z)} = \frac{1}{2}\left[erf\left(\frac{x+a}{\sqrt{\sigma_g^2}}\right) - erf\left(\frac{x-a}{\sqrt{\sigma_g^2}}\right)\right] + A - \frac{A}{2}\left[erf\left(\frac{x+a}{\sqrt{\sigma_w^2}}\right) - erf\left(\frac{x-a}{\sqrt{\sigma_w^2}}\right)\right], \quad \text{(A4)}$$

where $A > 1$ would be valid in the dose buildup region, i.e., at depths of the chamber front plane more shallow than that of the dose maximum, and $A < 1$ in the dose falloff region where range straggling prevails in the water medium lateral from the cavity. The mean square lateral displacements σ_g^2 and σ_w^2 are available from Eqs. (A1) and (A2).

It is immediately clear from considering Eq. (A4) that the first and the third term are similarly structured but with their denominators containing the slightly different parameters σ_g^2 and σ_w^2. Thus, the superposition of their lateral curve wings is expected to show a local oscillation. To give an example basically related to the Monte Carlo results shown in Fig. 2, we have numerically evaluated Eq. (A4) for 6 MeV electrons and a cavity with $a = 2.0$ cm and $\xi = 0.4$ cm, for the three cases

(a) $z = 5$ mm, $\sigma_g = 0.117$ cm, $\sigma_w = 0.141$ cm, $A = 1.06$ (i.e., in the buildup region),
(b) $z = 14$ mm, $\sigma_g = 0.195$ cm, $\sigma_w = 0.222$ cm, $A = 0.965$ (i.e., near the dose maximum),
(c) $z = 26$ mm, $\sigma_g = 0.265$ cm, $\sigma_w = 0.346$ cm, $A = 0.50$ (i.e., in the falloff region),

using the electron scattering power data of water at 4.5, 2.9, and 1.2 MeV from ICRU 35.[1]

As shown in Fig. 14, basically similar dose profiles have been obtained as in Figs. 1 and 2. This comprises the dose oscillation occurring (a) at small depths and (b) in the depth region of the dose maximum, as well as (c) the monotonous transition of the dose from its value in the cavity to that in the surrounding medium occurring in the falloff region of the depth-dose curve. This monotonous decrease tends toward a low asymptotic value, already coined by the range straggling which prevails in the surrounding water medium.

Admittedly, this annex uses the small-angle multiple scattering theory strictly applicable only at shallow depths, but it may serve to illustrate that the dose oscillation near the cavity's lateral boundary is simply the consequence of the superposition

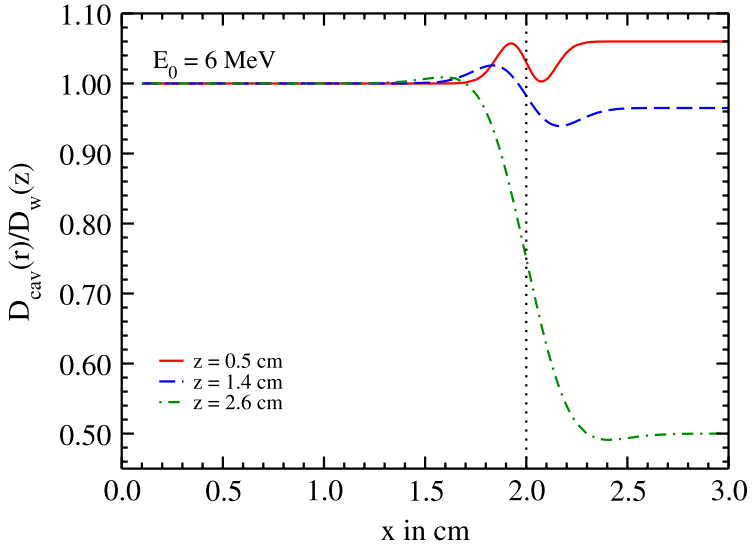

FIG. 14. Application of Eq. (A4) for a cavity of width $a = 2$ cm and height $\xi = 0.4$ cm for different depths z. The plotted radial dose profiles are valid for the bottom plane of the cavity, corresponding to slice 4 in Fig. 2. The model parameters σ_g, σ_w, and A are given in the text.

of the dose profiles of the electrons which have only traversed the gas-filled cavity and of those electrons which in the front surface plane of the cavity started with the same initial conditions but were slowed down and scattered in the surrounding water medium.

[a]Author to whom correspondence should be addressed. Electronic mail: klemens.zink@kmub.thm.de

[1]ICRU-35, *ICRU Report 35: Radiation Dosimetry: Electron Beams with Energies Between 1 and 50 MeV* (ICRU, Bethesda, MD, 1984).
[2]P. Andreo, D. T. Burns, K. Hohlfeld, M. S. Huq, T. Kanai, F. Laitano, V. Smyth, and S. Vynckier, Absorbed Dose Determination in External Beam Radiotherapy: An International Code of Practice for Dosimetry Based on Standards of Absorbed Dose to Water (International Atomic Energy Agency, Vienna, Technical Report series No. 398, 2000).
[3]P. R. Almond, P. J. Biggs, B. M. Coursey, W. F. Hanson, M. S. Huq, R. Nath, and D. W. Rogers, "AAPM's TG-51 protocol for clinical reference dosimetry of high-energy photon and electron beams," Med. Phys. **26**(9), 1847–1870 (1999).
[4]D. I. Thwaites, A. R. DuSautoy, T. Jordan, M. R. McEwen, A. Nisbet, A. E. Nahum, W. G. Pitchford, and I. P. E. M. Working Party, "The IPEM code of practice for electron dosimetry for radiotherapy beams of initial energy from 4 to 25 Mev based on an absorbed dose to water calibration," Phys. Med. Biol. **48**(18), 2929–2970 (2003).
[5]DIN 6800-2 (2008), "Procedures of dosimetry with probe-type detectors for photon and electron radiation - Part 2: Ionization chamber dosimetry of high energy photon and electron radiation" (Normenausschuss Radiologie (NAR) im DIN, Deutsches Institut für Normung, Berlin, Germany, 2008).
[6]H. Svensson and A. Brahme, "Fundamentals of electron beam dosimetry," in *Proceedings of the Symposium on Electron Beam Therapy*, edited by F. C. H. Chu and J. S. Laughlin (Memorial Sloan-Kettering Cancer Center, New York, NY, 1981), p. 17.
[7]D. Harder, "The effect of multiple electron scattering on ionization in gas-filled cavities," Biophysik **5**(2), 157–164 (1968).
[8]K. A. Johansson, L. O. Mattsson, L. Lindborg, and H. Svensson, "Absorbed-dose determination with ionization chambers in electron and photon beams having energies between 1 and 50 MeV," in *National and International Standardization of Radiation Dosimetry, IAEA Proceedings Series, Vienna* (IAEA, Vienna, Austria, 1978), Vol. 2, pp. 243–270.
[9]A. Van der Plaetsen, J. Seuntjens, H. Thierens, and S. Vynckier, "Verification of absorbed doses determined with thimble and parallel-plate ionization chambers in clinical electron beams using ferrous sulphate dosimetry," Med. Phys. **21**(1), 37–44 (1994).
[10]L. L. W. Wang and D. W. O. Rogers, "Replacement correction factors for plane-parallel ion chambers in electron beams," Med. Phys. **37**(2), 461–465 (2010).
[11]K. Zink and J. Wulff, "Beam quality corrections for parallel-plate ion chambers in electron reference dosimetry," Phys. Med. Biol. **57**(7), 1831–1854 (2012).
[12]IAEA, The Use of Plane Parallel Ionization Chambers in High Energy Electron and Photon Beams: An International Code of Practice for Dosimetry, IAEA technical report series 381 (International Atomic Energy Agency, Vienna, Technical Report 1997).
[13]M. Roos, K. Derikum, and A. Kraus, "Deviation of the effective point of measurement of the markus chamber from the front surface of its air cavity in electron beams," The Use of Plane Parallel Ionization Chambers in High Energy Electron and Photon Beams (IAEA, Vienna, Austria, Review of data and methods recommended in the international code of practice for dosimetry, IAEA TECDOC 1173, IAEA Technical Reports Series No. 381 2000).
[14]K. Zink and J. Wulff, "Positioning of a plane-parallel ionization chamber in clinical electron beams and the impact on perturbation factors," Phys. Med. Biol. **54**(8), 2421–2435 (2009).
[15]K. Zink and J. Wulff, "On the wall perturbation correction for a parallel-plate NACP-02 chamber in clinical electron beams," Med. Phys. **38**(2), 1045–1054 (2011).
[16]I. Kawrakow, "Accurate condensed history Monte Carlo simulation of electron transport. II. Application to ion chamber response simulations," Med. Phys. **27**(3), 499–513 (2000).
[17]I. Kawrakow, E. Mainegra-Hing, D. W. O. Rogers, F. Tessier, and B. R. B. Walters, "The EGSnrc code system: Monte Carlo simulation of electron and photon transport" (National Research Council of Canada, Ottawa, Canada, Report PIRS-701 2013).
[18]J. Wulff, K. Zink, and I. Kawrakow, "Efficiency improvements for ion chamber calculations in high energy photon beams," Med. Phys. **35**(4), 1328–1336 (2008).
[19]I. Kawrakow, E. Mainegra-Hing, F. Tessier, and B. R. B. Walter, "The EGSnrc c++ class library" (NRC Report PIRS-898 (Rev. A), Ottawa, Canada, 2009).
[20]L. L. W. Wang and D. W. O. Rogers, "Calculation of the replacement correction factors for ion chambers im megavoltage beams by Monte Carlo simulation," Med. Phys. **35**(5), 1747–1755 (2008).
[21]G. X. Ding, D. W. O. Rogers, and T. R. Mackie, "Calculation of stopping-power ratios using realistic clinical electron beams," Med. Phys. **22**(5), 489–501 (1995).
[22]L. L. W. Wang and D. W. O. Rogers, "Replacement correction factors for cylindrical ion chambers in electron beams," Med. Phys. **36**(10), 4600–4608 (2009).
[23]H. K. Looe, D. Harder, and B. Poppe, "Experimental determination of the effective point of measurement for various detectors used in photon and electron beam dosimetry," Phys. Med. Biol. **56**(14), 4267–4290 (2011).
[24]W. U. Laub, T. W. Kaulich, and F. Nüsslin, "A diamond detector in the dosimetry of high-energy electron and photon beams," Phys. Med. Biol. **44**(9), 2183–2192 (1999).
[25]M. Lauterbach, "The multiple scattering of high-energy electrons into gas-filled cavities (in German)," Ph.D. thesis, University of Göttingen, 1999.
[26]L. Eyges, "Multiple scattering with energy loss," Phys. Rev. **74**, 1534–1535 (1948).

International Journal of Medical Physics, Clinical Engineering and Radiation Oncology, 2017, 6, 150-161
http://www.scirp.org/journal/ijmpcero
ISSN Online: 2168-5444
ISSN Print: 2168-5436

On the Perturbation Correction Factor p_{cav} of the Markus Parallel-Plate Ion Chamber in Clinical Electron Beams

Philip von Voigts-Rhetz[1,2*], Hilke Vorwerk[2], Klemens Zink[1,2,3]

[1]Institut für Medizinische Physik und Strahlenschutz IMPS, Technische Hochschule Mittelhessen, University of Applied Sciences, Giessen, Germany
[2]University Medical Center Marburg, Department of Radiotherapy and Radiation Oncology, Philipps-University, Marburg, Germany
[3]Frankfurt Institute for Advanced Studies (FIAS), Frankfurt, Germany
Email: *philip.von.voigts-rhetz@lse.thm.de

How to cite this paper: von Voigts-Rhetz, P., Vorwerk, H. and Zink, K. (2017) On the Perturbation Correction Factor p_{cav} of the Markus Parallel-Plate Ion Chamber in Clinical Electron Beams. *International Journal of Medical Physics, Clinical Engineering and Radiation Oncology*, **6**, 150-161.
https://doi.org/10.4236/ijmpcero.2017.62014

Received: January 30, 2017
Accepted: May 20, 2017
Published: May 23, 2017

Abstract

Purpose: All present dosimetry protocols recommend well-guarded parallel-plate ion chambers for electron dosimetry. For the guard-less Markus chamber, an energy dependent fluence perturbation correction p_{cav} is given. This perturbation correction was experimentally determined by van der Plaetsen by comparison of the read-out of a Markus and a NACP chamber, which was assumed to be "perturbation-free". Aim of the present study is a Monte Carlo based reiteration of this experiment. **Methods:** Detailed models of four parallel-plate chambers (Roos, Markus, NACP and Advanced Markus) were designed using the Monte Carlo code EGSnrc and placed in a water phantom. For all chambers, the dose to the active volume filled with low density water was calculated for 13 clinical electron spectra (E_0 = 6 - 21 MeV) and three energies of an Electra linear accelerator at the depth of maximum and at the reference depth under reference conditions. In all cases, the chamber's reference point was positioned at the depth of measurement. Moreover, the dose to water D_W was calculated in a small water voxel positioned at the same depth. **Results:** The calculated dose ratio D_{NACP}/D_{Markus}, which according to van der Plaetsen reflects the fluence perturbation correction of the Markus chamber, deviates less from unity than the values given by van der Plaetsen, but exhibits similar energy dependence. The same holds for the dose ratios of the other well-guarded chambers. But, in comparison to water, the Markus chamber reveals the smallest overall perturbation correction which is nearly energy independent at both investigated depths. **Conclusion:** The simulations principally confirm the energy dependence of the dose ratio D_{NACP}/D_{Markus} as published by van der Plaetsen. But, as shown by our simulations of the ratio D_W/D_{Markus}, the conclusion drawn in all dosimetry protocols is questionable: in contrast to

all well-guarded chambers, the guard-less Markus chamber reveals the smallest overall perturbation correction and also the smallest energy dependence.

Keywords

EGSnrc, Monte Carlo, Cavity Perturbation, Ionization Chamber

1. Introduction

All present dosimetry protocols [1] [2] [3] [4] recommend the use of well-guarded, air-filled parallel-plate ion chambers for reference dosimetry in clinical electron beams. The recommendation of well-guarded chambers is especially based on report 35 of the International Commission on Radiation Units & Measurements (ICRU) [5] which was the principles of clinical electron dosimetry that are summarized. In this report, the so-called *in-scattering effect* is described in detail: based on the strong reduction of the energy losses and multiple scattering of the electrons in the gas-filled cavity compared to the surrounding phantom material, more electrons are scattered into than out of the cavity. As a result, at the lateral boundary of the air-filled cavity, a dose oscillation arises (see Figure (4.2) in ICRU 35) resulting in an over-response of the air-filled cavity, which according to all dosimetry protocols, has to be corrected by a fluence perturbation correction p_{cav}. In attempt to make the chamber signal insensitive to the in/out electrontransport imbalance and thereby, bringing p_{cav} to unity, modern parallel-plate chambers are equipped with a wide guard ring to keep the region of fluence perturbation at a safe distance from the chamber's collecting volume.

Moreover, all present dosimetry protocols assume a negligible influence of the entrance window and the surrounding wall material on the response of modern parallel-plate chambers, *i.e.* the wall perturbation correction defined in all dosimetry protocols is assumed to be unity.

In a previous publication, Zink *et al.* [6] reinvestigated in detail the in- and out-scattering of electrons in gas-filled cavities, which gave a new insight into the perturbation correction p_{cav} for parallel-plate chambers in clinical electron beams. With the help of spatially resolved Monte Carlo calculations, they have shown that the in-scattering effect indeed exists, but they have also shown that a guard ring has only a minor effect on the dose to a gas-filled cavity, especially for cavities with small diameters as in the case of the Markus chamber. The cavity diameter itself has a much larger impact on the dose within the cavity. This is a consequence of the deep radial penetration of the in- and out-bound transport of electrons into the gas-filled cavity. These results question not only the relevance of the guard ring for this chamber type but also the value of the perturbation correction p_{cav} for the guardless Markus chamber given in all present dosimetry protocols. These values are all based on an experimental study performed by Van der Pleatsen *et al.* [7] in the early 1990s. They compared the chamber's

dose D for the guardless Markus chamber with the dose of a NACP chamber in clinical electron beams, assuming that the NACP chamber represents a perturbation-free ion chamber. The ratio $\bar{D}_{NACP}/\bar{D}_{Markus}$ was interpreted as the fluence perturbation correction p_{cav} for the Markus chamber.

The aim of the present study is a Monte Carlo based reiteration of Van der Plaetsen's experiment against the background of the actual knowledge about the in-scattering effect in gas-filled cavities in clinical electron beams. The present data may be especially important regarding the planned update of the international dosimetry protocol IAEA TRS-398 [2].

2. Fundamentals

Following Bragg-Gray theory, the absorbed dose to water D_W may be derived from the dose to the air-filled detector D_{det}, the restricted stopping power ratio $s^{\Delta}_{w,a}$ of the materials water w and air a, and a perturbation correction p [5] [8]:

$$D_w = p \cdot s_{w,a} \cdot D_{\mathrm{det}} \tag{1}$$

It is assumed that the perturbation factor p may be factorized, for parallel-plate chambers it is traditionally split into three components:

$$p = p_{wall} \cdot p_{cav} \cdot p_{dis} \tag{2}$$

where p_{wall} stands for the fluence perturbation due to the chamber wall, p_{cav} the in-scattering of electrons from the surrounding phantom material into the air-filled cavity (P_{fl} in The American Association of Physicists in Medicine (AAPM) TG-51 [1]), and p_{dis} for fluence changes due to the replacement of the phantom material water by the air-filled cavity (P_{gr} in AAPM TG-51).

For parallel-plate chambers p_{dis} equals unity according to all present dosimetry protocols when the reference point of the chamber (center of the entrance plane of the air-filled cavity) is positioned at the depth of measurement z. Because of the thin entrance window of all parallel-plate chamber types, also the wall perturbation p_{wall} is assumed to be unity. As the NACP chamber is equipped with a wide guard ring (w = 0.33 cm), Van der Plaetsen *et al.* [7] moreover assumed that for this chamber type also p_{cav} is unity for all electron energies, *i.e.* the NACP chamber was considered a perturbation-free ion chamber. Therefore, the dose ratio D_{NACP}/D_{Markus} is interpreted as the perturbation correction p_{cav} for the Markus chamber due to in-scattering electrons as this chamber type is not equipped with a guard ring of sufficient width (w = 0.035 cm). The dose ratio was determined for several primary electron energies at the depth of the dose maximum z_{max} and could be fitted by a function of the mean electron energy $\bar{E}_{z,\max}$ at this depth:

$$\left(p_{cav}\right)_{Markus} = \bar{D}_{NACP}/D_{Markus} = 1 - 0.039 \cdot e^{-0.2816 \cdot \bar{E}_{z,\max}} \tag{3}$$

In the IAEA protocol [2], this equation was adapted to the actual beam quality specifier R_{50} and the reference depth z_{ref}:

$$\left(p_{cav}\right)_{Markus} = 1 - 0.037 \cdot e^{-0.27 R_{50}} \tag{4}$$

3. Methods and Material

Comparable to the experiments conducted by Van der Plaetsen, the dose ratio $\bar{D}_{\text{det}}/\bar{D}_{Markus}$ was calculated for the NACP chamber and additionally for the other well-guarded chambers, the Roos and the Advanced Markus chambers, using the Monte Carlo code EGSnrc (V4 2.4.0) [9] [10] [11] [12]. The ion chambers were modeled in detail with the egs++ geometry package according to the blueprints provided by the manufacturer PTW [13]. In the case of the NACP-02 chamber, the geometry is based on the information given in several publications [14]-[19]. Geometric details of the chambers with their material components are summarized in **Table 1** and **Figure 1**. The investigation was performed with thirteen clinical electron spectra (6 MeV < E_0 < 21 MeV) taken from literature [20] and a full modeled Elekta Synergy accelerator including an electron applicator with a field size of 10 × 10 cm^2 (see **Table 2** for details). For the accelerator model the energies of the primary electrons hitting the scattering foil were E_0 = 6, 12 and 18 MeV. The accelerator was modeled with the BEAMnrc code [21] according to the blueprints provided by the manufacturer.

The user code egs_chamber [22] was applied for the calculation of the dose

Table 1. Geometric details of the modeled parallel-plate chambers. V is the active chamber volume, r the radius of the active volume, h its height and w the width of the guard ring. Additionally the entrance window thickness d is given.

Chamber	V	r	h	w	d
	in cm^3	in cm	in cm	in cm	in cm
Roos (PTW-34001)	0.35	0.78	0.2	0.42	0.112
Markus (PTW-23343)	0.055	0.265	0.2	0.035	0.13
Adv. Markus (PTW-34045)	0.020	0.25	0.1	0.2	0.13
NACP-02	0.16	0.5	0.2	0.33	0.06

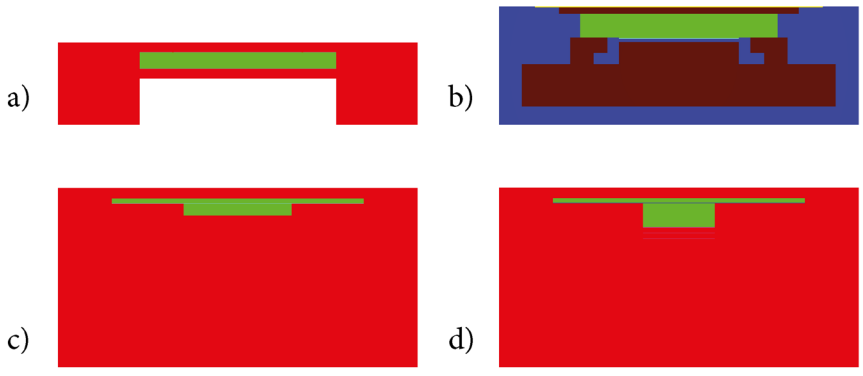

Figure 1. Schematic illustration of the outer dimension and materials of the used parallel-plate chambers: (a) Roos, (b) NACP, (c) Adv. Markus and (d) Markus. The green rectangle represents the air-filled cavity for all chambers. For the Roos, Markus and Adv. Markus the outer material PMMA is given in red. In contrast for die NCAP the outer material polystyrene is drafted in blue. The Markus and Adv. Markus chambers have a small air gap above their sensitive cavities. The NACP chamber has inside parts of 1.82 g/cm^3 carbon given in claret.

Table 2. Characteristic data of the electron sources applied in this study. The Elekta Synergy accelerator was modeled in detail including the electron applicator, for the other accelerators only spectra were used as electron sources [19]. The given data are the mean electron energy at the depth of the dose maximum $\bar{E}_{z,\max}$ and at the reference depth, the corresponding depths z_{max} and z_{ref} and the electron beam specifier R_{50}.

Linear Accelerator	Nominal Energy	$\bar{E}_{z,\max}$	$\bar{E}_{z,ref}$	R_{50}	z_{max}	z_{ref}
Philips SL75-20	5	2.27	2.32	2.11	1.2	1.17
	10	4.22	3.91	4.15	2.2	2.39
	14	7.22	5.35	6.03	2.4	3.52
	17	9.44	6.13	6.96	2.1	4.08
	20	12.5	7.07	8.07	1.6	4.74
Varian Clinac 2100D	6	2.87	2.74	2.65	1.4	1.49
	9	4.13	3.8	4.02	2.1	2.31
	12	5.05	4.68	5.19	2.8	3.02
	15	7.21	5.68	6.5	2.9	3.8
	18	10.17	6.65	7.73	2.5	4.54
Siemens KD2	6	2.37	2.49	2.31	1.35	1.29
	11	3.84	3.96	4.21	2.5	2.43
	21	10.65	7.04	8.3	2.8	4.85
Elekta Synergy	6	2.69	2.69	2.58	1.45	1.45
	12	4.68	4.4	4.84	2.65	2.81
	18	8.38	5.89	7.08	2.8	4.15

deposition $\bar{D}_{\text{det}}$ within the detectors and within a small water voxel (r = 0.5 cm, z = 0.02 cm) to determine the dose to water D_W.

To enable a comparison of the Monte Carlo data with the original data from Van der Plaetsen and with the data given in the IAEA protocol, the simulations were performed for two depths within a water phantom (30 × 30 × 30 cm^3): the depth of the dose maximum z_{max} and the reference depth z_{ref}. In all cases, the chambers were positioned with their reference point at the correspondent depth. The source-to-surface distance was 100 cm and the field size at the phantom surface 10 × 10 cm^2. Also to enable comparability with Van der Plaetsen we additionally determined the mean electron energy $\bar{E}$ at the depth of measurement. The determination of the mean electron energies at depth z within the water phantom was performed with the user code FLURZnrc [23]. To calculate the total perturbation correction p the dose to water was also calculated at depths z_{max} and z_{ref} within a small water voxel. To avoid the calculation of the stopping power ratios $s^{\Delta}_{w,a}$, the cavities of the chambers were filled with low-density water, *i.e.* water with the density of air, and a density correction corresponding to normal-density water [24]. In that case, the perturbation correction p can simply derived from the dose ratio $\bar{D}_W/\bar{D}_{\text{det}}$, *i.e.* $p = \bar{D}_W/\bar{D}_{\text{det}}$. The cutoff/threshold energies for the particle transport were set to 512 keV for elec-

trons and 10 keV for photons; all other EGS parameters were set to their default values.

4. Results

Figure 2 shows the ratio of the dose to the active volume of the well-guarded Roos, NACP and Advanced Markus chambers to the dose within the guardless Markus chamber. In the upper panel this dose ratio is given for the depth of the dose maximum z_{max} as a function of the mean electron energy $\bar{E}_{z,\max}$, *i.e.* these data are directly comparable with the results published by Van der Plaetsen. The fit according to Equation (3) is additionally shown. As can be seen, the dose for all guarded chambers is quite similar; for all energies they do not deviate from each other by more than 0.3%. For the largest mean energy $\bar{E}$, corresponding

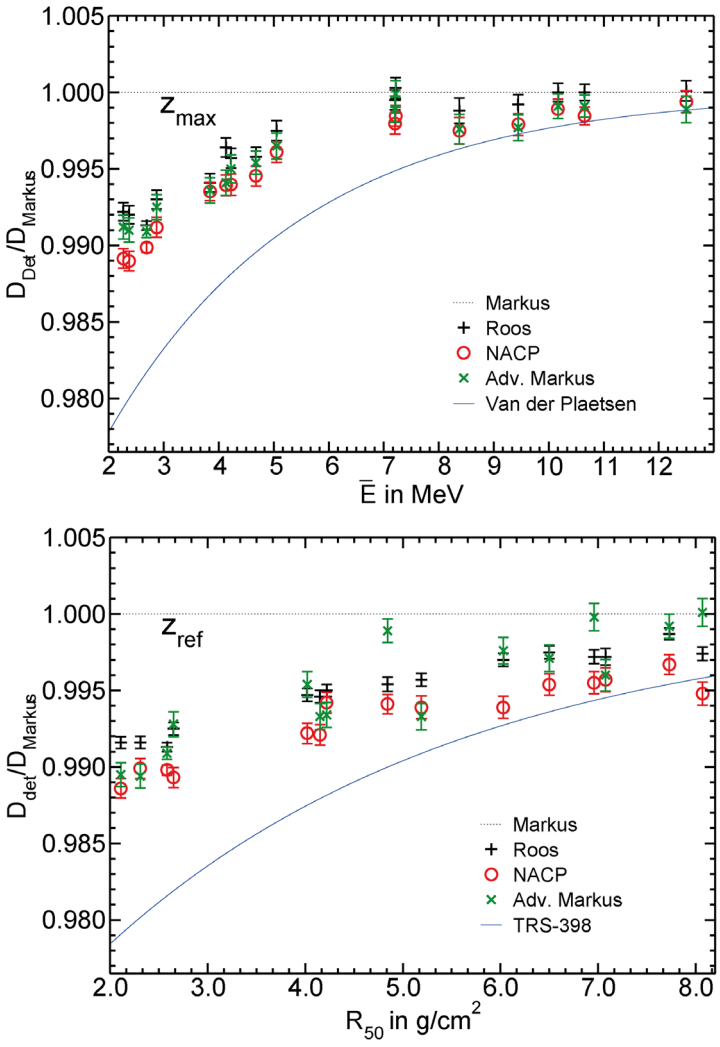

Figure 2. Dose within the active volume of well-guarded parallel-plate chambers (Roos, Adv. Markus, NACP) in relation to the dose within the guardless Markus chamber as a function of the beam quality specifiers and R_{50} respectively. Upper panel: dose ratios at the depth of the dose maximum zmax. Lower panel: dose ratios at the reference depth z_{ref}. The solid lines represent the data from Van der Plaetsen and IAEA TRS-398. The error bars indicate the statistical uncertainties of the Monte Carlo simulations (1σ).

to an incident energy of E_0 = 20 MeV, the dose ratio $\bar{D}_{\det}/\bar{D}_{Markus}$ approximately equals unity and decreases for smaller mean electron energies $\bar{E}_{z.\max}$ reaching a value of about 0.99 for the smallest energy investigated here. So, the Monte Carlo based data show an energy dependence similar to the data given by Van der Plaetsen, but the deviations from unity are smaller in comparison to Van der Plaetsen's data.

The data for the reference depth z_{ref} are quite similar with two exceptions: (I) The variation of the dose ratios as a function of the beam quality specifier R_{50} is smaller and even at the highest electron energy the dose ratio is below unity. This is in accordance with the data given in the TRS-398 protocol. (II) The scattering of the Monte Carlo based data points is much larger than for the positioning of the chamber at the maximum depth z_{max}, especially for larger electron energies. This may be an indication that the beam quality specifier R_{50} (and the corresponding reference depth) is not an ideal specifier.

As Van der Plaetsen *et al.* assumed that the NACP chamber is a perturbation-free chamber, the dose ratio $\bar{D}_{NACP}/\bar{D}_{Markus}$ was interpreted as the perturbation correction p_{cav} for the guardless Markus chamber (see Equation (3)). To check this interpretation, we also calculated the total perturbation correction $p = D_W/D_{\det}$ for all chambers. These data are given in **Figure 3**.

The total perturbation correction $p = D_W/D_{\det}$ decreases with increasing mean electron energy for the maximum depth z_{max} from about 1.017 to 1.005 for the Roos, NACP and the Adv. Markus chamber. Thus it appears that there is no change of p for energies larger than E_0 = 12 MeV (see upper panel). The perturbation correction p of the Markus chamber is smaller than for the other three parallel-plate chambers and varies between 1.001 and 1.005.

For the reference depth z_{ref} the total perturbation factor for the Roos, NACP and the Adv. Markus chamber decreases from about 1.015 to 1.005. In contrast, the perturbation for the guardless Markus chamber is only weakly dependent on energy with a mean value $\bar{p}$ of about 1.003 (see **Figure 3** lower panel).

5. Discussion

The new Monte Carlo results in principle confirm the experimental data from Van der Plaetsen, but the common interpretation of these results may be questionable. According to Van der Plaetsen and also according to all current dosimetry protocols, the dose ratio D_{NACP}/D_{Markus} is interpreted as the fluence perturbation correction p_{cav} of the guardless Markus chamber. This interpretation is based on the assumption that the NACP chamber is completely perturbation-free, *i.e.* $p_{wall} = p_{cav} = 1$. This assumption may be wrong, as revealed by the calculated total perturbation correction $p = D_W/D_{\det}$ (**Figure 3**).

There have been many experimental [25] [26] [27] [28] [29] as well as Monte Carlo based studies [30] [31] [32] published during the last two decades concerning the perturbation corrections of parallel-plate chambers in clinical electron beams. In all these studies, a wall correction factor $p_{wall} \neq 1$ for the different parallel-plate chambers was determined. For the NACP chamber, Kuchnir

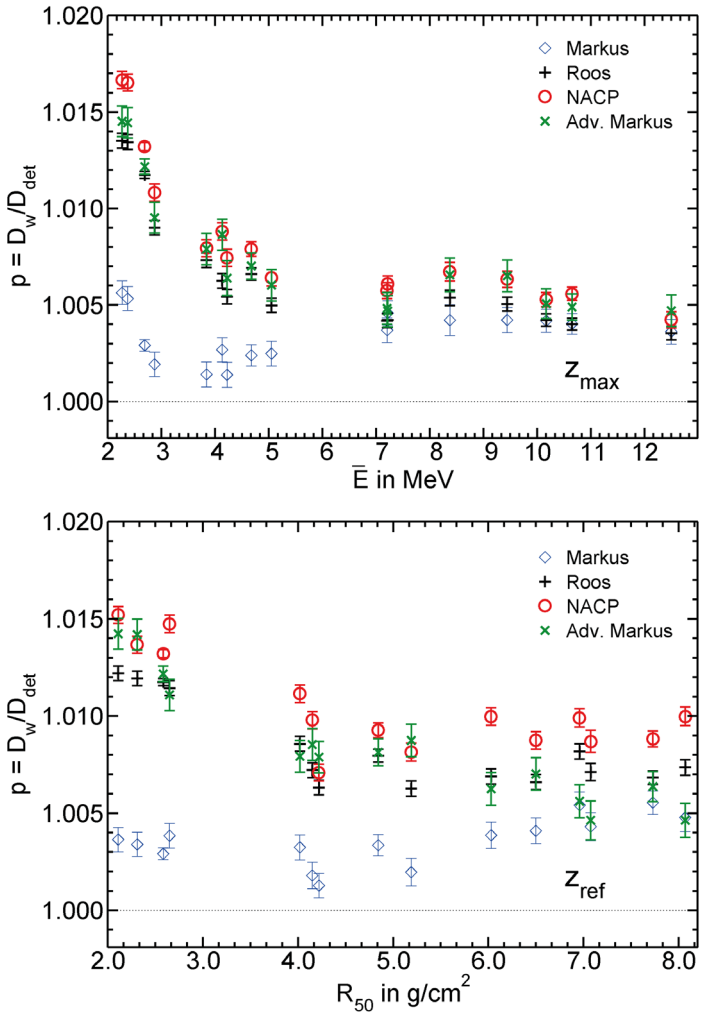

Figure 3. Total perturbation correction p of parallel-plate chambers as a function of the beam quality specifiers $\bar{E}_{z,max}$ and R_{50}. The error bars indicate the statistical uncertainties of the Monte Carlo simulations (1σ).

[33] [34] experimentally determined a wall perturbation correction factor of 1.015 for 4 MeV, 1.006 for 6 MeV and 1.001 for 24 MeV electrons. In more precise measurements, McEwen *et al.* [35] confirmed these results in 2006.

Monte Carlo simulations from Araki [36] also provide a wall perturbation correction p_{wall} for the NACP and Markus chambers from 1.02 for low energies (R_{50} = 1 cm) down to 1.005 for high energies (R_{50} = 8 cm). Comparable Monte Carlo simulations from our group [18] confirmed these values and gave additional values for the Advanced Markus and Roos chambers, which were also larger than unity. So, as far as we know, the influence of the wall for all parallel-plate ion chambers in clinical electron beams is not negligible, and it is larger than unity.

Regarding the perturbation correction p_{cav}, in a previous study [6] with spatially resolved Monte Carlo simulations within cavities comparable to those present in the parallel-plate chambers investigated here, we have shown that there is indeed an in-scattering effect resulting in p_{cav} values smaller than unity

for measuring depths below R_{50} = 0.5. As was shown, the increase in dose within air-filled cavities compared to the dose within a water voxel is mainly determined by the cavity radius and not as usually assumed [2] [5] by the guard ring width: the larger the cavity radius, the smaller the impact of in-scattering electrons. Compared to the radius of the air-filled cavity of the Markus chamber (r = 0.30 cm), those of the Roos and NACP chambers are quite large (r = 1.20 cm and r = 0.83 cm including the guard ring, see **Table 1**), *i.e.* the dose increase due to in-scattering of electrons is much more pronounced for the small Markus chamber. Numerical p_{cav} values for the different parallel-plate chambers for the entire clinical energy range have been published by Wang and Rogers [37] as well as by our group [18]. According to these data, large chambers such as the Roos and the NACP chambers reveal p_{cav} values which are near unity for all electron energies. For the small (and guardless) cavity of the Markus chamber, the calculated p_{cav} values were energy-dependent and below unity. For the smallest electron energy investigated in these studies ($R_{50} \approx 2\,\text{cm}$), p_{cav} deviates by about 1.5% from unity, *i.e.* p_{cav} = 0.985.

The radius of the cavity of the Advanced Markus chamber including the guard ring is r = 0.45 cm, *i.e.* also much smaller than those of the NACP and the Roos chambers. Therefore, also a non-unity p_{cav} value should be expected. However, in contrast to all other chambers investigated here, the cavity height of the Advanced Markus chamber is only 1 mm, half the value of the other chambers. Due to this small cavity height the in-scattering of electrons into the chamber's cavity is reduced and the p_{cav} value for the Advanced Markus chamber is near unity [18] [37].

As the total perturbation correction p given in **Figure 3** is the product of the above-mentioned factors p_{wall} and p_{cav} an interpretation for the different chambers and different electron energies emerges. For the NACP, Roos and Advanced Markus chambers the total perturbation correction p is determined mainly by the impact of the chamber walls, *i.e.* p_{wall}. The energy dependence of p at the depth of the maximum z_{max} as well as at the reference depth z_{ref} follows that of published p_{wall} data. For the simple Markus chamber the corrections p_{wall} and p_{cav} both deviate from unity, but in opposite directions ($p_{wall} > 1$, $p_{cav} < 1$), therefore, the total perturbation correction p for this chamber remain close to unity and is nearly independent of the energy (see **Figure 3**). Note that strictly speaking our conclusion applies only to the specific depths that were investigated: the reference depth and the depth of dose maximum.

6. Conclusions

In this study, we repeated an old experimental study performed by Van der Plaetsen using Monte Carlo methods. Van der Plaetsen compared a well-guarded NACP chamber and a guardless Markus chamber in clinical electron beams. The non-unity and energy-dependent signal ratio of both chambers was interpreted as the cavity perturbation correction p_{cav} of the Markus chamber. This result was adopted by all common dosimetry protocols, *i.e.* they recom-

mend applying this energy-dependent cavity perturbation correction p_{cav} for the Markus chamber in clinical electron dosimetry.

In our new Monte Carlo calculations, we also compared the signal ratio of different parallel-plate chambers. Additionally, we calculated the perturbation corrections for the different chambers themselves. The results show that the ratio D_{NACP}/D_{Markus} indeed follows an energy dependence similar to the one measured by Van der Plaetsen. However, as the calculation of the perturbation correction p for the different chambers clearly shows, the conclusion drawn by Van der Plaetsen is questionable. Based on the assumption that the NACP chamber is a perturbation-free chamber, he concluded that the ratio D_{NACP}/D_{Markus} corresponds to the cavity perturbation p_{cav} of the guardless Markus chamber. This assumption is according to our own Monte Carlo results which are in good agreement with previous experimental data for the NACP chamber.

Based on our results given in **Figure 3**, it seems likely that the recommendation for the cavity perturbation correction p_{cav} for the Markus chamber given in all current dosimetry protocols is incorrect. Furthermore, the assumption that well-guarded parallel-plate chambers are perturbation-free chambers should be revisited.

Acknowledgements

This research was performed as part of the doctoral thesis of one of the authors at Philipps-Universität Marburg.

References

[1] Almond, P.R., Biggs, P.J., Coursey, B.M., Hanson, W.F., *et al.* (1999) AAPM's TG-51 Protocol for Clinical Reference Dosimetry of High-Energy Photon and Electron Beams. *Medical Physics*, **26**, 1847-1870.

[2] Andreo, P., Burns, D.T., Hohlfeld, K., Huq, M.S., *et al.* (2000) Absorbed Dose Determination in External Beam Radiotherapy. An International Code of Practice for Dosimetry Based on Standards of Absorbed Dose to Water. *Technical Reports Series TRS*-398, International Atomic Energy Agency, Vienna.

[3] Thwaites, D.I., DuSautoy, A.R., Jordan, T., McEwen, M.R., *et al.* (2003) The IPEM Code of Practice for Electron Dosimetry for Radiotherapy Beams of Initial Energy from 4 to 25 MeV Based on an Absorbed Dose to Water Calibration. *Physics in Medicine and Biology*, **48**, 2929-2970. https://doi.org/10.1088/0031-9155/48/18/301

[4] DIN6800-2 (2008) Procedures of Dosimetry with Probe-Type Detectors for Photon and Electron Radiation—Part 2: Ionization Chamber Dosimetry of High Energy Photon and Electron Radiation.

[5] Ibbott, G.S. (1985) Radiation Dosimetry: Electron Beams with Energies between 1 and 50 MeV (ICRU Report No. 35). *Medical Physics*, **12**, 813. https://doi.org/10.1118/1.595780

[6] Zink, K., Czarnecki, D., Looe, H.K., von Voigts-Rhetz, P., *et al.* (2014) Monte Carlo Study of the Depth-Dependent Fluence Perturbation in Parallel-Plate Ionization Chambers in Electron Beams. *Medical Physics*, **41**, Article ID: 111707. https://doi.org/10.1118/1.4897389

[7] van der Plaetsen, A., Seuntjens, J., Thierens, H. and Vynckier, S. (1994) Verification

of Absorbed Doses Determined with Thimble and Parallel-Plate Ionization Chambers in Clinical Electron Beams Using Ferrous Sulphate Dosimetry. *Medical Physics*, **21**, 37-44. https://doi.org/10.1118/1.597362

[8] ICRU-33 (1980) ICRU Report 33: Radiation Quantities and Units. ICRU, Bethesda.

[9] Kawrakow, I. (2000) Accurate Condensed History Monte Carlo Simulation of Electron Transport. I. EGSnrc, the New EGS4 Version. *Medical Physics*, **27**, 485-498. https://doi.org/10.1118/1.598917

[10] Kawrakow, I. (2000) Accurate Condensed History Monte Carlo Simulation of Electron Transport. II. Application to Ion Chamber Response Simulations. *Medical Physics*, **27**, 499-513. https://doi.org/10.1118/1.598918

[11] Kawrakow, I., Mainegra-Hing, E., Rogers, D.W.O., Tessier, F., *et al.* (2013) The EGSnrc Code System: Monte Carlo Simulation Of Electron and Photon Transport. National Research Council of Canada, Report No. PIRS-701.

[12] Smilowitz, J.B., Das, I.J., Feygelman, V., Fraass, B.A., *et al.* (2015) AAPM *Medical Physics* Practice Guideline 5.a.: Commissioning and QA of Treatment Planning Dose Calculations—Megavoltage Photon and Electron Beams. *Journal of Applied Clinical Medical Physics*, **16**, 14-34. https://doi.org/10.1120/jacmp.v16i5.5768

[13] Kawrakow, I., Mainegra-Hing, E., Tessier, F. and Walter, B.R.B. (2009) The EGSnrc C++ Class Library. NRC Report PIRS-898 (rev A), Ottawa.

[14] Verhaegen, F., Zakikhani, R., Dusautoy, A., Palmans, H., *et al.* (2006) Perturbation Correction Factors for the NACP-02 Plane-Parallel Ionization Chamber in Water in High-Energy Electron Beams. *Physics in Medicine and Biology*, **51**, 1221-1235. https://doi.org/10.1088/0031-9155/51/5/012

[15] Chin, E., Shipley, D., Bailey, M., Seuntjens, J., *et al.* (2008) Validation of a Monte Carlo Model of a NACP-02 Plane-Parallel Ionization Chamber Model Using Electron Backscatter Experiments. *Physics in Medicine and Biology*, **53**, N119-N126. https://doi.org/10.1088/0031-9155/53/8/n01

[16] Chin, E., Palmans, H., Shipley, D., Bailey, M., *et al.* (2009) Analysis of Dose Perturbation Factors of a NACP-02 Ionization Chamber in Clinical Electron Beams. *Physics in Medicine and Biology*, **54**, 307-326. https://doi.org/10.1088/0031-9155/54/2/009

[17] Zink, K. and Wulff, J. (2011) On the Wall Perturbation Correction for a Parallel-Plate NACP-02 Chamber in Clinical Electron Beams. ..*Medical Physics*, **38**, 1045-1054. https://doi.org/10.1118/1.3544660

[18] Zink, K. and Wulff, J. (2012) Beam Quality Corrections for Parallel-Plate Ion Chambers in Electron Reference Dosimetry. *Physics in Medicine and Biology*, **57**, 1831-1854. https://doi.org/10.1088/0031-9155/57/7/1831

[19] von Voigts-Rhetz, P., Czarnecki, D. and Zink, K. (2014) Effective Point of Measurement for Parallel Plate and Cylindrical Ion Chambers in Megavoltage Electron Beams. *Zeitschrift für Medizinische Physik*, **24**, 216-223. https://doi.org/10.1016/j.zemedi.2013.12.001

[20] Ding, G.X., Rogers, D.W.O. and Mackie, T.R. (1995) Calculation of Stopping-Power Ratios Using Realistic Clinical Electron Beams. *Medical Physics*, **22**, 489-501. https://doi.org/10.1118/1.597581

[21] Rogers, D.W.O., Faddegon, B.A., Ding, G.X., Ma, C., *et al.* (1995) BEAM: A Monte Carlo Code to Simulate Radiotherapy Treatment Units. *Medical Physics*, **22**, 503-524. https://doi.org/10.1118/1.597552

[22] Wulff, J., Zink, K. and Kawrakow, I. (2008) Efficiency Improvements for Ion Chamber Calculations in High Energy Photon Beams. *Medical Physics*, **35**, 1328-1336. https://doi.org/10.1118/1.2874554

[23] Rogers, D.W.O., Walters, B. and Kawrakow, I. (2013) BEAMnrc Users Manual. National Research Council of Canada, Report PIRS-509(a) revL.

[24] Wang, L.L.W. and Rogers, D.W.O. (2008) Calculation of the Replacement Correction Factors for Ion Chambers in Megavoltage Beams by Monte Carlo Simulation. *Medical Physics*, **35**, 1747-1755. https://doi.org/10.1118/1.2898139

[25] Mattsson, L.O., Johansson, K.A. and Svensson, H. (1981) Calibration and Use of Plane-Parallel Ionization Chambers for the Determination of Absorbed Dose in Electron Beams. *Acta radiologica. Oncology*, **20**, 385-399. https://doi.org/10.3109/02841868109130228

[26] Nilsson, B., Montelius, A. and Andreo, P. (1996) Wall Effects in Plane-Parallel Ionization Chambers. *Physics in Medicine and Biology*, **41**, 609-623. https://doi.org/10.1088/0031-9155/41/4/003

[27] Cross, P. and Freeman, N. (1996) The Calibration of Plane Parallel Ionization Chambers for the Measurement of Absorbed Dose in Electron Beams of Low to Medium Energies. Part 1: The Nacp Chamber. *Australasian Physical and Engineering Sciences in Medicine*, **19**, 197-200.

[28] Cross, P. and Freeman, N. (1997) The Calibration of Plane Parallel Ionization Chambers for the Measurement of Absorbed Dose in Electron Beams of Low to Medium Energies. Part 2: The PTW/MARKUS Chamber. *Australasian Physical and Engineering Sciences in Medicine*, **20**, 117-120.

[29] Renaud, J., Sarfehnia, A., Marchant, K., McEwen, M., Ross, C. and Seuntjens, J. (2015) Direct Measurement of Electron Beam Quality Conversion Factors Using Water Calorimetry. *Medical Physics*, **42**, 6357-6368. https://doi.org/10.1118/1.4931970

[30] Buckley, L.A. and Rogers, D.W.O. (2006) Wall Correction Factors, Pwall, for Parallel-Plate Ionization Chambers. *Medical Physics*, **33**, 1788-1796. https://doi.org/10.1118/1.2199988

[31] Zink, K. and Wulff, J. (2008) Monte Carlo Calculations of Beam Quality Correction Factors k_Q for Electron Dosimetry with a Parallel-Plate Roos Chamber. *Physics in Medicine and Biology*, **53**, 1595-1607. https://doi.org/10.1088/0031-9155/53/6/006

[32] Zink, K. and Wulff, J. (2009) Positioning of a Plane-Parallel Ionization Chamber in Clinical Electron Beams and the Impact on Perturbation Factors. *Physics in Medicine and Biology*, **54**, 2421-2435. https://doi.org/10.1088/0031-9155/54/8/011

[33] Kuchnir, F.T. and Reft, C.S. (1992) Experimental Values for $P_{wall,x}$ and $P_{repl,E}$ for Five Parallel-Plate, Ion Chambers—A New Analysis of Previously Published Data. *Medical Physics*, **19**, 367. https://doi.org/10.1118/1.596910

[34] Kuchnir, F.T. and Reft, C.S. (1993) Experimental Determination of Fluence Perturbation Factors for Five Parallel-Plate Ionization Chambers. *Medical Physics*, 20, 331-335. https://doi.org/10.1118/1.597073

[35] McEwen, M., Palmans, H. and Williams, A. (2006) An Empirical Method for the Determination of Wall Perturbation Factors for Parallel-Plate Chambers in High-Energy Electron Beams. *Physics in Medicine and Biology*, **51**, 5167-5181. https://doi.org/10.1088/0031-9155/51/20/006

[36] Araki, F. (2008) Monte Carlo Calculations of Correction Factors for Plane-Parallel Ionization Chambers in Clinical Electron Dosimetry. *Medical Physics*, **35**, 4033-4040. https://doi.org/10.1118/1.2968102

[37] Wang, L.L.W. and Rogers, D.W.O. (2010) Replacement Correction Factors for Plane-Parallel Ion Chambers in Electron Beams. *Medical Physics*, **37**, 461-465. https://doi.org/10.1118/1.3276735

Phys. Med. Biol. **58** (2013) 3259–3282 doi:10.1088/0031-9155/58/10/3259

Difference in the relative response of the alanine dosimeter to megavoltage x-ray and electron beams

M Anton[1], R-P Kapsch[1], A Krauss[1], P von Voigts-Rhetz[2], K Zink[2] and M McEwen[3]

[1] Physikalisch-Technische Bundesanstalt, Bundesallee 100, D-38116 Braunschweig, Germany
[2] Institut für Medizinische Physik und Strahlenschutz (IMPS), University of Applied Sciences Giessen-Friedberg, Wiesenstr 14, D-35390 Giessen, Germany
[3] Ionizing Radiation Standards, National Research Council, Ottawa, Canada

E-mail: mathias.anton@ptb.de

Received 24 October 2012, in final form 14 March 2013
Published 24 April 2013
Online at stacks.iop.org/PMB/58/3259

Abstract

In order to increase the usefulness of the alanine dosimeter as a tool for quality assurance measurements in radiotherapy using MV x-rays, the response with respect to the dose to water needs to be known accurately. This quantity is determined experimentally relative to ^{60}Co for 4, 6, 8, 10, 15 and 25 MV x-rays from two clinical accelerators. For the calibration, k_Q factors for ionization chambers with an uncertainty of 0.31% obtained from calorimetric measurements were used. The results, although not inconsistent with a constant difference in response for all MV x-ray qualities compared to ^{60}Co, suggest a slow decrease from approximately 0.996 at low energies (4–6 MV) to 0.989 at the highest energy, 25 MV. The relative uncertainty achieved for the relative response varies between 0.35% and 0.41%. The results are confirmed by revised experimental data from the NRC as well as by Monte Carlo simulations using a density correction for crystalline alanine. By comparison with simulated and measured data, also for MeV electrons, it is demonstrated that the weak energy dependence can be explained by a transition of the alanine dosimeter (with increasing MV values) from a photon detector to an electron detector. An in-depth description of the calculation of the results and the corresponding uncertainty components is presented in an appendix for the interested reader. With respect to previous publications, the uncertainty budget had to be modified due to new evidence and to changes of the measurement and analysis method used at PTB for alanine/ESR.

1. Introduction

Dosimetry using alanine with read-out via electron spin resonance (ESR) is a convenient tool for quality assurance measurements for radiotherapy. The main reasons are the good

water-equivalence of alanine, the weak dependence on the irradiation quality, non-destructive read-out (different from thermoluminescence detectors) and the small size of the detectors.

Irradiation induces free radicals in the amino acid alanine. The radicals are stable: if the detectors are stored in a dry environment, the fading, i.e. the loss of radicals, is only of the order of a few parts in 10^3 per year, which makes them suitable for mailed dosimetry. The read-out is usually performed by ESR. Since the reading is not absolute, the ESR amplitude has to be calibrated.

Since the 1980s, alanine dosimetry has been used for (mailed) dosimetry for radiation processing, since the mid-nineties, the National Physical Laboratory (NPL, UK) (Sharpe *et al* 1996) and others (De Angelis *et al* 2005, Onori *et al* 2006) also have used alanine for mailed dosimetry in the therapy dose range, i.e. with doses lower than 10 Gy. Recently, advanced therapy modalities such as intensity modulated radiotherapy or the Cyberknife have been checked using alanine dosimetry (Budgell *et al* 2011, Garcia *et al* 2011). A large fraction of the Belgian therapy centres participated in a dosimetry audit using alanine/ESR (Schaeken *et al* 2011).

Several publications deal with the response of the alanine dosimeter to high-energy x-rays and megavoltage electrons, which are the radiation qualities for which the alanine dosimeter is best suited. The energy dependence is very weak. Between ^{60}Co (average photon energy 1.25 MeV) and 25 MV x-rays, the relative response of the alanine dosimeter varies by less than 1% (Sharpe 2003, Bergstrand *et al* 2003, Zeng *et al* 2004, Anton *et al* 2008). None of the listed publications gave evidence of a significant energy dependence for MV x-rays, which is why Sharpe (2003, 2006) from NPL suggested to use a common relative response of 0.994 for all MV qualities[4]. There were no contradictory results reported so far.

For electrons, the situation is similar, the most accurate measurements were published by the National Research Council (NRC, Canada) (Zeng *et al* 2004) and by the Swiss metrology institute METAS in cooperation with PTB (Vörös *et al* 2012). The results presented in these two publications agree (on average) within 0.1% and indicate that a common relative response of 0.988 for all megavoltage electron qualities will be appropriate, with an uncertainty of approximately 1%.

In spite of this apparent consensus situation we used the new electron accelerator facilities at PTB to determine the relative response of the alanine dosimeter for six qualities, namely 4, 6, 8, 10, 15 and 25 MV x-rays. The motivation for the new measurements was that more accurate values for the quality correction factor k_Q for ionization chambers are now available from measurements with the PTB water calorimeter, the uncertainty of the k_Q is 0.31% for all listed qualities. Due to the comparatively large number of measurements made and hence a small statistical uncertainty, a weak energy dependence, i.e. a small drop of the relative response for qualities with an accelerating voltage between 8 and 15 MV, could be identified.

In addition, data for 8 and 16 MV that had been published previously (Anton *et al* 2008) had to be revised. For 8 MV, there was no change apart from a slight increase of the uncertainty. The 16 MV value had to be corrected due to a wrong conversion factor that had been applied to the old data. A comparison between NRC and PTB is also reported; alanine dosimeter probes were irradiated at NRC and analysed at PTB. This was prompted by apparent discrepancies between the 25 MV results published by NRC (Zeng *et al* 2004) and our new data.

Monte Carlo simulations were carried out in order to find out whether the observed behaviour of the alanine dosimeter could be reproduced by the calculations. Zeng *et al* (2005) showed that it was necessary to use the density effect correction for crystalline alanine instead of

[4] This means that the dose determined by an alanine dosimeter—with a calibration using ^{60}Co—has to be multiplied by 1.006 in order to yield the correct dose. The uncertainty of Sharpe's data is 0.6%.

Table 1. Properties of the Harwell alanine pellets used.

Batch	Average mass (mg)	Diameter (mm)	Height (mm)	Density ($g\,cm^{-3}$)	CV (%)
AF594	59.4 ± 0.2	4.82 ± 0.01	2.8 ± 0.1	1.16	0.4
AJ598	59.8 ± 0.2	4.82 ± 0.01	2.7 ± 0.1	1.21	0.4
AL595	59.5 ± 0.2	4.82 ± 0.01	2.6 ± 0.1	1.25	0.3

a density effect correction for the alanine/paraffin mixture with the bulk density of the pellet in order to reproduce the relative response for high energy electrons. Therefore, calculations with the different density corrections were compared for the MV x-ray qualities under investigation. Additional simulations were made to determine some parameters of interest such as stopping power ratios, the mean secondary electron energy and electron ranges, which helped to explain the new results.

In an appendix, the uncertainty budget is detailed. This appeared necessary due to new evidence as well as to a slightly modified measurement and analysis method. Using the dose-normalized amplitude directly instead of a complete calibration curve saves several hours of measurement time per day and leads only to a moderate, but acceptable increase of the overall uncertainty. Details of the experimental results are also only given in the appendix. This will facilitate the reading of the main text, but will provide the interested reader with all the information necessary to follow the calculation of the results and their uncertainties. All uncertainties are standard uncertainties (coverage factor $k = 1$) and are determined according to the terms of reference stated in the *GUM*, the *Guide to the expression of uncertainty in measurement* (JCGM100 2008).

For the sake of simplicity, *dose* or *D* is to be understood as *absorbed dose to water* in the following, unless otherwise stated.

2. Materials and methods

2.1. Dosimeter probes

Alanine pellets with an addition of approximately 9% of paraffin as a binder, supplied by Harwell, were used. Their parameters are listed in table 1. The leftmost column lists the name of the batch. The following columns are the average mass in mg and the dimensions in mm. The rightmost column, denoted as CV (= coefficient of variation), quantifies the uncertainty of the intrinsic response, i.e. the signal per mass if the same dose is applied to different pellets of the same batch. This is due to variations of the composition. The CV value is usually specified by the supplier. An experimental verification for batch AL595 yielded the same CV of 0.3%. The uncertainty for an individual mass is estimated as $60\,\mu g$ and takes the loss of material due to handling for up to ten handling processes into account (see Anton 2005). Test pellets (irradiated in MV x-ray fields) and calibration pellets (irradiated in the ^{60}Co reference field) were always taken from the same batch.

One detector consists of a stack of four alanine pellets that has to be protected from the surrounding water. All detectors that were used for the determination of the relative response were irradiated in a polymethylmethacrylate (PMMA) holder fitting inside a watertight PMMA sleeve for a NE 2571 (Farmer) ionization chamber (see Anton 2006). A small additional set of detectors shrink-wrapped in polyethylene (PE) was irradiated. The detectors together with their holder are referred to as *probes*.

The two different probes are shown as schematic drawings (to scale) in figure 1. Panel (a) shows the detector with a Farmer holder and sleeve with a total PMMA wall thickness of 2 mm.

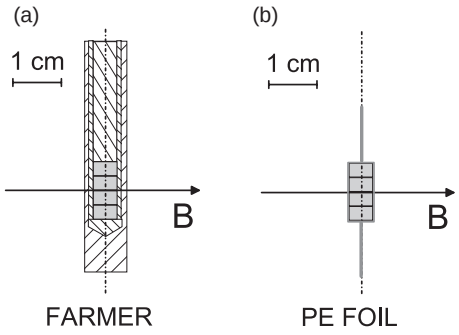

Figure 1. Different probes used—panel (a) detector with a PMMA holder fitting in a watertight sleeve for a Farmer chamber; panel (b) a detector shrink-wrapped in 0.2 mm strong PE foil. The capital B denotes the beam axis, the dash-dotted line indicates the symmetry axis of the detector.

Panel (b) shows a sketch of the PE foil probe. The thickness of the PE foil is 0.18–0.20 mm (photograph see Vörös *et al* 2012). A possible influence of the holder on the relative response of the alanine dosimeter was investigated for ^{60}Co, 4 and 25 MV radiation.

2.2. Irradiation in the reference fields of the PTB

2.2.1. Irradiations in the ^{60}Co *reference field.* The calibration probes were irradiated in the ^{60}Co reference field. The field size was 10 cm × 10 cm at the reference depth of 5 cm. The geometrical centre of the probes (see figure 1) was placed at the reference depth in a 30 cm × 30 cm × 30 cm cubic water phantom.

The contribution to the relative uncertainty of the delivered dose of 0.05% is due to positioning uncertainties. The lateral dose profile (in the plane perpendicular to the beam axis) over the volume of the alanine probe and over the sensitive volume of a Farmer chamber is flat, no correction and no additional uncertainty contribution had to be taken into account.

The relative uncertainty of the absorbed dose to water as determined with the PTB water calorimeter is 0.2% (Krauss 2006). Taking an additional small contribution for the source shutter into account led to a relative uncertainty of the delivered dose of 0.22%.

2.2.2. Irradiations in MV x-ray fields. Photon beams with nominal accelerating voltages of 4, 6, 8, 10, 15 and 25 MV were supplied by two *Elekta Precise* linear accelerators. Irradiations were performed at the reference depth of 10 cm in a cubic water phantom (30 cm edge length) with a source-surface distance of 100 cm. The field size was 10 cm × 10 cm at the reference depth. The dose rate at the reference depth was set to a value between 1 and 2 Gy min^{-1}. The tissue-phantom ratio TPR_{10}^{20} for each quality was determined experimentally.

All measurements performed at the linear accelerators are normalized to the reading of a large-area transmission ionization chamber which was calibrated every day via a secondary standard ionization chamber before *and* after the irradiations of the alanine pellets. In most cases, a Farmer NE 2571 chamber was used but for a few irradiations a watertight IBA FC65-G chamber was employed. For the reproducibility of the dose, an uncertainty component of 0.12% was estimated (see Krauss and Kapsch 2007).

For the individual ionization chambers used, quality correction factors k_Q had been determined using the water calorimeter. The uncertainty of the k_Q values for the 10 cm × 10 cm

Table 2. Non-uniformity correction: ratio of dose averaged over the volume of the four alanine pellets to the dose averaged over the volume of a Farmer chamber.

MV	$D_{\mathrm{det}}/D_{\mathrm{ic}}$	u	u_{indep}
4	1.0009	0.0001	0.0009
6	1.0002	0.0003	0.0008
8	1.0008	0.0001	0.0009
10	0.9980	0.0002	0.0013
15	1.0000	0.0001	0.0008
25	0.9984	0.0002	0.0010

field is 0.31%[5]. The uncertainty of the ^{60}Co calibration coefficient for the reference ion chambers NE 2571 and FC65-G is 0.25%.

For all MV beams used, the dose distribution in the reference depth in a plane vertical to the beam axis was measured. From these distributions, non-uniformity corrections were calculated by numerical integration over the sensitive volume of the ionization chamber and the alanine detector. The ratio $D_{\mathrm{det}}/D_{\mathrm{ic}}$ of the dose integrated over the alanine detector D_{det} and over the ionization chamber D_{ic} is listed in table 2. The absorbed dose as determined by the ionization chamber has to be multiplied by that ratio in order to obtain the absorbed dose for the alanine detector.

The uncertainty of this correction, due to positioning uncertainties of the probes, was determined using Monte Carlo methods. A positioning uncertainty of 1 mm in both directions perpendicular to the beam axis was assumed. The column u lists the resulting uncertainty of $D_{\mathrm{det}}/D_{\mathrm{ic}}$ for the usual case when both chamber and alanine were irradiated in the same sleeve. The column u_{indep} is required for the single case (15 MV, hl15 of 2012-01-26 in table A4) when ionization chamber and alanine were positioned independently, hence the index $_{\mathrm{indep}}$.

The uncertainty contribution from the depth determination was comparable to the one for the ^{60}Co field due to similar gradients of the depth dose curves.

2.2.3. Irradiation temperature. The irradiation temperature is an important influence quantity for alanine dosimetry and was registered with an uncertainty of 0.1 °C. Since it was only possible to measure the temperature of the surrounding water, a time delay of 10 min is usually inserted between the placing of the detector in the water and the beginning of the irradiation. For the measurements in the cobalt reference field and at the accelerators two different sensors were used.

2.3. ESR measurements and analysis

ESR measurements were performed usually one or two weeks after irradiation, using a Bruker EMX 1327 ESR spectrometer, with an 8″ magnet and an X-band microwave bridge. The high-sensitivity resonator ER 4119 HS was used throughout. The measurement parameters are listed in a previous publication (Anton 2006), which also contains a detailed description of the hardware and the evaluation method.

To a measured spectrum—which contains the signal contributions from both the irradiated alanine (ala) and from a reference substance (ref)—two base functions are fitted, thereby yielding the corresponding coefficients A^{ala} and A^{ref}. The base functions, one containing

[5] These results remain to be published in a separate paper. A similar uncertainty budget is detailed in the publication cited above (Krauss and Kapsch 2007), but for the k_Q-factors determined at the PTB's former linear accelerator.

a pure alanin signal, one containing the signal of the reference (plus background), are determined experimentally from spectra of unirradiated pellets and from spectra of alanine pellets irradiated in the ^{60}Co reference field to 25 Gy. Four to eight pellets with a dose of 25 Gy as well as the same number of unirradiated ones have to be measured on the same day as the test pellets. Examples for the base functions were displayed in previous publications (Anton 2005, 2006).

The readings from the four pellets making up one detector are averaged to yield the dose-normalized amplitude $\mathcal{A}_D$, which is defined as

$$\mathcal{A}_D = \frac{A_m}{\overline{m}} \cdot k_T \cdot \frac{\overline{m}^{\mathrm{b}}}{k_T^{\mathrm{b}}} \cdot D^{\mathrm{b}}. \tag{1}$$

The index b refers to the base function. $A_m = \overline{m} \sum A_i/m_i$ is the mass-normalized amplitude for one detector ($A_i = A^{\mathrm{ala}}/A^{\mathrm{ref}}$, $i = 1 \ldots n = 4$ pellets), $\overline{m}$ and $\overline{m}^{\mathrm{b}}$ are the average masses of test and base function detectors, respectively, and k_T and k_T^{b} are the corresponding temperature correction factors (temperature correction coefficient taken from Krystek and Anton (2011)).

Usually, the dose-normalized amplitude (1) serves to set up a calibration curve with a resulting measurement function (Anton 2006)

$$D^{\mathrm{c}} = N \cdot \mathcal{A}_D + D_0. \tag{2}$$

The upper index c is used to distinguish the calculated dose D^{c} from the delivered dose D. Ideally, we would have $N = 1, D_0 = 0$ due to the definition of $\mathcal{A}_D$. This ideal measurement curve is implicitly assumed if $\mathcal{A}_D$ is identified with D^{c}. Compared to measurements using a complete calibration curve, direct use of $D^{\mathrm{c}} = \mathcal{A}_D$ reduces the time required for calibration by at least 2 h per day. The price to pay for the reduced measurement time is a slightly higher uncertainty. The measurement results presented below contain data evaluated with an explicit calibration curve as well as data where $D^{\mathrm{c}} = \mathcal{A}_D$ was used directly (which method was used for which dataset is explained in section A.3).

2.4. The relative response

From the determined dose D^{c} and the known value of the delivered dose D, an empirical value r of the relative response is simply

$$r = \frac{D^{\mathrm{c}}}{D}. \tag{3}$$

Due to the calibration as described (^{60}Co base, ^{60}Co calibration curve, ionization chamber calibrated to indicate dose to water for the quality under consideration), r represents the relative response with respect to the dose to water, relative to ^{60}Co-radiation. The response thus determined is dependent not only on the material but also on the geometry of the detector. The correction factors for alanine detector arrangements with a completely different geometry (different size, more massive holder) may differ from the values presented in this study.

In order to determine a reliable value $\langle r \rangle_Q$ for the relative response for every quality Q, several separate values $r_{j,Q}$ were obtained (the subscript $_Q$ is dropped for the sake of simplicity in the following). Between $n_j = 4$ and $n_j = 9$ values were produced for every quality. Every value r_j is obtained from one irradiation set, i.e. a set of test probes, comprising $n_i = 3 \ldots 8$ detectors irradiated to dose values between 5 and 20 Gy on the same day, plus some irradiated detectors required for the calibration as outlined above. The determination of $\langle r \rangle$ as well as the uncertainty budget are detailed in the appendix.

Table 3. Relative response of alanine to MV x-rays. Columns from left to right: nominal accelerating voltage in MV; tissue-phantom ratio TPR_{10}^{20}; dose-to-water response relative to ^{60}Co-radiation $\langle r \rangle$; the uncertainty component u or u_{mod} from (A.1) or (A.6) (see appendix), the combined uncertainty $u(\langle r \rangle)$ including the uncertainties of the calibration factor and k_Q for the ionization chambers; square sum of residuals q^2 from (A.5); number of datasets n_j; finally whether the q^2 criterion was satisfied.

	MV	TPR_{10}^{20}	$\langle r \rangle$	u or u_{mod}	$u(\langle r \rangle)$	q^2	n_j	$q^2 < n_j - 1$?
	4	0.638	0.9953	0.0010	0.0036	2	4	y
	6	0.683	0.9970	0.0007	0.0035	6.5	9	y
	8	0.714	0.9958	0.0022	0.0041	9.8	5	n
(2008 rev.)	8	0.716	0.9959	0.0022	0.0041	4.8	4	n
	10	0.733	0.9940	0.0011	0.0036	10.0	8	n
	15	0.760	0.9890	0.0011	0.0036	2.9	6	y
(2008 rev.)	16	0.762	0.9908	0.0010	0.0035	0.1	4	y
	25	0.799	0.9893	0.0012	0.0036	7.9	7	n

3. Results and discussion

3.1. Experimental results

The results of each individual irradiation and measurement set j are listed in tables A3 and A4 of section A.3. The final result $\langle r \rangle$, the relative response averaged over all n_j data sets obtained for a specific quality, is shown in table 3. The leftmost column lists the nominal accelerating voltage in MV, the following column represents the tissue-phantom ratio TPR_{10}^{20}. The third column contains $\langle r \rangle$, the following column lists u or u_{mod} according to equations (A.4) and (A.6), respectively. The combined uncertainty $u(\langle r \rangle)$ contains also the uncertainty of the calibration of the ionization chamber and the uncertainty of the quality correction factors k_Q for each quality. The values of the parameter q^2 (A.5) and the number of datasets n_j are displayed in the following columns, the rightmost column indicates whether the consistency criterion according to (A.5) was satisfied (y) or not (n). If not, u_{mod} according to equation (A.6) was used instead of u from (A.4) as the uncertainty of the weighted mean, which was the case for 8, 10 and 25 MV[6]. Only for 8 MV u_{mod} was significantly larger than u. However, the effect is not dramatic for the overall uncertainty $u(\langle r \rangle)$.

In addition to the new measurements, the results that had been published earlier (Anton *et al* 2008) had to be revised. They are also contained in table 3 and labelled (2008 rev.). There is no change in the old 8 MV data, the published value was 0.9959 which is identical to the revised result. The uncertainty turned out to be higher than previously published, the new value is 0.0041 whereas the published value was 0.0028. One of the main reasons for this increase is that the uncertainty contributions from the intrabatch homogeneity and the calibration factor of the ionization chamber had been erroneously omitted. The situation is more dramatic for the 16 MV data, the response changed from the published value 0.9967 ± 0.0027 to the revised value of 0.9908 ± 0.0035. The value of the published 16 MV response was in error, due to an incorrect conversion factor that had been used. The reasons for the modified uncertainty are the same as for the 8 MV value.

The data from table 3 are displayed in figure 2 as a function of the tissue-phantom ratio. The reference, ^{60}Co-radiation, is represented by the filled circle. Filled triangles indicate the

[6] This was already the case for the 8 MV data published earlier (Anton *et al* 2008). There is still no evidence as to which of the uncertainty components might be underestimated. A significant amount of work was invested in testing different options. Reporting all these attempts to identify the unknown source(s) would be outside the scope of this publication.

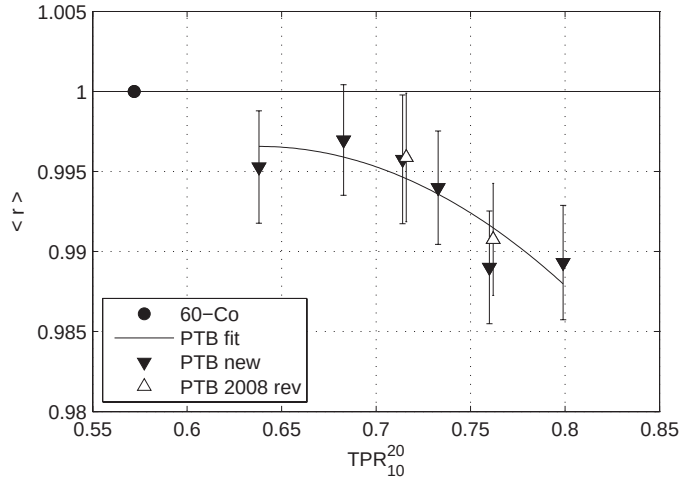

Figure 2. The relative response $\langle r \rangle$ and its uncertainty as a function of TPR^{20}_{10}. The reference ^{60}Co is indicated by the filled circle, the new data are represented by the filled triangles. The revised values of our 2008 data are added as open triangles. The fit curve is only shown to guide the eye and for later comparisons.

Table 4. Mean ratio $\mathcal{R}_{\mathrm{PE,Farmer}}$ as defined in (4) and its uncertainty for three different radiation qualities Q.

Q	$\mathcal{R}_{\mathrm{PE,Farmer}}$	$u(\mathcal{R}_{\mathrm{PE,Farmer}})$
^{60}Co	0.9997	0.0016
4 MV	0.9993	0.0019
25 MV	1.0014	0.0018

new values, open triangles represent the revised 2008 data. The error bars correspond to $u(\langle r \rangle)$ according to table 3. A parabolic curve which was obtained by a least-squares fit to the data is also shown, only to guide the eye. For the lower energies, the response values are consistent with the recommendation of Sharpe while the value for the highest energy is interestingly similar to the value obtained for the response to high-energy (MeV) electrons (Vörös *et al* 2012).

3.2. Comparison of different holders

For three qualities, namely ^{60}Co, 4 and 25 MV, several detectors were irradiated with doses between 10 Gy and 25 Gy, but in two different holders. One was the Farmer holder with a wall thickness of 2 mm, the other one was a shrink-wrapping with 0.2 mm PE (see figure 1). A weighted mean $\langle \mathcal{A}_D/D \rangle$ was calculated for three to four detectors per holder and quality. The uncertainties have been estimated as described in the appendix. The results are summarized in table 4: for each quality the mean ratio

$$\mathcal{R}_{\mathrm{PE,Farmer}} = \frac{\langle \mathcal{A}_D/D \rangle_{\mathrm{PE}}}{\langle \mathcal{A}_D/D \rangle_{\mathrm{Farmer}}} \tag{4}$$

and its uncertainty are given for the three qualities under consideration.

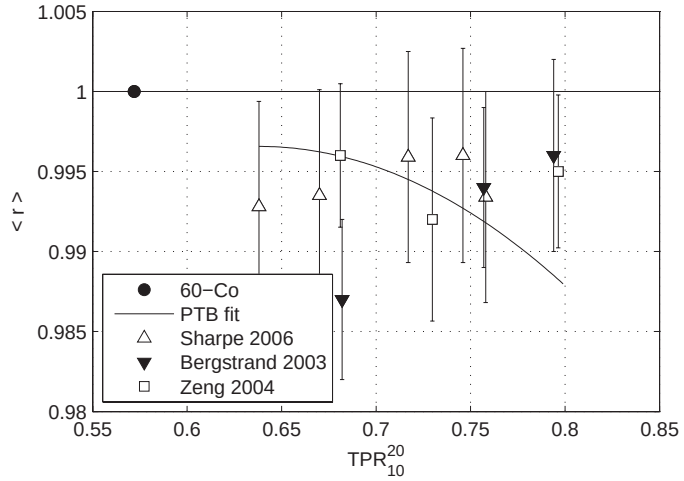

Figure 3. The relative response and its uncertainty as a function of TPR^{20}_{10}. The reference ^{60}Co is indicated by the filled circle. For the sake of clarity, the new PTB data are represented by the fit curve only. Open triangles: NPL, Sharpe (2006) with only approximate TPR values; filled triangles: Bergstrand *et al* (2003); open squares: Zeng *et al* (2004).

Within the limits of uncertainty, no influence of the holder can be discerned. Since the PE foil probe is a very good approximation to using the alanine detector without any holder at all, we concluded that it would be justified to neglect the holder in the Monte Carlo simulations (see section 4). This conclusion may not be valid if a more massive holder (i.e. wall thickness >2 mm) were to be used, although McEwen *et al* (2006) showed that no holder effect was seen in MeV electron fields for sleeve thicknesses up to 4 mm .

3.3. Comparison to other experimental data

For the sake of clarity, the fit curve shown in figure 2 is also used to compare the new results to the results of other authors. In figure 3, published data by Bergstrand *et al* (2003), Zeng *et al* (2004) and by Sharpe (2006) are displayed.

The data from Bergstrand *et al*, which are indicated by the filled triangles, show a trend which is just the inverse of what our new measurements seem to indicate, albeit with the largest uncertainties. The NRC data from Zeng *et al* which are indicated by the open squares and the NPL data which are represented by the open triangles are consistent with the proposal by Sharpe (2006) to use a constant, energy independent response of 0.994 for the whole range of MV therapy qualities.

3.4. NRC—new data and revised results

The systematic nature of the deviation between the new PTB data and those presented in the literature—increasing to ≈0.6% at 25 MV—is grounds for further investigation. Therefore, alanine pellets were irradiated by NRC in the spring of 2012 and evaluated by PTB. The data set comprised four sets of test detectors, one for ^{60}Co-irradiation and one for each of the three nominal voltages of 6, 10 and 25 MV that are available at the NRC's *Elekta Precise* accelerator. Irradiations at NRC were carried out in a similar way as at PTB using a watertight PMMA sleeve for the detector, i.e. a stack of four pellets. For each quality, $n_i = 3$ to $n_i = 4$ detectors

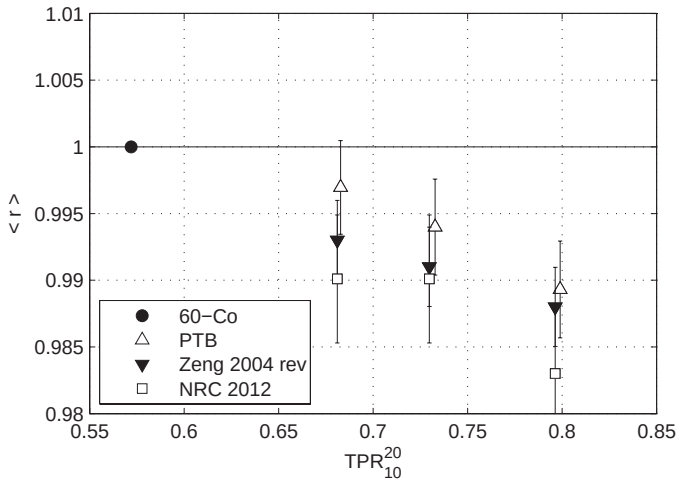

Figure 4. The relative response and its uncertainty as a function of TPR_{10}^{20}. The reference ^{60}Co is indicated by the filled circle. The PTB data are represented by the open triangles. The data obtained using probes irradiated at NRC and evaluated at PTB are represented by the open squares. The revised data from Zeng *et al* (2004) are shown as filled triangles. Error bars indicate the standard uncertainties including the primary standard(s).

Table 5. Relative response values for alanine detectors irradiated at NRC in May 2012 and analysed at PTB.

Quality	TPR_{10}^{20}	n_i	n_c	r_j	$u(r_j)$
^{60}Co	0.572	4	5	0.9999	0.0047
6 MV	0.681	4	5	0.9901	0.0048
10 MV	0.730	3	5	0.9901	0.0048
25 MV	0.796	3	5	0.9830	0.0048

were irradiated with doses of approximately 10, 15 and 20 Gy. Doses were derived from a reference ionization chamber calibrated against the NRC primary standard water calorimeter.

Evaluation and analysis were carried out as outlined above. The results are summarized in table 5. The leftmost column lists the quality. In the next column, the tissue-phantom ratio is given, and n_i and n_c are the number of test- and calibration detectors. The uncertainties were determined as explained in the appendix. They are slightly higher than for the data where irradiation and analysis were both carried out at PTB because two different primary standards are now involved.

From the key comparison BIPM.RI(I)-K4 (absorbed dose to water, primary standards) it was expected that the ^{60}Co-irradiated probes would exhibit a slightly lower signal if evaluated with calibration probes irradiated at PTB (to be precise, a difference of 0.19% was expected). Indeed, the dose ratio ($r_j = 0.9999$) was consistent with this value within the combined standard uncertainty of 0.47%.

The MV data tabulated in table 5 are displayed in figure 4 as open squares. All response values lie below the PTB data for the corresponding qualities which are displayed as open triangles. There is no significant contradiction in view of the uncertainties. If the data in table 5 are compared to the corresponding data in tables A3 and A4, only for 6 MV, the measured value is outside the range of observations at PTB, but still within the limits of uncertainty. Surprisingly the NRC value of r_j is now less than the PTB value at all energies.

Table 6. Relative response for alanine, values as published by Zeng *et al* (2004) and revised values using new k_Q corrections and uncertainties.

		Published		Revised	
Quality	TPR_{10}^{20}	$\langle r \rangle$	u_r in %	$\langle r \rangle$	u_r in %
^{60}Co	0.572	1		1	
6 MV	0.681	0.996	0.45	0.993	0.30
10 MV	0.730	0.992	0.65	0.991	0.30
25 MV	0.796	0.995	0.48	0.988	0.30

Due to this unexpected result, the data published by Zeng *et al* (2004) was revisited and it was found that different k_Q data had been used for the reference ion chamber than had been used for the 2012 irradiations. The high-precision k_Q data presented in McEwen (2010) was not available at the time of the Zeng *et al* irradiations. The revised data are listed along with the published ones in table 6 and displayed as filled triangles in figure 4 (compare figure 3). The revised values are shifted to slightly lower values. The most pronounced change is observed for the 25 MV response which now agrees very well with the new PTB data. In summary, NRC and PTB data appear to agree better than expected from the published data alone. The somewhat higher deviation of the new set of measurements can not be considered a severe problem since the data are equivalent to just one r_j measurement (according to the nomenclature defined in the appendix) whereas the revised published data as well as the measurements presented in this paper represent weighted averages $\langle r \rangle$ over at least 4 r_j-values.

To complete this discussion, one should also consider the potential differences between the NRC and PTB standards in high-energy linac beams, which could speak to the apparent difference between the two laboratories indicated in figure 4. In the both the PTB and NRC irradiations, a calibrated NE2571 ion chamber was used to determine the dose delivered to the alanine pellets and therefore there are a number of sources we can refer to in determining the NRC/PTB dose ratio. Aalbers *et al* (2008) collated k_Q data from a larger number of investigations (but not PTB) and showed that the NRC data were consistent with an unweighted fit of all data at the 0.2% level for 6, 10, and 25 MV beams. Muir *et al* (2011) analysed unpublished data from a large inter-laboratory comparison (including PTB) and showed again that the NRC results were consistent with the global fit (figure 1 of that paper). Although the other lab's results were anonymous it can be seen that there are no significant outliers and therefore one can conclude that the PTB and NRC results are consistent at the 0.3% level. A final comparison is possible through the recently-initiated BIPM.RI(I)-K6 program, where each laboratory's dose standard is compared directly with the BIPM graphite calorimeter. Results for both NRC and PTB are available (Picard *et al* 2010, 2011) and these indicate agreement between the two laboratories within the stated uncertainties. Combining these results one can conclude that the data represented in figure 4 are not sensitive at the 0.3% level to the specific primary standards operated at the two laboratories.

4. Monte Carlo simulations

The apparent decrease in the relative response of alanine for $TPR_{10}^{20} > 0.72$ was unexpected and the literature, based on either Monte Carlo or experimental results (Zeng *et al* 2004, Anton 2006), provided no satisfactory explanation. However, the fact that the asymptotic value of the response for higher energies approaches the one observed for electrons gave a hint towards a

possible explanation: Zeng *et al* (2005) stated in their publication on the relative response of alanine to MeV electron radiation that it was necessary to take the density correction for the crystalline alanine into account. This is justified by the fact that the interactions which produce the free radicals necessarily take place within the alanine microcrystals. In the publication by Vörös *et al* (2012), the density correction for crystalline alanine was also successfully applied but was not explicitly mentioned.

The simulations presented in this work were carried out at the Institut für Medizinische Physik und Strahlenschutz-IMPS (University of Applied Sciences Giessen-Friedberg, Germany) using the EGSnrc package with the user code DOSRZnrc (Kawrakow 2000, Kawrakow *et al* 2010). With DOSRZnrc, the geometry is simplified assuming cylindrical symmetry about the beam axis. The dose scoring volume with a radius and a depth of 5 mm, representing the alanine detector, was placed inside a cylindrical water phantom with a radius of 20 cm and a depth of 30 cm. The geometrical centre of the scoring volume was placed 5 cm behind the phantom surface for the ^{60}Co simulations and 10 cm behind the surface for the MV x-rays. Parallel beams were assumed for the simulation.

For the ^{60}Co reference field, the spectrum was obtained from a MC simulation, taking the realistic geometry of the irradiation source and its surroundings into account. A BEAMnrc (Rogers *et al* 2004) simulation carried out at PTB of one of the *Elekta* accelerators provided the spectra for 6 and 10 MV. For 8 and 16 MV, published spectra had been modified to reproduce the experimental depth dose curves (see Anton *et al* 2008). For the 25 MV beam, a spectrum published by Sheikh-Bagheri and Rogers (2002) was used. For 4 MV, no spectrum was available.

4.1. Simulation of the relative response

For each of the qualities ^{60}Co, 6, 8, 10, 16 and 25 MV, the calculation was carried out three times: the first one for a dose scoring volume made of water to obtain D_W; the second and third one with a dose scoring volume consisting of a homogeneous mixture of the atomic constituents of the alanine/paraffin pellets, in order to obtain D_{ala}. Two separate sets for D_{ala} were obtained, one taking the density correction for crystalline alanine into account, the other one using a density correction for the bulk density of the pellets. The calculations were performed with threshold/cut-off energies for the particle transport set to ECUT = AE = 521 keV and PCUT = AP = 1 keV and continued until a preselected statistical uncertainty was achieved. For the other parameters of the simulation, the default settings of DOSRZnrc were used. For each quality, the ratio(s) D_{ala}/D_W were then calculated and referred to the corresponding ratio for ^{60}Co, i.e. r_Q^{MC}, the simulated dose-to water response for the quality Q, relative to ^{60}Co, is given as

$$r_Q^{MC} = \frac{(D_{ala}/D_W)_Q}{(D_{ala}/D_W)_{Co}}. \tag{5}$$

The results are displayed in figure 5 along with the previously-shown fit curve to the new PTB data. The results of the DOSRZnrc simulation with the density correction for the bulk density are represented by the open circles whereas the results obtained using the density correction for the crystalline alanine are displayed as filled squares. The error bars indicate the statistical uncertainties. TPR_{10}^{20} values were obtained from simulated depth-dose curves. The data obtained using the bulk density correction are approximately unity and inconsistent with any published experimental results. Within the limits of uncertainty, simulated data using the crystalline alanine density corrections and measured data agree very well. Although this had been pointed out by Zeng *et al* (2005) for MeV electrons already, this finding is new for MV x-rays.

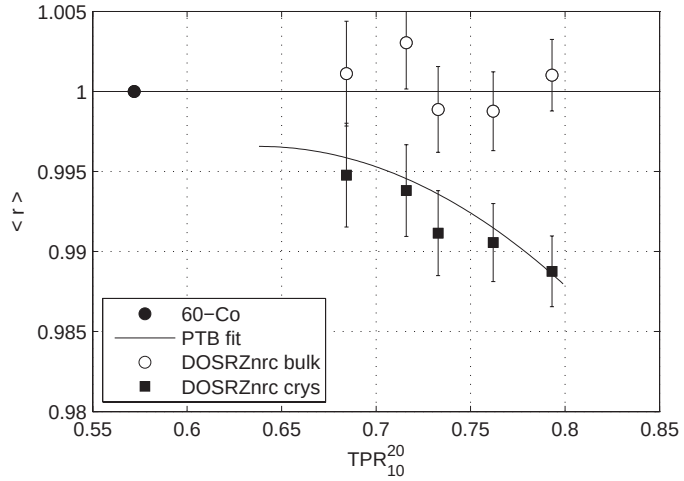

Figure 5. The relative response and its uncertainty as a function of TPR^{20}_{10}. The reference ^{60}Co is indicated by the filled circle. The measured data are represented by the continuous fit curve. MC results obtained using the bulk density correction are shown as open circles, the results obtained using the density correction for crystalline alanine are indicated by the filled squares. The error bars represent the statistical uncertainties.

4.2. Further considerations concerning the possible energy dependence

With the aim to understand the apparent decrease of the relative response of the alanine dosimeter with increasing photon energy, further investigations were made using the MC method.

From the photon spectra that were used for the MC simulations, the spectra in 5 cm depth (Co) and in 10 cm depth (MV x-rays) were calculated using the absorption coefficients compiled and published by the National Institute of Standards and Technology (NIST, USA) based on the publications by Seltzer (1993) and Hubbell (1982). From the attenuated spectra, the average mass energy absorption ratios for alanine and water were determined. The $(\mu_{en}/\rho)_{ala,W}$-ratio is listed in table 8 and displayed in figure 6 as a function of TPR^{20}_{10} (filled circles). With the help of the user codes SPRRZnrc and FLURZnrc from the EGSnrc package, the stopping power ratios $s_{ala,W}$ and the mean electron energies E_{av} in water were also calculated. In table 8 and figure 6, two sets of data for $s_{ala,W}$ are supplied, one using the density correction for the crystalline alanine (designated by *crystal*) the second one using the bulk density of the pellets (designated by *bulk*). The latter are indicated by the open triangles in figure 6, the former are displayed as filled triangles. From the mean secondary electron energy E_{av} listed in table 8, the corresponding electron ranges in the continuous slowing down approximation (CSDA) for the medium water and for alanine (using the same value for the mean energy) were obtained using the NIST/ESTAR database (Berger *et al* 2005) available at the web site of NIST[7]. The CSDA ranges are also given in table 8, converted from g cm^{-2} to cm using the density of water and of alanine (1 and 1.4 g cm^{-3}, respectively).

Finally, we repeated the DOSRZnrc calculation with alanine (crystalline density correction) and with water as a detector material, but with the parameter ECUT set to a value larger than the maximal photon energy *outside* the detector volume. This means all electrons

[7] The stopping powers obtained from the NIST/ESTAR database as well as the density corrections in the EGSnrc software are calculated according to ICRU Report 37 (ICRU 1984).

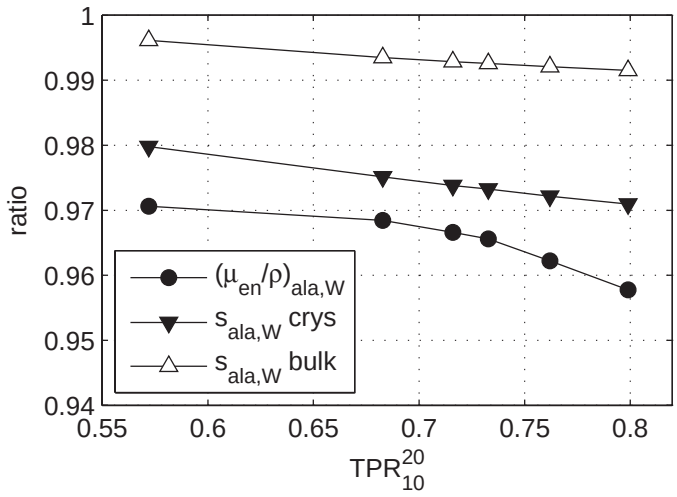

Figure 6. Ratios of mass-energy-absorption coefficients and stopping power ratios for alanine and water. Filled circles: $(\mu_{en}/\rho)_{\mathrm{ala},W}$; filled triangles: $s_{\mathrm{ala},W}$, density correction for crystalline alanine; open triangles: $s_{\mathrm{ala},W}$, density correction for bulk density of the pellet. Lines are shown to guide the eye.

generated outside are not transported and therefore cannot enter the detector volume. We then calculated the ratio of the absorbed dose inside the scoring volume with ECUT = 521 keV inside and with ECUT larger than the maximal photon energy on the outside to the absorbed dose with ECUT = 521 keV everywhere (see the results from the previous section). This yielded the *fraction of the absorbed dose* which is due to the secondary electrons generated by *photon interactions inside* the detector. This fraction is denoted as f_γ in table 8. The values listed are average values for alanine and water as a detector material. For ^{60}Co-radiation, 76% of the dose to the detector are due to secondary electrons that were generated by photon absorption inside the detector volume whereas for the highest energies about 80% of the dose are due to secondary electrons generated outside the detector volume. Speaking in terms of Bragg–Gray theory, the alanine probe becomes an electron probe for the highest voltages. Thus, for the higher energies the relative response should be determined almost exclusively by the stopping power ratio $s_{\mathrm{ala},W}$ and it should approach the value for electrons, which is the case for the experimental data as well as for the simulated ones.

In addition to the photon qualities investigated, the corresponding relevant parameters were also determined for two electron beams with maximum energies of 6 MeV and 18 MeV, using spectra published by Ding *et al* (1995). The parameters obtained for the two electron beams confirm the transition to an electron detector for the higher photon energies as mentioned above, as can be seen by comparing the data in table 8 and in figure 7.

However, it is important to keep in mind that the response thus determined is dependent not only on the material but also on the geometry of the detector. The correction factors for alanine detector arrangements with a completely different geometry (e.g. for much larger detectors or for alanine film dosimeters) may differ from the values presented in this study.

From figure 6 two important facts can be immediately deduced: first, both the $(\mu_{en}/\rho)_{\mathrm{ala},W}$-ratio as well as the stopping power ratio $s_{\mathrm{ala},W}$ *for the crystalline alanine density correction* decrease by approximately 1% between ^{60}Co and 25 MV. Therefore, the observed decrease of the relative response should not be so surprising after all. Second, if we take the ratio as

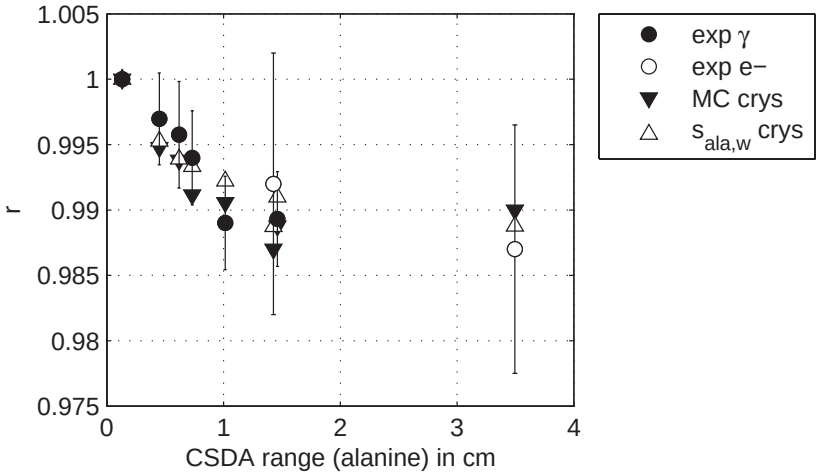

Figure 7. Relative response as a function of the CSDA range in alanine with a density of 1.4 g cm^{-3}, in cm. Filled circles with error bars: experimental data, this work; open circles with error bars: Vörös *et al* (2012) for electrons; filled triangles: MC simulation with density correction for crystalline alanine; open triangles: stopping power ratios $s_{\mathrm{ala},W}$ relative to cobalt, density correction for crystalline alanine.

Table 7. Monte Carlo simulation using DOSRZnrc: for each quality Q the tissue-phantom ratio TPR_{10}^{20} is given along with the simulation results, the ratio $D_{\mathrm{ala}}/D_{\mathrm{W}}$ of the dose to alanine to the dose to water, its relative (statistical) uncertainty and the resulting value of r_Q^{MC}. The left block of data was obtained using the density of crystalline alanine for the density correction, the right block was obtained using the bulk density of the pellets.

		Density of crystalline alanine				Density of pellet bulk			
Q	TPR_{10}^{20}	$D_{\mathrm{ala}}/D_{\mathrm{W}}$	u_r in %	r_Q^{MC}	$u(r_Q^{\mathrm{MC}})$	$D_{\mathrm{ala}}/D_{\mathrm{W}}$	u_r in %	r_Q^{MC}	$u(r_Q^{\mathrm{MC}})$
^{60}Co	0.567	0.9735	0.14			0.9749	0.14		
6 MV	0.660	0.9684	0.30	0.9948	0.0032	0.9760	0.30	1.0011	0.0033
8 MV	0.716	0.9675	0.25	0.9938	0.0029	0.9779	0.26	1.0030	0.0029
10 MV	0.733	0.9649	0.23	0.9911	0.0027	0.9739	0.23	0.9989	0.0027
16 MV	0.762	0.9643	0.21	0.9906	0.0024	0.9737	0.21	0.9988	0.0025
25 MV	0.793	0.9625	0.18	0.9888	0.0022	0.9759	0.18	1.0010	0.0022

approximations to D_{ala}/D_w, both $(\mu_{\mathrm{en}}/\rho)_{\mathrm{ala},W}$ and $s_{\mathrm{ala},W}$ values for cobalt are very close to the D_{ala}/D_w from the MC simulation, as can be seen from table 7. The stopping power ratio obtained using the bulk density correction is more than 2% too high, furthermore the decrease with increasing energy is weaker than for the crystalline density correction. This underlines the conclusion from the previous section that for simulations of the response of the alanine dosimeter to MV x-rays, the use of the density correction for crystalline alanine is absolutely essential.

In figure 7 the relative response is displayed as a function of the CSDA range (in alanine) from table 8. Experimental photon data are represented by filled circles with error bars. Two values for electrons have been added, the experimental data are from Vörös *et al* (2012): the 6 MeV point was directly measured, the 18 MeV point is interpolated between the 16 MeV and the 20 MeV measurements from the cited paper. The experimental electron data are shown as open circles with error bars. The results of the MC simulation are represented by the filled

Table 8. Some parameters for the simulated radiation qualities: ratio of mass-energy absorption coefficients $(\mu_{en}/\rho)_{ala,W}$; stopping power ratios $s_{ala,W}$ obtained from SPRRZnrc using the two different density corrections (pellet bulk density and density of crystalline alanine); mean energy E_{av} of the secondary electrons obtained from the electron fluence spectrum using FLURZnrc and a water detector; the CSDA range in water and alanine for the given mean energies; finally the fraction f_γ of the dose due to photon interactions inside the detector volume.

Q	TPR_{10}^{20}	$(\frac{\mu_{en}}{\rho})_{ala,W}$	$s_{ala,W}$ crystal	$s_{ala,W}$ bulk	E_{av} MeV	CSDA range water in cm	CSDA range ala in cm	f_γ
^{60}Co	0.572	0.971	0.980	0.996	0.4	0.13	0.09	0.76
6 MV	0.683	0.968	0.975	0.993	1.0	0.44	0.32	0.46
8 MV	0.716	0.967	0.974	0.993	1.3	0.60	0.44	0.38
10 MV	0.733	0.966	0.973	0.993	1.5	0.71	0.52	0.34
16 MV	0.762	0.962	0.972	0.992	2.0	0.98	0.73	0.27
25 MV	0.799	0.958	0.971	0.992	2.8	1.41	1.04	0.19
6 MeV	–	–	0.969	0.991	2.7	1.35	1.00	–
18 MeV	–	–	0.969	0.990	6.6	3.35	2.49	–

triangles, the data are the same as in the previous section, with the crystalline alanine density correction. In addition, the stopping power ratio $s_{ala,W}$ relative to its value for ^{60}Co radiation is also shown.

If the CSDA range is greater than two to three times the depth of the detector which is approximately 0.5 cm, the relative response remains constant. The ratio of the stopping power ratios for both electron energies to the stopping power ratio for cobalt radiation is 0.988 (from table 8), which is identical to the average value for the relative response published by Vörös *et al* (2012).

As a conclusion, it may be stated that the energy dependence of the alanine dosimeter can be understood from the well known ratios of the mass energy absorption coefficients and the stopping power ratios for alanine and water, provided the density correction for the crystalline alanine is taken into account.

5. Summary and outlook

In order to increase the usefulness of the alanine dosimeter as a tool for quality assurance measurements in radiotherapy using MV x-rays, the response with respect to the dose to water needs to be known accurately. This quantity was determined relative to the reference quality ^{60}Co for six different qualities, namely 4, 6, 8, 10, 15 and 25 MV x-rays from clinical accelerators. The measurement series was motivated by the availability of new k_Q factors for ionization chambers with an uncertainty of 0.31% obtained from calorimetric measurements.

The measurement results seem to favour a slow decrease of the relative response from approximately 0.996 for the lower energies to 0.989 for the highest energy, 25 MV. The relative uncertainty achieved varies between 0.35% and 0.41%. The modified uncertainty budget, necessitated by new evidence as well as by a slight change in methodology is detailed in the appendix. The measured data and their uncertainties would be consistent with the assumption of an energy independent relative response of 0.993, which is in accordance with the results published by other authors. However, there are some arguments in favour of a slow decrease as observed.

Published data from NRC (Zeng *et al* 2004) have been revised using more recently available new k_Q values determined at the NRC with a lower uncertainty (McEwen 2010). The revised results agree very well with the measurement results from PTB, i.e. they also exhibit a slow decrease with increasing energy instead of remaining constant.

Monte Carlo simulations using a density correction for crystalline alanine yielded very good agreement between measured and simulated response data. This is not the case if the density correction for the bulk density of the pellet is used, as was demonstrated previously by Zeng *et al* (2005) for MeV electron radiation and confirmed by the results of Vörös *et al* (2012). This is a new result for megavoltage x-rays.

The relative response for 25 MV agrees within 0.1% with the measured and the simulated value of 0.988 for MeV electrons (Vörös *et al* 2012). This appears logical if one considers that the fraction of the dose due to secondary electrons generated within the detector volume decreases from 76% for ^{60}Co to 19% for 25 MV x-rays, i.e. the alanine dosimeter is more of a photon probe for ^{60}Co but mainly an electron probe for 25 MV, speaking in terms of Bragg–Gray theory. The fraction was also determined using Monte Carlo simulation.

In fact two different quantities are contrasted if r_Q^{MC} is compared directly to the experimental data $\langle r \rangle$: the MC simulation yields a ratio of absorbed dose values whereas the experimental data are ratios of (detected) free radical concentrations. The ratios are equal if the free radical yield, i.e. the number of free radicals generated per absorbed dose, is equal for all qualities under consideration. One could potentially combine the experimental and MC data to determine a value for the free radical yield but the overall combined uncertainty would be too large to make this a worthwhile exercise.

In summary, one may state that both the measured and the simulated data suggest that the dose-to-water response of the alanine dosimeter relative to ^{60}Co radiation decreases from $\approx$0.996 for the MV x-ray qualities with the lowest energies to a value almost equal to the relative response to MeV electrons for the highest voltages. This behaviour is well understood in terms of the stopping power ratios or the ranges of the secondary electrons, provided the density correction for the crystalline alanine is taken into account. Although, a pragmatic approach would be to use an energy-independent correction factor of 1.007 for the difference between ^{60}Co and MV photons this discards the theoretical insight that there is a slow transition from a photon detector to an electron detector. As noted earlier, for significantly different geometries of detector this transition could be very different with no 'simple' offset observed.

While bridging the gap between MV photons and MeV electrons is a very interesting result, some work remains to be done, especially concerning the response of the alanine dosimeter for the small fields employed in modern radiotherapy: the change of the radiation quality with field size may have an influence, as well as the material of the surroundings, if one aims at the verification of treatment plans in anthropomorphic phantoms. However, this will be the subject of future studies.

Acknowledgments

We wish to thank T Hackel, D-M Boche, C Makowski, K-H Mühlbradt, M Schrader and O Tappe (PTB) for their help during preparation, irradiation and measurements. We also thank J Illemann (PTB) for providing the BEAM-simulations for the *Elekta* accelerator. Thanks are due to M Krystek (PTB) for many helpful discussions as well as for having a critical eye on the uncertainty budget. Thanks are also due to P Sharpe (NPL) for providing the NPL response data as well as for helpful discussions. Inspiring discussions with V Nagy (AFRRI, USA) are also gratefully acknowledged. A part of the research presented here has received funding from

the European Commission (EC) according to the EC grant agreement no. 217257 from the Seventh Framework Programme, ERA-NET Plus.

Appendix. Uncertainty budgets and details on the experimental data

A.1. Definitions

For each specific irradiation set, a value r_j is obtained using

$$r_j = \sum_{i=1}^{n_i} w_{ji} \cdot r_{ji} \tag{A.1}$$

where r_{ji} is the response obtained from the determined dose D_{ji}^{c} for one detector and the corresponding delivered dose D_{ji} according to (3). r_j is the weighted mean (compare the appendix of Anton *et al* 2008) of the individual r_{ji}. The weights are determined by their uncertainties $u(r_{ji})$, given by

$$w_{ji} = \left(\frac{u_j}{u(r_{ji})}\right)^2 \quad \text{where} \quad u_j = \left(\sum_{i=1}^{n_i} \frac{1}{u^2(r_{ji})}\right)^{-1/2}. \tag{A.2}$$

From these data, $\langle r \rangle$ is obtained in a similar manner:

$$\langle r \rangle = \sum_{j=1}^{n_j} w_j r_j \tag{A.3}$$

where r_j is obtained from (A.1) and (A.2) and

$$w_j = \left(\frac{u}{u(r_j)}\right)^2 \quad \text{and} \quad u = \left(\sum_{j=1}^{n_j} \frac{1}{u^2(r_j)}\right)^{-1/2}. \tag{A.4}$$

If the consistency criterion (see Anton *et al* 2008, Weise and Wöger 1993)

$$q^2 < n_j - 1 \qquad \text{where} \qquad q^2 = \sum_{j=1}^{n_j} \left(\frac{r_j - \langle r \rangle}{u(r_j)}\right)^2 \tag{A.5}$$

is violated, e.g. if the uncertainties $u(r_j)$ are too small compared to the scatter of the individual values r_j, a modified value u_{mod} has to be calculated. According to Dose (2003), u_{mod} is

$$u_{\text{mod}}^2 = \frac{\langle r^2 \rangle - \langle r \rangle^2}{n_j - 3}, \quad \text{where} \quad \langle r^2 \rangle = \sum_{j=1}^{n_j} w_j r_j^2, \tag{A.6}$$

and w_j given by (A.4). In case (A.5) is not fulfilled, u_{mod} replaces u as the uncertainty of the weighted mean $< r >$ in the following uncertainty calculations. It has to be stressed that u_j is only a component of the combined uncertainty $u(r_j)$ and u or u_{mod} are only a component of the combined overall uncertainty of the final result.

A.2. Uncertainty budget

A.2.1. Uncertainty of the determined dose. At least three effects contribute to the uncertainty of the mass normalized amplitude A_m: the first one is the repeatability of the amplitude determination. For the chosen parameters and $D^{b} = 25$ Gy, this corresponds to 40 mGy ($= u(A_i) \cdot D^{b}$) for a single pellet or 20 mGy for an average over 4 pellets ($= u(A_m) \cdot D^{b}$). This value of $u(A_m)$ is independent of dose between 2 and 25 Gy. The second part is the variation of

Table A1. Example uncertainty budget for $D^c = \mathcal{A}_D$ for one test detector (four pellets) irradiated to a dose of 10 Gy. The left column contains a label which is referred to in the text, the middle column describes the source of the uncertainty, the right column lists the relative standard uncertainty component in per cent.

Label	Component	u_r in %
	From test detector ($n = 4$ pellets):	
1a	A_m. Amplitude repeatability	0.20
2a	A_m. Individual background	0.10
3a	A_m. Intrabatch homogeneity	0.15
4	k_T. Irradiation temperature	0.05
5	$\overline{m}$. Average mass of n probes	0.05
	Subtotal test detector	**0.28**
	From base function ($n = 4$ pellets):	
1b	A_m. Amplitude repeatability	0.08
2b	A_m. Individual background	0.04
3b	A_m. Intrabatch homogeneity	0.15
6	k_T^b. Irradiation temperature	0.05
7	$\overline{m}^b$. Average mass of n probes	0.05
	Subtotal	**0.19**
8	Systematic component	0.15
	Subtotal base function	**0.24**
9	D^b. Repeatability of irradiation	0.05
	D^b. Primary standard	0.22
	Total	**0.43**

the individual background signal which amounts to approximately 20 mGy for a single pellet (Anton 2005). The third part is the intrabatch homogeneity, i.e. the variation of the alanine content within a certain batch (see column CV in table 1). The same estimates apply to the base function amplitudes.

In table A1, an example of an uncertainty budget is given for one detector (4 pellets), irradiated to a dose of 10 Gy in the ^{60}Co reference field and is valid for the case when no calibration curve is constructed, i.e. assuming $D^c = \mathcal{A}_D$. The base functions were constructed from the spectra of one detector irradiated to 25 Gy and four unirradiated pellets as outlined above. For the higher doses, the relative uncertainty due to amplitude readout repeatability decreases, $u(A_m)$ being constant. The limiting components are the intrabatch homogeneity and an additional systematic component of 0.15%. The latter was deduced from repetitive measurements of calibration and test data sets, where the dose calculated with and without using a calibration line was compared to the known delivered dose. The non-systematic component (subtotal) for the single base of 0.19% agrees very well with type A estimates that were used in previous publications (Anton 2006). If the base is constructed from spectra of *two* irradiated detectors and eight unirradiated pellets (double base), the subtotal for the non-systematic part reduces from 0.19% to 0.14%.

Due to the time delay of less than one week between the irradiation of the calibration probes and the test probes, in all but one case fading corrections were negligible (see Anton 2006, 2008).

The uncertainty of D^c determined *with* a calibration curve is calculated only from 1a, 2a, 3a, 4 and 5 from table A1 using equation (16) from Anton (2006): all uncertainty components

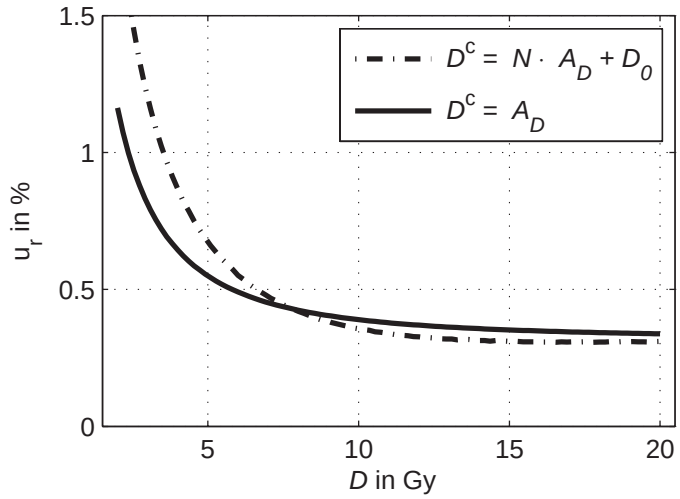

Figure A1. Relative uncertainty of the determined dose D^{c}—excluding the primary standard—with (dash-dotted curve) and without using a calibration curve (continuous curve). The data are valid for a 25 Gy base, ^{60}Co -irradiated detectors and a calibration line determined from four detectors with doses of 5, 10, 15 and 20 Gy.

associated to the base function cancel if the *same* set of base functions is used to determine the amplitude for the test- and the calibration detectors. Different from earlier work, the parameters of the calibration curve are now obtained from a linear weighted total least squares fit (Krystek and Anton 2007) to n_c data pairs $(D, \mathcal{A}_D)$ (calibration data set).

The uncertainties with and without using a calibration curve, but excluding the primary standard, are shown as a function of the delivered dose in the range between 2 Gy and 20 Gy in figure A1. The data for $D^{c} = \mathcal{A}_D$ are represented by the continuous curve, the uncertainty for the determined dose using a calibration curve is displayed by the dash-dotted curve. The data are obtained using $D^{b} = 25$ Gy and a calibration curve constructed from the amplitudes for four detectors irradiated with doses of 5, 10, 15 and 20 Gy. All irradiations are assumed to be carried out in the ^{60}Co reference field.

It is notable that the uncertainty for $D^{c} = \mathcal{A}_D$ is lower at the low-dose end of the dose range shown. The scatter of data points at the lower end of the calibration data set may lead to larger variations of the slope and the *y*-axis intersection than the simple assumption of an ideal calibration curve with intersection zero and slope unity. This is still true within the range of the calibration curve ($D \geqslant 5$ Gy). However, for $D > 7$ Gy, the results obtained using a calibration curve are more accurate.

A.2.2. Uncertainty of the relative response values r_j. The variance $u^2(r_{ji}) = u^2(D^{c}_{ji}) + u^2(D_{ji})$ for each individual dose is obtained as follows: for D^{c}_{ji}, components 1a, 2a, 3a, 4 and 5 from table A1 have to be taken into account. For the delivered dose D_{ji}, only the reproducibility for opening/closing the shutter (^{60}Co) and the stability of the monitor (MV x-rays) are relevant at this stage. Using these components, the weighted mean values r_j and the uncertainty component u_j are obtained.

An example is given in table A2 for $n_i = 4$ ($D_{ji} \approx 10$, 12.5, 15 and 17.5 Gy). In the upper part of the table, the left column shows the uncertainties $u(r_{ji})$ in case no calibration curve is used ($D^{c} = \mathcal{A}_D$) whereas the right column shows the corresponding components in case a

Table A2. Uncertainty budget for r_j for a typical irradiation set j. Here, $n_i = 4$ test doses of approximately 10, 12.5, 15 and 17.5 Gy were chosen. The budgets for an evaluation with $D^c = \mathcal{A}_D$ (left) and using a calibration curve (right) with data points at 5, 10, 15 and 20 Gy are compared. The subtotal u_j/r_j is obtained from (A.1) and (A.2).

Component		u_r in %	
		$D^c = \mathcal{A}_D$	Calibration line
r_{j1}	($D_{j1} \approx 10$ Gy)	0.28	0.32
r_{j2}	($D_{j2} \approx 12.5$ Gy)	0.24	0.27
r_{j3}	($D_{j3} \approx 15$ Gy)	0.22	0.25
r_{j4}	($D_{j4} \approx 17.5$ Gy)	0.21	0.24
subtotal u_j/r_j		**0.12**	**0.13**
Base function		0.24	–
Reproducibility $D_{MV} = D_{ji}$			0.12
Reproducibility D_{Co}			0.05
k_T (systematic part)			0.04
$\mathbf{u(r_j)/r_j}$		**0.30**	**0.19**

calibration curve is used. In this example, a ^{60}Co calibration curve with data points at 5, 10, 15 and 20 Gy was used. The resulting relative value u_j/r_j from equations (A.1) and (A.2) is given for both cases (subtotal, printed in bold).

Where a calibration curve is not used, the uncertainty components for the base (1b, 2b, 3b, 6, 7 and 8 from table A1) have to be included after the calculation of the weighted mean r_j which yield another 0.24%.

For each irradiation set j, the positioning of the sleeve in the phantom which contains the pellets and the ionization chamber for the irradiation of the test probes was made only once, therefore this component for the uncertainty of D_{ji} has to be added *after* calculating the weighted mean r_j. A similar component associated with the reproducibility of the irradiation of calibration and base probes is also added after calculating the weighted mean because the whole set is usually irradiated without moving the sleeve. An uncertainty component for the temperature correction due to a possible systematic deviation of 0.1 K between the two different temperature sensors used at the Cobalt irradiation source and at the accelerator is included as well. Other components such as the uncertainty of the ^{60}Co calibration factor of the ionization chamber have to be added only *after* calculating the weighted mean $\langle r \rangle$ (see next section).

The example presented in table A2 is typical in the sense that the relative uncertainty of r_j is approximately 0.2% if a calibration curve is used and 0.3% for $D^c = \mathcal{A}_D$. Actual values vary slightly due to different sizes of test and calibration data sets. All results r_j and their corresponding uncertainties $u(r_j)$ are shown below in tables A3 and A4.

A.2.3. Uncertainty of the final result $\langle r \rangle$. The weighted mean values $\langle r \rangle$ were calculated from $n_j = 4$ up to $n_j = 9$ values r_j using (A.3) and (A.4). The values $u(r_j)$ listed in tables A3 and A4 served to calculate the weights according to (A.4). In addition to the uncertainty components u from equation (A.4) or u_{mod} from equation (A.6), the contributions from the ^{60}Co calibration of the ionization chamber and the k_Q-factors have to be taken into account. The uncertainty of the primary standard of 0.2% cancels because the calibration factor for the ionization chamber, the dose rate of the ^{60}Co reference field and the k_Q values were determined using the same calorimeter. The contributions to be added are finally $u_r(IC) = 0.15\%$ for the

Table A3. Relative response r_j for the irradiation sets investigated, 4 to 8 MV. Columns from left to right: nominal accelerating voltage in MV, irradiation set label, date of measurement, number of test detectors n_i (1 detector = 4 pellets); number of calibration detectors n_c; number of base detectors n_b; r_j using equations (A.1) and (A.2); the uncertainty $u(r_j)$, see section A.2.2 and the example in table A2.

MV	Set j	Date	n_i	n_c	n_b	r_j	$u(r_j)$
4	hl22	2012-03-22	4	4	1	0.9970	0.0020
4	hl22	2012-03-29	4	4	1	0.9959	0.0020
4	hl28	2012-06-26	4	5	1	0.9951	0.0020
4	hl31	2012-07-12	4	5	1	0.9931	0.0020
6	hf34	2008-06-11	5	5	1	0.9973	0.0019
6	hf37	2008-11-19	5	5	1	0.9974	0.0019
6	hj03	2009-01-30	5	5	1	0.9988	0.0019
6	hj05	2009-02-13	5	5	1	0.9988	0.0019
6	hj33	2010-10-05	6	–	2	0.9932	0.0033
6	hj37	2010-11-02	4	5	1	0.9938	0.0021
6	hj38	2010-11-18	4	–	2	0.9942	0.0030
6	hj45	2011-03-23	4	4	2	0.9967	0.0030
6	hj45	2011-03-31	4	5	1	0.9978	0.0021
8	hj31	2010-09-15	6	–	1	0.9908	0.0033
8	hj39	2010-12-14	8	–	1	0.9910	0.0033
8	hj49	2011-05-18	5	6	1	0.9954	0.0019
8	hl01	2011-06-22	5	6	1	0.9952	0.0018
8	hl22	2012-03-29	4	4	1	1.0004	0.0020

Table A4. Relative response r_j for the irradiation sets investigated, 10 to 25 MV. Columns from left to right: nominal accelerating voltage in MV, irradiation set label, date of measurement, number of test detectors n_i (1 detector = 4 pellets); number of calibration detectors n_c; number of base detectors n_b; r_j using equations (A.1) and (A.2); the uncertainty $u(r_j)$, see section A.2.2 and the example in table A2.

MV	Set j	Date	n_i	n_c	n_b	r_j	$u(r_j)$
10	hf34	2008-05-29	4	4	1	0.9943	0.0021
10	hf36	2008-07-22	5	5	1	0.9954	0.0052
10	hf37	2008-11-13	5	5	1	0.9939	0.0019
10	hj03	2008-12-16	5	5	1	0.9929	0.0019
10	hj07	2009-03-12	6	5	1	0.9937	0.0019
10	hj41	2011-01-06	4	5	1	0.9897	0.0021
10	hj45	2011-03-23	4	–	2	0.9958	0.0030
10	hj45	2011-03-30	4	6	1	0.9987	0.0021
15	hl15	2012-01-24	6	–	2	0.9915	0.0027
15	hl15	2012-01-26	3	–	2	0.9900	0.0028
15	hl15	2012-01-26	3	–	2	0.9899	0.0029
15	hl16	2012-02-09	6	–	1	0.9880	0.0029
15	hl16	2012-02-14	6	–	1	0.9901	0.0030
15	hl20	2012-03-02	3	4	1	0.9864	0.0021
25	hj29	2010-08-18	6	–	2	0.9860	0.0029
25	hj32	2010-09-29	8	–	1	0.9921	0.0033
25	hj34	2010-10-13	8	–	1	0.9935	0.0033
25	hj49	2011-05-17	5	6	1	0.9918	0.0019
25	hl01	2011-06-17	5	6	1	0.9867	0.0018
25	hl03	2011-08-09	4	6	1	0.9883	0.0019
25	hl09	2011-11-02	3	–	2	0.9906	0.0028

calibration factors and $u_r(k_Q) = 0.31\%$ for the quality correction factors of the ionization chamber(s).

A.3. Details of the experimental results

The results of each individual irradiation and measurement set j are listed in tables A3 and A4. The first column lists the nominal accelerating voltage in MV, the second one a label attached to each irradiation set[8] and the third column contains the date of measurement. The following three columns describe the size of the dataset: n_i is the number of test detectors irradiated in the MV x-ray field. Their doses are always interspersed between the lowest and the highest dose of the calibration set. The latter consisted of n_c probes with doses between 5 and 25 Gy. n_b is the number of base detectors. $n_\mathrm{b} = 2$ means that there were spectra from two irradiated detectors and eight unirradiated pellets used to construct the base functions. The individual relative response values r_j are listed in the following column and were obtained using equations (A.1) and (A.2). The uncertainties of these values are denoted as $u(r_j)$ and are listed in the rightmost column. The calculation of these values is described in section A.2.2, an example is given in table A2.

With a calibration curve, the uncertainty of the individual values is approximately 0.2% whereas the quicker evaluation without a calibration curve leads to a higher uncertainty of approximately 0.3%. For the latter case, it appears to be insignificant whether a single ($n_\mathrm{b} = 1$) or a double ($n_\mathrm{b} = 2$) set of pellets was used for the construction of the base functions. There appears to be no correlation between the value of r_j and whether or not a calibration curve was employed. The uncertainties are in general slightly smaller if the data sets are bigger, which is no surprise. However, a small set of test data ($n_i = 3$) evaluated *with* a calibration curve yields more accurate results than a large set ($n_i = 8$) evaluated without. The higher value of $u(r_j)$ for the 10 MV set hf36 is due to a fading correction and its associated uncertainty.

References

Aalbers A H L, Hoornaert M-T, Minken A, Palmans H, Pieksma M W H, de Prez L A, Reynaert N, Vynckier S and Wittkämper F W 2008 Code of practice for the absorbed dose determination in high energy photon and electron beams *NCS Report*18 *Nederlandse Commissie voor Stralingsbescherming*

Anton M 2005 Development of a secondary standard for the absorbed dose to water based on the alanine EPR dosimetry system *Appl. Radiat. Isot.* **62** 779–95

Anton M 2006 Uncertainties in alanine/ESR dosimetry at PTB *Phys. Med. Biol.* **51** 5419–40

Anton M 2008 Postirradiation effects in alanine dosimeter probes of two different suppliers *Phys. Med. Biol.* **53** 1241–58

Anton M, Kapsch R P, Krystek M and Renner F 2008 Response of the alanine/ESR dosimetry system to MV x-rays relative to ^{60}Co radiation *Phys. Med. Biol.* **53** 2753–70

Berger M, Coursey J S, Zucker M A and Chang J 2005 ESTAR, PSTAR, and ASTAR: computer programs for calculating stopping-power and range tables for electrons, protons, and Helium ions (version 1.2.3) *Technical Report* (Gaithersburg, MD: National Institute of Standards and Technology) http://www.nist.gov/pml/data/star/index.cfm

Bergstrand E S, Shortt K R, Ross C K and Hole E O 2003 An investigation of the photon energy dependence of the EPR alanine dosimetry system *Phys. Med. Biol.* **48** 1753–71

Budgell G, Berresford J, Trainer M, Bradshaw E, Sharpe P and Williams P 2011 A national dosimetric audit of IMRT *Radiother. Oncol.* **99** 246–52

De Angelis C, De Coste V, Fattibene P, Onori S and Petetti E 2005 Use of alanine for dosimetry intercomparisons among italian radiotherapy centers *Appl. Radiat. Isot.* **62** 261–5

Ding G X, Rogers D W O and Mackie T R 1995 Calculation of stopping-power ratios using realistic clinical electron beams *Med. Phys.* **22** 489–501

[8] hf: from batch AF594, hj: from batch AJ598, hl: from batch AL595.

Dose V 2003 Bayesian inference in physics: case studies *Rep. Prog. Phys.* **66** 1421–61
Garcia T, Lacornerie T, Popoff R, Lourenço V and Bordy J-M 2011 Dose verification and calibration of the cyberknife® by EPR/alanine dosimetry *Radiat. Meas.* **46** 952–7
Hubbell J H 1982 Photon mass attenuation and energy-absorption coefficients from 1 keV to 20 MeV *Appl. Radiat. Isot.* **33** 1269–90
ICRU 1984 Stopping powers for electrons and positrons *ICRU Report No. 37* (Washington, DC: ICRU)
JCGM100 2008 Evaluation of measurement data—guide to the expression of uncertainty in measurement. GUM 1995 with minor corrections *Technical Report* JCGM 100, Working Group 1 of the Joint Committee for Guides in Metrology JCGM/WG 1
Kawrakow I 2000 Accurate condensed history Monte Carlo simulation of electron transport: I. EGSnrc, the new EGS4 version *Med. Phys.* **27** 485–98
Kawrakow I, Mainegra-Hing E, Rogers D W O, Tessier F and B Walters B R 2010 The EGSnrc code system: Monte Carlo simulation of electron and photon transport *NRC Report* PIRS-701 (Ottawa, Canada: NRCC)
Krauss A 2006 The PTB water calorimeter for the absolute determination of absorbed dose to water in ^{60}Co radiation *Metrologia* **43** 259–72
Krauss A and Kapsch R-P 2007 Calorimetric determination of k_Q factors for NE 2561 and NE2571 ionization chambers in 5 cm × 5 cm and 10 cm × 10 cm radiotherapy beams of 8 MV and 16 MV photons *Phys. Med. Biol.* **52** 6243–59
Krystek M and Anton M 2007 A weighted total least-squares algorithm for fitting a straight line *Meas. Sci. Technol.* **18** 1–5
Krystek M and Anton M 2011 A least-squares algorithm for fitting data points with mutually correlated coordinates to a straight line *Meas. Sci. Technol.* **22** 1–9
McEwen M R 2010 Measurement of ionization chamber absorbed dose k_Q factors in megavoltage photon beams *Med. Phys.* **37** 2179–93
McEwen M, Sephton J and Sharpe P 2006 Alanine dosimetry for clinical applications *Technical Report PTB-Dos-51, Physikalisch-Technische Bundesanstalt* pp 9–14
Muir B, McEwen M R and Rogers D W O 2011 Monte Carlo calculations of the beam quality conversion factor k_Q for cylindrical ionization chambers: comparison with published data *Med. Phys.* **38** 4600–9
Onori S, Bortolin E, Calicchia A, Carosi A, De Angelis C and Grande S 2006 Use of commercial alanine and TL dosemeters for dosimetry intercomparisons among italian radiotherapy centres *Radiat. Prot. Dosim.* **120** 226–9
Picard S, Burns D T, Roger P, Allisy-Roberts P J, Kapsch R-P and Krauss A 2011 Key comparison BIPM.RI(I)-K6 of the standards for absorbed dose to water of the PTB, Germany and BIPM in accelerator photon beams *Metrologia* **48** 06020
Picard S, Burns D T, Roger P, Allisy-Roberts P J, McEwen M R, Cojocaru C D and Ross C K 2010 Comparison of the standards for absorbed dose to water of the NRC and the BIPM for accelerator photon beams *Metrologia* **47** 06025
Rogers D W O, Walters B and Kawrakow I 2004 BEAMnrc User's Manual *NRC Report* PIRS 509(a)revH (Ottawa, Canada: NRCC)
Schaeken B, Cuypers R, Lelie S, Schroeyers W, Schreurs S, Janssens H and Verellen D 2011 Implementation of alanine/EPR as transfer dosimetry system in a radiotherapy audit programme in Belgium *Radiother. Oncol.* **99** 94–96
Seltzer S M 1993 Calculation of photon mass energy-transfer and mass energy-absorption coefficients *Radiat. Res.* **136** 147–70
Sharpe P H G 2003 Progress report on radiation dosimetry at NPL *Technical Report* (Sèvres: BIPM)
Sharpe P H G 2006 Alanine dosimetry for clinical applications *Technical Report* PTB-Dos-51, Physikalisch-Technische Bundesanstalt pp 3–8
Sharpe P H G, Rajendran K and Sephton J P 1996 Progress towards an alanine/ESR therapy level reference dosimetry service at NPL *Appl. Radiat. Isot.* **47** 1171–5
Sheikh-Bagheri D and Rogers D W O 2002 Monte Carlo calculations of nine megavoltage photon beam spectra using the BEAM code *Med. Phys.* **29** 391–402
Vörös S, Anton M and Boillat B 2012 Relative response of alanine dosemeters for high-energy electrons determined using a Fricke primary standard *Phys. Med. Biol.* **57** 1413–32
Weise K and Wöger W 1993 A Bayesian theory of measurement uncertainty *Meas. Sci. Technol.* **4** 1–11
Zeng G G, McEwen M R, Rogers D W O and Klassen N V 2004 An experimental and Monte Carlo investigation of the energy dependence of alanine/EPR dosimetry: I. Clinical x-ray beams *Phys. Med. Biol.* **49** 257–70
Zeng G G, McEwen M R, Rogers D W O and Klassen N V 2005 An experimental and Monte Carlo investigation of the energy dependence of alanine/EPR dosimetry: II. Clinical electron beams *Phys. Med. Biol.* **50** 1119–29

IOP Publishing | Institute of Physics and Engineering in Medicine Physics in Medicine & Biology

Phys. Med. Biol. **60** (2015) 175–193 doi:10.1088/0031-9155/60/1/175

Response of the alanine/ESR dosimeter to radiation from an Ir-192 HDR brachytherapy source

M Anton[1], T Hackel[1], K Zink[2], P von Voigts-Rhetz[2] and H-J Selbach[1]

[1] Physikalisch-Technische Bundesanstalt, Bundesallee 100, D-38116 Braunschweig, Germany

[2] Institut für Medizinische Physik und Strahlenschutz—IMPS, University of Applied Sciences Giessen-Friedberg, Wiesenstr. 14, D-35390 Giessen, Germany

E-mail: mathias.anton@ptb.de

Received 9 July 2014, revised 11 September 2014
Accepted for publication 21 October 2014
Published 9 December 2014

Abstract

The response of the alanine dosimeter to radiation from an Ir-192 source with respect to the absorbed dose to water, relative to Co-60 radiation, was determined experimentally as well as by Monte Carlo simulations. The experimental and Monte Carlo results for the response agree well within the limits of uncertainty. The relative response decreases with an increasing distance between the measurement volume and the source from approximately 98% at a 1 cm distance to 96% at 5 cm. The present data are more accurate, but agree well with data published by Schaeken *et al* (2011 *Phys. Med. Biol.* **56** 6625–34). The decrease of the relative response with an increasing distance that had already been observed by these authors is confirmed. In the appendix, the properties of the alanine dosimeter with respect to volume and sensitivity corrections are investigated. The inhomogeneous distribution of the detection probability that was taken into account for the analysis was determined experimentally.

Keywords: absorbed dose to water, response, alanine, ESR, brachytherapy, iridium, volume correction

(Some figures may appear in colour only in the online journal)

1. Introduction

The need for dosimetry audits and improved dosimetry for brachytherapy is likely to increase due to the rising numbers of cancer incidence cases (Guedea *et al* 2007, Palmer *et al* 2014). Dosimetry using alanine with a read-out via electron spin resonance (ESR) is a convenient

tool for quality assurance measurements for radiotherapy. The main reasons are the good water-equivalence of alanine, the weak dependence on the irradiation quality, the non-destructive read-out (different from thermoluminescence detectors) and the comparatively small size of the detectors. In addition, alanine detectors are non-poisonous, which may be an advantage with respect to *in-vivo* measurements.

Irradiation induces free radicals in the amino acid alanine. The radicals are stable: if the detectors are stored in a dry environment, the fading, i.e. the loss of radicals with time, is only of the order of a few parts in 10^3 per year. The read-out is usually performed by ESR. Since the reading is not absolute, the ESR amplitude has to be calibrated, usually with the help of alanine detectors irradiated in a Co-60 reference field.

Although the first applications of alanine dosimetry for brachytherapy date back to the eighties of the last century (Ciesielski *et al* 1988), only a few centres have used the technique so far for quality assurance measurements in brachytherapy (Kuntz *et al* 1996, Schaeken and Scalliet 1996, De Angelis *et al* 1999, Olsson *et al* 2002, Calcina *et al* 2005, Schultka *et al* 2006, Anton *et al* 2009). However, the method has good potential, as do measurements using ESR imaging techniques (Kolbun *et al* 2010) or developments using other free radical dosimeter materials (Antonovic *et al* 2009, Adolfsson *et al* 2010).

A prerequisite for a possible use of the alanine dosimeter in the field of an Ir-192 brachytherapy source is the accurate knowledge of its response with respect to the relevant radiation quality. In 2011, response data for Ir-192 radiation were published by Schaeken *et al* (2011) with an uncertainty of 1.8% (excluding the uncertainty of the dose rate constant Λ). The goal of the present investigation was to reduce the uncertainty further, at the same time trying to reproduce the decrease of the alanine response with an increasing distance from the source reported by Schaeken *et al* (2011).

A challenge concerning dose measurements in the near field of an iridium source is the strong variation of the dose with the distance in connection with the finite size of the detectors. The dose distribution within each detector was calculated using the update to TG43 (Rivard *et al* 2004). Different from other publications, also the inhomogeneous distribution of the detection probability of the radicals connected with the shapes of the electromagnetic fields inside the microwave resonator of the ESR spectrometer was taken into account. The relative sensitivity as a function of the position within the resonator was determined experimentally, which is briefly explained in the appendix. The second appendix deals with the calculation of correction factors for the volume effect and the inhomogeneous sensitivity which is of general importance for measurements in spatially strongly varying fields using the alanine dosimeter.

For the sake of simplicity, *dose* or D is to be understood as *absorbed dose to water* in the following, unless otherwise stated. Uncertainties were determined according to the guidelines given by the GUM (Guide to the expression of uncertainty in measurement) (JCGM100 2008). Unless otherwise stated, *uncertainty* means *standard uncertainty*.

2. Materials and methods

2.1. ESR measurements and analysis: the dose-normalized amplitude $\mathcal{A}_D$

Alanine pellets produced by Harwell (UK) with an addition of approximately 9% of paraffin as a binder were used. The pellets from batch AL 598 with an average mass of 59.8 mg have a diameter of 4.85 mm and a height of approximately 2.7 mm. This corresponds to a bulk density of $\approx 1.2\ \mathrm{g\cdot cm^{-3}}$.

ESR measurements were conducted with a Bruker EMX 1327 ESR spectrometer, with an 8″ magnet and an x-band microwave bridge. The high-sensitivity resonator ER 4119 HS was

used throughout. The parameters are listed in a previous publication (Anton 2006), which also contains a detailed description of the hardware.

The data analysis method has been described in detail in previous publications as well (Anton 2006, Anton *et al* 2013). In principle, two coefficients A^{ala} and A^{ref} are obtained for each pellet by fitting two base functions to the experimental signals. The base functions for the alanine signal and the signal of a reference substance which is measured simultaneously, are obtained by measuring pellets irradiated with a known dose in the Co-60 reference field and by measuring unirradiated pellets. With the help of the amplitude A for one pellet which is the ratio $A = A^{\mathrm{ala}}/A^{\mathrm{ref}}$, the dose-normalized amplitude $\mathcal{A}_D$ is defined as

$$\mathcal{A}_D = \frac{A}{m} \cdot k_T \cdot \frac{\overline{m}_{\mathrm{Co}}}{k_{T,\mathrm{Co}}} \cdot D_{0,\mathrm{Co}} \,. \tag{1}$$

With A being dimensionless, $\mathcal{A}_D$ has the dimension of dose (hence the name). m is the mass of the pellet and $\overline{m}_{\mathrm{Co}}$ is the average mass of the pellets which received the dose $D_{0,\mathrm{Co}}$ and which are used to construct the (alanine) base function. Usually, $D_{0,\mathrm{Co}} = 25$ Gy. The correction factor $k_T = 1 - c_T(T - T_0)$ takes the influence of the irradiation temperature into account. The temperature coefficient is $c_T \approx 1.8 \cdot 10^{-3}$ K^{-1}; $k_{T,Co}$ is the corresponding correction for the alanine base function. The reference temperature T_0 is 20° C. As was reported previously (Anton 2006, Anton *et al* 2013), $\mathcal{A}_D$ is independent of the time delay between irradiation and measurement.

2.2. The relative response

The spatial distribution of the dose can be written as

$$D_{\mathrm{Co}} = D_{0,\mathrm{Co}} \cdot f_{\mathrm{Co}}\,(\vec{x}) \tag{2}$$

$$\text{and} \quad D_{\mathrm{Ir}} = D_{0,\mathrm{Ir}} \cdot f_{\mathrm{Ir}}\,(\vec{x}) \tag{3}$$

for radiation from a Co-60 source and from the Ir-192 source, respectively, where D_0 denotes in both cases the dose at the point of measurement and f is a spatial distribution function which is unity at the point of measurement. The coefficient A_{ala} can then be expressed as

$$A_{\mathrm{ala}} = \frac{r \cdot D_{0,\mathrm{Ir}} \cdot \int f_{\mathrm{Ir}} \cdot s \cdot \mathrm{d}V}{D_{0,\mathrm{Co}} \cdot \int f_{\mathrm{Co}} \cdot s \cdot \mathrm{d}V} \tag{4}$$

where s is a function describing the spatial variation of the relative sensitivity of the spectrometer and the volume integral extends over the volume of an alanine pellet. The factor r is the relative response[3] which is sought for and is equal to the inverse of the quality correction factor k_{Ir}. Combining (1) and (4), we get

$$r = \frac{\mathcal{A}_D}{D_{0,\mathrm{Ir}}} \cdot k_s \cdot k_V \tag{5}$$

with the volume correction factor k_V and the sensitivity correction factor k_s given by

$$k_V = \frac{\int f_{\mathrm{Co}} \cdot dV \,/ \int dV}{\int f_{\mathrm{Ir}} \cdot \mathrm{d}V \,/ \int \mathrm{d}\,V} \tag{6}$$

[3] The response r so defined is the response with respect to the dose to water, relative to Co-60 radiation.

$$k_s = \frac{\int f_{\mathrm{Co}} \cdot s \cdot \mathrm{d}V \,/\, \int f_{\mathrm{Co}} \cdot \mathrm{d}V}{\int f_{\mathrm{Ir}} \cdot s \cdot \mathrm{d}V \,/\, \int f_{\mathrm{Ir}} \cdot \mathrm{d}V} \tag{7}$$

The volume correction is the ratio of the average Co-60 dose (for the pellets used for the construction of the base functions) and the average Ir-192 dose. The sensitivity correction can be viewed as the ratio of weighted means of the sensitivity, where the weights are the corresponding dose distributions. The sensitivity distribution was determined experimentally which is described in appendix A. Details on the calculation of the correction factors k_V and k_s are given in section 2.5 and in appendix B.

2.3. Irradiations in the Co-60 reference field

The pellets used for the calibration were irradiated in the Co-60 reference field of the Physikalisch-Technische Bundesanstalt (PTB). The field size was 10 cm × 10 cm at the reference depth of 5 cm in water. For the calibration, four pellets were irradiated simultaneously. They were irradiated inside a holder made of polymethylmethacrylate (PMMA) which fitted inside a watertight sleeve of an NE 2571 (Farmer) ionization chamber, also made of PMMA. The geometrical centre of the detector was placed at the reference depth in a 30 cm × 30 cm × 30 cm water phantom.

The depth was determined with calipers with an uncertainty of 0.12 mm, resulting in a contribution to the relative uncertainty of the delivered dose of 0.05% . The lateral dose profile (in the plane perpendicular to the beam axis) over the volume of the alanine detector is flat; no correction and no additional uncertainty contribution had to be taken into account. The relative depth-dose curve decays approximately linearly at the reference depth.

The relative uncertainty of the absorbed dose to water as determined with the PTB water calorimeter is 0.2% (Krauss 2006). Taking an additional small contribution for the source shutter and the positioning of the probe into account led to a relative uncertainty of the delivered dose $D_{0,\mathrm{Co}}$ of 0.22%.

The irradiation temperature was registered with an uncertainty of 0.1° C. Since it was only possible to measure the temperature of the surrounding water, a time delay of 10 min was inserted between the placing of the detector in the water and the beginning of the irradiation.

2.4. Irradiation arrangement in the field of an HDR Ir-192 source

A high dose rate iridium source from Nucletron, type microSelectron V2 # NLF 01036C907 was used. The source was handled using an afterloader, a custom product made for PTB. The reference air kerma rate (RAKR) was determined at PTB and was $7.5441 \cdot 10^{-4}$ Gy h^{-1} on 13 November 2012. Irradiation times were obtained from the reference air kerma rate, the dose rate constant Λ and the inverse square law, choosing $D_{0,\mathrm{Ir}} \approx 15$ Gy. The radioactive decay of the source during irradiation was taken into account, as well as the attenuation due to the steel needle which held the source. The attenuation was determined experimentally by measuring the air kerma rate with and without the steel needle. The exact dose distribution inside the pellet was calculated later on (see next section). The resulting irradiation times varied between approximately 2 h and 45 h, depending on the distance between the source and the detector. Due to the long irradiation times, the transit dose, i.e. the dose received by the detectors while the source was not in its final position, was less than $2 \cdot 10^{-4}$ of the delivered dose and was therefore neglected.

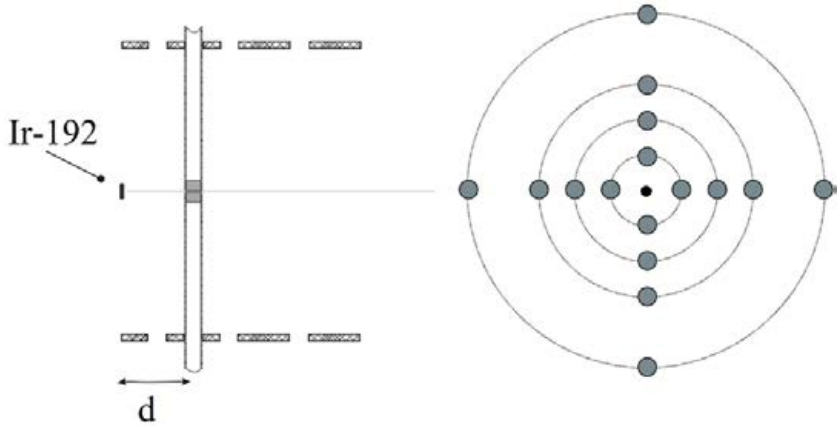

Figure 1. Schematic drawing of the arrangement during irradiation. Left: side view. *d* is the distance in the midplane between the centre of the source and the centre of one detector, i.e. the point between two alanine pellets situated just above and below the midplane. Right: top view showing the irradiation positions.

In order to achieve accurate results, especially close to the irradiation source, the minimization of geometrical uncertainties is essential. A schematic drawing of the arrangement is depicted in figure 1. A photograph is reproduced in figure 2.

A Nucletron trocar needle with a diameter of 1.3 mm made of stainless steel which contains the iridum source during irradiation is fixed in the centre of the arrangement. For each of the four distances *d* (1 cm, 2 cm, 3 cm and 5 cm), four positions distributed around the source at angles of 0°, 90°, 180° and 270° are prepared to hold four tubes made of PMMA with a wall thickness of 0.65 mm. For each irradiation, only four tubes for a specified distance *d* were equipped with alanine detectors, the other places remained empty, i.e. without tubes and without detectors.

The positions of the tubes are secured via two parallel planes made of machinable ceramic (MACOR). The latter provides higher mechanical accuracy than PMMA. The vertical distance between the planes is 8 cm. The centre of the source is located in the middle between these planes. Inside each PMMA tube, two alanine pellets are positioned so that the top face of the lower pellet and the bottom face of the top pellet coincide with the midplane (same plane as the centre of the source). The uncertainty of the horizontal position of the source within the applicator needle is averaged by the geometry of this arrangement. The maximum relative uncertainty associated with the horizontal source position was $5 \cdot 10^{-5}$, after averaging over the four detectors at different angles and was therefore considered negligible. The uncertainty of the vertical position of the source was 0.13 mm (see appendix C). For each distance *d*, eight pellets were thus irradiated simultaneously. For the distance $d = 1$ cm, 32 pellets were irradiated in total whereas for the larger distances only 16 pellets were irradiated. Between each irradiation, the tubes containing the pellets were rotated by 180° in order to average over the deviation of the tube from ideal straightness. The standard uncertainty associated with the deviation from the ideal position was 0.05 mm (see appendix C). For the irradiations, the whole arrangement was placed inside a water phantom with the dimensions 40 cm × 40 cm × 60 cm. The temperature of the water was measured before and after the irradiation. Due to the air conditioning of the environment and the large size of the phantom, the temperature was stable. On average, the temperature was 17.5° C; the uncertainty is estimated as 0.3° C.

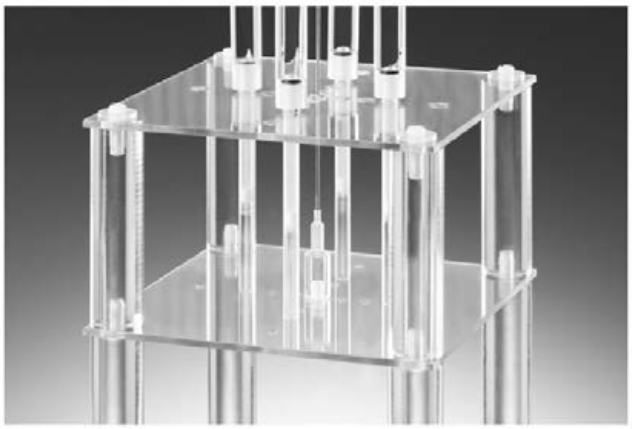

Figure 2. A photograph of the device holding the applicator needle and four tubes equipped with alanine detectors.

2.5. Calculation of the correction factors k_V and k_s

The dose distribution inside the volume of the alanine pellets irradiated with the Ir-192 source was determined using the formalism from the update to protocol TG43 (Rivard *et al* 2004):

$$\dot{D}(r,\theta) = S_K \cdot \Lambda \cdot \frac{G_L(r,\theta)}{G_L(r_0,\theta_0)} \cdot g_L(r) \cdot F(r,\theta) \tag{8}$$

S_K is the air kerma strength and Λ is the dose rate constant[4]. The geometry function G_L is given in equation (4) of Rivard *et al* (2004). The values of the radial dose function $g_L(r)$ and the anisotropy function $F(r, \theta)$ were taken from the AAPM/ESTRO consensus dataset for the relevant source type (Perez-Calatayud *et al* 2012), available e.g. via the internet site of the University of Valencia at www.uv.es/braphyqs/. A possible modification of the spatial dose distribution due to the presence of the steel needle which held the source was not taken into account.

The effect of the uncertainty of the relative position of the pellet and the Ir-192 source was determined by a Monte Carlo analysis carried out in Matlab. Due to symmetry reasons, the calculation had to be performed for only one alanine pellet at each distance of 1 cm, 2 cm, 3 cm and 5 cm. The volume of the pellet was subdivided into a grid with a uniform spacing of 0.9 mm[5]. For $5.5 \cdot 10^4$ points inside the volume of each pellet, the dose was obtained from equation (8). The experimentally determined sensitivity function s (see appendix A) was then interpolated to these points as well to calculate the product $k_r = k_s \cdot k_V$ directly (compare equations (4), (6) and (7)). For every distance d, the calculation was repeated 200 times. Each time, three new values for the offset of the centre of the pellet in the three directions were obtained from a random generator producing normally distributed numbers with a mean of zero and a standard deviation of 0.05 mm and 0.13 mm corresponding to the horizontal and vertical positioning uncertainties of the pellets with respect to the source (see appendix C). These values were added to the theoretical position of the centre of the pellet. The results for k_V, k_s and

[4] At PTB, the product of the RAKR and Λ is used instead. The RAKR was determined at PTB with a relative uncertainty of 0.9% . For the dose rate constant Λ, the value of $1.113 \cdot 10^4$ published by Selbach *et al* (2012) with an uncertainty of 1.8% was used.

[5] Calculations with higher spatial resolution did not yield different results.

Table 1. Correction factors k_V and k_s and their product k_r and its relative uncertainty in % are given as a function of the distance d from the geometrical centre of the source to the geometrical centre of the detector for one single pellet. For the calculation of the uncertainty $u_r^{\mathrm{pos}}(k_r)$ an uncertainty of the pellet position of 0.05 mm in both horizontal directions and of 0.13 mm in the vertical direction was assumed. $u_r^{\mathrm{TG43}}(k_r)$ is an estimate of the uncertainty of k_r caused by uncertainties of the radial dose function and the geometry function from (8).

d in cm	k_V	k_s	k_r	$u_r^{\mathrm{pos}}(k_r)$ (%)	$u_r^{\mathrm{TG43}}(k_r)$ (%)
1	0.9970	1.0016	0.9986	1.13	0.06
2	0.9865	1.0004	0.9869	0.56	0.10
3	0.9829	1.0002	0.9831	0.42	0.08
5	0.9872	1.0001	0.9872	0.24	0.01

their product $k_r = k_V \cdot k_s$, listed in table 1 above, were obtained as the arithmetic mean of the 200 values for each position. The relative uncertainty u_r^{pos} given in the fifth column of table 1 is the standard deviation calculated from the scatter of the 200 values. The largest part of the uncertainty of u_r^{pos} is caused by the position itself (dose at the centre of the pellet).

In order to estimate the uncertainty due to the uncertainties of the radial dose function and the geometry function, the calculation was repeated using only a $1/r^2$ dependence of the dose distribution. The difference of the resulting k_r $(1/r^2)$ corrections to the k_r corrections obtained using (8) was multiplied by 6% . For the range of distances between 1 cm and 5 cm, a value of 6% was taken from the publication by Rivard *et al* (2004) as a conservative estimate of the relative uncertainty associated with the radial dose function and the geometry function. The resulting relative uncertainty u_r^{TG43} is listed in the rightmost column of table 1 and attains its maximum value of 0.1% at a distance of 2 cm.

2.6. Uncertainty considerations

The uncertainty budget is presented in table 2. The left column describes the source of the uncertainty. The following columns list the relative uncertainty components in per cent, for distances d = 1 cm, 2 cm, 3 cm and 5 cm (from left to right). When only one value is given, it is the same for all distances. Except for the uncertainties u_r^{pos} of the correction k_r which are of type A, the stated values of the relative standard uncertainties are type B uncertainties according to the GUM (JCGM100 2008).

The first component from the alanine measurement is the uncertainty due to the irradiation of the pellets required for calibration. The following components are associated with the amplitude of the base and the amplitude of the probes used for the actual measurement[6]. For the base, $N_b = 4$ pellets irradiated with 25 Gy and $N_b = 4$ unirradiated ones were used. At d = 1 cm, four simultaneous irradiations of 8 pellets were carried out, for the larger distances only two irradiations per distance were deemed necessary, leading to a total of n = 32 (d = 1 cm) and n = 16 pellets (elsewhere). For each pellet i, a value $r_i = \mathcal{A}_{D,i} / D_{0,\mathrm{Ir}}$ was obtained. All n values were averaged. Care had to be taken as to which uncertainty components would be reduced by averaging and which ones would not, due to correlations.

[6] The calculation of the amplitude uncertainties was detailed in previous publications (Anton 2006, Anton *et al* 2013). Components for the uncertainties of the mass, the irradiation temperature, the homogeneity of the alanine/paraffin mixture and the amplitude determination itself are included.

Table 2. Uncertainty budget for the determination of the response r of the alanine dosimeter to Ir-192 radiation relative to Co-60 radiation.

	Relative uncertainty component in %			
Source of the uncertainty	d = 1 cm	d = 2 cm	d = 3 cm	d = 5 cm
Alanine measurement				
Dose $D_{0,Co}$ of the base (Co-60)		0.22		
Base amplitude (25 Gy 0 Gy^{-1}, N_b = 4)		0.23		
Probe amplitude (n = 32/n = 16)	0.13	0.17	0.17	0.17
Correction factor k_r, positioning	0.57	0.28	0.21	0.12
Correction factor k_r, TG43	0.06	0.10	0.08	0.01
Subtotal (excluding $D_{0,Co}$)	0.63	0.41	0.36	0.31
Ir-192 source calibration				
Reference air kerma rate RAKR		0.9		
Dose rate constant Λ		1.8		
Total	2.12	2.07	2.06	2.05

The calculation of the correction k_r and its uncertainty were detailed in the previous section. The values of $u_r^{pos}(k_r)$ listed in table 1, which are valid for one single pellet position, are divided by $\sqrt{4}$ because essentially four independent positions are averaged, corresponding to the four PMMA tubes. It may be discussed whether a repeated irradiation corresponds to a new, independent position (which would reduce the uncertainty further), but since a correlation of the position for repeated irradiations cannot be excluded, the approach presented is preferred. However, this means that in spite of the efforts to minimize geometrical uncertainties, at d = 1 cm the major contribution to the uncertainties associated with the alanine measurement is still due to k_r. The uncertainty component u_r^{TG43} is not reduced by multiple measurements.

The subtotal given in the next line of the budget sums up all components due to the alanine measurement, apart from the calibration dose $D_{0,Co}$ (irradiation in the reference field) and varies between 0.3% and 0.6% for d = 5 cm and d = 1 cm, respectively. Compared to the uncertainties of the RAKR and the dose rate constant Λ, the uncertainty associated with the alanine measurements is rather small.

2.7. Monte Carlo simulations

The simulations presented in this work were carried out at the Institut für Medizinische Physik und Strahlenschutz IMPS (University of Applied Sciences Giessen, Germany) using the EGSnrc package (Kawrakow *et al* 2010) with the user codes egs_chamber (Wulff *et al* 2008) for the calculation of the alanine response and FLURZnrc (Kawrakow 2000) for an estimation of the mean photon energies at the measurement depth.

The iridium spectrum was taken from the NUDAT database (www.nndc.bnl.gov/nudat2) as recommended by AAPM and ESTRO (Perez-Calatayud *et al* 2012). The experimental set-up given in figure 2 including the steel needle was modelled using the egs + + geometry classes (Kawrakow *et al* 2009). The microSelectron V2 was modelled in detail according to (Ubrich *et al* 2014) and is illustrated in figure 3. The surface of the iridium core is an isotropic source with the spectrum from the NUDAT database. The active core is encapsulated by stainless steel AISI 316L.

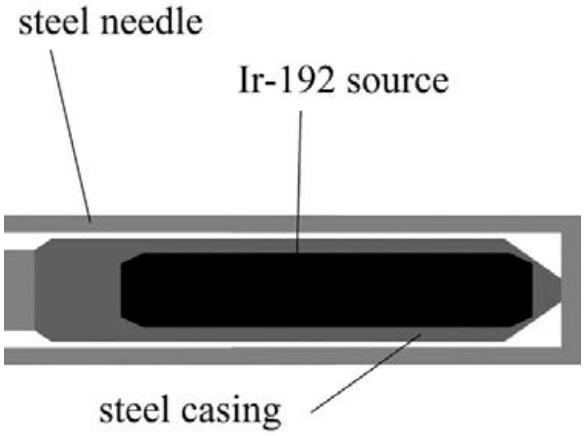

Figure 3. Schematic drawing of the egs + + model of the iridium source in its steel casing and inside the steel applicator needle. The casing (dark grey) around the iridium (shown in black) is stainless steel AISI 316L (ρ = 8.02 g cm^{-3}). The cable to which the casing is fixed (left) is also made of AISI 316L but with a lower density (ρ = 4.81 g cm^{-3}). The outer rectangle represents the applicator needle which is also made of stainless steel (ρ = 8.06 g cm^{-3}). The space between the casing and the needle is filled with air.

As there is no positioning uncertainty in the Monte Carlo simulations, only one of the four alanine holders was simulated.

For the Co-60 reference field, the spectrum was obtained from an MC simulation, taking the realistic geometry of the irradiation source and its surroundings into account. The Co-60 data at the reference depth refer to a previous publication (Anton *et al* 2013).

For each depth d the calculation was carried out twice: the first one for a dose scoring volume made of water to obtain D_W; the second one with a dose scoring volume consisting of a homogeneous mixture of the atomic constituents of the alanine/paraffin pellets, in order to obtain D_{ala}. For the alanine pellets a density correction, already explained previously (Zeng *et al* 2005, Vörös *et al* 2012, Anton *et al* 2013) was applied. The calculations were performed with threshold cut-off energies AE = ECUT = 516 keV for electrons and AP = PCUT = 1 keV for photons. The cross sections for photons were *xcom* and for bremsstrahlung, *NIST*. Around $1.5 \cdot 10^{10}$ histories were needed for a statistical uncertainty of less than 0.1%.

For each depth, the ratio D_{ala}/D_W was then calculated and referred to the corresponding ratio for Co-60, i.e. r^{MC}; the simulated dose-to-water response relative to Co-60, was calculated as[7].

$$r^{MC}_{\text{Ir-192},d} = \frac{(D_{ala} / D_W)_{\text{Ir-192},d}}{(D_{ala} / D_W)_{Co}} . \tag{9}$$

The mean photon energy as a function of the distance d, $E_{\text{mean},\Phi}(d)$, was calculated with the user code FLURZnrc. For that purpose the geometry was simplified. The iridium source was placed in the centre of a cylindrical water phantom with a radius of r = 20 cm and a height of h = 40 cm. $E_{\text{mean},\Phi}(d)$ was scored in a cylindrical water shell of thickness Δd, where Δd

[7] The subscript Ir-192, d is dropped in what follows for the sake of clarity.

Table 3. Response r of the alanine dosimeter to Ir-192 radiation relative to Co-60 radiation. Experimental results and results of a Monte Carlo simulation are listed as a function of the distance d between the centre of the source and the centre of the detector. For further explanations, please see the text.

$E_{\mathrm{mean},\Phi}$ in keV	d in cm	r	$u_r(r)$ ala in %	$u_r(r)$ total in %	r_{MC}	$u_r(r_{\mathrm{MC}})$ in %	r_{MC}/r
325.3	1	0.9808	0.66	2.12	0.9791	0.20	0.998
297.6	2	0.9696	0.47	2.07	0.9781	0.20	1.009
274.9	3	0.9662	0.43	2.06	0.9743	0.20	1.008
243.9	5	0.9602	0.38	2.05	0.9679	0.20	1.008

corresponds to the diameter of the alanine pellets. The shell height corresponded to the height of two alanine pellets (5.4 mm). The results are listed in table 3 along with the experimental data.

3. Results and discussion

Experimental and Monte Carlo results are summarized in table 3, as a function of the distance d between the centre of the source and the centre of the detector. The first column lists the mean photon energy at the distance to the source (mean with reference to the fluence Φ), the second one the distance d. The experimental results obtained for the relative response r are shown in the third column. The following ones display the associated relative uncertainty. The values listed under 'ala' represent the uncertainties without the components for the RAKR and Λ. Comparison with the subtotal in table 2 shows the small increase caused by the inclusion of the uncertainty component due to the calibration dose $D_{0,\mathrm{Co}}$. The values listed under 'total' include all components shown in table 2. The values of the relative response obtained from the Monte Carlo simulations are given in the next columns, along with their statistical uncertainty of 0.2%. The last column represents the ratio between the simulated and the experimental results. A graphical representation of the data is given in figure 4.

The experimentally determined relative response decreases from 98% at $d = 1$ cm to 96% at $d = 5$ cm. The decrease is slightly weaker for the Monte Carlo simulation results. For $d \geqslant 2$ cm the calculated response is about 1% higher than the experimental value. Although the difference is not significant in view of the measurement uncertainty, it has to be kept in mind that the simulation yields the ratio of the absorbed dose to alanine relative to the absorbed dose to water whereas the experimental results reflect the radical concentration in alanine.

In two publications dealing with the alanine response to medium energy x-rays (Zeng and McCaffrey 2005, Waldeland *et al* 2010), a similar phenomenon was observed. For medium energy x-rays, the measured relative response was approximately 5% lower than the simulated response calculated according to equation (9). As pointed out by the authors, the discrepancy could be explained by a decrease of the relative detection efficiency[8] of the alanine dosimeter with decreasing energy of the impinging photons, as had been predicted by a microdosimetric one-hit detector model (Olko 2002, Olko and Waligórski 2002). The mean energy of the iridium radiation is larger than the mean energy of medium energy x-rays with their predicted relative efficiency of approximately 95% and the (reference) Co-60 spectrum, where the relative efficiency is 100% by definition. However, in view of the measurement uncertainties it is not possible to discern whether the observed difference between the simulated and the measured response is due to the decreasing efficiency or not.

[8] Relative efficiency means the number of radicals generated per unit of absorbed dose, relative to Co-60.

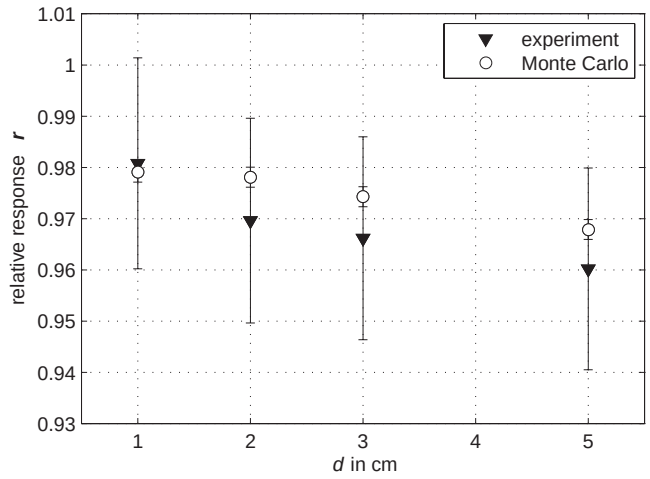

Figure 4. Response of the alanine dosimeter to Ir-192 radiation relative to Co-60 radiation as a function of the distance *d* between the centre of the source and the centre of the detector in cm. The filled triangles represent the experimental results, the error bars display the total uncertainty including primary standards and source calibration. The open circles display the Monte Carlo simulation results. For the Monte Carlo data, the error bars only show the statistical uncertainties.

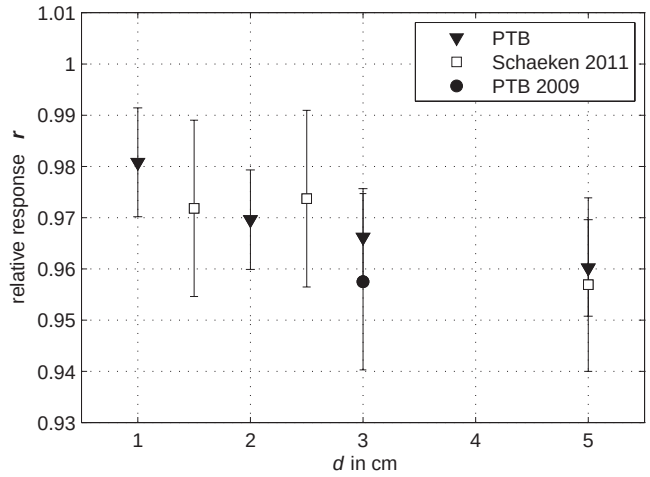

Figure 5. Response of the alanine dosimeter to Ir-192 radiation relative to Co-60 radiation as a function of the distance *d* between the centre of the source and the centre of the detector in cm. The filled triangles represent the experimental results, the open squares display experimental results by Schaeken *et al* (2011), the filled circle shows a result from a previous publication (Anton *et al* 2009). Error bars represent the total uncertainty excluding the uncertainty of the dose rate constant Λ.

Figure 5 compares our results to data published by Schaeken *et al* (2011) and to data from a previous publication (Anton *et al* 2009). The error bars represent the total uncertainty without the uncertainty of the dose rate constant Λ. Under these conditions, the relative uncertainty of Schaeken's data was stated as 1.8%, whereas the corresponding value for our data is 1.1%.

While there was practically no difference between Schaeken *et al* and this work concerning the alanine dosimetry itself (same type of pellets, nearly identical spectrometer, same parameters and data analysis method), there was a fundamental difference concerning the set-up for the irradiation: Schaeken and coworkers placed the detectors in the centre of the set-up and irradiated successively from six positions around the centre using trocar needles and an afterloader. Another difference is that the dose to the detectors was estimated with the help of a commercial therapy planning system. The fact that the inhomogeneous distribution of the sensitivity was not taken into account by Schaeken *et al* (2011) is probably insignificant, regarding the magnitude of the correction k_s. The agreement between the data of Schaeken *et al* (2011) and the present work is good within the stated limits of uncertainty. This is still true if a possible systematic difference of 0.4% is taken into account which may be due to the use of different values of Λ (PTB: $\Lambda = 1.113$, TG-43: $\Lambda = 1.109$). The most important result is that the decrease of the response with an increasing distance from the source of approximately -0.4% cm^{-1} that was observed by Schaeken *et al* is confirmed. The decrease can be related to the decrease of the mean energy of the photons with an increasing distance of the measurement volume from the source.

The measurement result from 2009 was obtained for a distance $d = 3$ cm, albeit in the water-equivalent plastic RW-1. A value of $r = 0.958 \pm 0.017$ was obtained (Anton *et al* 2009), where the uncertainty does not contain the uncertainty of Λ. Within the limits of uncertainty, the agreement is still good, especially if one considers that the detector used in our earlier publication consisted of a mixture of alanine and paraffin powder which was compressed to a pellet only after irradiation.

Whereas authors of earlier publications assumed that the response of alanine to radiation from an Ir-192 source would be the same as for Co-60 radiation, it should now be clear both from this work as well as from the work by Schaeken *et al* (2011) that the response is significantly smaller than unity and that it decreases with an increasing distance from the source. The response in the therapeutically relevant range should now be known with satisfactory accuracy so that the alanine dosimeter might well be employed for quality assurance measurements in HDR brachytherapy using Ir-192.

4. Summary and outlook

In order to extend the database of radiation quality correction factors available for the alanine dosimeter, the response of alanine to radiation from an Ir-192 source with respect to the dose to water, relative to radiation from Co-60, was investigated experimentally as well as by Monte Carlo simulations.

For the experiments, great care was taken to minimize geometrical uncertainties, which is essential for accurate measurements in the near field of a radioactive source. Corrections for the dose distribution within the detector volume and the inhomogeneous detection probability were obtained from numerical calculations. The dose distribution was calculated using the update to the protocol TG-43 (Rivard *et al* 2004). The spatial variation of the relative detection probability within the resonator of the ESR spectrometer was determined experimentally.

Monte Carlo results were obtained using the EGSnrc code system. The simulation yielded the ratio of dose to alanine and dose to water. These values are on average approximately 1% higher than the experimentally determined values of the relative response for the distances from the source of 1 cm, 2 cm, 3 cm and 5 cm that were investigated. Approximate values for the mean energies of the photons at the measurement volumes were obtained using FLURZnrc. The decrease of the relative response with an increasing distance can be related

to the decrease of the mean photon energy. The difference between the simulation and experimental results may possibly be related to a decrease of the relative efficiency of the alanine dosimeter with decreasing photon energy, which was predicted by a microdosimetric one hit detector model (Olko 2002, Olko and Waligórski 2002). This, however, cannot be decided regarding the measurement uncertainty.

The decrease of the response with an increasing distance was observed earlier by Schaeken *et al* (2011). The uncertainties of our results are smaller, however, the agreement with Schaeken's data is good and the decrease thereby confirmed.

To sum up, the relative response of the alanine dosimeter is now known with an uncertainty of 1.1%, if the uncertainty of the dose rate constant is not taken into account. The corresponding correction factors for the radiation quality, which are just the reciprocal values of the relative response, depend on the distance d between the measurement point and the source and vary between $k_{\mathrm{Ir}}(d = 1\mathrm{cm}) = 1.020$ and $k_{\mathrm{Ir}}(d = 5\mathrm{cm}) = 1.041$.

Equipped with these data, measurements in near-clinical situations can now be performed, for example, in the fields of partially shielded applicators. Another interesting perspective for future work would be the extension of the measurement range of the alanine dosimeter towards even lower energies. This might even offer the opportunity of performing measurements in the fields of the novel miniature x-ray sources used in brachytherapy.

Acknowledgments

We wish to thank M Meier and D-M Boche for their help during the preparation, irradiation and measurement phases of this investigation. The accurate work of our mechanic O Tappe, which was essential for the success of this research, is also gratefully acknowledged.
Special thanks go to two very attentive referees for their constructive criticism which helped to improve this publication.
This work is supported by the EMRP joint research project MetrExtRT which has received funding from the European Union on the basis of Decision No 912/2009/EC. The EMRP is jointly funded by the EMRP participating countries within EURAMET and the European Union.

Appendix A. Distribution of the detection probability inside the HS resonator

In order to determine the relative sensitivity of the ESR spectrometer as a function of the distance ρ from the central axis (horizontal variation), a grain of alanine powder irradiated with a dose of several kGy was placed inside a small piece of a quartz capillary and fixed with molten paraffin wax. Nine unirradiated alanine pellets were prepared by drilling holes parallel to their symmetry axis with distances of 0.4 mm and between 0.8 mm and 2 mm in steps of 0.2 mm from the centre (see figure A1). The capillary was placed inside the holes. For each pellet, five scans were acquired. Between the scans the pellets were rotated by 72°, i.e. the resulting horizontal variation of the response represents an average over different angles. This corresponds to the experimental situation during the read-out of irradiated pellets. The dependence of the amplitude on the distance ρ from the centre, relative to the amplitude of the pellet with the irradiated alanine in the centre, is shown in figure A2. The data are normalized to the maximum of the fit.

The dependence of the amplitude on the vertical position was measured in a way described in a previous publication (Anton 2005). Horizontal and vertical dependencies s_ρ and s_z,

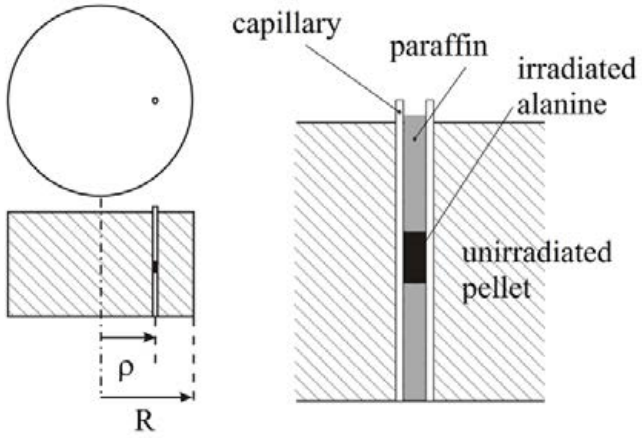

Figure A1. Schematic sketch of the arrangement used for measuring the relative sensitivity as a function of the distance ρ from the centre of the resonator. An (unirradiated) pellet with a quartz capillary and a grain of irradiated alanine placed at a distance ρ from the centre of the pellet is indicated. Left: top and side view. Right: detail.

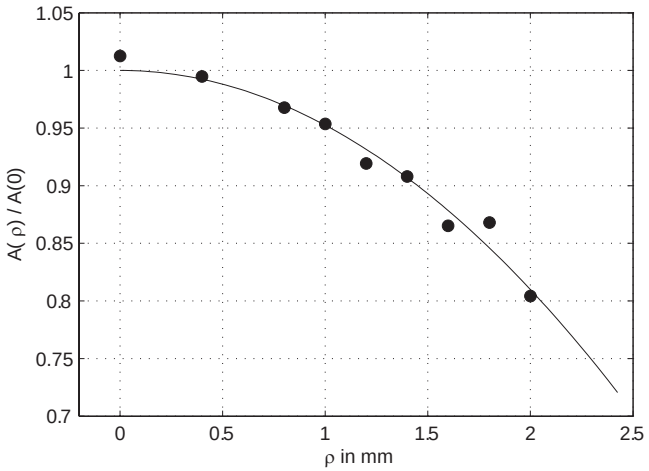

Figure A2. Relative amplitude measured with a grain of alanine irradiated with a high dose placed inside a quartz capillary and inside different unirradiated alanine pellets as a function of the radial distance ρ of the irradiated alanine from the centre of the pellet (compare figure A1). The filled circles represent the measurements whereas the continuous line displays a second order polynomial fit. The pellet radius R is 2.425 mm.

respectively, were approximated by parabolae with their apexes in the centre of the pellet to be read out. The dependence on the vertical position is much weaker.

$$s_\rho = A(\rho)/A(0) = 1 - 4.7522\cdot10^{-2}\,\mathrm{mm}^{-2}\cdot\rho^2 \tag{A.1}$$

$$s_z = A(z)/A(0) = 1 - 6.1615\cdot10^{-3}\,\mathrm{mm}^{-2}\cdot z^2 \tag{A.2}$$

In view of the comparatively small influence of the sensitivity distribution on the overall uncertainty budget, no detailed uncertainty analysis was carried out for $A(\rho)/A$ (0) and $A(z)/A$ (0). The sensitivity function s used above can therefore be stated as

$$s = s_\rho \cdot s_z = (1 - a\cdot\rho^2)\cdot(1 - b\cdot z^2) \tag{A.3}$$

with $a = 4.7522 \cdot 10^{-2}\text{mm}^{-2}$ and $b = 6.1615 \cdot 10^{-3}\text{mm}^{-2}$.

Appendix B. Volume- and sensitivity corrections: an analytical approximation

In order to gain some insight into the behaviour of the volume- and sensitivity correction factors k_V and k_s, an attempt was made to calculate the factors analytically according to equations (6) and (7). The geometry that was used is shown in figure B1. A cylindrical polar coordinate system is assumed to be centred at the centre of a pellet with radius R and height H. The pellet is indicated from above, the radiation is assumed to propagate in the $x-$ direction.

First, let us assume a dose distribution with a constant gradient g across the diameter of the pellet. The dose distribution f_{Co} defined in (2) can then be written as

$$f_{\text{Co}} = 1 - g\cdot\rho\cdot\cos\phi\,. \tag{B.1}$$

The dose is assumed not to vary in the y- and z-directions. This situation is representative for irradiations in the Co-60 reference field at a depth of 5 cm or a megavoltage x-ray reference field at a depth of 10 cm, when the beam direction is perpendicular to the symmetry axis of the irradiated pellets.

Using the sensitivity s from A.3, the integral

$$\int f_{\text{Co}}\cdot s\cdot \mathrm{d}V = \int_0^{2\pi}\mathrm{d}\,\phi\int_{-H/2}^{H/2}\mathrm{d}\,z\int_0^R \mathrm{d}\,r\cdot r\cdot(1 - g\cdot r\cdot\cos\phi)\cdot(1 - a\cdot\rho^2)\cdot(1 - bz^2) \tag{B.2}$$

yields the result

$$\int f_{\text{Co}}\cdot s\,\mathrm{d}V = \pi R^2 H\cdot\left(1 - a\frac{R^2}{2}\right)\cdot\left(1 - b\frac{H^2}{12}\right), \tag{B.3}$$

which is independent of g. Although it may be counterintuitive at first sight, the same result is obtained for pellets irradiated with the beam direction parallel to the symmetry axis of the pellet, i.e. if $f_{\text{Co}} = 1 - g\cdot z$. The result for $\int f_{\text{Co}}\mathrm{d}V$ is obtained by setting $a = 0$ and $b = 0$ which leaves just the volume of the cylinder. Hence, the expression on the right of the volume in equation (B.3) is the numerator of the sensitivity correction factor k_s. This again means that if the pellets under investigation also have a constant dose gradient across their diameter, the sensitivity correction as well as the volume correction will be unity (since the numerator and denominator of (6) and (7) will be equal), independent of the orientation of the pellet with respect to the beam direction. Thus, we have obtained the favourable result that the *alanine dosimeter will indicate the dose at the centre of the pellet as long as the pellets are exposed to radiation fields with a constant dose gradient*.

At least in the vicinity of a radioactive source, a significant deviation of the depth-dose curve from a constant gradient has to be expected. With the simplifying assumption that the radiation impinges only parallel to the beam axis from an iridium source at a distance d from the centre of the pellet, the dose distribution f_{Ir} can be written as

$$f_{\text{Ir}} = \frac{d^2}{(d+x)^2} = \left(1 + \frac{\rho\cos\phi}{d}\right)^{-2}. \tag{B.4}$$

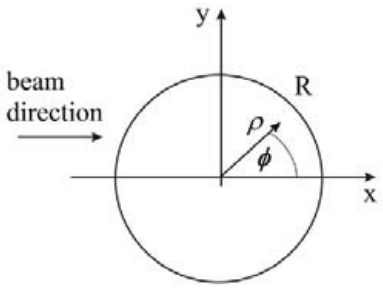

Figure B1. Sketch of the geometry for analytical calculations of the correction factors k_V and k_s. The pellet with radius R is shown from above. The radiation is assumed to be parallel to the x-axis. Cylindrical coordinates ρ, ϕ and z, adapted to the geometry of the pellet, are used.

Table B1. Sensitivity correction factor k_s analytically approximated (columns 2 and 3) compared to the numerical result using TG43 (last column) as a function of the distance d between source and detector.

d in cm	k_s approx		k_s
	R^2	R^6	
1	1.0023	1.0025	1.0016
2	1.0006	1.0006	1.0004
3	1.0003	1.0003	1.0002
5	1.0001	1.0001	1.0001

Even under these assumptions, computation of the three-dimensional integrals required for the calculation of k_V and k_s is a formidable task. On the other hand, the integration over a function like

$$f = 1 + c_1 \cdot x + c_2 \cdot x^2 + \ldots c_n \cdot x^n = 1 + c_1 \cdot \rho \cos\phi + c_2 \cdot (\rho\cos\phi)^2 + \ldots c_n \cdot (\rho\cos\phi)^n \tag{B.5}$$

may be tedious but not really difficult. A Taylor expansion of (B.4) up to x^6 yields the coefficients

$$c_2 = \frac{3}{d^2}, \quad c_4 = \frac{5}{d^4} \quad \text{and} \quad c_6 = \frac{7}{d^6}.$$

Coefficients for uneven exponents are not needed since the corresponding integrals over $\cos^{2m+1}\phi$ will vanish. Hence this (admittedly crude) approximation to the integral $\int f_{\mathrm{Ir}} s \mathrm{d}V$ yields

$$\int f_{\mathrm{Ir}}\, s\, \mathrm{d}V \approx H\, \pi\, R^2 \left(1 - b\frac{H^2}{12}\right) \cdot \left[1 + c_2 \cdot \frac{1}{4} R^2 + c_4 \cdot \frac{1}{8} R^4 + c_6 \cdot \frac{5}{64} R^6 \ldots \right.$$
$$\left. \ldots - \frac{a}{2} R^2 \cdot \left(1 + c_2 \cdot \frac{1}{3} R^2 + c_4 \cdot \frac{3}{16} R^4 + c_6 \cdot \frac{1}{8} R^6\right)\right] \tag{B.6}$$

The result for $\int f_{\mathrm{Ir}} \mathrm{d}V$ is again obtained by setting $a = 0$ and $b = 0$ in (B.6). Also using the results from the previous section, one obtains

$$k_s \approx \frac{1-\frac{a}{2}R^2}{1-\frac{a}{2}R^2\,\frac{1+\left(\frac{R}{d}\right)^2+\frac{15}{16}\left(\frac{R}{d}\right)^4+\frac{21}{24}\left(\frac{R}{d}\right)^6}{1+\frac{3}{4}\left(\frac{R}{d}\right)^2+\frac{5}{8}\left(\frac{R}{d}\right)^4+\frac{35}{64}\left(\frac{R}{d}\right)^6}} \approx \frac{1-\frac{a}{2}R^2}{1-\frac{a}{2}R^2\,\frac{1+\left(\frac{R}{d}\right)^2}{1+\frac{3}{4}\left(\frac{R}{d}\right)^2}} \tag{B.7}$$

The results are listed in table B1, where R^2 means the approximation only up to the second order is used (rightmost part of (B.7)) and R^6 means orders up to six are also used (middle part of (B.7)). The rightmost column gives the results from the fully three-dimensional, numerical calculation including the TG43 data for the dose distribution. In view of the strong simplifications that have been made, the approximation for the sensitivity correction is surprisingly good. Apart from confirming the correct order of magnitude of the numerically obtained results, the method outlined above may also serve to estimate possible volume and sensitivity corrections for other irradiation conditions such as irradiations in small fields used in modern radiotherapy, which made the effort worthwhile.

The volume correction k_V could be calculated as the ratio of (B.3) and (B.6), setting $a = 0$ and $b = 0$. However, in view of the large differences between our simplified assumptions and the more realistic dose distribution given by (8), this approximation would be too coarse. A comparison with the numerical results was therefore not considered to be worthwhile.

Appendix C. Geometrical uncertainties

This appendix describes briefly how the geometrical uncertainties, i.e. the uncertainties for the relative positions of the source and the detectors, were estimated.

The two mounting plates which hold the applicator needle and the tubes with the alanine detectors were produced on a CNC (computer numerical control) milling machine with a tolerance of 0.01 mm, corresponding to a standard uncertainty of 0.006 mm. This value applies to the horizontal as well as to the vertical direction. The distance pieces and the holder for the applicator needle were machined with a similar uncertainty. The resulting vertical uncertainty of the support for the needle is 0.03 mm. The same value applies for the vertical position of the tubes containing the alanine pellets. The largest component of the uncertainty is the vertical position of the source itself with respect to the mid plane between the two mounting plates which amounts to 0.12 mm. This value results from the measurement of the position of the bottom inside the applicator needle with respect to the outside of the needle. The uncertainty of the vertical position of the source inside the needle is assumed to be zero because the afterloader drives the source to a dead stop (end of the needle).

The excentricity of the PMMA tubes with respect to the centre of the arrangement was measured in the mid plane using a calliper. The tube was rotated bei 360° and the maximum difference between the readings of the calliper was 0.1 mm, which corresponds to a standard uncertainty of 0.03 mm. The inner diameter of the tubes was 4.95 mm, whereas the diameter of the alanine pellets is 4.85 mm. The full width of the rectangular distribution, thus describing the uncertainty of the horizontal pellet position inside the tube, is therefore 0.1 mm, i.e. the associated standard uncertainty is also 0.03 mm. The relative uncertainty of the horizontal position of the source inside the applicator needle is reduced to 10^{-5} by the geometry of the arrangement and is therefore neglected.

The geometrical uncertainty components are summarized in table C1. The mid column gives the full width of the rectangular distribution, the rightmost column the resulting standard uncertainties. The totals for the horizontal and vertical positioning uncertainty, which have been used for the calculation of the uncertainty of the correction k_r are shown in boldface.

Table C1. Uncertainty budget for the geometry.

Uncertainty component (Positioning)	Full width rectangular distribution in mm	Standard uncertainty in mm
Horizontal direction:		
Applicator needle	0.02	0.01
Detector tube	0.02	0.01
Tube excentricity	0.10	0.03
Space inside tube	0.10	0.03
Total:		**0.05**
Vertical direction:		
Base plate	0.02	0.01
Applicator needle	0.10	0.03
Source position	0.40	0.12
Detector tube	0.10	0.03
Total:		**0.13**

References

Adolfsson E, Alm Carlsson G, Grindborg J -E, Gustafsson H, Lund E and Carlsson Tedgren A 2010 Response of lithium formate EPR dosimeters at photon energies relevant to the dosimetry of brachytherapy *Med. Phys.* **37** 4946–59

Anton M 2005 Development of a secondary standard for the absorbed dose to water based on the alanine EPR dosimetry system *Appl. Radiat. Isot.* **62** 779–95

Anton M 2006 Uncertainties in alanine/ESR dosimetry at PTB *Phys. Med. Biol.* **51** 5419–40

Anton M, Kapsch R P, Krauss A, von Voigts-Rhetz P, Zink K and McEwen M 2013 Difference in the relative response of the alanine dosimeter for megavoltage x-ray and electron beams *Phys. Med. Biol.* **58** 3259–82

Anton M, Wagner D, Selbach H-J, Hackel T, Hermann R M, Hess C F and Vorwerk H 2009 *In vivo* dosimetry in the urethra using alanine/ESR during ^{192}Ir HDR brachytherapy of prostate cancer: a phantom study *Phys. Med. Biol.* **54** 2915–31

Antonovic L, Gustafsson H, Carlsson G A and Tedgren A C 2009 Evaluation of a lithium formate EPR dosimetry system for dose measurements around Ir-192 brachytherapy sources *Med. Phys.* **36** 2236–46

Calcina C S G, de Almeida A, Rocha J R O, Abrego F C and Baffa O 2005 Ir-192 HDR transit dose and radial dose function determination using alanine/ESR dosimetry *Phys. Med. Biol.* **50** 1109–17

Ciesielski B, Wielopolski L and Reinstein L E 1988 The energy response of agar-alanine phantom dosimeter to gamma radiation *Med. Phys.* **15** 380–3

De Angelis C, Onori S, Petetti E, Piermattei A and Azario L 1999 Alanine/EPR dosimetry in brachytherapy *Phys. Med. Biol.* **44** 1181

Guedea F, Ventura M, Polo A, Skowronek J, Malicki J, Bulski W, Zwierzchowski G, Torrecilla J L, Bilbao P and Borràs J M 2007 Patterns of care for brachytherapy in Europe (PC BE) in Spain and Poland: comparative results *Rep. Pract. Oncol. Radiother.* **12** 39–45

JCGM100 2008 Evaluation of measurement data: guide to the expression of uncertainty in measurement. GUM 1995 with minor corrections *Technical Report* BIPM, Working Group 1 of the Joint Committee for Guides in Metrology (JCGM/WG 1) (www.bipm.org/utils/common/documents/jcgm/JCGM_100_2008_E.pdfw)

Kawrakow I 2000 Accurate condensed history Monte Carlo simulation of electron transport: I. EGSnrc, the new EGS4 version *Med. Phys.* **27** 485–98

Kawrakow I, Mainegra-Hing E, Rogers D W O, Tessier F and Walters B R B 2010 The EGSnrc code system: Monte Carlo simulation of electron and photon transport *Technical Report NRC Report* PIRS-701 National Research Council Canada

Kawrakow I, Mainegra-Hing E, Tessier F and Walter B R B 2009 The EGSnrc C + + class library *NRC Report* PIRS-898 (rev A), Ottawa, Canada

Kolbun N, Levêque P, Abboud F, Bol A, Vynckier S and Gallez B 2010 Experimental determination of the radial dose distribution in high gradient regions around Ir-192 wires: comparison of electron paramagnetic resonance imaging, films and Monte Carlo simulations *Med. Phys.* **37** 5448–55

Krauss A 2006 The PTB water calorimeter for the absolute determination of absorbed dose to water in ^{60}Co radiation *Metrologia* **43** 259–72

Kuntz F, Pabst J Y, Delpech J P, Wagner J P and Marchioni E 1996 Alanine-ESR *in vivo* dosimetry: a feasibility study and possible applications *Appl. Radiat. Isot.* **47** 1183–8

Olko 2002 The microdosimetric one-hit detector model for calculating the response of solid state detectors *Radiat. Meas.* **35** 255–67

Olko P and Waligórski M P R 2002 Microdosimetric one hit detector model for calculation of dose and energy response of some solid state detectors *Radiat. Prot. Dosim.* **99** 381–2

Olsson S, Bergstrand E S, Carlsson A K, Hole E O and Lund E 2002 Radiation dose measurements with alanine/agarose gel and thin alanine films around a ^{192}Ir brachytherapy source, using ESR spectroscopy *Phys. Med. Biol.* **47** 1333–56

Palmer A L, Bradley D A and Nisbet A 2014 Dosimetric audit in brachytherapy *Br. J. Radiol.* **87** 20140105

Perez-Calatayud J, Ballester F, Das R K, DeWerd L A, Ibbott G S, Meigooni A S, Ouhib Z, Rivard M J, Sloboda R S and Williamson J F 2012 Dose calculation for photon-emitting brachytherapy sources with average energy higher than 50 keV: report of the AAPM and ESTRO *Med. Phys.* **39** 2904–29

Rivard M J, Coursey B M, DeWerd L A, Hanson W F, Saiful Huq M, Ibbott G S, Mitch M G, Nath R and Williamson J F 2004 Update of AAPM task group No. 43 report: a revised AAPM protocol for brachytherapy dose calculations *Med. Phys.* **31** 633–74

Schaeken B, Cuypers R, Goossens J, Van den Weyngaert D and Verellen D 2011 Experimental determination of the energy response of alanine pellets in the high dose rate ^{192}Ir spectrum *Phys. Med. Biol.* **56** 6625–34

Schaeken B and Scalliet P 1996 One year of experience with alanine dosimetry in radiotherapy *Appl. Radiat. Isot.* **47** 1177–82

Schultka K, Ciesielski B, Serkies K, Sawicki T, Tarnawska Z and Jassem J 2006 EPR/Alanine dosimetry in LDR brachytherapy: a feasibility study *Radiat. Prot. Dosim.* **120** 171–5

Selbach H-J, Bambynek M, Aubineau-Lanièce I, Gabris F, Guerra A S, Toni M P, de Pooter J, Sander T and Schneider T 2012 Experimental determination of the dose rate constant for selected ^{125}I- and ^{192}Ir-brachytherapy sources *Metrologia* **49** S219–22

Ubrich F, Wulff J, Engenhart-Cabillic R and Zink K 2014 Correction factors for source strength determination in HDR brachytherapy using the in-phantom method *Z. Med. Phys.* **24** 138–52

Vörös S , Anton M and Boillat B 2012 Relative response of alanine dosemeters for high-energy electrons determined using a Fricke primary standard *Phys. Med. Biol.* **57** 1413–32

Waldeland E, Hole E O, Sastuen E and Malinen E 2010 The energy dependence of lithium formate and alanine EPR dosimeters for medium energy x-rays *Med. Phys.* **37** 3569–73

Wulff J, Zink K and Kawrakow I 2008 Efficiency improvements for ion chamber calculations in high energy photon beams *Med. Phys.* **35** 1328–36

Zeng G G and McCaffrey J P 2005 The response of alanine to a 150 kev x-ray beam *Rad. Phys. Chem.* **72** 537–40

Zeng G G, McEwen M R, Rogers D W O and Klassen N V 2005 An experimental and Monte Carlo investigation of the energy dependence of alanine/EPR dosimetry: II. Clinical electron beams *Phys. Med. Biol.* **50** 1119–29

IOP Publishing | Institute of Physics and Engineering in Medicine Physics in Medicine & Biology

Phys. Med. Biol. **61** (2016) N70–N79 doi:10.1088/0031-9155/61/3/N70

Note

Perturbation correction for alanine dosimeters in different phantom materials in high-energy photon beams

P von Voigts-Rhetz[1], M Anton[2], H Vorwerk[3] and K Zink[1,3]

[1] Institut für Medizinische Physik und Strahlenschutz—IMPS, Technische Hochschule Mittelhessen, University of Applied Sciences Giessen, Germany
[2] Physikalisch-Technische Bundesanstalt, Braunschweig, Germany
[3] Department of Radiotherapy and Radiation Oncology, University Medical Center Marburg, Philipps-Universität, Marburg, Germany

E-mail: philip.von.voigts-rhetz@kmub.thm.de

Received 31 August 2015, revised 27 October 2015
Accepted for publication 4 November 2015
Published 13 January 2016

Abstract

In modern radiotherapy the verification of complex treatments plans is often performed in inhomogeneous or even anthropomorphic phantoms. For dose verification small detectors are necessary and therefore alanine detectors are most suitable. Though the response of alanine for a wide range of clinical photon energies in water is well know, the knowledge about the influence of the surrounding phantom material on the response of alanine is sparse. Therefore we investigated the influence of twenty different surrounding/phantom materials for alanine dosimeters in clinical photon fields via Monte Carlo simulations. The relative electron density of the used materials was in the range $n_e/n_{e,w} = 0.20$ up to 1.69, covering almost all materials appearing in inhomogeneous or anthropomorphic phantoms used in radiotherapy. The investigations were performed for three different clinical photon spectra ranging from 6 to 25 MV-X and Co-60 and as a result a perturbation correction k_{env} depending on the environmental material was established. The Monte Carlo simulation show, that there is only a small dependence of k_{env} on the phantom material and the photon energy, which is below $\pm 0.6\%$. The results confirm the good suitability of alanine detectors for *in-vivo* dosimetry.

Keywords: perturbation correction, alanine, EGSnrc, phantom material, Monte Carlo

(Some figures may appear in colour only in the online journal)

1. Introduction

In modern radiotherapy, quality assurance measurements such as verifications of complicated treatment plans implying the use of small fields are becoming more and more important. One method of verification is the use of anthropomorphic phantoms and small dosimeters with a good spatial resolution. Commercial or home-made phantoms may consist of a variety of tissue-equivalent materials. For accurate *in vivo* dosimetry it is important to know the influence of the surrounding material on the response of clinically used dosimeters.

Several publications describe the general behaviour of alanine dosimeters (Ciesielski and Wielopolski 1994, Ruckerbauer *et al* 1996, Sharpe *et al* 1996, Schaeken and Scalliet 1996, Nagy *et al* 2002, Bergstrand *et al* 2003, Zeng *et al* 2004, 2005, Onori *et al* 2006, Waldeland and Malinen 2011). The use of alanine for clinical photon and electron beams is described by Anton *et al* (2013) and Vörös *et al* (2012). Previous publications investigated the suitability of alanine dosimeters for *in vivo* dosimetry (Indovina *et al* 1989, Anton *et al* 2009, Rech *et al* 2014, Wagner *et al* 2011). For that purpose Anton also investigated the influence of the surrounding material on the response of alanine dosimeters to Co-60 radiation (Anton *et al* 2009).

The aim of this work is to extend the investigation of Anton *et al* (2009) to a broader range of clinically applied photon beam qualities and a broader range of phantom materials and to establish a correction factor k_{env} to account for the different responses of alanine in different environments.

2. Materials and methods

The influence of different surrounding materials on the response of alanine dosimeters was investigated via Monte Carlo simulations using the EGSnrc code system (Kawrakow 2000a, 2000b, Kawrakow *et al* 2013). All simulations were performed with the DOSRZnrc user code (Rogers *et al* 2013a). The calculations were performed with the same EGSnrc parameter settings as in Anton *et al* (2013), i.e. the threshold/cut-off energies for the particle transport were set to ECUT = AE = 521 keV and PCUT = AP = 1 keV and all other transport parameters were set to their defaults. The photon sources were adapted with BEAMnrc (Rogers *et al* 2013b) to the Elekta linear accelerator ($E_0 = 6$, 10 and 25 MeV)[4] located at the Physikalisch-Technische Bundesanstalt (PTB), Braunschweig. For the Co-60 reference field, the spectrum was obtained from a Monte Carlo simulation of the irradiation facility of PTB (Chofor *et al* 2007).

Anton *et al* (2013) defined the relative response r_Q of alanine to radiation of quality Q in water relative to the reference beam quality Co-60 as

$$r_Q = \frac{(D_{\mathrm{ala}}/D_{\mathrm{w}})_{Q,\mathrm{w}}}{(D_{\mathrm{ala}}/D_{\mathrm{w}})_{\mathrm{Co-60,w}}}, \tag{1}$$

where D_{ala} is the dose to alanine, D_{w} is the absorbed dose to water and Q denotes the beam quality specifier. Replacing the surrounding water w in the clinical beam by a medium env yields

$$r_{Q,\mathrm{env}} = \frac{(D_{\mathrm{ala}}/D_{\mathrm{w}})_{Q,\mathrm{env}}}{(D_{\mathrm{ala}}/D_{\mathrm{w}})_{\mathrm{Co-60,w}}}. \tag{2}$$

The relationship between both quantities r_Q and $r_{Q,\mathrm{env}}$ is given by

[4] In the following, these qualities will be designated as 6 MV-X, 10 MV-X and 25 MV-X, respectively.

Table 1. Phantom materials examined in this study. The first line indicates the reference, liquid water. The second group comprises commercially available tissue equivalent materials, the third group consists of materials with a given composition, but with a scaled density. n_e is the mass-normalized electron density (in m_u^{-1}, where m_u is the atomic mass unit), $n_{e,w}$ is the corresponding value for water. d is the depth of measurement in cm.

Material	n_e in m_u^{-1}	$n_e/n_{e,w}$	d in cm
Water	0.5556	1.000	5.0
SB-3 (bone)	0.9386	1.689	3.0
POM	0.7472	1.345	3.7
ICRU PMMA	0.6313	1.136	4.4
PA-6	0.6266	1.128	4.4
RW3	0.5606	1.009	5.0
LN450	0.2433	0.438	11.4
LN300	0.1623	0.292	17.1
CB2—10% CaCO3	0.6340	1.141	4.4
CB2—30% CaCO3	0.7135	1.284	3.9
CB2—50% CaCO3	0.8160	1.469	3.4
Water 1.5	0.8333	1.500	3.3
Water 0.5	0.2778	0.500	10.0
Water 0.4	0.2222	0.400	12.5
Water 0.35	0.1944	0.350	14.3
Water 0.3	0.1667	0.300	16.7
Water 0.25	0.1389	0.250	20.0
Water 0.2	0.1111	0.200	25.0
LN350	0.1894	0.341	14.7
LN325	0.1758	0.316	15.8

$$r_{Q,\mathrm{env}} = \frac{(D_{\mathrm{ala}}/D_{\mathrm{w}})_{Q,\mathrm{w}}}{(D_{\mathrm{ala}}/D_{\mathrm{w}})_{\mathrm{Co-60,w}}} \cdot \frac{(D_{\mathrm{ala}}/D_{\mathrm{w}})_{Q,\mathrm{env}}}{(D_{\mathrm{ala}}/D_{\mathrm{w}})_{Q,\mathrm{w}}} = r_Q \cdot r_{\mathrm{env}}, \tag{3}$$

hence the correction factor k_{env} is given as

$$k_{\mathrm{env}} = \frac{1}{r_{\mathrm{env}}} = \frac{(D_{\mathrm{ala}}/D_{\mathrm{w}})_{\mathrm{Q,w}}}{(D_{\mathrm{ala}}/D_{\mathrm{w}})_{\mathrm{Q,env}}}. \tag{4}$$

In order to determine $r_{Q,\mathrm{env}}$ and k_{env}, different tissue-equivalent materials ranging from SB-3 (cortical bone) to LN-300 (lung) were used as a phantom material for our investigation (see table 1). All information on the materials was taken from the data sheets supplied by GAMMEX RMI, Germany. Two material compositions (water and the lung-equivalent LN 300) were additionally scaled to different densities with the aim of extending the density range covered. In all cases the reference material was liquid water.

A cylindrical phantom with a radius of 30 cm and a depth of 60 cm, consisting of the respective material, was designed to house a cylindrical scoring volume with a diameter of 1.0 cm and a depth of 0.5 cm, the latter representing a stack of four alanine pellets that often serves as a detector in alanine dosimetry. In order to simulate D_{ala}, the scoring volume consisted of an alanine/paraffin mixture, corresponding to the composition of commercially available Harwell pellets (Anton *et al* 2013) see. The same volume was filled with water in order to simulate D_{w}. The geometrical centre of the scoring volume was positioned in the phantom at a water-equivalent depth of $d_{\mathrm{w}} = 5$ cm:

Table 2. Monte Carlo based results of the response of alanine dosimeters with respect to the absorbed dose to water for different surrounding phantom materials and beam qualities. If this value is referred to $(D_{ala}/D_w)_{Co-60,w}$ for Co-60 radiation under reference conditions, the relative response $r_{Q,env}$ is obtained (see equation (3)). The first line indicates the reference, liquid water. The first group of data was obtained for commercially available tissue-equivalent materials, the second group for fictitious materials with a given composition, but with a scaled electron density.

		Co-60			6 MV-X		
Surrounding material	$n_e/n_{e,w}$	$(D_{ala}/D_w)_{Q,env}$	$r_{Q,env}$	k_{env}	$(D_{ala}/D_w)_{Q,env}$	$r_{Q,env}$	k_{env}
Water	1.000	0.9739	1.0000	1.0000	0.9676	0.9936	1.0000
SB-3(bone)	1.689	0.9729	0.9990	1.0010	0.9654	0.9913	1.0023
POM	1.345	0.9733	0.9994	1.0006	0.9679	0.9939	0.9997
ICRU PMMA	1.136	0.9732	0.9993	1.0007	0.9683	0.9943	0.9992
PA-6	1.128	0.9731	0.9992	1.0008	0.9676	0.9936	1.0000
RW3	1.009	0.9734	0.9996	1.0004	0.9695	0.9955	0.9981
LN450	0.438	0.9732	0.9994	1.0006	0.9704	0.9965	0.9971
LN300	0.292	0.9722	0.9984	1.0017	0.9680	0.9940	0.9996
CB2—10%	1.141	0.9730	0.9991	1.0009	0.9684	0.9944	0.9992
CB2—30%	1.284	0.9743	1.0005	0.9995	0.9671	0.9931	1.0005
CB2—50%	1.469	0.9739	1.0001	0.9999	0.9696	0.9957	0.9979
Water 1.50	1.50	0.9726	0.9987	1.0013	0.9675	0.9935	1.0001
Water 0.50	0.500	0.9740	1.0002	0.9998	0.9683	0.9943	0.9992
Water 0.40	0.400	0.9736	0.9998	1.0002	0.9688	0.9948	0.9988
Water 0.35	0.350	0.9734	0.9995	1.0005	0.9683	0.9943	0.9993
Water 0.30	0.300	0.9738	0.9999	1.0001	0.9705	0.9965	0.9970
Water 0.25	0.250	0.9743	1.0005	0.9995	0.9686	0.9946	0.9989
Water 0.20	0.200	0.9736	0.9998	1.0002	0.9695	0.9956	0.9980
LN350	0.341	0.9729	0.9990	1.0010	0.9667	0.9926	1.0010
LN325	0.316	0.9727	0.9988	1.0012	0.9681	0.9941	0.9994

$$d_w = d \cdot \frac{n_{e,w}}{n_e} \tag{5}$$

This means that the geometrical centre of the detector volume was placed at a depth of $d = 3$ cm for the bone-equivalent SB-3, whereas for the lung-equivalent material LN-300 a depth of $d = 17$ cm resulted (see table 1). In all cases the photon source, modelled as a point source, was placed 100 cm in front of the phantom surface, the radius of the circular field was $R = 5$ cm at the surface. The dose was scored within the detector volume once for an alanine/paraffin mixture and once for liquid water. From the two results, the ratio of the absorbed dose to alanine and the absorbed dose to water was calculated and compared to the corresponding ratio under reference conditions (irradiation with a Co-60 source, field radius $R = 5$ cm at the phantom surface, 5 cm depth in a water phantom), yielding $r_{Q,env}$ according to equation (2). The number of histories to be calculated was chosen so that a statistical uncertainty of 0.13% resulted for D_{ala} and 0.1% for D_w in each phantom material. In total, a relative (statistical) uncertainty of approximately 0.2% for the relative response $r_{Q,env}$ resulted.

Table 3. Monte Carlo based results of the response of alanine dosimeters with respect to the absorbed dose to water for different surrounding materials and radiation qualities. If this value is referred to $(D_{ala}/D_w)_{Co-60,w}$ for Co-60 radiation under reference conditions, the relative response $r_{Q,env}$ is obtained (see equation (3)). The first line indicates the reference, liquid water. The first group of data was obtained for commercially available tissue-equivalent materials, the second group for fictitious materials with a given composition, but with a scaled electron density.

		10 MV-X			25 MV-X		
Surrounding material	$n_e/n_{e,w}$	$(D_{ala}/D_w)_{Q,env}$	$r_{Q,env}$	k_{env}	$(D_{ala}/D_w)_{Q,env}$	$r_{Q,env}$	k_{env}
Water	1.000	0.9655	0.9914	1.0000	0.9642	0.9901	1.0000
SB-3(bone)	1.689	0.9609	0.9867	1.0047	0.9592	0.9850	1.0052
POM	1.345	0.9651	0.9910	1.0004	0.9641	0.9900	1.0001
ICRU PMMA	1.136	0.9664	0.9924	0.9990	0.9647	0.9906	0.9995
PA-6	1.128	0.9672	0.9931	0.9982	0.9642	0.9901	1.0000
RW3	1.009	0.9659	0.9919	0.9995	0.9646	0.9905	0.9996
LN450	0.438	0.9664	0.9924	0.9990	0.9652	0.9911	0.9990
LN300	0.292	0.9671	0.9931	0.9983	0.9671	0.9931	0.9970
CB2—10%	1.141	0.9663	0.9923	0.9991	0.9644	0.9903	0.9998
CB2—30%	1.284	0.9668	0.9928	0.9986	0.9651	0.9911	0.9990
CB2—50%	1.469	0.9660	0.9919	0.9994	0.9637	0.9895	1.0006
Water 1.50	1.500	0.9678	0.9938	0.9976	0.9651	0.9910	0.9991
Water 0.50	0.500	0.9662	0.9921	0.9993	0.9641	0.9900	1.0001
Water 0.40	0.400	0.9669	0.9929	0.9985	0.9657	0.9916	0.9985
Water 0.35	0.350	0.9670	0.9929	0.9985	0.9667	0.9927	0.9974
Water 0.30	0.300	0.9677	0.9937	0.9977	0.9675	0.9935	0.9966
Water 0.25	0.250	0.9686	0.9946	0.9968	0.9675	0.9934	0.9966
Water 0.20	0.200	0.9691	0.9951	0.9963	0.9694	0.9955	0.9946
LN350	0.341	0.9657	0.9916	0.9997	0.9659	0.9918	0.9983
LN325	0.316	0.9659	0.9919	0.9995	0.9662	0.9922	0.9979

3. Results

For each of the beam qualities investigated, tables 2 and 3 list the ratio $(D_{ala}/D_w)_{Q,env}$, the relative response $r_{Q,env}$ and the correction factor for the environment k_{env} according to equation (4).

Figures 1 and 2 show the relative response $r_{Q,env}$ as a function of the scaled electron density $n_e/n_{e,w}$ for different photon beam qualities. The filled symbols represent the data from this work for the water-equivalent depth of 5 cm. The open triangles represent the Monte Carlo based values of the relative response r_Q taken from Anton *et al* (2013) for a water environment at a depth of 10 cm, and the open circles indicate the corresponding experimental values also taken from Anton *et al* (2013). A more comprehensive comparison with the literature data is given in table 4.

For Co-60 radiation, the response $r_{Q,env}$ of the alanine dosimeter appears to be completely independent of the composition of the environment, at least within the range of materials investigated. Within uncertainty limits, its value is $r_{Q,env} = 1.0$, which means that k_{env} is approximately unity as well. This agrees with previous results (Anton *et al* 2009). Regarding the results for the photon spectra (6, 10 and 25 MV-X) two changes are obvious: (I) the mean value $\bar{r}_{Q,env}$ over the relative electron density slightly decreases with the photon energy. (II) For higher photon energies (10 and 25 MV-X) there is a small variation of the response

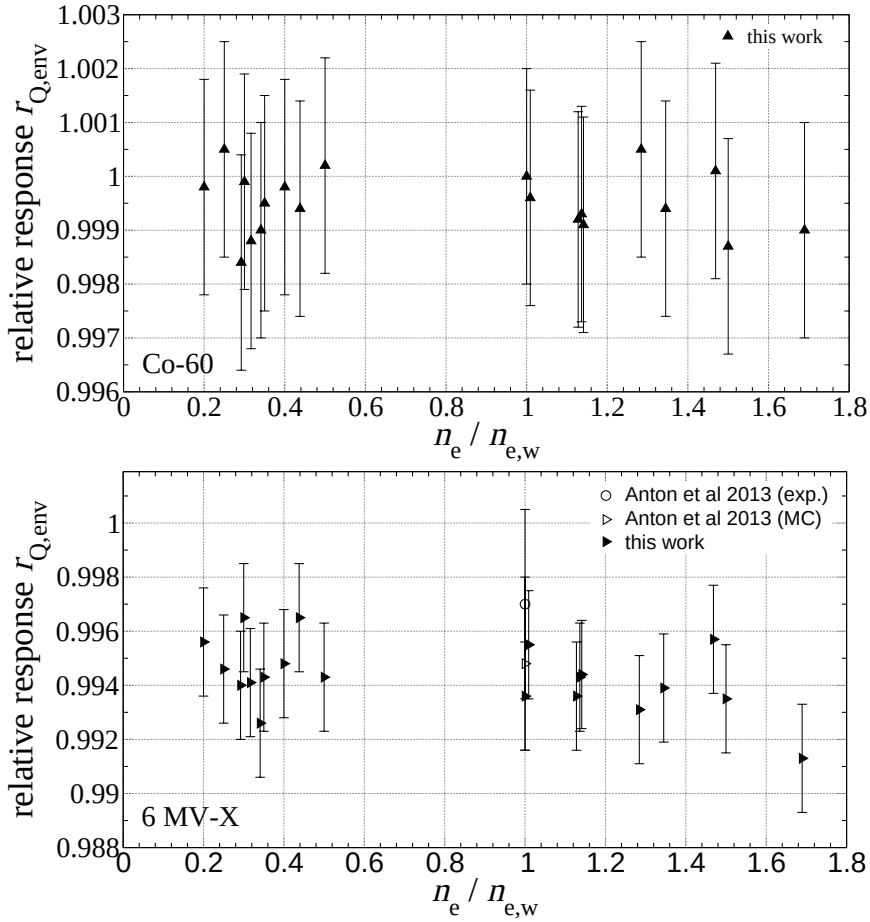

Figure 1. Relative response $r_{Q,\mathrm{env}}$ of alanine for different phantom materials as a function of the scaled electron density $n_e/n_{e,\mathrm{w}}$ for different photon beam qualities. Top: Co-60, bottom: 6 MV-X. The error bars represent the Type A uncertainties of the Monte Carlo data and the total uncertainty of the experimental data, respectively.

$r_{Q,\mathrm{env}}$ with the relative electron density of the surrounding phantom material for $n_e/n_{e,\mathrm{w}} < 0.4$ and $n_e/n_{e,\mathrm{w}} > 1.5$, which is not present for the 6 MV-X spectrum. The variation of k_{env} for $n_e/n_{e,\mathrm{w}} < 0.4$ is for the 25 MV-X spectrum more pronounced than for the 10 MV-X spectrum and statistically significant. The data point at $n_e/n_{e,\mathrm{w}} \approx 1.7$ is for all spectra somewhat below the mean value of k_{env}, for the 10 and 25 MV-X spectra this deviation is statistically significant. The mentioned small decrease of the alanine response r_Q with the photon beam quality Q was already established in our previous work, where only water was assumed as a phantom material (Anton *et al* 2013). Assuming a factorization of the effect of the beam quality and of the effect of the surrounding phantom material on the response of alanine, a correction factor k_{env} according to equations (3) and (4) may be established.

The data for k_{env} obtained from our simulation results are displayed in figure 3. The variation of k_{env} with the photon beam energy for electron densities $0.4 < n_e/n_{e,\mathrm{w}} < 1.5$ is within 0.2–0.3% and its value is close to unity, as can be seen in figure 3. For low electron density materials ($n_e/n_{e,\mathrm{w}} < 0.4$) a slight decrease of k_{env} is visible and this decrease is largest for the

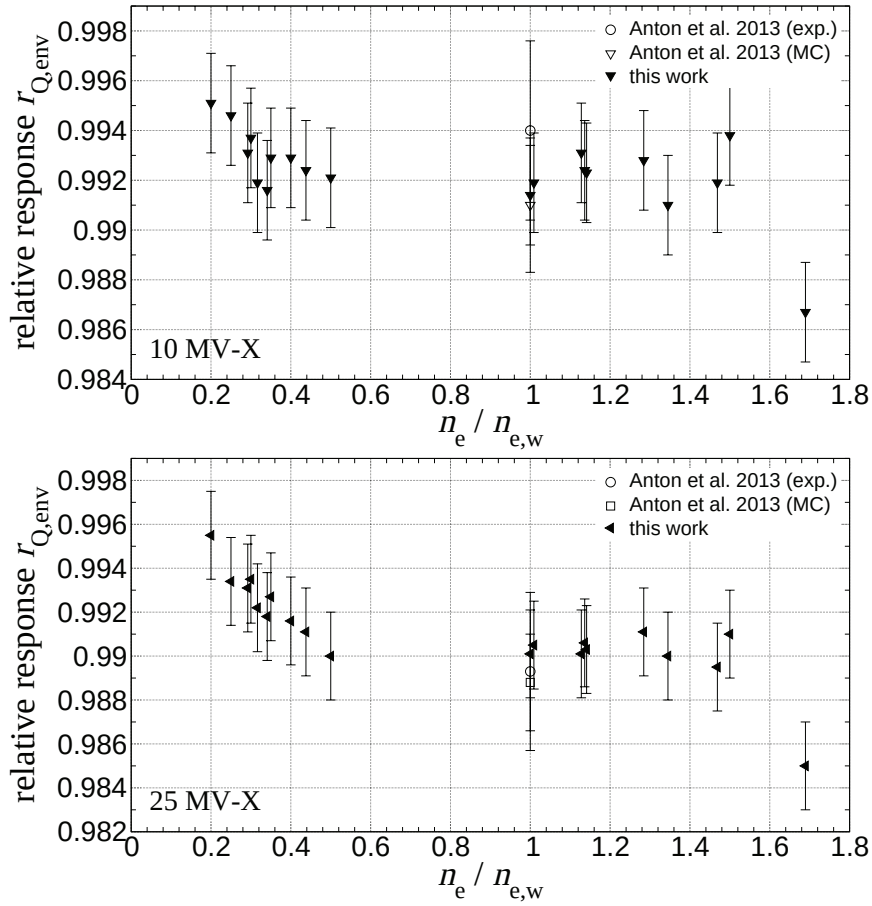

Figure 2. Relative response $r_{Q,\mathrm{env}}$ of alanine for different phantom materials, as a function of the scaled electron density $n_e/n_{e,\mathrm{w}}$ for different beam qualities. Top: 10 MV-X, bottom: 25 MV-X. The error bars represent the Type A uncertainties of the Monte Carlo data and the total uncertainty of the experimental data, respectively.

highest photon energy (25 MV-X). For densities $n_e/n_{e,w} > 1.6$, an increase of k_{env} is observed which is also more pronounced for the higher photon energies. However, the overall variation of k_{env} is within $\pm$0.5–0.6%, demonstrating the good suitability of alanine detectors for in vitro measurements in different phantom materials.

For a relative electron density in the range of $0.4 \leqslant n_e/n_{e,\mathrm{w}} \leqslant 1.5$, the influence of the environment is negligible for all MV-X qualities. For low and high-density environments, however, a correction might be desirable. One possibility to obtain a correction factor would be to interpolate the tabulated data. A more practical approach would be to use a common correction for all MV-X qualities, which may be obtained from the data given in table 5.

The mean values $\bar{k}_{\mathrm{env}}^{\mathrm{MV-X}}$ and there uncertainties $\bar{u}_{\mathrm{env}}^{\mathrm{MV-X}}$ over all three MV-X photon beam qualities were calculated assuming a rectangular distribution of the data with uncertain limits (see, e.g. Weise and Wöger (1999)), where the uncertainty of the limits is given by the statistical uncertainties. The relative (statistical) uncertainty of k_{env} for the whole range of beam qualities is $\sim$0.2%, the resulting uncertainty of the mean values $\bar{k}_{\mathrm{env}}^{\mathrm{MV-X}}$ is $\leqslant$0.19%.

Table 4. Comparison of the relative response $r_{Q,\mathrm{env}}$ of alanine in water ($n_e/n_{e,\mathrm{w}} = 1$) with experimental (exp.) and Monte Carlo (MC) based data given in literature. $u_{r_{Q,\mathrm{env}}}$ denotes the uncertainty of the data.

	6 MV-X		10 MV-X		24 MV-X	
	$r_{Q,\mathrm{env}}$	$u_{r_{Q,\mathrm{env}}}$	$r_{Q,\mathrm{env}}$	$u_{r_{Q,\mathrm{env}}}$	$r_{Q,\mathrm{env}}$	$u_{r_{Q,\mathrm{env}}}$
This work	0.994	0.002	0.991	0.002	0.990	0.002
Bergstrand *et al* (2003) (exp.)	—		0.987	0.005	—	
Zeng *et al* (2004) (MC)	0.997	0.003	0.995	0.003	0.994	0.003
Zeng *et al* (2004) (exp.)	0.996	0.005	0.992	0.006	0.995	0.005
Waldeland *et al* (2011) (MC)	0.998	0.011	1.002	0.010	1.004	0.011
Anton *et al* (2013) (exp.)	0.993	0.003	0.991	0.003	0.988	0.003

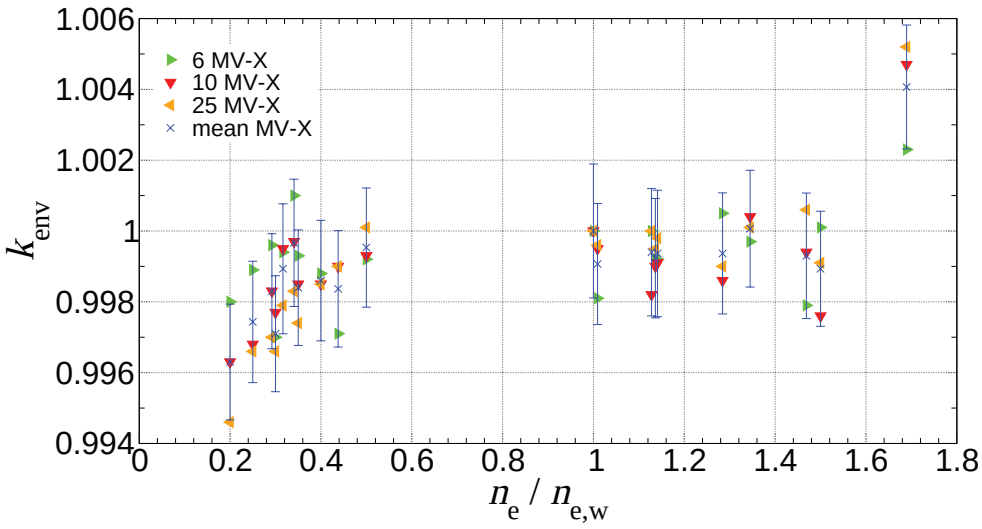

Figure 3. Environment correction factors k_{env} for different radiation qualities as a function of the relative electron density. The blue dots represent the mean of 6, 10 and 25 MV-X, the error bars indicate their standard uncertainty of the mean.

4. Conclusion

The response of alanine detectors in different phantom materials and photon beam qualities was investigated with Monte Carlo simulations. The results exhibit only a small variation of the defined environmental correction factor k_{env} with beam quality and electron density of the surrounding material (±0.5–0.6%), confirming the suitability of alanine detectors for *in vivo* dosimetry. Numerical data for a wide range of phantom materials and photon beam qualities are presented for the correction factor k_{env}. The data presented may help to decrease the uncertainties for *in vivo* dosimetry using alanine dosimeters in different phantom material environments.

Table 5. Mean value $\bar{k}_{\mathrm{env}}^{\mathrm{MV-X}}$ over photon energy of the environmental corrections factor and its standard uncertainty $\bar{u}_{\mathrm{env}}^{\mathrm{MV-X}}$. The first line indicates the reference, liquid water. The left group comprises commercially available tissue equivalent materials, the right group consists of materials with a given composition, but with a scaled density.

Material	$\bar{k}_{\mathrm{env}}^{\mathrm{MV-X}}$	$\bar{u}_{\mathrm{env}}^{\mathrm{MV-X}}$
water	1	0.001 89
SB-3 (bone)	1.0041	0.0018
POM	1.0001	0.0017
ICRU PMMA	0.9992	0.0017
PA-6	0.9994	0.0018
RW3	0.9991	0.0017
LN450	0.9984	0.0017
LN300	0.9983	0.0016
CB2—10% CaCO3	0.9994	0.0018
CB2—30% CaCO3	0.9994	0.0017
CB2—50% CaCO3	0.9993	0.0018
Water 1.5	0.9989	0.0016
Water 0.5	0.9995	0.0017
Water 0.4	0.9986	0.0017
Water 0.35	0.9984	0.0016
Water 0.3	0.9974	0.0016
Water 0.25	0.9971	0.0017
Water 0.2	0.9963	0.0016
LN350	0.9997	0.0018
LN325	0.9989	0.0018

Acknowledgments

This research was performed as part of the doctoral thesis of one of the authors at Philipps-Universität Marburg.

The work of one of the authors (M.A.) was supported by the EMRP joint research project MetrExtRT which received funding from the European Union on the basis of Decision No 912/2009/EC. The EMRP was jointly funded by the EMRP participating countries within EURAMET and the European Union.

We like thank the referees for the constructive criticism and the help to discover and correct a mistake at the electron density ratio.

References

Anton M, Kapsch R P and Hackel T 2009 Is there an influence of the surrounding material on the response of the alanine dosimetry system? *Phys. Med. Biol.* **54** 2029–35

Anton M, Kapsch R P, Krauss A, von Voigts-Rhetz P, Zink K and McEwen M 2013 Difference in the relative response of the alanine dosimeter to megavoltage x-ray and electron beams *Phys. Med. Biol.* **58** 3259–82

Anton M, Wagner D, Selbach H J, Hackel T, Hermann R M, Hess C F and Vorwerk H 2009 *In vivo* dosimetry in the urethra using alanine/ESR during (192)Ir HDR brachytherapy of prostate cancer–a phantom study *Phys. Med. Biol.* **54** 2915–31

Bergstrand E S, Shortt K R, Ross C K and Hole E O 2003 An investigation of the photon energy dependence of the EPR alanine dosimetry system *Phys. Med. Biol.* **48** 1753–71

Chofor N, Looe H K, Kapsch R P, Harder D, Willborn K C, Rühmann A and Poppe B 2007 Characterization of the radiation quality of Co-60 therapy units by the fraction of air kerma attributable to scattered photons *Phys. Med. Biol.* **52** N137

Ciesielski B and Wielopolski L 1994 The effects of dose and radiation quality on the shape and power saturation of the EPR signal in alanine *Radiat. Res.* **140** 105

Indovina P L, Benassi M, Giacco G C, Primavera A and Rosati A 1989 *In vivo* ESR dosimetry in total body irradiation *Strahlenther Onkol* **165** 611–6

Kawrakow I, Mainegra-Hing E, Rogers D W O, Tessier F and Walters B R B 2013 The EGSnrc code system: Monte Carlo simulation of electron and photon transport *PIRS-701* National Research Council of Canada

Kawrakow I 2000a Accurate condensed history Monte Carlo simulation of electron transport. I. EGSnrc, the new EGS4 version *Med. Phys.* **27** 485–98

Kawrakow I 2000b Accurate condensed history Monte Carlo simulation of electron transport. II. Application to ion chamber response simulations *Med. Phys.* **27** 499–513

Nagy V, Sholom S V, Chumak V V and Desrosiers M F 2002 Uncertainties in alanine dosimetry in the therapeutic dose range *Appl. Radiat. Isot.* **56** 917–29

Onori S, Bortolin E, Calicchia A, Carosi A, Angelis C and Grande S 2006 Use of commercial alanine and TL dosemeters for dosimetry intercomparisons among Italian radiotherapy centres *Radiat. Prot. Dosim.* **120** 226–9

Rech A B, Barbi G L, Ventura L H A, Guimaraes F S, Oliveira H F and Baffa O 2014 *In vivo* dose evaluation during gynaecological radiotherapy using L-alanine/ESR dosimetry *Radiat. Prot. Dosim.* **159** 194–8

Rogers D W O, Kawrakow I, Seuntjens J P, Walters B R B and Mainegra-Hing E 2013a NRC user codes for EGSnrc *Report* PIRS-702 National Research Council of Canada

Rogers D W O, Walters B and Kawrakow I 2013b BEAMnrc Users Manual *Report PIRS-509(a)revL* National Research Council of Canada

Ruckerbauer F, Sprunck M and Regulla D F 1996 Numerical signal treatment for optimized alanine/ESR dosimetry in the therapy-level dose range *ESR Dosimetry and Applications: Proc. of the 4th Int. Symp.* vol **47** pp 1263–8

Schaeken B and Scalliet P 1996 One year of experience with alanine dosimetry in radiotherapy *ESR Dosimetry and Applications: Proc. of the 4th Int. Symp.* vol **47** pp 1177–82

Sharpe P H G, Rajendran K and Sephton J P 1996 Progress towards an alanine/ESR therapy level reference dosimetry service at NPL *ESR Dosimetry and Applications: Proc. of the 4th Int. Symp.* vol **47** pp 1171–5

Vörös S, Anton M and Boillat B 2012 Relative response of alanine dosemeters for high-energy electrons determined using a Fricke primary standard *Phys. Med. Biol.* **57** 1413–32

Wagner D, Anton M and Vorwerk H 2011 Dose uncertainty in radiotherapy of patients with head and neck cancer measured by *in vivo* ESR/alanine dosimetry using a mouthpiece *Phys. Med. Biol.* **56** 1373–83

Waldeland E and Malinen E 2011 Review of the dose-to-water energy dependence of alanine and lithium formate EPR dosimeters and LiF TL-dosimeters—comparison with Monte Carlo simulations *Radiat. Meas.* **46** 945–51

Weise K and Wöger W 1999 *Messunsicherheit und Messdatenauswertung* (Weinheim: Wiley)

Zeng G G, McEwen M R, Rogers D W O and Klassen N V 2004 An experimental and Monte Carlo investigation of the energy dependence of alanine/EPR dosimetry: I. Clinical x-ray beams *Phys. Med. Biol.* **49** 257–70

Zeng G G, McEwen M R, Rogers D W O and Klassen N V 2005 An experimental and Monte Carlo investigation of the energy dependence of alanine/EPR dosimetry: II. Clinical electron beams *Phys. Med. Biol.* **50** 1119–29

IOP Publishing | Institute of Physics and Engineering in Medicine Physics in Medicine & Biology

Phys. Med. Biol. **62** (2017) 5462–5472 https://doi.org/10.1088/1361-6560/aa6ee2

Feasibility study of entrance and exit dose measurements at the contra lateral breast with alanine/electron spin resonance dosimetry in volumetric modulated radiotherapy of breast cancer

Daniela M Wagner[1], Petra Hüttenrauch[1], Mathias Anton[2], Philip von Voigts-Rhetz[3], Klemens Zink[3] and Hendrik A Wolff[4]

[1] Department of Radiotherapy and Radiation Oncology, University Hospital Goettingen, Robert-Koch-Str. 40, 37075 Goettingen, Germany
[2] Physikalisch-Technische Bundesanstalt, Bundesallee 100, 38116 Braunschweig, Germany
[3] Institut für Medizinische Physik und Strahlenschutz—IMPS, University of Applied Sciences Giessen-Friedberg, Wiesenstr. 14, 35390 Giessen, Germany
[4] University Hospital Goettingen, Radiology Munich, Burgstr. 7, 80331 Munich, Germany

E-mail: d.m.wagner@med.uni-goettingen.de

Received 7 November 2016, revised 10 April 2017
Accepted for publication 24 April 2017
Published 13 June 2017

Abstract

The Physikalisch-Technische Bundesanstalt has established a secondary standard measurement system for the dose to water, D_W, based on alanine/ESR (Anton *et al* 2013 *Phys. Med. Biol.* **58** 3259–82). The aim of this study was to test the established measurement system for the out-of-field measurements of inpatients with breast cancer.

A set of five alanine pellets were affixed to the skin of each patient at the contra lateral breast beginning at the sternum and extending over the mammilla to the distal surface. During 28 fractions with 2.2 Gy per fraction, the accumulated dose was measured in four patients. A cone beam computer tomography (CBCT) scan was generated for setup purposes before every treatment. The reference CT dataset was registered rigidly and deformably to the CBCT dataset for 28 fractions. To take the actual alanine pellet position into account, the dose distribution was calculated for every fraction using the Acuros XB algorithm. The results of the ESR measurements were compared to the calculated doses.

The maximum dose measured at the sternum was 19.9 Gy ± 0.4 Gy, decreasing to 6.8 Gy ± 0.2 Gy at the mammilla and 4.5 Gy ± 0.1 Gy at the distal surface of the contra lateral breast. The absolute differences between the calculated and measured doses ranged from −1.9 Gy to 0.9 Gy. No systematic error could be seen.

It was possible to achieve a combined standard uncertainty of 1.63% for $D_W = 5$ Gy for the measured dose. The alanine/ESR method is feasible for *in vivo* measurements.

Keywords: radiation therapy, alanine, breast cancer, contra lateral breast, surface dosimetry, EPR, ESR

(Some figures may appear in colour only in the online journal)

Introduction

The Physikalisch-Technische Bundesanstalt (PTB) has established a secondary standard measurement system for the dose to water, D_W, based on alanine/ESR (Anton *et al* 2013). Irradiation induces free radicals in the amino acid alanine, which are detected via ESR. The radiation transport properties of the detector material are very similar to those of water (Regulla and Deffner 1982, Bergstrand *et al* 2003). The relative response of the alanine detectors to megavoltage x-rays depends only very weakly on the photon beam quality and has a relative uncertainty of less than 0.4% (Anton *et al* 2013). The aim of this study was to test the established measurement system for out-of-field measurements. Therefore, we placed a set of five alanine pellets on the surface of the contra lateral breast from the sternum over the mammilla to the distal surface to measure the entrance and exit dose at the surface of the contra lateral breast during VMAT irradiation of the region. The findings were compared with the calculated dose of the TPS.

In this publication, all the stated uncertainties are standard (coverage factor $k = 1$) and were determined according to the terms of the reference stated in the GUM, which is the guide to the expression of uncertainty in measurement (JCGM100 2008). For the sake of simplicity, the dose or D is to be understood to be an absorbed dose to water in the following, unless otherwise stated. The measured dose D_{meas} is obtained using a correction factor $k_{Q,in\ vivo}$ which takes the different response of the alanine dosimeter to both the radiation quality Q and the different environments into account.

Methods and materials

Patient alanine dosimeter pellet irradiation and analysis

Four randomly chosen patients with breast cancer were included in this study. They all gave their informed consent to the quality assurance measurements.

Three patients received radiotherapy of the whole breast (prescribed dose 50.4 Gy) and the tumour was boosted (prescribed dose 61.6 Gy). For one patient, the sternal and parasternal lymph nodes were included (prescribed dose 45 Gy). For the planning protocols, we followed the RTOG guidelines (White *et al* 2017).

Two partial arcs were planned on the basis of a 5 mm spacing CT scan in the supine position (Tsai *et al* 2012, Pasler *et al* 2015). Optimization was done using the PRO algorithm V. 13.5; the dose distribution was calculated with Eclipse Version 13.5, using the Acuros

XB algorithm V. 13.5 (Varian Medical Systems, Helsinki, Finland) with a grid size of 2.5 mm × 2.5 mm × 2.5 mm (Vassiliev *et al* 2010). The treatment plans were approved by a physician based on dose volume histograms (DVH) and dose distributions on every CT slice in accordance with ICRU report 50.

For each patient, a set of five pellets (shrink-wrapped with 0.2 mm thick polyethylene foil) was placed on the surface of the contra lateral breast beginning at the sternum, extending over the mammilla to the distal surface, with a spacing of 4 cm to 5 cm. In order to facilitate reproducible positioning, the position of each labelled pellet set was marked on the surface of the contra lateral breast. Patient temperature at the surface was measured to be corrected for during the analysis process.

Before the VMAT treatment, the patient was set up on the treatment couch and a set of alanine pellets that was specific to the patient was attached every treatment day for 28 fractions. A CBCT scan was generated and compared to the reference image used for the treatment planning process. With the aid of the daily CBCT images for each patient, we were able to determine the positions of the alanine pellets in the *x*-, *y*- and *z*-direction.

To correct the calculated dose for daily positioning inaccuracies, the reference CT dataset was rigidly and deformably registered to the 28 daily CBCT datasets of each patient. In total, 112 rigid registrations and 112 deformable registrations were performed. Furthermore, the position of each of the five alanine pellets per patient was reconstructed on the reference CT dataset for every treatment day.

After reconstruction, the dose distribution was calculated on the deformed reference CT dataset, which presents the actual daily treatment setup using original Hounsfield units (HU) for the inhomogeneity correction for dose distribution calculation. It was thereby ensured that the dose to the surface of the contra lateral breast could be analysed. Dose distributions for the deformed reference CT dataset were calculated for all 28 fractions for each patient. The separate dose values were then summed and compared to the measured dose. The additional dose from the daily CBCT scanning was taken into account during the analysis process.

After the last fraction, the alanine pellets were sent to PTB in Braunschweig for analysis. The integrated doses measured by means of the alanine dosimeters D_{meas} were compared to the calculated doses D_{cal} from the TPS. The uncertainties are listed in table 1.

Please note, to demonstrate the potential of the alanine/ESR method, the measured dose and its corresponding uncertainties were differentiated from the delivered dose and its corresponding uncertainties. The term ‘calculated dose’ describes the delivered dose and includes the uncertainties of the TPS calculation process as well as the uncertainties of the treatment delivery process, like the monitor output fluctuation of the treatment machine as well. The term ‘measured dose’ describes the dose measured by the alanine/ESR method and includes, therefore, the uncertainties corresponding to the alanine/ESR method.

Reference irradiation

For the irradiation in the 6 MV photon beam reference fields at the UMG, stacks of four pellets served as a detector. The detector was contained in a polymethylmethacrylate (PMMA) holder, which fitted inside a watertight PMMA sleeve for a PTW M23332 ionization chamber and was irradiated in a water phantom. A dose of 15.0 Gy was delivered and repeated every four weeks. The pellets served to verify the calculated dose under reference conditions on the treatment machine. The alanine pellets used for the calibration were irradiated in the Co-60 reference field at PTB, as described previously (Anton *et al* 2013).

Table 1. List of uncertainties for D_{meas} and D_{cal}. All uncertainties are type B according to the GUM.

D_{meas}			D_{cal}		
Source of the uncertainty contribution	Relative standard uncertainty in %		Source of the uncertainty contribution	Relative standard uncertainty in %	
	Reference, $D_W = 15$ Gy	Surface, $D_W = 5$ Gy		In-field	Out-of- field
Primary standard	—	0.22%	Monitor output fluctuations of treatment machine	0.75%	
Base function detectors			In-field dose calculation of TPS	1.5%	
Reproducibility of irradiation	0.07%		Out-of-field dose calculation of TPS		14%
Irradiation temperature	0.05%		Basic data measurements	1.0%	
Intrabatch homogeneity	0.11%		**Combined uncertainty**	2.0%	14.1%
Average mass of eight pellets	0.04%				
ESR amplitude	0.09%				
Test detectors					
Reproducibility of irradiation	0.12%	0.12%			
Irradiation temperature	0.06%	0.35%			
Intrabatch homogeneity	0.15%	0.30%			
Average mass of four pellets	0.05%	0.10%			
ESR amplitude	0.18%	1.01%			
Further corrections					
Fading corrections k_F	0.14%				
Quality corrections k_Q	0.35%	—			
Quality and environment corrections $k_{Q,env}$	—	1.00%			
CBCT dose correction	—	0.54%			
Combined uncertainty	0.52%	1.63%			

ESR measurements and analysis

ESR measurements were conducted at PTB. The parameters are listed in a previous publication (Anton 2006), which also contains a detailed description of the hardware.

The data analysis method and uncertainty calculation has been described in detail in previous publications (Anton 2006, 2008, Anton *et al* 2013). The uncertainties for the measured dose D_{meas} are listed in table 1.

Uncertainty considerations

The calculation of the uncertainties associated with the alanine measurements was described in detail in the appendix of a previous publication (Anton *et al* 2013) and the determination of the uncertainties associated with the dose calculation and dose delivery by Wagner *et al* (2008). Additional uncertainties specific to the surface measurements have to be taken into account.

The irradiation conditions for the surface measurements are far from reference conditions: radiation may impinge on the detector directly without any tissue in front of it, or it may impinge on the detector from the inside of the patient, i.e. with air on the back and the resulting reduced backscatter. Therefore the correction factor $k_{Q,\mathrm{surface}}$ for the quality corrections was determined at the Institut für Medizinische Physik und Strahlenschutz IMPS (University of Applied Sciences Giessen, Germany) using Monte Carlo (MC) simulations with the EGSnrc package, user code DOSRZnrc (Kawrakow 2000, Kawrakow *et al* 2010), which is $k_{Q,in\ vivo} = 0.988$ with a relative standard uncertainty of 1%.

An uncertainty of 1.5% was taken into account for the accuracy of the in-field dose calculation of VMAT treatment plans using Eclipse Version 13.5 and the photon algorithm Acuros XB. As a result, a calculated dose uncertainty of 2.0% was obtained. For the uncertainty of the out-of-field dose, the average deviation between the measured and calculated out-of-field doses determined by Taddai *et al* (2013) was used and is 14.0%. Taddai *et al* (2013) measured the out-of-field dose using thermoluminescent dosimeters. The dose was calculated using Eclipse and the analytical anisotropic algorithm AAA V. 8.9. A combined standard uncertainty for the in-field calculated dose of 2.0% and a combined standard uncertainty for the out-of-field dose of 14.1% was obtained, respectively.

The maximum dose delivered by the CT per fraction is 4.7 mGy (manual dose in CBCT 2012), which corresponds to 132 mGy for the whole treatment. However, this is the maximum dose received by any detector for the whole treatment. The minimum is assumed to be zero. Following GUM for the determination of the CBCT dose uncertainty, the expected value is 65.8 mGy with an uncertainty of 38 mGy (JCGM100 2008). The radiation quality used for CBCT was 110 kV. For this quality, the response of the alanine dosimeter is ~0.7 relative to the response to Co-60 radiation (Anton and Büermann 2015). The measured dose due to CBCT is therefore estimated to be 46 mGy with an uncertainty of 27 mGy. This dose has to be viewed as a systematic deviation. According to the GUM (JCGM100 2008), the value of 46 mGy has to be subtracted from the measured dose and an uncertainty component of 27 mGy has to be included in the list of uncertainties.

Although the measurement uncertainty for the patients' temperature was 0.5 °C, an uncertainty of 1.7 °C was taken into account in order to allow for individual variations. This leads to an uncertainty in the correction factor of 0.3% since the patients' mean temperature was 34.5 °C, which yielded with a correction of 0.975.

Statistical considerations

The uncertainties have been determined according to the guidelines given by the International Organization for Standardization (ISO) in the 'guide to the expression of uncertainty in measurement (GUM)' (JCGM100 2008). According to the classification given in the GUM, all uncertainty components tabulated in table 1 are type B uncertainties, which means that the probability distributions (and hence the variances) associated with the measurements were obtained from previous measurements, scientific judgement or experience (Anton 2006, Anton *et al* 2013).

Results

Reference alanine dosimeter pellet irradiation

Reference pellets were irradiated on six different days during patient treatment, starting with the first treatment of the first patient and ending with the last treatment of the last patient.

Table 2. Dose difference in Gy. The values are highlighted where the discrepancy exceeds the uncertainty. The total uncertainty for the in-field dose is 2.5% and for the out-of-field dose 14.1%, respectively. The in-field is defined as the negative distance from the field edge in cm to zero, and the out-of-field as the positive distance from the field edge in cm, respectively. Please note that the dosimeter probe at the sternum for the first patient was removed after 14 fractions. For a better comparison, the sternum dose for patient 1 was multiplied by 25/14 to show the estimated dose for the whole treatment.

Patient	Used CBCT datasets for analyses	Distance from field edge in cm	D_{cal} in Gy	D_{meas} in Gy	$D_{cal} - D_{meas}$ in Gy	Dose difference > uncertainty (%)
1	25/28	2.8	16.1	16.4	−0.4	<14.1
		6.7	10.9	10.7	0.2	<14.1
		10.7	5.7	5.8	−0.1	<14.1
		14.6	3.4	4.0	**−0.6**	>14.1
		18.4	2.8	3.0	−0.2	<14.1
2	27/28	1.0	10.4	12.3	**−1.9**	>14.1
		5.0	5.7	6.2	−0.5	<14.1
		8.9	5.3	4.9	0.4	<14.1
		12.9	4.6	4.7	−0.1	<14.1
		16.7	3.3	4.5	**−1.2**	>14.1
3	20/28	0.0	17.5	17.7	−0.2	<2.5
		4.4	10.5	9.9	0.6	<14.1
		9.1	5.5	5.5	0.0	<14.1
		13.8	3.1	3.5	−0.4	<14.1
		18.8	2.7	1.8	**0.9**	>14.1
4	24/28	−4.1	20.6	19.9	**0.7**	>2.5
		0.3	10.2	9.5	0.7	<14.1
		3.8	6.7	6.8	−0.1	<14.1
		7.8	4.1	3.9	0.2	<14.1
		11.8	3.0	4.1	**−1.1**	>14.1

A dose of 15.0 Gy was delivered. The mean dose determined by the secondary standard measurement system of PTB was 15.0 Gy ± 0.1 Gy. The relative deviation between the determined dose and the stated dose was always less than 1%, which is well within the total uncertainty of 1.3%. For D_{meas}, the uncertainties for the base function and test detectors as well as further correction were taken into account, and for D_{cal}, the uncertainties for monitor output fluctuation and basic data measurements were also accounted for. The uncertainty for the primary standard of 0.22% was not taken into account when comparing the reference irradiation to the national standard, since the primary standard is common to both measurements.

Comparison of measured and calculated dose

The results are presented in table 2. Figure 1 presents a comparison of the measured and calculated dose, where the calculated dose is shown as dark grey bars and the measured dose as light grey bars, both as a function of the distance from the field edge. Figure 2 presents the deviation between the measured and calculated dose as a function of the distance from the field edge.

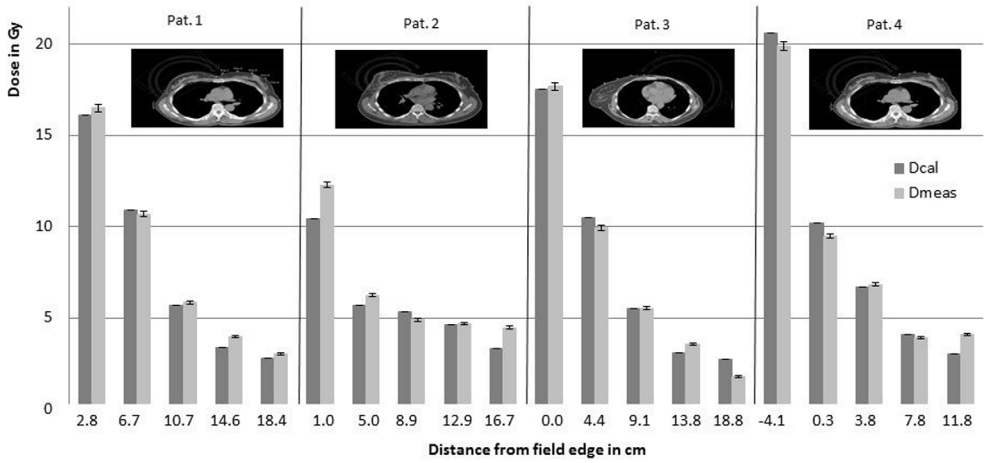

Figure 1. Display of the calculated dose in dark grey bars and the measured dose in light grey bars as a function of the distance from the field edge in cm. The probe position is visible on the representative CT layer of each patient, as well as the arcs, the PTV and CTV. The dose values are given in Gy. Please note that the dosimeter probe at the sternum for the first patient was removed after 14 fractions. For a better comparison, the sternum dose for patient 1 was multiplied by 25/14 to show the estimated dose for the whole treatment.

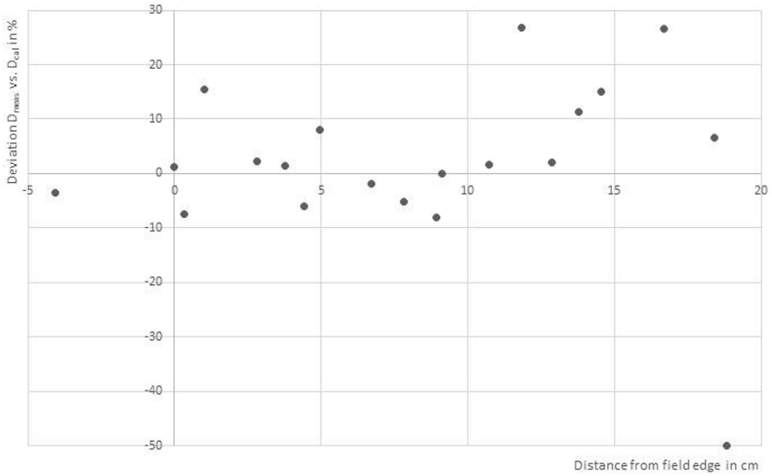

Figure 2. Display of the deviation between the measured and calculated dose in % as a function of distance from the field edge in cm. Please note that the dosimeter probe at the sternum for the first patient was removed after 14 fractions. For a better comparison, the sternum dose for patient 1 was multiplied by 25/14 to show the estimated dose for the whole treatment.

Out of the 28 acquired CT datasets, only a subset showed an image quality that was sufficient for image registration. Table 2 shows which CT scans were chosen for further analysis for each patient. For patient one, the alanine pellets were accidentally stored inside the treatment room during one treatment day—luckily outside the treatment beams. However, neither the reference pellets nor the unirradiated 'controls' showed any inadvertent irradiation. The probe positioned at the sternum was removed after 14 fractions. At the sternum, the dose

delivered over all the fractions was estimated to lie outside the useable range of the alanine dosimeter, which is 2 Gy–25 Gy due to the calibration curve used in this study. For patient two, the alanine pellets unfastened after CBCT generation during one treatment fraction. Therefore, a reconstruction of the calculated dose for this fraction was not possible.

The distance from the field edge ranged from –4.1 cm to 18.8 cm. The calculated doses ranged from 20.6 Gy in-field to 2.7 Gy out-of-field, and the measured doses from 19.9 Gy to 1.8 Gy, respectively. The term 'in-field' is defined as negative distances, and the term 'out-of-field' as positive distances. The dose difference between the calculated and measured dose is less than 2 Gy. The highlighted value lies outside the estimated total uncertainty for the ESR method and the dose delivery process, including the TPS calculation.

Discussion

The results show no systematic error. Overall, the dose differences were within the estimated uncertainties, but there were some outliers. For example, for patient four the first alanine pellet was positioned well within the high-dose area (distance from field edge −4.08 cm). The corresponding dose difference was 0.7 Gy, and therefore higher than the estimated combined uncertainty of 2.5% for in-field measurements. In comparison, the dose difference for the first alanine pellet of patient three was −0.2 Gy at a distance from the field edge of 0.0 cm, and therefore well within the estimated combined uncertainty. For distances far outside the treatment fields, the dose difference was sometimes well within the estimated combined uncertainty and sometimes far from it. For example, the dose difference for alanine pellet five of patient one was −0.2 Gy, and the deviation between the measured and calculated dose of 6.7% for alanine pellet five of patient three was 0.9 Gy with a deviation of −50%, respectively. The distance from the field edge was comparable in both cases (patient one versus patient three, 18.4 cm versus 18.8 cm, respectively).

Photon algorithm

The alanine pellets were positioned on the surface of the patients in the build-up region. Even with advanced algorithms TPS does not provide accurate dosimetry in this region. The grid size for dose calculation plays an important role, and for accurate dosimetry a small grid size should be used (Akino *et al* 2013). The dose discrepancies are smaller using IMRT techniques. This possible explanation applies to the calculated dose.

Breathing of the patient

Before delivering the dose, a CBCT dataset was acquired. This dataset was rigidly and deformably registered to the original CT dataset, which was acquired for the treatment planning process. The setup inaccuracy was thereby reduced to a minimum and the actual alanine pellet position was used for the analysis on every treatment day; however, the breathing motion was not minimized.

The dose difference between the measured and calculated dose was not lower at the distal location than in the other locations, which could mean that all the pellets were affected by the same breathing amplitude. The breathing amplitude should be characterized at each

measurement position. According to Ono *et al* (2011), this could easily be performed using a smartphone, with the possible explanation applying to the calculated dose.

Steep dose gradients at the field edge and beam data measurements

During VMAT treatment, steep dose gradients are generated. Slight changes in the positioning of the pellets in the region of the steep dose gradient at the field edge between the high dose area and the low dose area highly influence the measured dose values.

Out-of-field dose measurements during basic data acquisition were undertaken up to 7 cm outside of the beam. The pellets at the distal surface of the contra lateral breast were positioned well outside this range. The TPS dose calculation was therefore carried out using interpolated data for this region of interest. In general, the uncertainty of the measurement increases if the dose is reduced (Kron *et al* 2016). The distal alanine pellets were affected most by the limited beam data measurements. As shown in figure 2, the deviation between D_{cal} and D_{meas} near the field edge is comparable to other locations away from the field edge. These results show that the movement of the detector is particularly unimportant. To strengthen this statement, measurements in a static phantom setup should carried out.

Clinical application

The alanine pellets can be applied easily, and due to markings on patients' skin and the easily reachable anatomical region, daily positioning was reproducible. From a clinical point of view, the positioning and realization of these measurements were easy to perform and also feasible.

For a systematic analysis, a total of four patients presents a small data set. However, figure 2 shows a slight tendency of the results to exhibit larger measured values than planned. The possible causes have to be clarified. Either more patients or phantom studies without breathing motion should be carried out to rule out whether the TPS calculation gets the off-axis dose wrong systematically. In conclusion, alanine/ESR is feasible for *in vivo* measurements.

Some other studies showed recently the potential of alanine/ESR dosimetry for *in vivo* dosimetry tasks (Baffa and Kinoshita 2014, Rech *et al* 2014, Alves *et al* 2015, Knudtsen *et al* 2016). Alanine/ESR dosimetry fulfils many of the required properties for several clinical applications, such as water-equivalent composition, independence of the sensitivity for the energy range used in therapy and high precision (Baffa and Kinoshita 2014), from which our study benefits.

Conclusion

We tested alanine/ESR to measure the dose at the surface of the contra lateral breast for patients with breast cancer during VMAT irradiation.

For the irradiation of alanine dosimeter pellets under reference conditions, relative deviations of less than 1% referring to the national standard were achieved. For the surface measurements, the absolute differences between the measured and the calculated dose ranged from −1.1 Gy to 1.9 Gy at the surface of the contra lateral breast.

It was possible to achieve a combined standard uncertainty of 1.63% for $D_W = 5$ Gy for the measured dose. The alanine/ESR method is feasible for *in vivo* measurements.

Acknowledgments

We wish to thank Professor Dr Hess for his suggestion to conduct this study. We wish to thank T Hackel and D-M Boche (PTB) for their help during the preparation, measurement and irradiation of the pellets used for the calibration. We thank K Steenken for his help with the treatment planning. We also thank the patients for enduring the repeated fixture and removal of the alanine pellets.

Conflict of interest notification

There are no conflicts of interest to be stated.

References

Alves G G, Kinoshita A, Oliveira H F, Guimaraes F S, Amaral L L and Baffa O 2015 Accuracy of dose planning for prostate radiotherapy in the presence of metallic implants evaluated by electron spin resonance dosimetry *Braz. J. Med. Biol. Res.* **48** 644–9

Anton M 2006 Uncertainties in alanine/ESR dosimetry at PTB *Phys. Med. Biol.* **51** 5419–40

Anton M 2008 Postirradiation effects in alanine dosimeter probes of two different suppliers *Phys. Med. Biol.* **53** 1241–58

Anton M and Büermann L 2015 Relative response of the alanine dosimeter to medium energy x-rays *Phys. Med. Biol.* **60** 6113–29

Anton M, Kapsch R P, Krauss A, von Voigts-Rhetz P, Zink K and McEwen M 2013 Difference in the relative response of the alanine dosimeter for megavoltage x-ray and electron beams *Phys. Med. Biol.* **58** 3259–82

Akino Y, Das I J, Bartlett G K, Zhang H, Thompson E and Zook J E 2013 Evaluation of superficial dosimetry between treatment planning system and measurement for several breast cancer treatment techniques *Med. Phys.* **40** 011714

Baffa O and Kinoshita A 2014 Clinical applications of alanine/electron spin resonance dosimetry *Radiat. Environ. Biophys.* **53** 233–40

Bergstrand E S, Shortt K R, Ross C K and Hole E O 2003 An investigation of the photon energy dependence of the EPR alanine dosimetry system *Phys. Med. Biol.* **48** 1753–71

ICRU Report 50 1994 International commission and radiation units and measurements. prescribing, recording, and reporting photon therapy (Bethesda, MD: ICRU) www.icru.org/home/reports/prescribing-recording-and-reporting-photon-beam-therapy-report-50

JCGM 100 2008 Evaluation of measurement data—guide to the expression of uncertainty in measurement GUM 1995 with minor corrections, Technical report, BIPM, Working Group 1 of the Joint Committee for Guides in Metrology (JCGM/WG 1) www.bipm.org/utils/common/documents/jcgm/JCGM_100_2008_E.pdfw

Kawrakow I 2000 Accurate condensed history Monte Carlo simulation of electron transport: I. EGSnrc, the new EGS4 version *Med. Phys.* **27** 485–98

Kawrakow I, Mainegra-Hing E, Rogers D W O, Tessier F and Walters B R B 2010 The EGSnrc code system: Monte Carlo simulation of electron and photon transport, NRC report PIRS-701 *Technical Report* National Research Council, Canada

Knudtsen I S, Svestad J G, Skaug Sande E P, Rekstad B L, Rodal J, van Elmpt W, Öllers M, Hole E O and Malinen E 2016 Validation of dose painting of lung tumours using alanine/ESR dosimetry *Phy. Med. Biol.* **61** 2243–54

Kron T, Lehmann J and Greer P B 2016 Dosimetry of ionizing radiation in modern radiation oncology *Phys. Med. Biol.* **61** 167–205

Ono T, Takegawa H, Ageishi T, Takashina M, Numasaki H, Matsumoto M and Teshima T 2011 Respiratory monitoring with an acceleration sensor *Phys. Med. Biol.* **56** 6279–89

Pasler M, Lutterbach J, Björnsgard M, Reichmann U, Bartelt S and Georg D 2015 VMAT techniques for lymph node-positive left sided breast cancer *Z. Med. Phys.* **25** 104–11

Rech A B, Barbi G L, Ventura L H, Guimaraes F S, Oliveira H F and Baffa O 2014 *In vivo* dose evaluation during gynaecological radiotherapy using L-alanine/ESR dosimetry *Radiat. Prot. Dosim.* **159** 194–8

Regulla D F and Deffner U 1982 Dosimetry by ESR spectroscopy of alanine *Int. J. Rad. Appl. Instrum.* A **40** 1039–43

Taddai P J, Jalbout W, Howell R, Khater N, Geara F, Homann K and Newhauser W D 2013 Analytical model for out-of-field dose in photon craniospinal irradiation *Phys. Med. Biol.* **58** 7463–79

Tsai P F, Lin S-M, Lee S H, Yeh C Y, Huang Y T, Lee C C and Hong J H 2012 The feasibility study of using multiple partial volumetric-modulated arcs therapy in early stage left-sided breast cancer patients *J. Appl. Clin. Med. Phys.* **13** 3806

Vassiliev O N, Wareing T A, McGhee J, Failla G, Salehpour M R and Mourtada F 2010 Validation of a new grid-based Boltzmann equation solver for dose calculation in radiotherapy with photon beams *Phys. Med. Biol.* **55** 581–98

Wagner D, Anton M, Vorwerk H, Gsänger T, Christiansen H, Poppe B, Hess C F and Hermann R M 2008 *In vivo* alanine/electron spin resonance (ESR) dosimetry in radiotherapy of prostate cancer: a feasibility study *Radiother. Oncol.* **88** 140–7

White J *et al* 2017 RTOG radiation therapy oncology group, breast cancer atlas for radiation therapy planning www.rtog.org/LinkClick.aspx?fileticket=vzJFhPaBipE%3d&tabid=236

Tagungsbeiträge

[1] von Voigts-Rhetz P, Vorwerk H and Zink K (2017), Experimental and Monte Carlo investigation of the depth-dependent fluence perturbation of parallel-plate chambers in clinical electron beams, International Conference on Monte Carlo Techniques for Medical Applications (MCMA2017), 15. - 18. Oktober 2017, Neapel, Italien

[2] Pretzsch T, Czarnecki D, von Voigts-Rhetz P, Zink K (2017), Monte Carlo based investigation of the beam quality correction factor kQ depending on the chamber‘s level of detail. International Conference on Monte Carlo Techniques for Medical Applications (MCMA2017), 15. - 18. Oktober 2017, Neapel, Italien

[3] Czarnecki D, von Voigts-Rhetz P, Zink K (2017), Investigation of Monte Carlo calculations for reference dosimetry regarding new ICRU-90 recommendations. International Conference on Monte Carlo Techniques for Medical Applications (MCMA2017), 15. - 18. Oktober 2017, Neapel, Italien

[4] von Voigts-Rhetz, P., Vorwerk, H. and Zink, K. (2017), Experimental investigation of the depth-dependent fluence perturbation of parallel-plate chambers in clinical electron beams. 2017 AAPM Annual Meeting, 30. July - 3 August Denver CO

[5] Zink K, Czarnecki D, von Voigts-Rhetz P (2017), Impact of new ICRU recommendations on clinical photon and electron reference dosimetry. Jahrestagung Biomedizinische Technik und Dreiländertagung der Medizinischen Physik, 10.-13. September 2017, Dresden

[6] Alissa M, von Voigts-Rhetz P, Zink K (2017), Response of ionization chambers in the presence of magnetic fields. Jahrestagung Biomedizinische Technik und Dreiländertagung der Medizinischen Physik, 10.-13. September 2017, Dresden

[7] Czarnecki D, von Voigts-Rhetz P, Poppe B and Zink K (2016), SU-G-TeP1-03: Beam Quality Correction Factors for Linear Accelerator with and Without Flattening Filter. Med. Phys., 43: 3652. doi: 10.1118/1.4956993 AAPM Annual Meeting, 31 July - 4 August, Washington DC

[8] von Voigts-Rhetz P., Pretzsch, T., Czarnecki, D., Vorwerk, H. and Zink, K. (2016), SU-F-T-72: Experimental Determination of the Positionuncertainties for ROOS Ionization Chambers in Clinical Electron Beams. Med. Phys., 43: 3478.
doi: 10.1118/1.4956208 AAPM Annual Meeting, 31 July - 4 August, Washington DC

[9] von Voigts-Rhetz P, Czarnecki D and Zink K (2016), On the relative response of

alanine dosimeters in clinical photon beams. 18th International Conference on Solid State Dosimetry, SSD18, Munich

[10] Pretsch T, von Voigts-Rhetz P, Zink K (2016), Experimentelle Untersuchung der Positioniergenauigkeit einer Roos-Flachkammer in klinischen Elektronenfeldern 47. Jahrestagung der DGMP, 7. - 10. September 2016, Würzburg

[11] Czarnecki D, von Voigts-Rhetz P and Zink K (2015), SU-E-T-525: Ionization Chamber Perturbation in Flattening Filter Free Beams. Med. Phys., 42: 3456. doi: 10.1118/1.4924887 AAPM Annual Meeting, 12 -16 July, Anaheim CA

[12] Langner N, Czarnecki D, von Voigts-Rhetz P and Zink K (2015), SU-E-T-350: Effective Point of Measurement and Total Perturbation Correction P for Parallel-Plate Ion Chambers in High-Energy Photon Beams. Med. Phys., 42: 3414. doi: 10.1118/1.4924711 AAPM Annual Meeting, 12 -16 July, Anaheim CA

[13] von Voigts-Rhetz P, Anton M, Czarnecki D and Zink K (2015), SU-E-T-608: Perturbation Corrections for Alanine Dosimeters in Different Phantom Materials in High-Energy Photon Beams. Med. Phys., 42: 3476. doi: 10.1118/1.4924971 AAPM Annual Meeting, 12 -16 July, Anaheim CA

[14] Czarnecki D., von Voigts-Rhetz P., Shishechian D. U. and Zink K. (2015), SU-E-J-69: Iterative Deconvolution of the Initial Photon Fluence for EPID Dosimetry: A Monte Carlo Based Study. Med. Phys., 42: 3279. doi: 10.1118/1.4924156 AAPM Annual Meeting, 12 -16 July, Anaheim CA

[15] Czarnecki D, von Voigts-Rhetz P, Zink K (2015), Dosimetrie kleiner Photonenfelder Ausgleichsfilterfreier Linearbeschleuniger. 46. Jahrestagung der Deutschen Gesellschaft für Mediznische Physik e.V., 9.-12. September 2015, Marburg

[16] Czarnecki D, von Voigts-Rhetz P, Zink K (2015), Untersuchungen zur Bestimmung der Kammerstörfaktoren im 60Co Strahlenfeld mittels Monte-Carlo-Simula-tionen. 46. Jahrestagung der Deutschen Gesellschaft für Mediznische Physik e.V., 9.-12. September 2015, Marburg

[17] von Voigts-Rhetz P, Pretzsch T, Vorwerk H, Zink K (2015), Experimentelle Bestimmung des Gesamtstörfaktors von zylindrischen Ionisationskammern in klinischen Elektronenfeldern. 46. Jahrestagung der Deutschen Gesellschaft für Mediznische Physik e.V., 9.-12. September 2015, Marburg

[18] Langner N, Czarnecki D, von Voigts-Rhetz P, Zink K (2015), Effektive Messpunktverschiebung und Gesamtstörungsfaktor p von Flachkammern in hochenergetischer

Photonenstrahlung. 46. Jahrestagung der Deutschen Gesellschaft für Mediznische Physik e.V., 9.-12. September 2015, Marburg

[19] Czarnecki D, von Voigts-Rhetz P and Zink K (2014), TH-E-BRE-06: Challenges in the Dosimetry of Flattening Filter Free Beams. Med. Phys., 41: 566–567. doi: 10.1118/1.4889658 AAPM Annual Meeting Austin TX July 20 - July 24

[20] von Voigts-Rhetz P and Zink K (2014), SU-E-T-448: On the Perturbation Factor P_{cav} of the Markus Parallel Plate Ion Chambers in Clinical Electron Beams, Monte Carlo Based Reintegration of An Historical Experiment. Med. Phys., 41: 329. doi: 10.1118/1.4888781 AAPM Annual Meeting Austin TX July 20 - July 24

[21] von Voigts-Rhetz P, Anton M, Zink K (2014), Determination of the relative response of alanine dosimeters in Ir-192 HDR photon fields. Joint Conference of Medical Physics, Zürich, Schweiz, 7.-10. September 2014

[22] Czarnecki D, von Voigts-Rhetz P, Zink K (2014), A study of ionization chamber perturbation corrections in flattening filter free beams. Joint Conference of Medical Physics, Zürich, Schweiz, 7.-10. September 2014

[23] von Voigts-Rhetz P, Czarnecki D, Zink K (2014), Perturbation corrections for parallel plate chambers in clinical electron beams: a reiteration of a historical experiment. Joint Conference of Medical Physics, Zürich, Schweiz, 7.-10. September 2014

[24] von Voigts-Rhetz P and Zink K. (2013), EP-1130: Determination of the effective point of measurement for parallel plate and cylindrical ionization chambers. Radiotherapy and Oncology, 106(2): 426. doi: 10.1118/1.4888781 2nd ESTRO Forum 19-23 April 2013, Geneva

[25] Zink K, von Voigts-Rhetz P (2013), Verdrängungseffekt p_dis und Fluenzstörung p_cav bei Flachkammern in klinischen Elektronenfeldern – die Wiederholung eines historischen Experiments. 44. Jahrestagung der Deutschen Gesellschaft für Medizinische Physik e.V. (DGMP), 18 – 21. September 2013,Köln. Abstractband (ISBN: 978-3-9816002-1-6), 58-62

[26] von Voigts-Rhetz P, Zink K (2012), Bestimmung des effektiven Messpunktes von Zylinderkammern und Flachkammern in primärer Elektronenstrahlung mittels Monte Carlo Simulation. 43. Jahrestagung der Deutschen Gesellschaft für Medizinische Physik e.V. (DGMP), 26.-29. September 2012, Jena

[27] von Voigts-Rhetz P, Zink K (2011), Untersuchung der Energieabhängigkeit des Strahlungsqualitäts-Korrektionsfaktors kE von Thermolumineszenz- und Alanindo-

simetern in primärer Elektronenstrahlung. Drei Länder Tagung Medizinische Physik, ÖGMP-DGMP-SGSMP, ISBN: 3-925218-89-0, Wien 2011

[28] von Voigts-Rhetz P, Kunz M, Zink K (2011), Bestimmung des Ansprechvermögens von Alanin in MV-X Bestrahlungsfeldern – Ein Vergleich zwischen FLUKA und EGSnrc. Drei Länder Tagung Medizinische Physik, ÖGMP-DGMP-SGSMP, ISBN: 3-925218-89-0, Wien

[29] von Voigts-Rhetz P, Wulff J, Zink K (2010), Verschiebung des Messortes einer zylindrischen Kompaktionisationskammer im Feld hochenergetischer Photonen. DGMP 2010, Herausgeber N. Hodapp, J. Hennig, M. Mix, ISBN 3-925218-88-2, Freiburg

A Verzeichnis der akademischen Lehrer

Meine akademischen Lehrer waren die Damen und Herren:

An der Fachhochschule Gießen-Friedberg:
Breckow; Böckmann; Cemic; Dammann; Dworschak; Fiebich; Gabrich; Gokorsch; Kirschbaum; Kleinöder; Klös; Koch; Leicht; Metz; Prehn; Seipp; Subke; Trampisch; Zink

An der Universität Umeå:
Olofsson; Tölki

An der Technische Hochschule Mittelhessen:
Breckow; Fiebich; Koch; Schanze; Zink

B Danksagung

Ich möchte allen meinen tiefsten Dank aussprechen die mich ermutigt, unterstützt und motiviert haben diese Doktorarbeit zu erstellen.
Als erstes möchte ich mich bei Frau Hilke Vorwerk für die Möglichkeit bedanken unter ihrer Betreuung die Promotion an der Philipps-Universität Marburg durchführen zu können.
Einen ganz besonderen Dank möchte ich an Herrn Klemens Zink richten für seine Bereitschaft der Betreuung. Die unermüdliche Unterstützung in Kombination mit seinem Fachwissen, ermöglichte erst die Durchführung dieser Arbeit. Des Weiteren möchte ich Klemens Zink für sein Engagement in meiner persönlichen Weiterbildung auf Kongressen und Tagungen weltweit danken.
Zuletzt möchte ich mich bei den Kollegen und Kolleginnen aus dem Institut für medizinische Physik für die ereignisreiche Zeit bedanken.